Optical studies of compact binaries in globular clusters and the Galactic disk

Cover: the globular cluster M4 at optical and X-ray wavelengths. Both strips are $14' \times 2'$ in size and cover the same part of the sky (North to the right, East on top). The optical image is an average of three 2 min exposures in the V-band image, obtained on February 21, 2002 with the *Wide Field Imager* at the ESO 2.2 meter telescope at La Silla, Chile. The X-ray image was constructed from the 25 ks *Chandra* observation from June 30, 2000 and covers part of the ACIS-S3 and S4 chips. See Chapter 2 for more information

Omslag: De bolvormige sterrenhoop M4 in optisch en röntgen licht. Beide opnames zijn $14' \times 2'$ groot en beslaan hetzelfde gedeelte aan de hemel (Noord naar links en oost boven). De optische opname is het gemiddelde van drie 2 min belichtingen in de V-band, verkregen op 21 februari 2002 met de *Wide Field Imager* van de ESO 2.2 meter telescoop op La Silla, Chili. De röntgenopname is gemaakt van de 25 ks *Chandra* waarneming van 30 juni 2000 en beslaat delen van de ACIS-S3 en S4 chips. Zie hoofdstuk 2 voor meer informatie.

This thesis was typeset in LaTeX by the author and printed by Haveka in Alblasserdam.

ISBN-10: 90–393–4401–9
ISBN-13: 978–90–393–4401–9

Optical studies of compact binaries in globular clusters and the Galactic disk

Optische studies van compacte dubbelsterren
in bolvormige sterrenhopen en de Melkweg

(met een samenvatting in het Nederlands)

Proefschrift

ter verkrijging van de graad van doctor aan de Universiteit Utrecht
op gezag van de rector magnificus, prof. dr. W.H. Gispen,
ingevolge het besluit van het college voor promoties
in het openbaar te verdedigen op

maandag 11 december 2006 des middags te 2.30 uur

door

Cornelis Gerrit Bassa

geboren op 16 oktober 1978, te Tiel

Promotoren: Prof. dr. F. W. M. Verbunt
Prof. dr. M. H. van Kerkwijk

This research has been supported by the Netherlands Organization for Scientific Research (NWO).

Aan mijn ouders

Hoe het tijdsbestek van een generatie
het verschil kan maken
tussen keuzevrijheid
en traditie

To my parents

How the timeframe of a generation
can make the difference
between freedom of choice
and tradition

Contents

Chapter 1

Introduction and summary

With the advent of the telescope, several stars which appeared single to the naked eye were resolved into close pairs: so-called optical doubles. Based on the argument of probability, John Michell showed (Michell 1767) that most of these optical doubles must be physically related, and that the small angular distance between the stars in such pairs was not due to chance. It was not until 1803 that William Herschel, the discoverer of the planet Uranus, perceived the motion between the stars in the optical double Castor (α Geminorum). In Herschel (1803), he writes;

> *Having thus ascertained that no perceptible change in the distance of the stars has taken place, we are now to examine the angle of position. In the year 1779, it was 32°47′ north preceding; and, by a mean of the three last measures I have taken, it is now only 10°53′. In the space of about 23 years and a half, therefore, the angle of position has manifestly undergone a diminution, of no less than 21°54′; and, that this change has been brought on by a regular and gradual decrease of the angle, will be seen when the rest of the measures come to be examined.*

Though he cannot exclude the possibility that the apparent motion between the two stars can be explained by the proper motions of the two stars and the motion of our solar system, he considers this unlikely, as he has also measured changes in the position angle in the optical doubles γ Leonis, ϵ Bootis, ζ Herculis, δ Serpentis and γ Virginis. He concludes;

> *In this manner, we may certainly account for the phenomena of the changes which have taken place with the two stars of α Geminorum. But the complicated requisites of the motions which have been exposed to our view, must surely compel every one who considers them to acknowledge, that such a combination of circumstances involves the highest degree of improbability in the accomplishment of its conditions. On the other hand, when a most simple and satisfactory*

> *explanation of the same phenomena may be had by the effects of mutual attraction, which will support the moving bodies in a permanent system of revolution round a common centre of gravity, while at the same time they follow the direction of a proper motion which this centre may have in space, it will hardly be possible to entertain a doubt to which hypothesis we ought to give the preference.*

Combining his measurements with a measurement made by Bradley in 1759 (which was independently confirmed by Maskelyne in 1760), Herschel estimates the orbital period of Castor to be slightly longer than 342 years. The present value for the orbital period is 467 ± 12 years (Heintz 1988).

Herschel was the first to observe the motion of two stars around a common center of gravity. In such a *visual* binary, both binary members are resolved. At the beginning of the 20th century, spectroscopic observations of these stars showed that both of them (α Geminorum A and B) display radial velocity variations and are *spectroscopic* binaries. With orbital periods of $P_b = 9.21$ days for Aa and Ab and 2.93 days for Ba and Bb (Curtis 1906; Stebbins 1914), these binaries are much smaller and cannot be resolved into a visual binary. However, this is not the end of the story about Castor. It was found that Castor is a sextuple system, as a tight spectroscopic binary ($P_b = 0.814$; Joy & Sanford 1926) shares the same parallax and proper motion as the center of mass of the Castor AB system. For Castor C, the binary members periodically eclipse each other, making this system an *eclipsing* binary.

In the two centuries that passed since Herschel's discovery of the first binary star, binaries became one of the cornerstones of astrophysics. Besides providing the ability to accurately determine stellar masses, radii and luminosities, stars in binaries will, in general, evolve differently from a single star with the same properties. Due to the gravity of both stars and their motion around the common center of mass, the effective potential of either star is limited to the tear-drop shaped Roche equipotential surface surrounding both stars. Points inside the Roche lobes are bound to one of the binary members. If the radius of a binary member expands and fills its Roche lobe, matter is transferred to the other member. As a result, the binary orbit changes, and because the binary members have gained or lost matter, they evolve differently as compared to single stars of the same mass and metallicity.

This thesis deals with optical and X-ray observations of binaries in the form of radio pulsars and X-ray sources, located in globular clusters and in the Galactic disk. From the observations various properties of the binaries and the binary members are determined. The following sections introduce the scientific background to the systems studied in this thesis.

1.1 Binaries in globular clusters

Globular clusters are bound groups of a few thousand to more than a million stars, and are the densest stellar systems in our Galaxy. At present, about 150 globular clusters are known in the Milkyway (Harris 1996). They are amongst the oldest structures present in our Galaxy, with ages of about 10–13 Gyr (see Carretta et al. 2000 for a review). However, globular clusters are unstable for gravitational collapse. Due to the distribution of energy between the single stars in a cluster, some stars obtain velocities large enough to cross the tidal boundary and

remove energy from the cluster. This in turn causes the inner regions to shrink, increasing the average velocity of the stars, leading to more evaporation. This runaway process is called the *gravothermal collapse* and would lead to a collapse of the core of a globular cluster (Lynden-Bell & Wood 1968).

To reverse such a collapse, energy must be added to the globular cluster core. During the early life of the globular cluster, wind-driven mass loss from the most massive stars acts as an energy source. However, the most important energy sources are the binary stars. Binaries in the core of the cluster can interact with single stars and convert binding energy of the binary into kinetic energy of the single star, and reverse the collapse of the core. Through this process the binaries act as an energy reservoir which can be tapped in times of need. Through this mechanism, the globular cluster can enter a prolonged state of core oscillations (see Goodman 1987 for simulations of clusters containing stars with identical masses).

The presence of binaries in globular clusters was dramatically proved by the first X-ray observations of *Uhuru* and *OSO-7* (Giacconi et al. 1974; Clark et al. 1975). These showed that the bright X-ray sources (with $L_X > 10^{36}\,\mathrm{erg\,s^{-1}}$) that were discovered in globular clusters, represented a significant overabundance when compared to sources in the Galactic field. Though these globular clusters contain $\lesssim 0.1\%$ of the stars of our Galaxy, they contain 10% of the bright X-ray sources (Katz 1975). It was soon realized that these sources were neutron stars accreting matter from stellar binary companions (low-mass X-ray binaries), and that these binaries were likely to be formed through dynamical interactions (Clark 1975), either through three-body interactions or two-body tidal capture.

However, besides these bright X-ray sources, not many binary systems were known at the time. This was primarily due to selection effects, as spectroscopic radial velocity studies could only monitor a few bright giants, and as photometric variability suffered from crowding in the dense globular cluster cores. As a result, only a few dozen binaries were clearly identified by the time of the review of Hut et al. (1992).

With the turn of the millennium, the field received an enormous boost with the launch of the *Chandra* X-ray Observatory. Due to the improved sensitivity and spatial resolution of the instruments aboard *Chandra* many new low-luminosity X-ray sources were discovered and some of the sources found by *Einstein* and *ROSAT* were resolved into several individual sources. Using *Chandra* X-ray observations of 12 globular clusters, Pooley et al. (2003) showed that the number of low-luminosity X-ray sources above an X-ray luminosity of $L_X = 4 \times 10^{30}\,\mathrm{erg\,s^{-1}}$ scales with the encounter frequency Γ. The encounter frequency estimates the number of encounters between single stars in a globular cluster, and can be defined as $\Gamma \propto \rho_0^{3/2} r_c^2$ (see Hut & Verbunt 1983; Verbunt 2003). Here, ρ_0 is the central luminosity density and r_c the core radius of the cluster. The correlation between the encounter frequency and the number of X-ray sources provided clear evidence that low-luminosity X-ray sources in globular clusters are formed through stellar encounters.

The sub-arcsecond spatial resolution of *Chandra* allowed, for the first time, the secure identification of optical counterparts in *Hubble Space Telescope* observations of several globular clusters. In combination with archival *Hubble Space Telescope* observations, the *Chandra* X-ray observations of NGC 6397 (Grindlay et al. 2001b), NGC 6752 (Pooley et al. 2002a) and 47 Tuc (Grindlay et al. 2001a; Edmonds et al. 2003a,b) showed that the low-luminosity

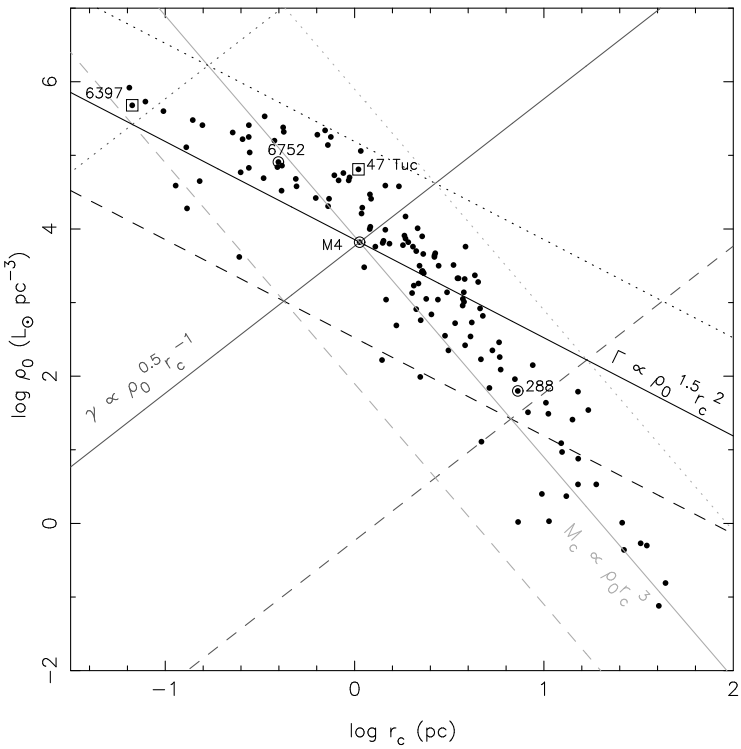

Figure 1.1: *The central density ρ_0 of a globular cluster versus its core radius r_c for 150 globular clusters with lines of constant encounter and disruption frequencies (after Verbunt 2003). Values for ρ_0 and r_c are taken from the 2003 revision of Harris (1996). The three sets of three diagonal lines indicate the loci of constant encounter frequency $\Gamma \propto \rho_0^{3/2} r_c^2$, constant disruption frequency for an individual binary $\gamma \propto \rho_0^{1/2} r_c^{-1}$ and the cluster (core) mass, $M_c \propto \rho_0 r_c^3$. These lines are normalized to the values of M4, where solid lines indicate values equal to that of M4, dashed lines values of a factor 100 lower than that of M4 and dotted lines values of a factor 100 higher than that of M4.*

X-ray sources in globular clusters can be classified into four categories of systems; i) quiescent low-mass X-ray binaries, ii) cataclysmic variables, iii) magnetically/chromospherically active binaries, and iv) millisecond pulsars. For the first two systems, mass is transferred from a stellar companion to a compact object (either a neutron star or a white dwarf), through an accretion disk, from where the X-rays originate. In magnetically/chromospherically active binaries (RS CVn, BY Dra or W UMa systems) tidal interactions lead to an increase in the rotational period of one or both of the binary members, resulting in enhanced magnetic activity and consequently, X-ray emission. For both isolated and binary millisecond pulsars in globular clusters, the X-ray radiation is believed to originate from the polar cap.

As the quiescent low-mass X-ray binaries typically are bright ($L_X \gtrsim 10^{32}\,\mathrm{erg\,s^{-1}}$) and have soft X-ray spectra, they can be identified from X-ray observations alone. Using these

identifications, Gendre et al. (2003) and Heinke et al. (2003) showed that the number of quiescent low-mass X-ray binaries in globular cluster scales with the encounter frequency Γ, and are formed dynamically. Also, from the optical identifications in 47 Tuc, NGC 6397 and NGC 6752, it became clear that the majority of the X-ray sources with $L_{\rm X} \gtrsim 4 \times 10^{30}$ erg s^{-1} used by Pooley et al. (2003) are cataclysmic variables, and that these are also formed in dynamical encounters (see also Heinke et al. 2003). The dominance of formation through encounters is partly due to the fact that primordial binaries that would evolve into cataclysmic variables if unperturbed, would be vulnerable to disruption (Davies 1997). The disruption frequency for an individual binary, $\gamma \propto \rho_0^{1/2} r_{\rm c}^{-1}$ (Verbunt 2003), parametrizes the number of encounters a single binary would undergo in a globular cluster with a central density ρ_0 and core radius $r_{\rm c}$ and describes the likelihood of a binary surviving in a globular cluster. As such, it would be possible for primordial binaries to evolve into a cataclysmic variable in clusters with a low disruption frequency γ (see Fig. 1.1).

1.2 Millisecond pulsars in binaries

Radio pulsars with millisecond spin periods (in practice, loosely taken as less than 0.1 s) are either very young or very old (see Fig. 1.2). The young variants are those that were formed in a supernova (such as the Crab-pulsar), while the majority of the old variants are found in binary systems (see the ATNF pulsar catalogue, Manchester et al. 2005). About 80 out of the 1600 pulsars known in our Galaxy reside in binaries. In the widely accepted "recycling" model of Alpar et al. (1982), matter is transferred from the binary companion to a neutron star (which may or may not be a pulsar), which spins up the neutron star to millisecond spin periods, and by means poorly understood, decreases its magnetic field.

Millisecond pulsars are also abundant in globular clusters. At present, 129 pulsars are known in 24 globular clusters, of which about half actually resides in binaries, whereas the vast majority has spin periods less than 10 ms (see Fig. 1.2). For a review, see Camilo & Rasio (2005). An up-to-date list is maintained by Paolo Freire[1]. Though not all globular cluster millisecond pulsars presently have binary companions, the fact that the majority is recycled indicates that in the past they have.

The majority of pulsars in binary systems located in the Galactic field have low-mass helium-core white dwarf companions and are called low-mass binary pulsars (LMBPs), the MSP+He-WD's in Fig. 1.2. Such low-mass white dwarfs can only be formed in binary systems, as the main-sequence stage of a single star evolving into such a low-mass white dwarf would be longer than a Hubble time. The evolution of these systems has been described by e.g. Driebe et al. (1998) and Tauris & Savonije (1999). In a nutshell, this is what happens: if, after the formation of the neutron star in a supernova event, the binary is not disrupted, a $\approx 1\,{\rm M}_\odot$ main-sequence companion star evolves into a giant and fill its Roche lobe. This starts a period of mass-transfer from the giant onto the neutron star, which is recycled to millisecond periods. During this period, which can last from a Myr to a few Gyrs (Tauris & Savonije 1999), the accretion disk emits X-rays and the system can be observed as a low-mass X-ray

[1] http://www.naic.edu/~pfreire/GCpsr.html

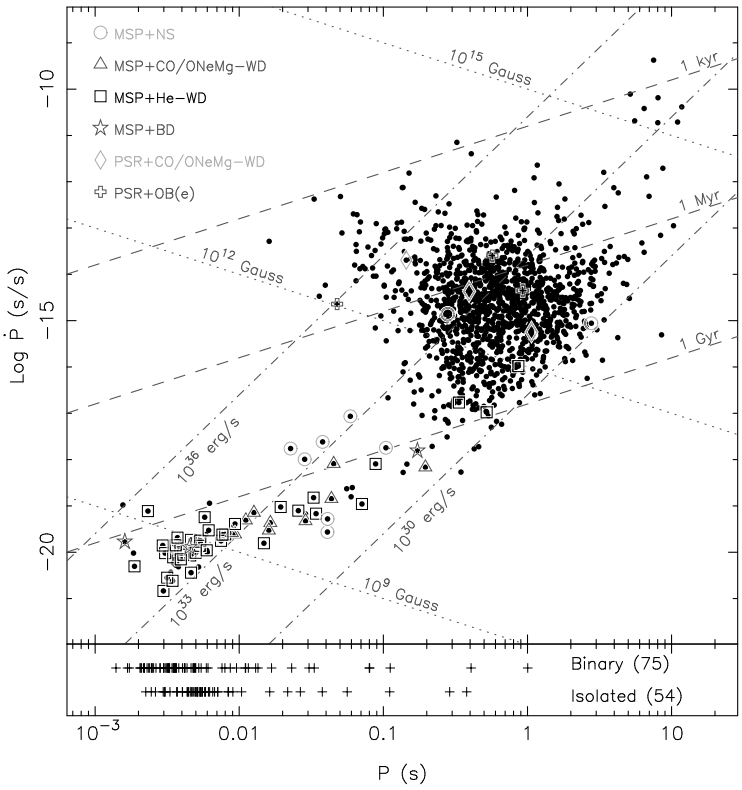

Figure 1.2: *Rotational parameters for all known radio pulsars. The spin period P versus the spin period derivative $\dot{P}$ for pulsars in the Galactic field and Small and Large Magellanic Clouds* (top panel). *Diagonal lines depict the dipolar magnetic field strengths and the characteristic spindown ages of these pulsars. Pulsars located in binaries are indicated with symbols according to the different types of systems (see van Kerkwijk et al. 2005 for a description of these types); millisecond (recycled) pulsars with neutron star companions* (MSP+NS)*, millisecond (recycled) pulsars with carbon-oxygen (CO) or oxygen-neon-magnesium (ONeMg) white dwarf companions* (MSP+CO/ONeMg-WD)*, millisecond (recycled) pulsars with helium-core white dwarfs* (MSP+He-WD)*, normal (non-recycled) pulsars with CO or ONeMg white dwarf companions* (PSR+CO/ONeMg-WD) *and normal (non-recycled) pulsars with O, B or B(e) stars as companions* (PSR+OB(e))*. The bottom panel shows the observed spin periods of isolated and binary pulsars in globular clusters. For most of these pulsars, no reliable spin period derivatives are known, as these are polluted by the gravitational potential of the cluster they inhabit.*

binary. When the envelope mass falls below a critical value (typically 0.01 to 0.001 $M_\odot$; Driebe et al. 1999; Althaus et al. 2001), mass transfer stops and the companion will contract to a white dwarf while the millisecond pulsar turns on.

As the pulsars in these systems are recycled, they can have accreted a significant amount of matter. Assuming that the mass transfer is conservative, the evolution of a 1 $M_\odot$ main-

sequence star into a $0.2\,M_\odot$ white dwarf would implicate that the mass difference is accreted by the pulsar. Due to general relativity, neutron star equations-of-state imply a maximum mass for a rotating neutron star (e.g. Cook et al. 1994; Lattimer & Prakash 2004). Hence, mass measurements of potentially heavy millisecond pulsars can provide constraints on the neutron star equation-of-state.

The interest in millisecond pulsars with low-mass helium-core white dwarfs is largely due to the fact that they provide means to measure the mass of the pulsar. Phase resolved optical spectroscopy of the white dwarf allows the determination of its radial velocity orbit, which, combined with the pulsar timing ephemeris, determines the mass-ratio of the binary. Due to gravitational settling, the atmosphere of a white dwarf is made of pure hydrogen, which can be modelled to determine the surface gravity and effective temperature of the white dwarf. A mass-radius relation from cooling models then constrains the mass of the white dwarf, and through the mass-ratio, the mass of the pulsar. As this approach is only feasible for millisecond pulsars with sufficiently bright counterparts, nearly all of these systems were surveyed in the optical to identify those bright enough (see van Kerkwijk et al. 2005 for a review).

The evolution of low-mass binary pulsars provides a prediction which can be tested through observations. As both the white dwarf and the millisecond pulsar are formed after the cessation of mass-transfer, one would expect the characteristic age of the pulsar to match the cooling age of the white dwarf. The characteristic age of the pulsar can be determined from the pulsar spin period and spin period derivative, while pulsar timing also provides an estimate for the mass of the companion. Combining the latter with a temperature determination of the companion (through optical photometry or spectroscopy), evolutionary white dwarf models predict white dwarf cooling ages.

From observations of low-mass binary pulsars in the Galactic field, it has become clear that there is a dichotomy in the cooling properties of the helium-core white dwarf companions to millisecond pulsars (see van Kerkwijk et al. 2005 for a review). In particular, the optical observations of PSR J1012+5307 (van Kerkwijk et al. 1996; Callanan et al. 1998) showed that the white dwarf has a temperature of 8600 K, while those in PSR J0437−4715 (Danziger et al. 1993) and PSR B1855+09 (van Kerkwijk et al. 2000) have temperatures of 4000-5000 K. Paradoxically, with a characteristic spindown age of 8.9 Gyr (Lange et al. 2001), PSR J1012+5307 is nearly twice as old as the other two pulsars, which have spindown ages of about 5 Gyr. After a flurry of modelling (Alberts et al. 1996; Driebe et al. 1998; Althaus et al. 2001), the dichotomy was explained by the thickness of the hydrogen envelope surrounding the helium-core of the white dwarf; in thick envelopes ($\sim 0.01\,M_\odot$) residual hydrogen burning slows down the cooling, while for white dwarfs with masses above approximately $0.2\,M_\odot$, the mass of the initially thick envelope is reduced through instabilities in the residual hydrogen burning, leading to thermonuclear flashes (Webbink 1975; Sarna et al. 2000; Althaus et al. 2001), which allows the white dwarf to cool more rapidly later-on. Through the relation between the orbital period of a low-mass binary pulsar and mass of the white dwarf (Joss et al. 1987; Rappaport et al. 1995; Tauris & Savonije 1999), the threshold in mass between thin and thick hydrogen envelopes translates into a threshold in orbital period. Observationally, the threshold lies around 1.5 days, where systems having orbital pe-

riods smaller than this are expected to have thick hydrogen envelopes (van Kerkwijk et al. 2005).

1.3 Ultra-compact X-ray binaries

About 150 low-mass X-ray binaries are known (Liu et al. 2001), and observations have shown that these systems have orbital periods ranging from several days to several minutes (Ritter & Kolb 2003). For systems with orbital periods below approximately 80 min, ordinary hydrogen rich stars cannot fit inside the Roche lobe (Nelson et al. 1986), and mass is transferred from a white dwarf (instead of a giant or a main-sequence star) onto the neutron star. These systems are called ultra-compact X-ray binaries.

Ultra-compact X-ray binaries are found both in the Galactic field and in globular clusters. A list of confirmed and candidate ultra-compact X-ray binaries is given in Nelemans & Jonker (2006). Of the 13 bright X-ray sources in globular clusters, those in NGC 6624, NGC 6712 and the second source in M15 have orbital periods of 11 min (Stella et al. 1987), 13 or 21 min (Homer et al. 1996) and 23 min (Dieball et al. 2005) respectively. In the Galactic field, 9 more systems are known, including 3 of the 7 known accretion driven millisecond X-ray pulsars (see reviews by Poutanen 2005; Wijnands 2005).

Ultra-compact X-ray binaries can be formed in several different ways. Neutron stars in globular clusters can collide with giants, where the energy in the collision removes the envelope of the giant, leaving a binary with the neutron star and the core of the giant (Verbunt 1987). In a different scenario, the expanding envelope of a giant may engulf the neutron star, leading to a spiral-in and forming a binary consisting of a neutron star and the helium-burning core of the giant (Savonije et al. 1986). After the spiral-in, further angular momentum loss will bring the neutron star and the compact core into contact. Depending on the time this takes, the helium burning core may or may not have completed core helium burning to become a carbon-oxygen (CO) white dwarf with a very thin helium envelope. If the core has a low mass ($M < 0.45\,\mathrm{M}_\odot$), the helium burning is incomplete and the CO core is surrounded by a thick helium layer (Yungelson et al. 2002). Finally, a binary consisting of a neutron star and a main-sequence star may evolve into an ultra-compact X-ray binary when strong magnetic braking is present (Tutukov et al. 1985; Podsiadlowski et al. 2002). However, the very narrow range in initial orbital period makes the contribution of this scenario to the overall population of ultra-compact X-ray binaries virtually negligible (van der Sluys et al. 2005a,b).

The study of ultra-compact X-ray binaries is important because the emission of gravitational wave radiation results in the gradual shortening of the orbital period, making ultra-compact X-ray binaries strong sources of gravitational wave radiation. Furthermore, as the formation scenarios predict differences in the composition of the matter transferred to the neutron star, observations of ultra-compact X-ray binaries may provide insight in which formation channels are important. Finally, ultra-compact X-ray binaries provide a direct look at stellar interiors.

1.4 Summary of this thesis

Chapters 2 and 3

Most of the globular clusters that were observed with *Chandra* and in which optical counterparts were identified had relatively high encounter frequencies (see Fig. 1.1), as these were the clusters where most X-ray sources were expected. To investigate the number and types of binaries in a globular cluster with a low encounter frequency, we analyzed *Chandra* and *Hubble Space Telescope* observations of the globular clusters M4 (Chapter 2) and NGC 288 (Chapter 3), allowing the classification of most of the X-ray sources.

For M4, which is the nearest globular cluster, our X-ray observations provide one of the deepest views of a globular cluster to date. We find that the majority of the sources are chromospherically active binaries. Comparing the number of such sources in this cluster with those in 47 Tuc and NGC 6397, we find evidence that the number of active binaries scales with the mass of the globular cluster. The scaling on cluster mass would indicate that these systems have evolved from primordial binaries.

In Chapter 3, we investigate the population of low-luminosity X-ray sources in a cluster that has both a low encounter frequency Γ, and a low disruption frequency γ, NGC 288. Though 11 X-ray sources are detected inside the cluster half-mass radius, we find that about half are background galaxies and unrelated to the cluster. Of the remaining sources, one has the clear characteristics of a cataclysmic variable, while two or three others are likely active binaries. Based on the scaling by Pooley et al. (2003), no X-ray sources with $L_X \gtrsim 4 \times 10^{30}$ erg s^{-1} are expected in this cluster, while three or four such sources are found. This suggests that these sources all evolved from primordial binaries.

Chapters 4 and 5

In Chapter 4 we identify the optical counterpart to the millisecond pulsar PSR J1911−5958A, which is located only 6.′4 from the globular cluster NGC 6752 and may be associated with this cluster. If this pulsar is associated with NGC 6752, its circular orbit and present position in the halo of the cluster is problematic. This led Colpi et al. (2002) to conjecture that PSR J1911−5958A might be ejected from the core of NGC 6752 by a scattering event between the pulsar binary with a binary consisting of two black holes with masses of 3–100 $M_\odot$. In such an encounter, the pulsar binary can be regarded as a point source compared to the black hole binary and no eccentricity is imparted on the pulsar orbit upon ejection. They argued that this scenario was more probable than a scattering or exchange encounter involving cluster stars or a scenario in which the pulsar is born from a primordial binary in either the halo or the core of the cluster, and furthermore that it provides an explanation for the large mass-to-light ratio of NGC 6752. In a subsequent publication, Colpi et al. (2003) showed that either a binary of a 50 $M_\odot$ black hole with one of 10 $M_\odot$, a binary black hole of 200 $M_\odot$ and 10 $M_\odot$ or a single black hole of $\gtrsim$ 500 $M_\odot$ could eject PSR J1911−5958A to its current position.

We find that the colours and magnitudes of the counterpart to PSR J1911−5958A are consistent with a helium-core white dwarf located at the distance and reddening of the cluster. Furthermore, if the system is associated with NGC 6752, the white dwarf is relatively young,

which constrains the formation and ejection of the binary. However, the main result of our research was that the companion is bright when compared to other white dwarfs in low-mass binary pulsars. With $V = 22.1$ and an orbital period of $P_b = 20$ hours, the system is ideally suited for phase resolved spectroscopy, allowing the measurement of the pulsar mass, which sofar has only been possible for another system, PSR J1012+5307 (van Kerkwijk et al. 1996; Callanan et al. 1998).

Chapter 5 deals with the measurement of the mass of PSR J1911−5958A using the method described above, which we find to be consistent with canonical value of $1.35\,M_\odot$ (Thorsett & Chakrabarty 1999). The spectroscopic observations also provide two ways to test the membership of the binary with NGC 6752. Unfortunately, both tests neither conclusively confirm nor disprove the association between the binary and the globular cluster.

Chapter 6

The millisecond pulsar PSR J1740−5340 is located in the dense globular cluster NGC 6397, and is one of the few pulsars in globular clusters believed to have a main-sequence star as a companion (see Ferraro et al. 2001; Edmonds et al. 2002). Based on the timing observations of PSR J1740−5340 by D'Amico et al. (2001b), irradiation in this system should be important: the pulsar has one of the highest spindown luminosities (energy loss due to rotation; $L_{sd} \propto P\dot{P}^{-3} = 1.4 \times 10^{35}$ erg s^{-1}) known, equalling 19 times the bolometric luminosity of the companion. It has been argued that the pulsar wind impinging on the companion may drive a wind which explains the observations of eclipses of the radio signal when the companion is near the line-of-sight towards the pulsar (D'Amico et al. 2001b).

The irradiation of the companion by the pulsar wind would heat the hemisphere of the companion that faces the pulsar, which in turn would lead to sinusoidal variations in the brightness of the companion, where one periodically sees the irradiated and the non-irradiated hemisphere of the companion (one maximum and minimum per orbital cycle). However, the companion displays ellipsoidal variations (two maxima and minima per orbital cycle) (Ferraro et al. 2001; Orosz & van Kerkwijk 2003; Kaluzny et al. 2003), reminiscent of the teardrop shape of a star (partly) filling its Roche lobe, which indicates that the companion is not heated significantly. A number of solutions were considered by Orosz & van Kerkwijk (2003), but it was found that most could be rejected. The most viable solution was that the pulsar was part of a triple, where the extra acceleration of the pulsar contributes to the observed spin period derivative and leads to an over estimate of the spindown luminosity.

Somewhat by chance we found that the timing position of PSR J1740−5340 was inconsistent with the celestial position of the optical counterpart. As the determination of both the spin period and period derivative depend on the celestial position of a pulsar, this would suggest that these parameters, the spin period derivative in particular, were in error. In Chapter 6 we present the celestial position of the optical companion to PSR J1740−5340 and investigate the effects of the optical position on the spin period derivative. A new timing position, using more data, was presented by Possenti et al. (2005), which was in better agreement with the optical position. More importantly, this ephemeris showed that the original spin period derivative was indeed in error and led to an over estimate of the spindown luminosity. No significant irradiation of the pulsar companion is expected from

the new pulsar parameters, solving the problems discussed by Orosz & van Kerkwijk (2003).

Chapter 7

In Chapter 7 we study PSR J0751+1807, the low-mass binary pulsar with the shortest orbital period (6 hours), well below the threshold between thick and thin envelopes. As such, the white dwarf in this system is expected to have a thick hydrogen envelope. However, our observations to confirm this clearly show that is does not. In fact, we find that the magnitude and colours of the white dwarf suggest an envelope consisting of helium or a mix of hydrogen and helium. A scenario proposed by Ergma et al. (2001), in which the hydrogen envelope is removed through irradiation by the pulsar, may explain our observations, however, we do not find evidence that irradiation is important in this system.

Chapter 8

Orbital periods of ultra-compact X-ray binaries can be determined through variability studies at optical and X-ray wavelengths, as well as through timing of the accreting X-ray pulsars. However, such observations require considerable amounts of observing time and may not work for all sources. Hence, it is worthwhile to investigate if candidate ultra-compact X-ray binaries satisfy the basic properties that are expected for such sources. One such property is that the intrinsic brightness at optical wavelengths of ultra-compact X-ray sources is lower than for normal low-mass X-ray binaries.

Under the assumption that the optical emission of low-mass X-ray binaries originates from reprocessed X-ray radiation in the accretion disk of the binary, van Paradijs & McClintock (1994) derived a simple relation between the X-ray luminosity, the orbital period and the absolute visual magnitude of a low-mass X-ray binary. According their model, systems with $M_V \gtrsim 4$ are likely to have ultra-compact orbital periods. In Chapter 8 we analyze optical observations of two low-mass X-ray binaries to test whether these systems satisfy the constraint for ultra-compact X-ray binaries according to the model of van Paradijs & McClintock (1994).

Chapter 9

After being discovered in 1975, the presumed ultra-compact X-ray binary 1H 1905+000 was observed by several X-ray satellites and remained active for about 10 to 15 years, after which it was not detected by *Chandra* in 2003 (Juett & Chakrabarty 2005). In Chapter 9 we present a deeper *Chandra* observation and optical observations of 1H 1905+000. We fail to detect both the X-ray source and its optical counterpart. The limit on the X-ray luminosity places a stringent constraint on the cooling mechanism of the neutron star, while the non-detection of the optical counterpart constrains the properties of the binary companion.

Chapter 2

X-ray sources and their optical counterparts in the globular cluster M4

C. G. Bassa, D. Pooley, L. Homer, F. Verbunt, B. M. Gaensler,
W. H. G. Lewin, S. F. Anderson, B. Margon, V. M. Kaspi, M. van der Klis

Astrophysical Journal 2004, 609, 755-765

Abstract We report on the *Chandra X-ray Observatory* ACIS-S3 imaging observation of the Galactic globular cluster M4 (NGC 6121). We detect 12 X-ray sources inside the core and 19 more within the cluster half-mass radius. The limiting luminosity of this observation is $L_{\rm X} \approx 10^{29}$ erg s^{-1} for sources associated with the cluster, the deepest X-ray observation of a globular cluster to date. We identify 6 X-ray sources with known objects and use *ROSAT* observations to show that the brightest X-ray source is variable. Archival data from the *Hubble Space Telescope* allow us to identify optical counterparts to 16 X-ray sources. Based on the X-ray and optical properties of the identifications and the information from the literature, we classify two (possibly three) sources as cataclysmic variables, one X-ray source as a millisecond pulsar and 12 sources as chromospherically active binaries. Comparison of M4 with 47 Tuc and NGC 6397 suggests a scaling of the number of active binaries in these clusters with the cluster (core) mass.

2.1 Introduction

Faint X-ray sources ($L_X \lesssim 10^{35}$ erg s^{-1}) were first discovered in observations made with the *Einstein* and *ROSAT* observatories (Hertz & Grindlay 1983; Verbunt 2001). It was only with *Chandra*, however, that a large number of faint sources was identified: more than one hundred in 47 Tuc, and up to a few dozen each in e.g. NGC 6397, NGC 6752, NGC 6440, and ω Cen (Grindlay et al. 2001a,b; Pooley et al. 2002a,b; Rutledge et al. 2002). These faint sources represent a mix of objects with different X-ray luminosities. Brightest are the neutron stars accreting at a low rate from a companion (quiescent low mass X-ray binaries or qLMXBs), followed by white dwarfs accreting from low-mass companions (cataclysmic variables or CVs). The active binaries (ABs) tend to be the faintest, while radio pulsars with short periods (millisecond or recycled pulsars, MSPs) have X-ray luminosities in a similar range as CVs. The three types of chromospherically or magnetically active binaries are detached binaries of two main sequence stars (BY Dra systems), detached binaries of a main sequence star and a giant or a sub-giant (RS CVn systems) and contact binaries (W UMa systems).

Globular clusters contain many more neutron star binaries per unit mass than the galactic disk. Hence, if in a globular cluster one finds a binary with a neutron star (which is rather difficult to make via ordinary evolution of an initial binary), it is highly probable that this binary was formed via a close encounter between stars (Fabian et al. 1975; Hills 1976). Isolated millisecond pulsars in globular clusters are thought to have been formed in such binaries, and thus are probably also a result of close stellar encounters.

On the other hand, binaries that are common in the field, are more likely to be of primordial origin in globular cluster, including the chromospherically active binaries. Cataclysmic variables are relatively common in the Galactic disk, and those in globular clusters could in principle originate from primordial binaries or stellar encounters. Pooley et al. (2003) showed that the number of faint sources above the threshold $L_X > 4 \times 10^{30}$ erg s^{-1} in a cluster scales with its collision number Γ, which is a theoretical estimate for the number of close encounters. Since the majority of such sources are cataclysmic variables, this suggests that most cataclysmic variables in globular clusters are in fact formed via close stellar encounters.

Most clusters investigated with *Chandra* so far have relatively high collision numbers (see e.g. Table 1 in Pooley et al. 2003); because the limit to which X-ray sources in these clusters could be detected is relatively high, most X-ray sources known in these clusters are either neutron stars (accreting or radio pulsars), or cataclysmic variables. So far, a sizable number of X-ray sources has been identified as chromospherically active binaries only in 47 Tuc (Edmonds et al. 2003a,b). In this paper, we discuss a globular cluster with a relatively low collision number, M4 (NGC 6121). This cluster is a relatively nearby cluster with a moderate absorption (d = 1.73 kpc, A_V = 1.32, Richer et al. 1997). The core and half-mass radii of M4 are 49.″8 and 3.′65, respectively (Harris 1996). We use these values throughout the paper.

A priori, we would thus expect that the majority of X-ray sources in this cluster to be chromospherically active binaries. That chromospherically active binaries exist in this cluster is evident from optical studies. For example, Kaluzny et al. (1997) discovered a number of optical variables, including several contact binaries.

The presence of a recycled radio pulsar PSR B1620−26 (Lyne et al. 1988) in M4 is remarkable, but can be explained by noting that the small collision numbers of many globular clusters still add up, so that at least some of the clusters with small Γ should contain a binary with a neutron star (Verbunt & Hut 1987). PSR B1620−26 is in a 191 day orbit around a white dwarf of $\sim 0.3\ M_\odot$; the binary is accompanied by a third object of planetary mass in an orbit of $\sim$ 100 years (Thorsett et al. 1999; Sigurdsson et al. 2003).

2.2 X-ray observations and analysis

M4 was observed for 25.8 ks on 2000 June 30 with the Advanced CCD Imaging Spectrometer (ACIS) on the *Chandra X-ray Observatory* with the telescope aimpoint on the back-side illuminated S3 chip. The data were taken in timed-exposure mode with the standard integration time of 3.24 s per frame and telemetered to the ground in faint mode.

Data reduction was performed using the CIAO 2.3 software provided by the *Chandra* X-ray Center (CXC)[1]. We reprocessed the data using the CALDB 2.21 set of calibration files (gain maps, quantum efficiency, quantum efficiency uniformity, effective area) without including the pixel randomization that is added during standard processing. This method slightly improves the point spread function. We filtered the data using the standard *ASCA* grades, and we excluded both bad pixels and software-flagged cosmic ray events. Intervals of background flaring were searched for, but none were found, hence we simply applied the good-time intervals supplied by the CXC.

2.2.1 Source detection

The CIAO wavelet-based *wavdetect* tool was employed for source detection in both the 0.5–6.0 keV band and 0.3–10.0 keV band. We detected 41 sources on the entire S3 chip in the 0.5–6.0 keV band; for the *wavdetect* settings we used, approximately one of those detections may be spurious. Of these sources, 30 lie within the half-mass radius of the cluster.

We also searched part of the adjacent S4 CCD since part of the half-mass region fell on this chip, but no sources were detected in this area. One additional source was detected on S3 in the broader 0.3–10.0 keV band with three counts, two of which were between 8 and 10 keV. The significance of this source, as well as its possible membership of the cluster, is questionable. For completeness, however, we leave it in our source list (Table 2.1) as the last source. The sources are numbered according to detected counts in the 0.5–6.0 keV band.

From the $\log N - \log S$ relationships of Giacconi et al. (2001), we expect between 5 and 6 background sources within the cluster half-mass radius. However, as M4 is located towards the bulge of the galaxy ($l = 351\overset{\circ}{.}0$, $b = 16\overset{\circ}{.}0$, Harris 1996) this relation would underestimate the galactic contribution of background sources and provide a lower limit only. We have analyzed ACIS-S3 data from the October 15, 2002 *Chandra* observation of the low-mass X-ray binary (LMXB) MXB 1659−298, which has $l = 353\overset{\circ}{.}8$ and $b = 7\overset{\circ}{.}3$. In the 27 ks of this observation the 1/4 sub-array of the S3 CCD shows 5 sources, other than the LMXB

[1] http://asc.harvard.edu

Table 2.1: Chandra *X-ray sources within the half-mass radius of M4. The Chandra positions have been corrected for a shift of* 0.″15 *in declination (see Sect. 2.3.2). Positional uncertainties are given in parentheses and refer to the last quoted digit and are the centroiding uncertainties given by wavdetect.*

CX[a]	R.A.	Decl.	Counts (detected/corrected)[b]			L_X[c]		
	J2000		X_{soft}	X_{med}	X_{hard}	(ergs s^{-1})	Counterpart[d]	ID[e]
1	$16^h23^m34^s.128(1)$	−26°31′34.″85(2)	154/381.2	379/736.4	275/313.0	8.3×10^{31}	Opt.?/R9?	CV
2	$16^h23^m46^s.399(3)$	−26°31′15.″67(8)	48/117.5	72/138.3	30/33.8	6.0×10^{30}	Opt.	CV
3	$16^h23^m38^s.073(3)$	−26°31′38.″18(4)	46/113.6	75/145.2	29/32.8	5.4×10^{30}	Opt.	AB
4	$16^h23^m34^s.321(4)$	−26°30′39.″27(5)	28/68.8	56/108.9	36/41.3	3.6×10^{30}	Opt.	CV/AB
5	$16^h23^m34^s.300(4)$	−26°29′56.″47(6)	23/55.6	35/66.7	12/13.4	2.5×10^{30}	V56	amb.
6	$16^h23^m38^s.058(9)$	−26°29′21.″81(14)	15/35.2	26/47.8	12/12.9	1.8×10^{30}	–	
7	$16^h23^m45^s.848(12)$	−26°28′55.″03(19)	23/54.9	25/46.3	3/2.9	1.8×10^{30}	Opt.	fg.
8	$16^h23^m31^s.478(9)$	−26°30′57.″84(7)	17/41.2	24/46.0	7/7.8	1.7×10^{30}	V52	AB
9	$16^h23^m34^s.224(5)$	−26°29′55.″69(5)	17/41.0	23/43.7	6/6.7	1.7×10^{30}	V56	amb.
10	$16^h23^m35^s.047(8)$	−26°31′19.″18(7)	14/34.0	23/43.9	9/10.0	1.7×10^{30}	Opt.	AB
11	$16^h23^m32^s.399(7)$	−26°30′45.″63(6)	8/19.4	18/34.7	10/11.4	1.3×10^{30}	–	
12	$16^m23^m38^s.205(4)$	−26°31′54.″21(6)	16/39.3	17/32.7	2/2.2	1.2×10^{30}	Rad./Opt.	MSP
13	$16^m23^m34^s.326(7)$	−26°32′02.″33(10)	11/26.9	12/22.9	2/2.1	8.7×10^{29}	Opt./V49	AB
14	$16^m23^m25^s.948(15)$	−26°33′54.″62(10)	0/–	12/23.1	12/13.9	8.7×10^{29}	–	
15	$16^m23^m36^s.769(8)$	−26°31′44.″60(11)	10/24.6	11/21.1	1/1.0	8.0×10^{29}	Opt./V48	AB
16	$16^m23^m33^s.682(6)$	−26°34′17.″27(10)	2/4.7	6/11.4	7/7.9	4.3×10^{29}	–	
17	$16^m23^m35^s.975(11)$	−26°31′01.″89(8)	7/16.9	9/17.0	2/2.2	6.4×10^{29}	–	
18	$16^m23^m45^s.767(9)$	−26°31′16.″85(14)	7/17.0	7/13.2	0/–	5.0×10^{29}	Opt./V55	AB
19	$16^m23^m28^s.953(8)$	−26°29′51.″47(9)	4/9.5	7/13.3	3/3.3	5.0×10^{29}	–	
20	$16^m23^m36^s.881(11)$	−26°31′39.″43(15)	5/12.2	7/13.3	2/2.2	5.0×10^{29}	Opt.	AB
21	$16^m23^m34^s.610(5)$	−26°32′04.″60(19)	4/9.7	7/13.3	3/3.3	5.0×10^{29}	Opt.	
22	$16^m23^m33^s.362(9)$	−26°31′45.″65(15)	5/12.2	6/11.4	1/1.1	4.3×10^{29}	Opt.	AB
23	$16^m23^m40^s.189(20)$	−26°29′26.″10(25)	5/11.6	6/10.8	1/0.9	4.1×10^{29}	–	
24	$16^m23^m42^s.096(12)$	−26°31′37.″03(13)	3/7.2	5/9.4	2/2.2	3.6×10^{29}	Opt.	amb.
25	$16^m23^m33^s.503(9)$	−26°32′30.″28(8)	4/10.0	5/9.8	1/1.1	3.7×10^{29}	Opt.	AB
26	$16^m23^m38^s.884(11)$	−26°31′48.″26(8)	3/7.3	5/9.5	2/2.2	3.6×10^{29}	Opt.	AB
27	$16^m23^m33^s.290(5)$	−26°31′57.″81(25)	4/9.7	5/9.4	1/1.0	3.6×10^{29}	Opt.	AB
28	$16^m23^m34^s.969(12)$	−26°32′24.″65(10)	4/9.9	4/7.6	0/–	2.9×10^{29}	Opt.	AB
29	$16^m23^m19^s.486(19)$	−26°31′43.″39(26)	1/2.3	1/1.7	2/2.3	6.5×10^{28}	–	
30	$16^m23^m28^s.396(9)$	−26°30′22.″25(23)	2/5.9	3/7.0	1/1.4	2.6×10^{29}	–	
31	$16^m23^m29^s.424(9)$	−26°30′00.″19(11)	1/2.3	1/1.7	0/–	6.5×10^{28}	–	

[a] The sources are numbered according to their total counts.

[b] Corrections to the detected counts are described in Sect. 2.2.2. The X-ray bands are 0.5–1.5 keV (X_{soft}), 0.5–4.5 keV (X_{med}) and 1.5–6.0 keV (X_{hard}).

[c] For sources CX1–CX4, L_X (0.5–2.5 keV) comes from an average of the best-fit models for each source (Sect. 2.3.2). A linear relation between L_X and X_{med} counts for these sources was derived and used to estimate L_X for sources CX5–CX31 based on their X_{med} counts. Typical uncertainties in L_X are ∼ 15 %.

[d] Type of counterpart (optical and/or radio) found and associations (if any) with previously reported sources. The "V" numbers refer to optical variables by Kaluzny et al. (1997) and Mochejska et al. (2002). R9 is an X-ray source detected by *ROSAT* (Verbunt 2001).

[e] Classification of the sources; see Sect. 2.4. The abbreviation MSP stands for millisecond pulsar, CV for cataclysmic variable and AB for active binary. Sources for which the classification is ambiguous are abbreviated with *amb.* and the foreground source CX7 is classified as *fg.*. See text for details.

itself, in the 0.5–6.0 keV band. Scaling this up to the whole chip and taking into account Poissonian errors would give rise to some 20 sources within an area of the size of the M4 half-mass radius. Given that MXB 1659−298 is located about 10° closer to the galactic center this would overestimate the number of background sources towards M4. Though both limit determinations are very different in nature, we expect 6 to 20 background sources within the half-mass radius of M4, and zero or one within the core.

All sources are consistent with being point sources. However, CX5 and CX9 overlap somewhat. They were identified by *wavdetect* as two separate sources. It is possible that they are actually a single extended object, but the double-peaked nature of the image lends support to the interpretation as two point sources.

There is some evidence for excess emission on the approximately 32 200 pixels inside the core radius. The residual number of counts (i.e., the total counts minus those due to the 12 point sources inside the core) in the 0.5–6.0 keV band is 438 ± 20 counts, while we would expect 287 ± 15 background counts on the basis of the number of counts that we measure in a source-free region outside the core. This excess emission could be due to either unresolved point sources or diffuse emission.

A $5' \times 5'$ portion of the *Chandra* exposure of M4 is shown in Figure 2.1. The detected sources are encircled and numbered. The cross indicates the cluster center, while the circles denote the core and half-mass radius.

2.2.2 Count rates

We extracted source counts in the following bands: 0.5–1.5 keV (X_{soft}), 0.5–4.5 keV (X_{med}), and 1.5–6.0 keV (X_{hard}). The detected count rate was corrected for background, exposure variations, and foreground photoelectric absorption. We make these corrections in order to produce an X-ray color-magnitude diagram (CMD) that can be compared to the X-ray CMDs that have resulted from *Chandra* observations of other globular clusters. In addition, however, attention must be paid to differences in detector responses and, of course, exposure times and distances.

The background count rate in each band was estimated from a source-free region on the S3 chip outside the core and to the northwest. The density of background counts in each band (for the 25.8 ksec observation) is 0.0043 counts pixel^{-1} in X_{soft}, 0.0077 counts pixel^{-1} in X_{med}, and 0.0047 counts pixel^{-1} in X_{hard}. The background count rate in the core may be somewhat higher, but even factors of a few greater than this estimate have negligible effects on our analysis.

In general, the exposure variations among sources were at the ∼7% level or less, but CX30 had an exposure which was 20% less than the others. To account for these variations in exposure, we applied multiplicative corrections based on the ratio of the average effective area of the detector at the location of a source in each of the three bands to that in the same band of CX6, which had the highest average exposure. The individual effective area curves for the sources were made using the CIAO tool *mkarf*. The average effective area of the detector at the location of CX6 in each of the bands was 538 cm^2 (X_{soft}), 451 cm^2 (X_{med}), and 376 cm^2 (X_{hard}).

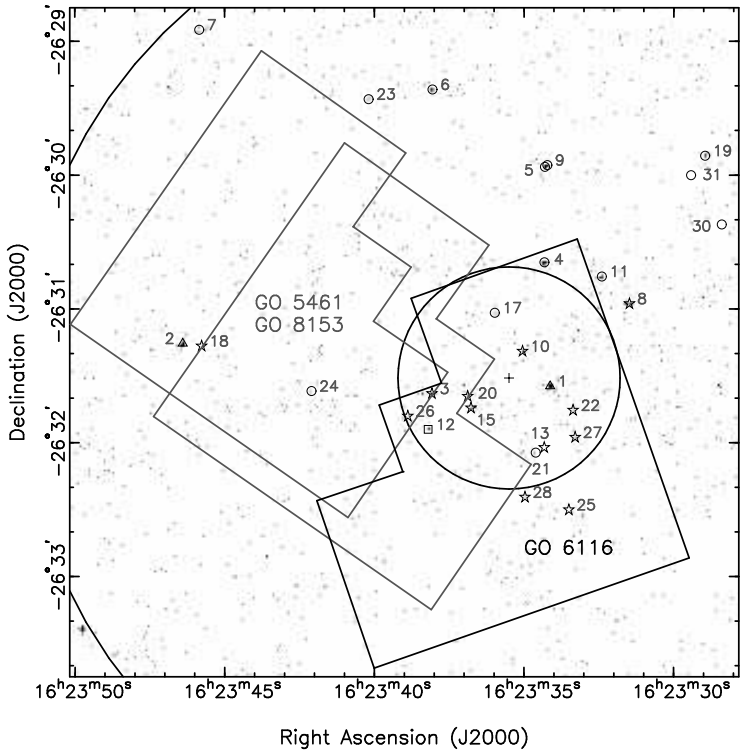

Figure 2.1: *X-ray image of a 5′ × 5′ region of M4. Shown are all counts in the 0.5–6.0 keV range. The cluster center, core and half-mass radii are indicated by a cross and two circles, respectively (Harris 1996). The detected X-ray sources are marked and numbered, omitting the "CX" prefix. X-ray sources classified as cataclysmic variables are indicated with triangles, chromospherically active binaries with stars, millisecond pulsars with squares and unclassified or ambiguous sources are indicated with circles. See Section 2.4 for the source classification. Also shown are three archival pointings of the* HST*/WFPC2 used to locate optical counterparts to the Chandra X-ray sources.*

While the previous corrections were relatively minor (at the few percent level or less), the correction for photoelectric absorption is appreciable for M4. The conversion of optical extinction to column density (Predehl & Schmitt 1995) gives a value of $N_{\rm H} = 2.36 \times 10^{21}$ cm^{-2}. We investigated the effects of such an absorption on three characteristic spectra: a 3 keV thermal bremsstrahlung, a 0.3 keV blackbody plus power law with photon index of $\Gamma = 2$, and a power law with a photon index of $\Gamma = 2$. The effects were most prominent in the $X_{\rm soft}$ band, where the absorbed count rate was a factor of 2.2–2.5 lower than the unabsorbed one (depending on the spectrum). Averaging the results of each spectrum in each band, we use the following correction factors: 2.38 ($X_{\rm soft}$), 1.87 ($X_{\rm med}$), and 1.10 ($X_{\rm hard}$). Table 2.1 lists both the observed and fully corrected counts in each band. The effect of the absorption correction on the X-ray CMD (Fig. 2.2) is a uniform shift of all points 0.27 units on the left axis and

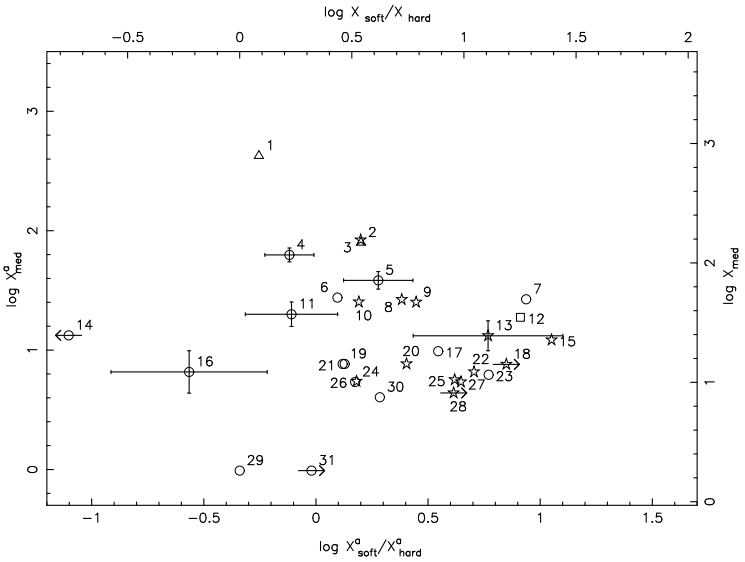

Figure 2.2: *X-ray color-magnitude diagram. The X-ray color is defined as the logarithm of the ratio of $X_{\rm soft}$ (0.5–1.5 keV) corrected counts to $X_{\rm hard}$ (1.5–6.0 keV) corrected counts, and the magnitude is the logarithm of $X_{\rm med}$ (0.5–4.5 keV) corrected counts. Our correction for photoelectric absorption has the effect of uniformly shifting the data +0.27 units on the left axis and +0.34 units on the bottom axis. The bottom and left axes provide the absorbed color and magnitude scales ($^{\rm a}$), i.e., the observed colors and magnitudes uncorrected for absorption. For the sake of clarity, only a few error bars (1σ) are shown. Sources CX14, CX18, CX28 and CX31 were not detected in either the $X_{\rm soft}$ or $X_{\rm hard}$ band, respectively. We illustrate their limits on* $\log X_{\rm soft}/X_{\rm hard}$ *by adopting a single count in these bands. The X-ray sources are marked as in Fig. 2.1. See Section 2.4 for the source classification.*

0.34 units on the bottom axis. The bottom and left axes give the X-ray color and magnitude without this shift (they do, however, include the small corrections for background subtraction and exposure variations).

2.2.3 Spectral fitting

We used the CIAO tool *dmextract* to extract spectra of sources CX1–CX4 in the 0.3–10 keV range. We binned the spectra to have at least 10 counts (20 counts for CX1) per bin and fit them in XSPEC (Arnaud 1996) using χ^2 statistics.

For CX2, CX3, and CX4, three different models (with absorption) were fit: thermal bremsstrahlung (TB), blackbody with a small (∼20%) power-law contribution (BB+PL), and power law (PL). We fixed $N_{\rm H}$ to the value from optical extinction. As expected for such low-count spectra, very few fits could be formally ruled out. We estimated the unabsorbed source luminosities by averaging the results from the three best-fit models for each source. The spread in $L_{\rm X}$ of the three models was ∼15% for each source. Fitting a linear relation

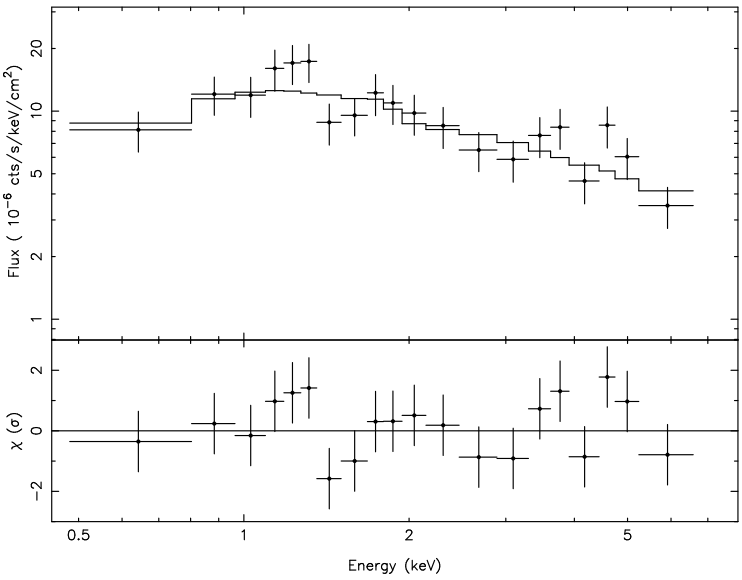

Figure 2.3: *Chandra spectrum of the brightest source, CX1. Datapoints are shown as crosses in the top panel, and an absorbed power-law model is shown as a solid line; residuals from this fit are shown in the bottom panel. Both the data and model have been divided by the instrument effective area for the purpose of plotting.*

to these luminosities versus corrected X_{med} counts, we have estimated the unabsorbed luminosities for sources CX5–CX31 based on their X_{med} counts (note though that any differences between spectra are not accounted for). These are listed in Table 2.1.

The X-ray color and magnitude of CX1 (Fig. 2.3) suggested that it might be a CV, but the spectral fits using an absorbed TB model (with N_H allowed to vary) preferred the maximum temperature allowed by the model in XSPEC, namely, $kT = 200$ keV, which gave a χ^2/d.o.f. of 36.0/39. Fixing the temperature at the more reasonable value of $kT = 25$ keV still allowed for a statistically acceptable fit (χ^2/d.o.f. of 42.1/40). The TB results indicated a rather hard spectrum, and an absorbed PL model (again with N_H allowed to vary) gave a best-fit photon index of 0.99 ± 0.17 and best-fit N_H of $(2.6^{+1.1}_{-0.7}) \times 10^{21}$ cm^{-2} with a χ^2/d.o.f. of 33.3/39. The PL fit is shown in Fig. 2.3, and the unabsorbed luminosity from this model is 6.8×10^{31} erg s^{-1} in the 0.5–2.5 keV band.

2.3 Optical observations

Three fields located inside the half-mass radius have been observed with the Wide Field Planetary Camera 2 (WFPC2) aboard the *Hubble Space Telescope* (*HST*), and are shown in Fig. 2.1. Deep observations (dataset GO-5461) of three fields were obtained to determine the mass and luminosity functions of the main and white dwarf sequence (Richer et al. 1995;

Richer et al. 1997) and two of these fields (see Fig. 2.1, gray outlines) fall within the cluster half-mass radius. These two fields were imaged for 11 800 s in F336W (hereafter U_{336}), 15 000 s in F555W (V_{555}) and 5 500 s in F814W (I_{814}) and were re-observed in I_{814}, with exposure times of 5 680 s, (GO-8153) approximately 5 years later. This allowed separation of field stars from the low luminosity cluster members through proper motion properties (Bedin et al. 2001). Finally there exist shallow (249 s) V_{555} and (249 s) I_{814} observations (GO-6116) originally obtained to search for the optical counterpart of PSR B1620−26. These observations (Fig. 2.1, black outline) cover nearly the entire region enclosed by the core radius. Of the 31 sources listed in Table 2.1, 18 coincide with the three *HST*/WFPC2 fields.

This section outlines the data reduction, photometry and astrometry of the *HST*/WFPC2 images.

2.3.1 Data reduction and photometry

The single *HST* images and the association products[2] were obtained from the ESO archive. The single images were already calibrated, including full bias subtraction and flat-fielding. The association products consist of co-added, cosmic-ray cleaned images and association files, which contain the shifts between the single images. These shifts were used as input for the further reduction of the data, using HSTphot 1.1 (Dolphin 2000b). This package is especially written for the reduction and photometry of *HST* images.

First, the HSTphot task *mask* was used on each image to mask bad pixels and image defects. This ensures that these pixels are not used in the further analysis. The task *crmask* was used to remove the cosmic ray hits, which are widely present in the separate images. For each filter the images were compared against each other to remove the cosmic ray events. The HSTphot task *hotpixels* was then used to mask the known hot pixels in the WFPC2 detectors.

To obtain photometry for each individual image we used the photometry task *hstphot* of HSTphot 1.1. This task takes as input all available images in each filter and produces a master list of positions and magnitudes for each star found. The positions and magnitudes are determined by fitting a model point spread function (PSF), to each star. After all stars are fitted it calculates aperture corrections and corrects for the charge transfer efficiency effect. These corrections, together with the zero-points are described in (Dolphin 2000a).

2.3.2 Astrometry

To search for optical counterparts to the *Chandra* X-ray sources we aim to place both the X-ray and the optical frame onto the International Celestial Reference System (ICRS). We use this approach to improve the absolute pointing accuracy of *Chandra* and *HST*, $0\farcs6$ and $1\farcs0$ (1σ) respectively (Aldcroft et al. 2000; Biretta 2000).

To place the *HST* images onto the ICRS we use two intermediate steps; first, we align a ground-based image onto the ICRS using an astrometric catalog, then we align the *HST* images onto the ground-based image. To bring the X-ray frame onto the ICRS we use three optical identifications of X-ray sources.

[2] http://archive.eso.org/archive/hst/wfpc2_asn/

A 2 minute V-band image, taken on February 21, 2002 with the Wide Field Imager (WFI) at the ESO 2.2 meter telescope on La Silla, was retrieved from the ESO archive and used to calibrate the *HST*/WFPC2 images. The WFI has an array of 8 CCDs, each CCD having a $8' \times 16'$ field of view, giving a total of $33' \times 34'$. M4 is roughly centered on one chip, and, to minimize the effects of geometric distortion, an $8' \times 8'$ sub-image, containing the entire area within the half-mass radius, was extracted from this chip.

We found 115 stars on this sub-image that matched entries in the USNO CCD Astrograph Catalog (UCAC1, Zacharias et al. 2000). Of these stars, 91 were not saturated and appeared stellar and unblended and were used to compute an astrometric solution, fitting for zero-point position, scale and position angle. Five outliers, having residuals larger than $0\farcs2$ were rejected from the fit. The final solution has rms residuals of $0\farcs05$ in both coordinates.

We calibrate the *HST* frames with the astrometric solution of the WFI image. First, the pixel positions of the stars in the *HST* datasets are placed on a single metaframe using the geometric distortion corrections and relative chip positions/orientations found by Anderson & King (2003). Next, using the astrometric solution in the FITS header of the *HST* images, nominal celestial coordinates are computed for some 300–400 of the brightest stars. These positions are then matched with stars on the WFI image and their centroids are measured. Similar selection criteria for saturation and blending are used as with the UCAC stars. An astrometric solution is calculated from the calibrated celestial coordinates and the metaframe positions of the *HST* stars. Outliers having residuals larger than three times the rms residual of the fit are removed, and a new solution is computed. This process is iterated until convergence. On average after convergence the astrometric solution contained some 200 stars with rms residuals of $0\farcs07$ in both right ascension and declination.

The 1σ uncertainty in the optical positions is $0\farcs12$, the quadratic sum of the positional uncertainty in the tie of the WFI image to the UCAC ($0\farcs07$) and the uncertainty in the transfer to the *HST* frames ($0\farcs09$) and the uncertainty in the tie of the UCAC onto the ICRS ($0\farcs02$, Assafin et al. 2003). By placing the *HST* and WFI observations onto the ICRS with the UCAC we effectively set these images at the epoch of the UCAC observation, which is 1999.4. This implies that any average proper motion between the epochs of the *HST* and WFI observations has been removed. The difference in proper motion between cluster members and background stars (Bedin et al. 2003) possibly explains why our uncertainty in the calibration between *HST* and WFI is larger than what we have found for similar calibrations of data from other clusters (e.g. Bassa et al. 2003b).

We use three optical identifications in the *HST* data of the *Chandra* X-ray sources to place the X-ray frame onto the ICRS frame of the *HST*/WFPC2 images: the white dwarf companion of PSR B1620−26 and two W UMa variables. At the UCAC epoch, 1999.4, the position of PSR B1620−26 is $\alpha_{J2000} = 16^{\rm h}23^{\rm m}38\fs2147(5)$, $\delta_{J2000} = -26°31'53\farcs95(4)$, where we use the position and proper motion from Thorsett et al. (1999). According to our optical astrometry, this position is compatible with a white dwarf, at an offset of $-0\farcs04 \pm 0\farcs09$ ($-0\fs003 \pm 0\fs006$) in right ascension and $0\farcs07 \pm 0\farcs10$ in declination for the GO-5461 dataset. (The uncertainty in this offset is the quadratic sum of the uncertainty in the optical astrometry and the uncertainty in the corrected pulsar position.) With our accurate position ($0\farcs12$) for the white dwarf, we confirm the identification by Sigurdsson et al. (2003) and Richer et al. (2003) of this white

dwarf as the companion of the pulsar. The position of X-ray source CX12 coincides with that of PSR B1620−26.

Five optical variables found by Kaluzny et al. (1997) and Mochejska et al. (2002), roughly coincide with *Chandra* X-ray sources, three of which are in the *HST* field(s) of view. Comparison of the Kaluzny et al. (1997) finding charts with our WFI and *HST* images shows that the variables are indeed excellent matches to the X-ray sources. The three variables coincident with the *HST* images are all identified as W UMa binaries. V55/CX18 is a single star on the *HST* images, and we are confident that it is the star responsible for the optical variability. However, the variables V48 and V49 both are blends of four and two stars respectively. In the case of CX13/V49 one of the stars is clearly above the main sequence, indicating that this star is the variable. However, for CX15/V48 all stars of the blend lie on the main-sequence, and none of these can be securely identified as the variable.

We therefore use the optical positions of the white dwarf companion to PSR B1620−26 and the variables V49 and V55 to compute the shift needed to place the X-ray positions of CX12, CX13 and CX18 onto the optical positions. We have a total of 6 measurements, as CX12 is in the field of view of datasets GO-6116, GO-5461 and GO-8153, CX13 only in that of GO-6116 and CX18 in those of GO-5461 and GO-8153. The weighted average shift is $0\farcs00 \pm 0\farcs05$ in right ascension and $0\farcs15 \pm 0\farcs05$ in declination, well within the 1σ uncertainty of the absolute *Chandra* pointing accuracy. We apply this shift as a boresight correction to the X-ray positions.

2.3.3 Identification of counterparts in the *HST* images

We search for optical/UV stars inside 95% confidence radii of the *Chandra* sources positions. The 1σ uncertainty in a source position is the quadratic sum of the positional uncertainty for the X-ray source (Table 2.1), the uncertainty in the optical astrometry ($0\farcs12$) and the uncertainty in the X-ray boresight correction ($0\farcs07$). The 95% confidence radius is a factor $[-2\log(1-0.95)]^{1/2} = 2.448$ larger than the 1σ uncertainty in the position.

Each of the X-ray source error circles was visually checked for stars that were not found during the initial run of *hstphot*. Stars that were missed were added by hand and the photometry task was executed again.

The resulting photometry lists were used to create a set of color-magnitude diagrams (CMDs), shown in Figure 2.4. The data from the GO-6116 dataset is separated into three panels, one for each *HST*/WFPC2 chip containing X-ray sources, as the cluster main sequence is displaced by about 0.1 magnitude in $V_{555} - I_{814}$ between the individual chips. Differential reddening towards M4 (Cudworth & Rees 1990) is the likely cause for this. The data from the two GO-5461 fields, shown in the last two panels, did not display these displacements in color and the data from all four chips is plotted.

We used the *hstphot* information indicating the goodness of fit for a star to exclude the diffraction spike artifacts from the star list. These artifacts are widely present, especially in the GO-5461 dataset, which had the longest exposures. For more information we refer to the HSTphot 1.1 manual[3].

[3] http://www.noao.edu/staff/dolphin/hstphot/

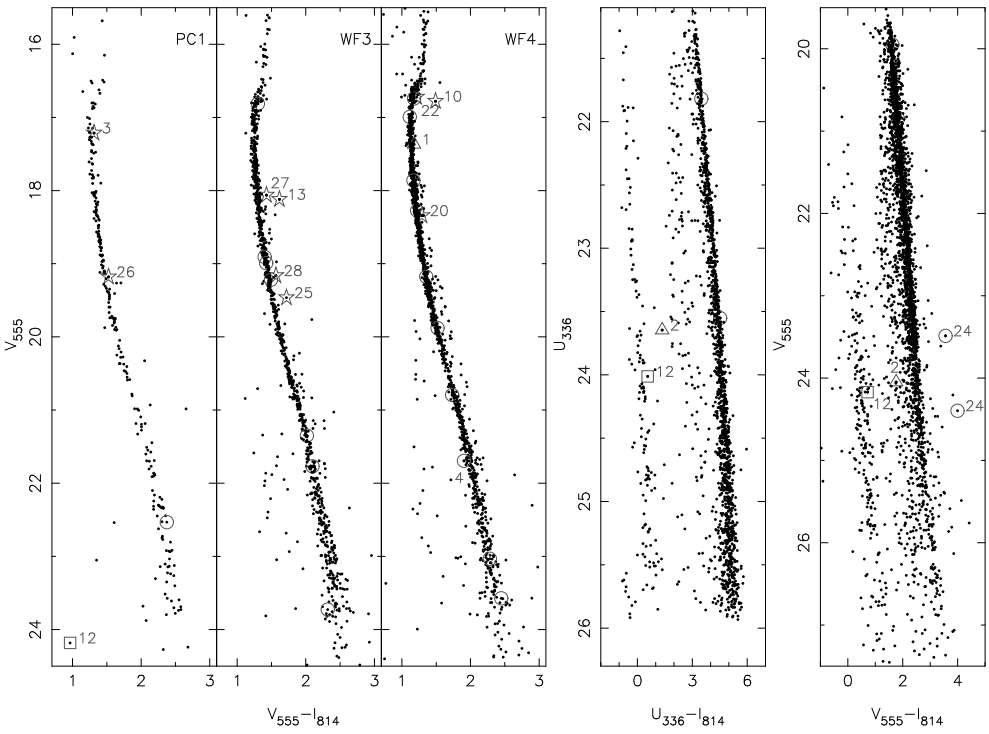

Figure 2.4: *Color-magnitude diagrams (CMDs) of the* HST/*WFPC2 observations of M4. The first three panels show CMDs from the GO-6116 dataset for the PC1, WF3 and WF4 chips, respectively (no X-ray sources coincide with the WF2 chip). The fourth and fifth panel show two CMDs of the data in both GO-5461 fields. All stars inside the 95% confidence error circles are marked, while the candidate counterparts are numbered. The X-ray sources are marked as in Fig. 2.1. The candidate counterpart to CX24 is plotted twice, as it was observed in both fields of the GO-5461 dataset and had varied in brightness. The candidate counterpart was brightest during the observation of the field closest to the core of M4.*

All stars within the 95% confidence radii of the *Chandra* source positions are marked in Figure 2.4. Stars with colors abnormal with respect to the cluster main sequence or giant branch are identified as candidate counterparts and are numbered in Fig. 2.4. Positional and color information for each candidate counterpart is tabulated in Table 2.2. Finding charts are shown in Figure 2.5.

2.3.4 Identification of counterparts in the WFI image

Several of *Chandra* X-ray sources coincide with stars on the WFI image. Two of these stars, identified by Mochejska et al. (2002) as variables V52 and V56 are coincident with X-ray sources CX8 and the possibly blended source CX5-9, respectively. The offset of the optical

Table 2.2: *Optical/UV Counterparts to Chandra X-ray Sources. Optical positions and magnitudes of the candidate counterparts. The optical positional is given by the Chandra value plus offset (in true seconds of arc) in each coordinate. Magnitude uncertainties are given in parentheses and refer to the last quoted digit. Stars that were saturated in a pass band are denoted with "sat." and stars that are not detected in a band are denoted with "und.".*

CX	GO[a]	$\Delta\alpha$ ($''$)	$\Delta\delta$ ($''$)	Δ (σ)	U_{336}	V_{555}	I_{814}	CX	GO	$\Delta\alpha$ ($''$)	$\Delta\delta$ ($''$)	Δ (σ)	U_{336}	V_{555}	I_{814}
1	6116	0.24	-0.14	2.0	…	17.37(1)	16.19(1)	20	6116	0.24	-0.13	1.1	…	18.34(1)	17.05(1)
2	5461	-0.02	-0.19	1.2	23.65(6)	24.05(3)	22.29(3)		5461	0.25	-0.15	1.1	19.62(1)	sat.	sat.
	8153	0.08	-0.07	0.7	…	…	22.04(1)		8153	0.26	-0.08	1.1	…	…	17.04(1)
3	6116	0.12	-0.00	0.8	…	17.22(1)	15.90(1)	22	6116	0.11	-0.03	0.5	…	16.73(1)	15.50(2)
	5461	0.19	-0.05	1.3	18.00(1)	sat.	sat.	24	5461	0.08	-0.46	1.8	und.	23.49(1)	19.93(1)
	5461	0.16	0.04	1.1	17.94(1)	sat.	sat.		5461	0.14	-0.52	2.1	und.	24.4(1)	20.40(3)
	8153	0.20	0.02	1.4	…	…	15.94(1)		8153	0.23	-0.38	1.8	…	…	19.93(1)
	8153	0.05	0.06	0.6	…	…	18.94(1)[b]		8153	0.20	-0.38	1.7	…	…	20.02(1)
4	6116	0.12	-0.01	0.8	…	21.69(3)	19.79(2)	25	6116	0.09	0.14	0.8	…	19.45(3)	17.75(1)
10	6116	-0.09	-0.21	1.2	…	16.78(1)	15.29(1)	26	6116	-0.03	-0.10	0.5	…	19.18(1)	17.66(1)
12	6116	0.02	-0.00	0.1	…	24.2(2)	23.2(2)		5461	…	…	…	sat.	sat.	sat.
	5461	0.08	0.03	0.5	24.01(8)	24.17(2)	23.45(4)		5461	0.02	-0.05	0.2	20.23(1)	sat.	sat.
	8153	0.11	0.02	0.7	…	…	23.49(3)		8153	0.06	-0.09	0.5	…	…	17.83(1)
13	6116	-0.08	0.03	0.4	…	18.11(1)	16.51(1)		8153	0.06	-0.09	0.5	…	…	17.76(2)
18	5461	-0.09	-0.05	0.4	17.76(1)	sat.	sat.	27	6116	-0.16	-0.18	0.8	…	18.06(1)	16.65(1)
	8153	-0.03	-0.04	0.2	…	…	15.64(1)	28	6116	0.29	0.11	1.3	…	19.16(1)	17.61(1)

[a]The *HST* GO dataset number from which the position and magnitudes are determined. For CX3, CX24 and CX26 the first entry for dataset GO5461 and GO8153 refers to the field nearest to the cluster center.

[b]This measurement is likely in error due to the proximity of the star to the edge of the chip.

positions with respect to the *Chandra* positions in Table 2.1 is $0\farcs06 \pm 0\farcs20$, $0\farcs22 \pm 0\farcs21$ for CX8 and V52, $-0\farcs29 \pm 0\farcs22$, $-0\farcs23 \pm 0\farcs21$ for CX5 and V56 and $0\farcs73 \pm 0\farcs20$, $0\farcs55 \pm 0\farcs21$ for CX9 and V56.

The X-ray source CX7 coincides with the UCAC1 star 22560073, a foreground star according to its proper motion (Cudworth & Rees 1990), star A330 with $V = 12.68$). The offset of the corrected X-ray position, as listed in Table 2.1, from the optical position from UCAC is $0\farcs38 \pm 0\farcs18$ in right ascension and $-0\farcs16 \pm 0\farcs20$ in declination. The error in this offset is dominated by the uncertainty in the X-ray position of CX7 in the *Chandra* frame; much smaller contributions to the error are due to the uncertainties in the X-ray to optical shift and in the optical position. Redetermining the X-ray to optical shift including CX7 with the other three optically identified X-ray sources, does not significantly change the value of the shift.

2.4 Source classification

In attempting to classify the X-ray sources detected in M4, we note that five of our optical counterparts to *Chandra* sources have a previously known classification. CX12 is a millisecond pulsar with a white dwarf companion (Thorsett et al. 1999); the optical counterpart corresponds to the white dwarf (Sigurdsson et al. 2003, see also Fig. 2.4). CX13/V49, CX15/V48

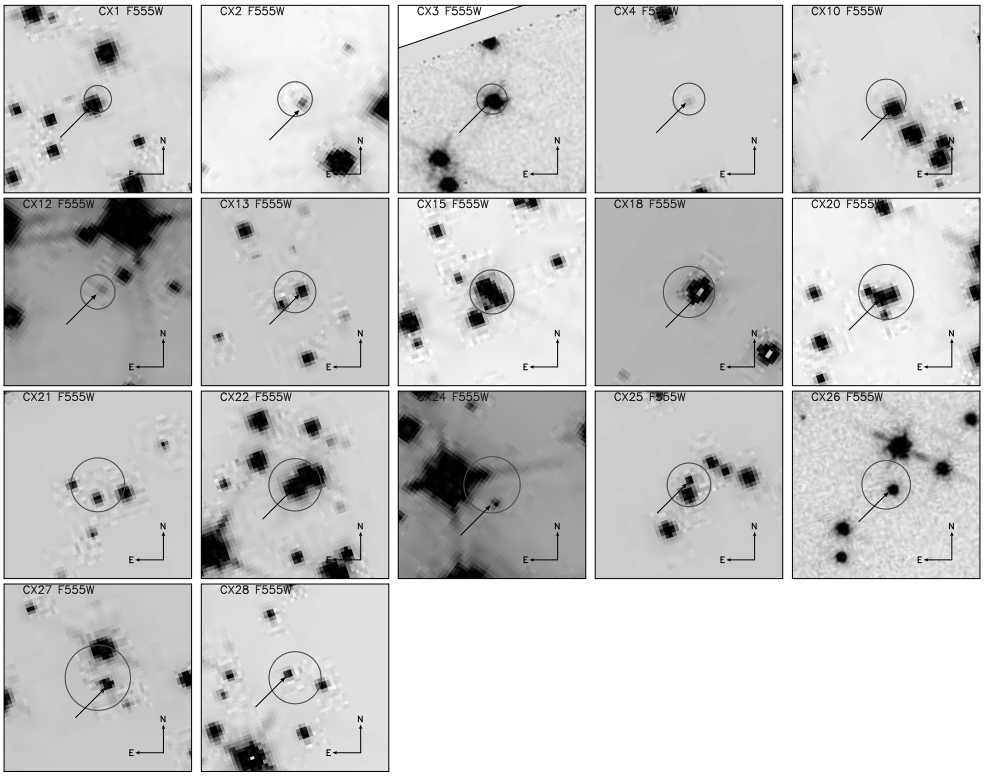

Figure 2.5: *5″ × 5″ finding charts for the candidate optical counterparts. The finding charts are constructed from the coadded V_{555} "association" images. For sources CX2, CX12, CX18 and CX24, images from the GO-5461 dataset were used, images from the GO-6116 dataset are used for the other candidate counterparts. The 95% confidence uncertainties on the Chandra positions are overlaid on these charts, while the candidate counterparts are indicated with an arrow. No arrow is present for sources CX15 and CX21 as no candidate counterparts were found. The pixel scale varies between sources coincident with WF chips and the PC1 chip (CX3 and CX26). The greyscale of these images is chosen as such to enhance the visibility of the candidate counterparts.*

and CX18/V55 are contact binaries, and CX8/V52 is a BY Dra system, i.e. these four sources are all magnetically active binaries (Kaluzny et al. 1997; Mochejska et al. 2002). The optical counterparts to CX13 and CX15 as identified from the ground based data, have both been resolved into multiple objects with *HST*/WFPC2. Kaluzny et al. (1997) noted that the optical counterpart to CX13, was brighter than expected for a contact binary with its period, placed at the distance and reddening of M4. This discrepancy is removed as our counterpart to CX13 is about a magnitude fainter than the blend (we note that the optical counterpart to CX13 appears to be too bright to be on the binary main sequence as it is about a magnitude brighter than a star on the main sequence with the same color, Fig. 2.4). For the optical counterpart of

CX15 the opposite appears to be the case. It was seen as a cluster member by Kaluzny et al. (1997), but *HST*/WFPC2 observations indicate that V48 is a blend of 3 or 4 stars. Hence, the contact binary is too faint to be a member, and may be a background object.

The possible blend of CX5 and CX9 coincides with the variable giant V56 found by Mochejska et al. (2002). If the giant is a member of a RS CVn binary then its variability and X-ray emission can be explained by magnetic activity. However, without more information on the optical properties of V56 the classification remains ambiguous.

In classifying the remaining X-ray sources we first look at the X-ray emission itself. A neutron star accreting at a low rate from a companion star, i.e. a low-luminosity (quiescent) low-mass X-ray binary (qLMXB), is characterized by a soft X-ray spectrum (black body color temperature $\lesssim 0.3$ keV) and a luminosity $L_X \gtrsim 10^{32}$ erg s^{-1} (Verbunt et al. 1994; Rutledge et al. 1999). None of the X-ray sources in our sample shows this characteristic, and we conclude that M4 does not contain a low-luminosity low-mass X-ray binary with an accreting neutron star.

We extract further information from the location of the optical star in the color-magnitude diagrams of Fig. 2.4: stars bluer than the main-sequence are possible cataclysmic variables, stars above the main-sequence possible magnetically active binaries. The ratio of X-ray to optical flux is also useful, as it roughly separates the cataclysmic variables from magnetically active binaries (Verbunt & Johnston 2000; Pooley et al. 2002a). We illustrate this in Fig. 2.6, where we plot data from 47 Tuc (Edmonds et al. 2003a,b) and NGC 6752 (Pooley et al. 2002a), and add our data from M4.

CX2 is a probable cataclysmic variable, because it is blue (Fig. 2.4) and has a relatively high X-ray to optical flux ratio (Fig. 2.6). High X-ray to optical flux ratios suggest that CX1 and CX4 also are cataclysmic variables, even though they are located on or close to the main sequence in the color-magnitude diagram (Fig. 2.4).

The X-ray luminosity of CX1 is too high for a magnetically active binary of two main sequence stars (i.e. a BY Dra system), and its optical magnitude excludes that it is a magnetically active binary with a sub-giant (i.e. a RS CVn system). This, and the relative hardness of the X-ray spectrum (Fig. 2.3) indicate that it is a cataclysmic variable. We note that the optical counterpart to CX1 is offset from the *Chandra* position by 2σ and might be a chance coincidence. This would indicate that the actual optical counterpart is even fainter, possibly lost in the glare of the bright star, leading to higher X-ray to optical flux ratios, as seen with most other CVs.

The less luminous counterpart to CX4 is probably a cataclysmic variable; its location near the main-sequence in $V_{555} - I_{814}$ has precedents in other globular clusters (Edmonds et al. 2003a,b).

The optical counterpart of CX24 varies by more than a magnitude in brightness (Fig. 2.4). It is located further above or to the right of the main-sequence than the binary sequence. Hence we believe that CX24 is either a fore or background object and unrelated to M4. The same argument could be made for CX10. However, stars at similar positions in the color-magnitude diagram of other old clusters are X-ray sources and confirmed members (albeit unexplained, see e.g. Mathieu et al. 2003 for M67 and Orosz & van Kerkwijk 2003 for NGC 6397) or probable members (Albrow et al. 2001; Edmonds et al. 2003a) for 47 Tuc).

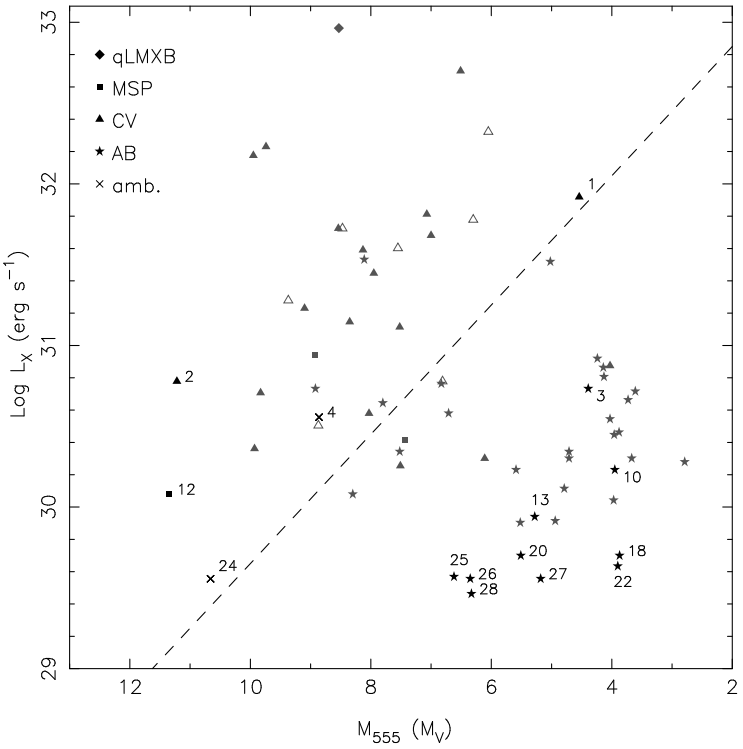

Figure 2.6: *The X-ray luminosity L_X (0.5–2.5 keV) and the absolute V_{555} (approximately V-band) magnitude for X-ray sources with identified optical counterparts. Five types of X-ray sources are shown, quiescent LMXBs (*diamonds*), MSPs (*squares*), CVs (*triangles*), ABs (*stars*) and unclassified (*crosses*). The closed points are sources from 47 Tuc (Grindlay et al. 2001a; Edmonds et al. 2003a) and the open points are from NGC 6752 (Pooley et al. 2002a). The numbered points are the optical counterparts to the Chandra X-ray sources in M4, the number corresponds to the source number. The absolute magnitude of the optical counterparts is computed from the V_{555} magnitudes and the V-band distance modulus as in Harris (1996) for 47 Tuc and NGC 6752 and that of Richer et al. (1997) for M4. The dashed line of constant X-ray to optical flux ratio roughly separates cataclysmic variables from active binaries.*

We therefore consider CX10 a probable cluster member.

Based on positional coincidence we identify CX7 with the UCAC1 star 22560073. This star has $V = 12.68$, $B - V = 0.88$ (Cudworth & Rees 1990), which is compatible with a K2V star at a distance of about 200 pc. Scaling the X-ray luminosity from Table 2.1 from the distance of M4 to a distance of 200 pc gives $L_X \approx 2.4 \times 10^{28}$ erg s^{-1}, well within the range observed for ordinary K2V stars (Verbunt 2001).

The relatively low X-ray to optical flux ratios of the remaining optical counterparts found with *HST*/WFPC2 suggests that they are active binaries. The counterparts of CX13 and

CX18, already known to be contact binaries from ground based data, are among these. (The V_{555} image of the optical counterpart of CX18 is over-exposed; we use the estimate $V_{555} = (U_{336} + I_{814})/2$.) The others (CX3, CX20, CX22, CX25, CX26, CX27, CX28) are at or above the main-sequence, as expected for binaries, and we conclude that all of them are magnetically active binaries. The X-ray-to-optical flux ratio of any of the 2 candidate counterparts of CX21 is comparable to that of an active binary.

2.5 Discussion

The X-ray luminosities of the *Chandra* sources in M4 are amongst the lowest ever observed in a globular cluster. More than half of the X-ray sources in this cluster have $L_X < 10^{30}$ erg s^{-1}, compared to 10% of the sources in 47 Tuc (Grindlay et al. 2001a) and 28% of the sources in NGC 6397 (Grindlay et al. 2001b).

It is therefore not surprising that only one of the X-ray sources detected with *Chandra* may have been detected before. The position of the marginal *ROSAT* HRI source R9 (Verbunt 2001) is 7.″5 from that of CX1. Even though this is further than expected from the error given for the *ROSAT* HRI source, we think the identification is probable. The X-ray luminosity of the *ROSAT* HRI source is only 1.3×10^{31} erg s^{-1}, a factor six below the luminosity detected with *Chandra*. The upper limit from the *ROSAT* PSPC observation is 1.5×10^{31} erg s^{-1}. (These luminosities are re-computed for a distance of 1.73 kpc and for the spectrum of CX1, and thus differ from those given by Verbunt; mainly because he used a distance of 2.2 kpc.) This large variability indicates that CX1 is a cataclysmic variable rather than a radio pulsar. Note that even if the *ROSAT* source is not identical to CX1, it still provides an upper limit to the flux of CX1 during the *ROSAT* observations, and thus proves that CX1 is highly variable.

Several other X-ray sources coincide with optical variables discovered by Kaluzny et al. (1997) and Mochejska et al. (2002). The sources CX13, CX15 and CX18 are coincident with W UMa variables V49, V48 and V55, with orbital periods of 0.283, 0.298 and 0.311 days, respectively. The upper limit on the X-ray luminosity of the other W UMa binaries found by Kaluzny et al. (1997), V44, V47, V50, V51, V53 and V54, is about 3×10^{29} erg s^{-1}. Both detections and upper limits of these W UMa variables are in agreement with the range of X-ray luminosities of W UMa binaries in the *ROSAT* All Sky Survey (Stępień et al. 2001).

CX8 coincides with the variable V52, which is classified as a BY Dra system with a period of 0.777 days. The possible blend of X-ray sources CX5 and CX9 coincides with the variable V56. No period is known for this object, but its variability (a rise of 0.1 mag in 4 days) and its location on the giant branch (Mochejska et al. 2002) are suggestive of an RS CVn variable. If it is, it is the first RS CVn binary detected in X-rays in a globular cluster – a marked contrast with old open clusters, where RS CVns dominate the X-ray sources (Belloni et al. 1998). The exposure of the eclipsing binary V54 is not as good as for the other sources, hence the upper limit on the X-ray luminosity of this source is somewhat higher. Detections and upper limits of these binaries are well within the range observed for magnetically active binaries, e.g. in the *ROSAT* All Sky Survey (Dempsey et al. 1993).

In trying to determine the X-ray luminosity function of M4, we can use the number of detected sources as a function of luminosity. However, the number of excess counts, not

allocated to individually detected sources, also contains information about the luminosity function. If we assume a luminosity function $dN \propto {L_X}^{-\gamma} d \log L_X$ and a reference luminosity L_r, then the ratio of the contributions to the total luminosity by sources in the ranges $(0.1–1)L_r$ and $(1–10)L_r$ is given by

$$R_L(L_r) \equiv \frac{\int_{0.1L_r}^{L_r} L_X dN}{\int_{L_r}^{10L_r} L_X dN} = 10^{\gamma-1} \tag{2.1}$$

and the ratio of the number of sources in the same ranges is

$$R_N(L_r) = 10^{\gamma} = 10 R_L(L_r). \tag{2.2}$$

In particular, we note that for $\gamma < 0.7$ and a luminosity function continuing to arbitrarily low luminosities the total luminosity of all sources with $L_X < L_r$ is less than the luminosity for the sources with $(1–10)L_r$. In the following we assume that the ratio of counts is proportional to the ratio of luminosities, and we use as a reference luminosity $L_r \equiv 6 \times 10^{29}$ erg s^{-1}.

Following the method described in Johnston & Verbunt (1996) and Pooley et al. (2002b) we derive from the list of detected X-ray sources (Table 2.1) that $\gamma = 0.71$ for X-ray luminosities above $L_X(0.5 - 2.5) = 4.4 \times 10^{29}$ erg s^{-1}. The K-S probability of this value is 93%. For K-S probabilities above 10% the slope of the luminosity function has $0.47 < \gamma < 1.07$.

In addition to the detected sources, we have an excess in the core of M4 of about 150 counts, uncorrected for absorption, which corresponds to roughly 300 counts corrected for absorption in the 0.5–6.0 keV band (which is the addition of counts in X_{soft} and in X_{hard}). In this band, the five faintest sources in the core, CX20, CX21, CX22, CX26 and CX27 have between 14 and 10 counts. A minimum number of sources required to explain the excess counts is found by assuming that each source has 10–14 counts, which gives 22–30 sources.

The total number of ~ 350 counts from sources *in the core* of M4 with $L_X < L_r$ (five detected sources and the excess) is similar to that of the 6 sources in the range $(1–10)L_r$. From our remark following Eqs. 2.1 and 2.2, we see that this implies that $\gamma \geq 0.7$; for lower values of γ the sources with $L_X < L_r$ do not contribute enough counts to explain the observed number. On the other hand, for $\gamma = 1$ the luminosity function must have a cutoff near $0.1L_r$, because otherwise the sources with $L_X < L_r$ would produce more counts than is observed. With 6 sources in the range (1–10) L_r, and for $\gamma = 0.7 - 1.0$ we have 30–60 core sources in the range $(0.1–1)L_r$.

In the core of 47 Tuc there are 14 sources in the range (10–100) L_r, which for $\gamma = 0.7-0.8$ leads to predicted numbers of 70–90 (of which 27 are already detected individually) in the range (1–10) L_r, and 350–560 in the range (0.1–1) L_r. These numbers are compatible with the total number of counts in the core of 47 Tuc from the observed sources plus the excess of about 500 counts, estimated by Grindlay et al. (2001a).

In Table 2.3 we compare the collision numbers and the masses of the cores of M4 and 47 Tuc. We expect that the numbers of cataclysmic variables scales with the collision number, and the number of magnetically active binaries with the mass. In the range (1–10) L_r the ratio of numbers of sources in the cores of M4 and 47 Tuc suggest that the ratio is set by mass rather than collision number. This in turn suggests that magnetically active binaries dominate the numbers at these luminosities, in agreement with our suggested identifications in M4.

Table 2.3: *Scaling Parameters of M4, NGC 6397 and 47 Tuc. Values for central density (ρ_0), core-radius (r_c), distance (d) and absolute visual magnitude (M_V) originate from Harris (1996) (version of February 2003). For M4, the values of ρ_0 and M_V are computed for the distance and reddening of Richer et al. (1997). The collision number is computed from $\Gamma \propto \rho_0^{1.5}\, r_c^2$ and the core mass from $M_c \propto \rho_0\, r_c^3$. Values for Γ and M_c are normalized to the value of M4.*

Cluster	$\log \rho_0$ ($L_\odot pc^{-3}$)	r_c ($''$)	d (kpc)	M_V	Γ	M_c
M4	4.01	49.8	1.73	−6.9	1.0	1.0
NGC 6397	5.68	3.0	2.3	−6.6	2.1	0.024
47 Tuc	4.81	24.0	4.5	−9.4	24.9	12.4

Comparison with NGC 6397 is also interesting, as its collision number is somewhat higher, $\Gamma = 2.1$ (normalized to the value of M4) while its total mass (as measured from its absolute magnitude) is somewhat lower than that of M4. Within its half-mass radius, NGC 6397 contains 9 cataclysmic variables, 4 magnetically active binaries and 10 as yet unclassified sources (generally of low X-ray luminosity). Within the half mass radius of M4 we find 2 or 3 cataclysmic variables, 12 magnetically active binaries and 15 unclassified sources, of which an estimated 6–12 are background sources. The ratio for the numbers in NGC 6397 and M4 of magnetically active binaries is as expected for a scaling with mass. As already noted by Pooley et al. (2003), NGC 6397 contains rather more cataclysmic variables than expected on the basis of its collision number. This is reflected in the flat slope of its X-ray luminosity function. If the high number of bright systems in NGC 6397 is explained by a higher mass of this cluster in the past (as suggested by Pooley et al. 2003), one would expect an accordingly higher number of magnetically active binaries, in contrast to what is observed (assuming that magnetically active binaries have a similar evaporation rate as cataclysmic variables, much lower than the evaporation rate of single stars). In this respect, it is worth noting that the time scale on which a binary can be destroyed by a close encounter is short in NGC 6397 compared to most other clusters, including M4 and 47 Tuc (Verbunt 2003, in particular Fig. 3b). Since magnetically active binaries tend to have longer orbital periods then cataclysmic variables, they would be easier destroyed by close encounters. This might explain the absence of large numbers of such binaries in NGC 6397.

2.6 Addendum

Astrophysical Journal 2005, 619, 1189

Luigi Bedin and Ivan King informed us that the X-ray source CX 2 is in fact the candidate quasi-stellar-object (QSO) identified by Bedin et al. (2003). Fig. 2.7 shows a finding chart of the area around the X-ray position of CX 2 and allows for a direct comparison with the finding chart (Fig. 5) of Bedin et al. (2003).

From the location of the proposed optical counterpart to CX 2 in the color-magnitude diagram (Fig. 2.4), together with the X-ray-to-optical flux ratio (Fig. 2.6), we concluded that

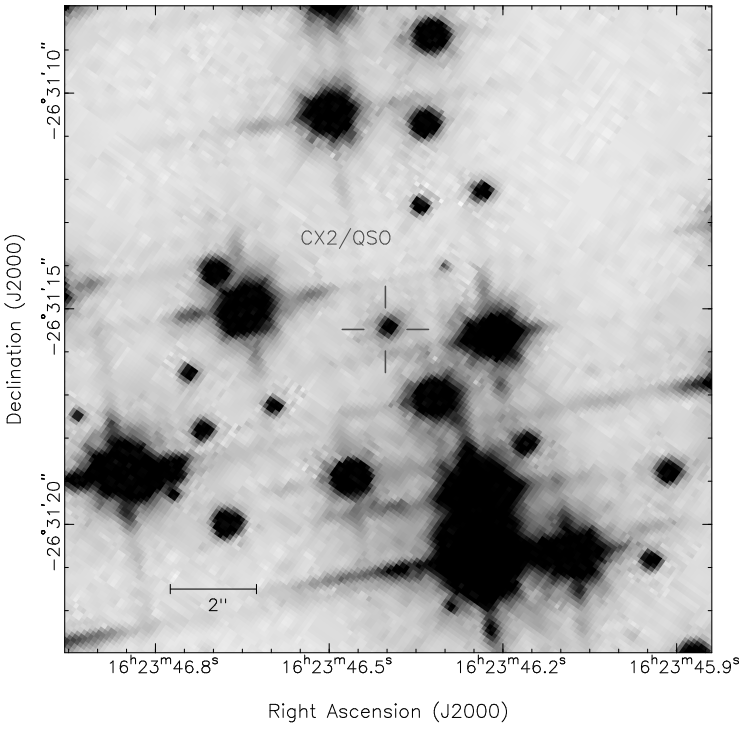

Figure 2.7: HST/*WFPC2* I_{814} *image of a* $15'' \times 15''$ *region around CX 2.*

this X-ray source is a probable cataclysmic variable (CV). That it now turns out probably to be an extra-galactic source underlines the difficulties in securely classifying X-ray sources in globular clusters.

After removal of CX 2 the number of CVs in M4 is one (CX 1) or possibly two (CX 4). This does not change the conclusions made in Section 2.5, as we only compared the core-radii of M4 and 47 Tuc, while CX 2 is at nearly 3 core-radii.

Chapter 3

Chandra and Hubble Space Telescope study of the globular cluster NGC 288

A. K. H. Kong, C. G. Bassa, D. Pooley, W. H. G. Lewin,
L. Homer, F. Verbunt, S. F. Anderson, B. Margon

Astrophysical Journal 2006, 647, 1065–1074

Abstract We report on the *Chandra X-ray Observatory* observations of the globular cluster NGC 288. We detect four X-ray sources within the core radius and seven additional sources within the half-mass radius down to a limiting luminosity of $L_X = 7 \times 10^{30}$ ergs s^{-1} (assuming cluster membership) in the 0.3–7 keV band. We also observed the cluster with the *Hubble Space Telescope* Advanced Camera for Surveys and identify optical counterparts to seven X-ray sources out of the nine sources within the *Hubble Space Telescope* field-of-view. Based on the X-ray and optical properties, we find 2–5 candidates of cataclysmic variables (CVs) or chromospherically active binaries, and 2–5 background galaxies inside the half-mass radius. Since the core density of NGC 288 is very low, the faint X-ray sources of NGC 288 found in the *Chandra* and *Hubble Space Telescope* observations is higher than the prediction on the basis of the collision frequency. We suggest that the CVs and chromospherically active binaries are primordial in origin, in agreement with theoretical expectation.

3.1 Introduction

The number of bright X-ray sources, with luminosities greater than 10^{36} erg s^{-1}, per star has been estimated to be ∼100 times as large in Galactic globular clusters as in the Galactic disk (Katz 1975; Clark 1975). A population of dim sources, with X-ray luminosities less than about $10^{34.5}$ erg s^{-1}, was discovered later (Hertz & Grindlay 1983; see also Verbunt 2001). The result by Pooley et al. (2003) suggests that the number of dim sources with $L_X > 4{\times}10^{30}$ erg s^{-1} (0.5–6 keV) scales roughly with the number of close stellar encounters in a cluster, and that the incidence per star of dim X-ray sources is also higher in globular clusters than in the galactic disk. There is evidence, from X-ray bursts associated with the nuclear burning of accreted matter, that the bright sources are neutron stars which are accreting matter from a companion. Although some of the dim sources may be neutron stars or even black holes in quiescence, it is likely that a majority of these, especially those with the lowest luminosities, are accreting white dwarfs and X-ray active main sequence/sub-giant binaries (see e.g., Pooley et al. 2003; Verbunt & Lewin 2006; Heinke et al. 2005).

To identify faint X-ray sources in globular clusters, the *Chandra* X-ray Observatory and *Hubble Space Telescope (HST)* are absolutely essential because the density of X-ray sources is expected to be high and sub-arcsecond spatial resolution is required to search for reliable optical counterparts in such crowded regions. Since the launch of *Chandra*, four globular clusters dominated by faint X-ray sources have been studied in detail with *Chandra* and *Hubble Space Telescope*: 47 Tuc (Grindlay et al. 2001a; Heinke et al. 2005), NGC 6397 (Grindlay et al. 2001b), NGC 6752 (Pooley et al. 2002a), and M4 (Bassa et al. 2004). Of these faint X-ray sources, many are believed to be cataclysmic variables (CVs) and X-ray active binaries (e.g. RS CVn and BY Dra systems). There are also quiescent low-mass X-ray binaries (qLMXBs; Heinke et al. 2003 and references therein) and millisecond pulsars (Edmonds et al. 2001; Grindlay et al. 2001b; Bassa et al. 2004).

We report here new *Chandra* and *Hubble Space Telescope* observations of the globular cluster NGC 288. NGC 288 is a globular cluster with a fairly low central density ($\log \rho_0 = 1.8\,L_\odot\,pc^{-3}$; Djorgovski 1993) with a core radius of 85″ and a half-mass radius of 2.25′ (Trager et al. 1993). The distance to this cluster is estimated at 8.4 kpc (Peterson 1993). The reddening is quite low with $E_{B-V} = 0.03$, corresponding to a neutral hydrogen column $N_H = 1.6 \times 10^{20}$ cm^2 (Predehl & Schmitt 1995). NGC 288 is located close to the Southern Galactic Pole ($l = 152.^\circ28$, $b = -89.^\circ38$) and thus we are looking directly out of the plane. As such, there will not be many foreground objects at optical and X-ray wavelengths. The cluster center is given by Webbink (1985) as $\alpha_{J2000} = 00^h52^m45.^s3$ and $\delta_{J2000} = -26^\circ34'43''$. The absolute visual magnitude of NGC 288 is −6.7 (Harris 1996, version of February 2003). An exceptionally high concentration of blue stragglers and binary systems in the core of NGC 288 suggests that the blue stragglers' production mechanism via binary evolution can be very efficient Bolte (1992); Bellazzini et al. (2002). In the X-ray waveband, NGC 288 has only been observed with *ROSAT* HRI (Sarazin et al. 1999). From the *ROSAT* data, only one X-ray source was within the half-mass radius (Sarazin et al. 1999).

In Sect.2̇, we describe our *Chandra* observations and analysis of NGC 288. We discuss the *Hubble Space Telescope* observations in Sect. 3, and source identification in Sect. 4. A

discussion and comparison with other globular clusters will be given in Sect. 5.

3.2 X-ray observations and analysis

NGC 288 was observed with *Chandra* for 55 ks on 2003 February 6 (OBSID 3777). The telescope aim point is on the Advanced CCD Imaging Spectrometer (ACIS) back-illuminated S3 chip. Data were telemetered in faint mode and were collected with a frame transfer time of 3.2 s. The $8' \times 8'$ S3 chip covers the entire cluster half-mass radius. In this paper, we only focus on the data taken with the S3 chip.

3.2.1 Data reduction

The data reduction and analysis was done with CIAO, Version 3.2.2 and ACIS Extract[1] (Broos et al. 2002). We reprocessed the level 1 event files with CALDB 3.1.0. In order to reduce the instrumental background, only data with *ASCA* grades of 0, 2, 3, 4, and 6 were included. Only events with photon energies in the range of 0.3–7.0 keV were included in our analysis. We also inspected the background count rates from the S1 chip; about 6 ks was eliminated due to high background count rate (count rate > 2 counts s^{-1}). The effective exposure time for the observation after filtering for background flares was 49 ks.

3.2.2 Source detection

Discrete sources in the *Chandra* images were found with WAVDETECT (Freeman et al. 2002) together with exposure maps. We performed source detection on the 0.3–1 keV, 1–2 keV, 2–7 keV, and 0.3–7 keV images. We set the detection threshold to be 10^{-6}, corresponding to less than one false detection due to statistical fluctuations in the background. For each of the four energy band images, we performed source detection using sequences of wavelet scales that increased by a factor of $\sqrt{2}$ from scales 1 to 16. We then combined the four source lists into a master source list. A total of 36 X-ray sources were detected. Fig. 3.1 shows the detected X-ray sources on the ACIS-S3 chip. Source counts in the three band passes were extracted from polygonal extraction regions which approximate 90% of the *Chandra* point spread function (PSF). Background was extracted from a circle centered on each source but excluding the 99% contour of the PSF around any point source.

Table 3.1 lists the 36 *Chandra* sources in our catalog, sorted in order of increasing right ascension. The columns give the source number, the position (J2000.0), the net counts in the three energy bands (soft: 0.3–1 keV; medium: 1–2 keV; hard: 2–7 keV), the 0.5–2.5 and the 0.3–7 keV unabsorbed fluxes. The conversion to fluxes assumes an absorbed power-law spectrum with a photon index of 2 and $N_{\rm H} = 1.6 \times 10^{20}$,$\rm cm^{-2}$. If we assume a thermal bremsstrahlung model with $kT = 10$ keV, then the flux will be $\sim 10\%$ higher than that of power-law model. It is worth noting that CX 15 is a very soft X-ray source with all photons coming from the 0.3–1 keV band. If we assumed a power-law model and that the counts

[1] http://www.astro.psu.edu/xray/docs/TARA/ae_users_guide.html

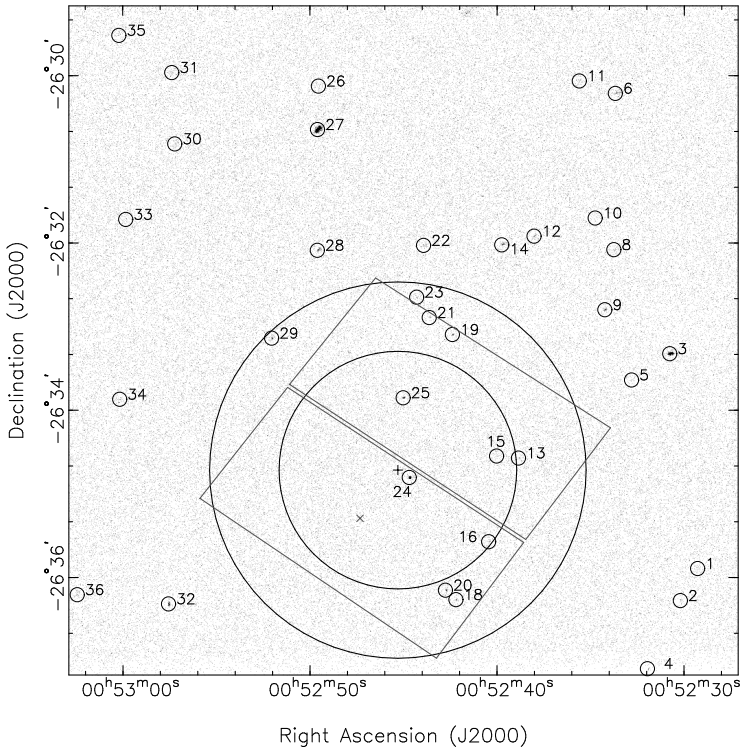

Figure 3.1: *Chandra ACIS-S3 0.3–7 keV image of NGC 288. The large circle represents the half-mass radius and the inner circle is the core radius. The cluster center is marked by a cross. The two rectangles denote the field-of-view of the* HST*/ACS. The detected X-ray sources are marked and numbered.*

were from the whole 0.3–7 keV range, the flux would be underestimated. Therefore, for CX 15, we convert the flux by assuming counts from 0.3–1 keV only. For the power-law model, the resulting 0.3–7 keV unabsorbed flux is 1.5×10^{-15} ergs cm^{-2} s^{-1}. If we assume a blackbody model with $kT = 0.1$ keV, then the flux will be 7.8×10^{-14} ergs cm^{-2} s^{-1}. The detection limit in the 0.5–2 keV band of our observation is about 3.2×10^{-16} ergs cm^{-2} s^{-1}. We estimated the number of background sources using *Chandra* deep field data (Brandt et al. 2001). Using the $\log N$–$\log S$ distribution derived from the deep field data, between 26–36 sources out of the 36 sources are background objects in the ACIS-S3. Within the half-mass radius, there are 11 sources and 7–9 sources are estimated to be background. For an expected number of 9 background sources, the probability of finding 11 or more background sources is 30%. Thus we cannot exclude that all our sources are background sources. Indeed, in the *Chandra* image shown in Fig. 3.1 the surface number density is not noticeably higher within the halfmass radius than outside it.

Table 3.1: Chandra *source properties. The positions have been corrected for boresight, in that the right ascensions and declinations resulting from the* Chandra *source detection with wavdetect have been corrected by* 0.″137 *and* −0.″055 *respectively (see Sect. 3.2). The positional uncertainties are in units of arcseconds given by wavdetect. The unabsorbed flux is in units of* 10^{-15} *ergs cm*$^{-2}$ *s*$^{-1}$ *and is derived assuming a power-law model (except for CX 15) with* $N_{\rm H} = 1.6 \times 10^{20}$ *cm*$^{-2}$ *and a photon index of 2.*

	Source	R.A.	Decl.	Net Counts			$f_{0.5-2.5}$	
CX	CXOU J	(J2000.0)	(J2000.0)	Soft	Medium	Hard		Counterpart
1	005229.4−263553	00$^{\rm h}$52$^{\rm m}$29.$^{\rm s}$413(0.30)	−26°35′53.″46(0.23)	0.7	4.8	0.5	0.46	
2	005230.3−263616	00$^{\rm h}$52$^{\rm m}$30.$^{\rm s}$336(0.21)	−26°36′16.″52(0.23)	1.7	2.8	2.6	0.54	
3	005230.9−263319	00$^{\rm h}$52$^{\rm m}$30.$^{\rm s}$909(0.07)	−26°33′19.″47(0.04)	98.7	69.8	28.5	15.16	
4	005232.0−263705	00$^{\rm h}$52$^{\rm m}$32.$^{\rm s}$092(0.12)	−26°37′05.″36(0.18)	0.9	11.0	5.9	1.37	
5	005232.9−263338	00$^{\rm h}$52$^{\rm m}$32.$^{\rm s}$950(0.22)	−26°33′38.″28(0.09)	1.8	2.8	2.6	0.56	
6	005233.8−263012	00$^{\rm h}$52$^{\rm m}$33.$^{\rm s}$818(0.24)	−26°30′12.″67(0.23)	22.7	27.2	7.4	4.43	
7	005233.8−262901	00$^{\rm h}$52$^{\rm m}$33.$^{\rm s}$838(0.26)	−26°29′01.″05(0.68)	4.8	5.9	5.5	1.26	
8	005233.8−263204	00$^{\rm h}$52$^{\rm m}$33.$^{\rm s}$899(0.28)	−26°32′04.″80(0.21)	4.5	0.0	5.3	0.76	
9	005234.3−263247	00$^{\rm h}$52$^{\rm m}$34.$^{\rm s}$380(0.09)	−26°32′47.″90(0.09)	12.7	12.8	9.6	2.71	
10	005234.8−263142	00$^{\rm h}$52$^{\rm m}$34.$^{\rm s}$897(0.39)	−26°31′42.″08(0.25)	2.4	1.6	4.1	0.33	
11	005235.7−263003	00$^{\rm h}$52$^{\rm m}$35.$^{\rm s}$748(0.40)	−26°30′03.″80(0.14)	15.7	7.2	1.1	1.86	
12	005238.1−263155	00$^{\rm h}$52$^{\rm m}$38.$^{\rm s}$162(0.19)	−26°31′55.″14(0.11)	1.6	0.0	13.3	1.14	
13	005238.9−263434	00$^{\rm h}$52$^{\rm m}$38.$^{\rm s}$991(0.13)	−26°34′34.″29(0.09)	0.0	0.0	7.7	0.60	*HST*
14	005239.8−263201	00$^{\rm h}$52$^{\rm m}$39.$^{\rm s}$888(0.11)	−26°32′01.″33(0.08)	9.7	15.8	13.5	3.02	
15	005240.1−263432	00$^{\rm h}$52$^{\rm m}$40.$^{\rm s}$164(0.23)	−26°34′32.″82(0.17)	3.9	0.0	0.0	0.32[a]	*HST*
							0.78[b]	
16	005240.5−263534	00$^{\rm h}$52$^{\rm m}$40.$^{\rm s}$585(0.18)	−26°35′34.″32(0.13)	2.9	4.9	4.8	0.97	
17	005241.7−262914	00$^{\rm h}$52$^{\rm m}$41.$^{\rm s}$735(0.23)	−26°29′14.″74(0.26)	25.4	25.3	13.9	5.01	
18	005242.3−263615	00$^{\rm h}$52$^{\rm m}$42.$^{\rm s}$337(0.10)	−26°36′15.″83(0.15)	0.0	6.9	3.8	0.83	*HST*
19	005242.5−263305	00$^{\rm h}$52$^{\rm m}$42.$^{\rm s}$526(0.14)	−26°33′05.″71(0.13)	2.9	8.9	2.8	1.12	*HST*
20	005242.6−263609	00$^{\rm h}$52$^{\rm m}$42.$^{\rm s}$622(0.08)	−26°36′09.″08(0.08)	8.9	8.9	7.8	1.97	*HST*
21	005243.7−263253	00$^{\rm h}$52$^{\rm m}$43.$^{\rm s}$764(0.12)	−26°32′53.″54(0.12)	3.9	6.9	0.0	0.83	
22	005244.0−263201	00$^{\rm h}$52$^{\rm m}$44.$^{\rm s}$070(0.22)	−26°32′01.″78(0.16)	8.7	3.8	1.5	1.08	
23	005244.4−263238	00$^{\rm h}$52$^{\rm m}$44.$^{\rm s}$435(0.18)	−26°32′38.″88(0.11)	1.9	1.9	1.7	0.43	
24	005244.8−263448	00$^{\rm h}$52$^{\rm m}$44.$^{\rm s}$832(0.03)	−26°34′48.″22(0.03)	29.9	99.9	71.8	15.64	*HST*, *ROSAT*
25	005245.1−263351	00$^{\rm h}$52$^{\rm m}$45.$^{\rm s}$158(0.10)	−26°33′51.″08(0.06)	11.9	15.9	7.8	2.76	*HST*
26	005249.6−263007	00$^{\rm h}$52$^{\rm m}$49.$^{\rm s}$682(0.25)	−26°30′07.″47(0.44)	0.0	1.4	11.2	0.97	
27	005249.7−263038	00$^{\rm h}$52$^{\rm m}$49.$^{\rm s}$731(0.06)	−26°30′38.″63(0.05)	184.2	210.5	102.9	38.50	
28	005249.7−263205	00$^{\rm h}$52$^{\rm m}$49.$^{\rm s}$744(0.11)	−26°32′05.″28(0.09)	2.7	16.8	19.5	3.02	
29	005252.1−263308	00$^{\rm h}$52$^{\rm m}$52.$^{\rm s}$184(0.10)	−26°33′08.″26(0.12)	0.0	6.9	16.6	1.81	
30	005257.3−263048	00$^{\rm h}$52$^{\rm m}$57.$^{\rm s}$360(0.18)	−26°30′48.″93(0.20)	2.2	11.4	12.6	2.03	
31	005257.5−262957	00$^{\rm h}$52$^{\rm m}$57.$^{\rm s}$519(0.28)	−26°29′57.″76(0.24)	10.5	11.8	3.8	2.01	
32	005257.7−263618	00$^{\rm h}$52$^{\rm m}$57.$^{\rm s}$700(0.08)	−26°36′18.″90(0.11)	42.8	5.9	0.6	3.80	
33	005259.9−263143	00$^{\rm h}$52$^{\rm m}$59.$^{\rm s}$980(0.34)	−26°31′43.″10(0.27)	2.4	2.5	3.5	0.65	
34	005300.3−263352	00$^{\rm h}$53$^{\rm m}$00.$^{\rm s}$307(0.19)	−26°33′52.″12(0.15)	0.0	5.7	7.4	1.02	
35	005300.3−262931	00$^{\rm h}$53$^{\rm m}$00.$^{\rm s}$341(0.43)	−26°29′31.″06(0.45)	2.1	11.7	12.4	2.01	
36	005302.5−263612	00$^{\rm h}$53$^{\rm m}$02.$^{\rm s}$583(0.33)	−26°36′12.″27(0.20)	0.7	5.8	3.4	0.77	

[a] Assuming a blackbody model with 0.1 keV and counts from 0.3–1 keV.
[b] Assuming a power-law model with photon index of 2 and counts from 0.3–1 keV.

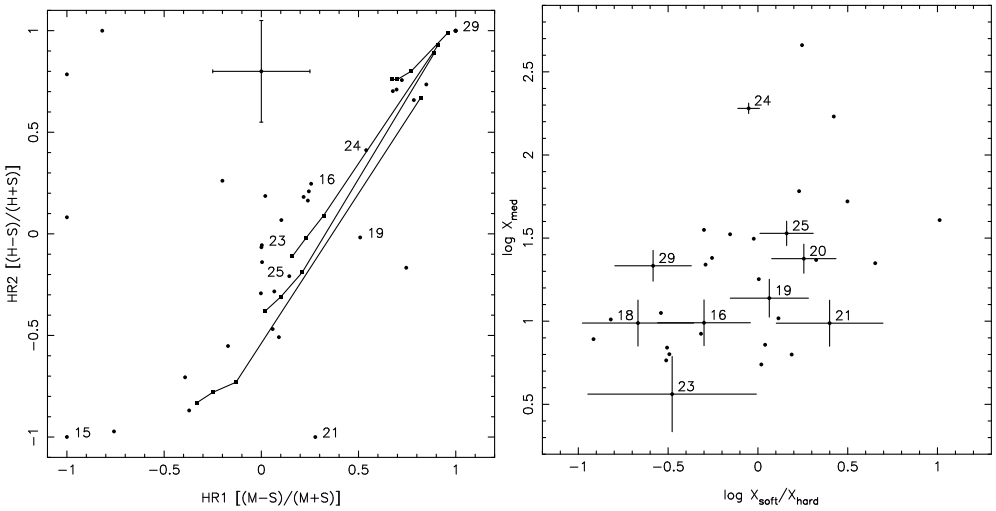

Figure 3.2: *Left: X-ray color-color diagram of Chandra sources in NGC 288. The numbers correspond to the source number inside the half-mass radius. Also plotted are the hardness ratios estimated from different spectral models. Top to bottom: Blackbody model with kT = 1 keV, thermal bremsstrahlung model with kT = 5 keV, power-law model with α = 2, and 3. For each model, N_H (squares) varies from the left as 1.6×10^{20}, 5×10^{20}, 10^{21}, and 10^{22} cm^{-2}. Right: X-ray color-magnitude diagram of NGC 288. The X-ray color is defined as the logarithm of the ratio of 0.5–1.5 keV (X_{soft}) counts to 1.5–6 keV (X_{hard}) counts, and the magnitude is the logarithm of 0.5–4.5 keV (X_{med}) counts. Sources within the half-mass radius are marked with error bars.*

3.2.3 X-ray colors and spectral fitting

Many of the sources in our catalog have < 100 counts, which makes it difficult to derive spectral parameters with meaningful constraints. However, hardness ratios can give a crude indication of the X-ray spectra in these cases. We therefore computed the hardness ratios for all the detected sources. These ratios were based on the source counts in three energy bands: S (0.3–1.0 keV), M (1–2 keV), and H (2–7 keV). The two hardness ratios are defined as HR1 $= (M - S)/(M + S)$ and HR2 $= (H - S)/(H + S)$. Fig. 3.2 shows the color-color diagram (left) and the color-magnitude diagram (right) of all X-ray sources detected in the ACIS-S3 chip. We have overlaid the color-color diagram with four lines showing the tracks followed by representative spectra with differing values of N_H. Note that the colors in the color-magnitude diagram were chosen to be consistent with previous work (e.g. Pooley et al. 2002b; Heinke et al. 2003; Bassa et al. 2004).

We extracted the energy spectra for the brightest three X-ray sources which have $\gtrsim 200$ counts and fitted them to simple one-component spectral models including absorbed power-law and thermal bremsstrahlung models. In order to employ χ^2 statistics, all spectra were grouped into at least 15 counts per spectral bin. We forced N_H to be $\gtrsim 1.6 \times 10^{20}\,cm^{-2}$, the cluster N_H derived from optical studies. All spectra can be fitted equally well with both

Table 3.2: *Spectral fits of the brightest sources. All quoted uncertainties are 90%. TB is an abbreviation for thermal bremsstrahlung; PL for power-law.*

CX	Model	$N_{\rm H}$ ($\rm cm^{-2}$)	kT/α	χ^2_ν/DOF	$f_{\rm X}$ (0.3–7 kev) ($\rm ergs\,cm^{-2}\,s^{-1}$)
3	TB	$1.6^{+3.4}_{-0.0} \times 10^{20}$	$1.7^{+0.9}_{-0.5}$	1.3/10	22.0×10^{-15}
	PL	$1.6^{+6.4}_{-0.0} \times 10^{20}$	$2.1^{+0.6}_{-0.2}$	1.1/10	28.0×10^{-15}
24	TB	$3.0^{+1.4}_{-1.1} \times 10^{20}$	$7.0^{+21.3}_{-3.4}$	0.9/10	48.0×10^{-15}
	PL	$35^{+1.9}_{-1.1} \times 10^{20}$	$1.7^{+0.4}_{-0.3}$	0.9/10	36.0×10^{-15}
27	TB	$3.9^{+3.1}_{-2.2} \times 10^{20}$	$4.4^{+2.4}_{-1.4}$	1.0/28	82.0×10^{-15}
	PL	$8.4^{+4.0}_{-4.0} \times 10^{20}$	$1.9^{+0.2}_{-0.2}$	0.9/28	96.0×10^{-15}

models. Table 3.2 summarizes the spectral fits. For CX 3, the N_H converged to values much lower than the cluster $N_{\rm H}$ derived from optical studies. For the other two sources, the $N_{\rm H}$ of the thermal bremsstrahlung model is slightly higher than the cluster value, while it is much higher for power-law model. The temperatures of the thermal bremsstrahlung model vary between 1.7 and 7 keV, while the photon index of the power-law model is consistent with 2.

3.3 Optical observations

NGC 288 was observed with *Hubble Space Telescope* Advanced Camera for Surveys (ACS) on 2004 September 20 (Proposal ID: 10120). The observations consist of deep F435W (B_{435}), F625W (r_{625}), and F658N (Hα_{658}) images covering the core of the cluster. The exposure time with the F435W, F625W, and F658N filters is 740 s, 320 s, and 1760 s, respectively. The ACS field-of-view covers the entire core radius of the cluster and about 73% of the half-mass radius (see Fig. 3.1). Three X-ray sources (CX 16, 18 and 20) coincide with an archival *Hubble Space Telescope* Wide Field and Planetary Camera 2 (WFPC2) observation of NGC 288. For this observations, the F255W (nUV$_{255}$), F336W (U_{336}), F555W (V_{555}) and F814 (I_{814}) filters were used. Exposure times were 700 s in F255W, 3760 s in F336W, 430 s in F555W and 585 s in F814W.

3.3.1 Data reduction and photometry

Images of each bandpass were shifted and co-added using the MultiDrizzle package in PyRAF, with masking of cosmic rays, saturated pixels, and bad pixels. We used the combined images for correcting astrometry and identifying optical counterparts of X-ray sources in the cluster. However, we used individual images to perform PSF photometry with the DOLPHOT package that is adapted from HSTphot (Dolphin 2000b) for the use of ACS data[2]. DOLPHOT is a stand-alone package to perform PSF photometry with a module for ACS data. We did not use the combined images for photometry because drizzled images require re-sampling producing suboptimal photometry. DOLPHOT can be run on multiple images of the same field and outputs the combined photometry for each filter. We first applied *acsmask* to mask

[2]http://purcell.as.arizona.edu/~andy/dolphot/

bad pixels according to the data quality image provided by STScI. We then used *calcsky* to create sky images for background determination. Finally, we performed PSF photometry using DOLPHOT with look-up tables for the ACS PSF and produced a master list of positions and magnitudes for each star found. The final magnitudes were corrected for aperture and charge transfer efficiency effects. Additional selection criteria were applied to eliminate cosmic rays, artifacts, and "stars" lying on the diffraction spikes of the very brightest stars. The final photometry data were used to construct the color-magnitude diagrams (CMDs) shown in Fig. 3.3. Stars are shown if they appear in all three filters.

The archival *Hubble Space Telescope*/WFPC2 observation was photometered using HSTphot 1.1.5b (Dolphin 2000b, see Bassa et al. 2004 for a more detailed description).

3.3.2 Astrometry

To identify optical counterparts to the *Chandra* X-ray sources in the field, we have to improve the astrometry of both datasets. We retrieved a 5 m V-band image of NGC 288 with the Wide Field Imager (WFI) at the ESO 2.2 meter telescope on La Silla, taken on 2004 June 14 and used that to calibrate the *Hubble Space Telescope*/ACS images. The WFI has an array of 8 CCDs, each CCD having a $8' \times 16'$ field of view, giving a total of $33' \times 34'$. An $8' \times 8'$ subsection of the WFI chip covering the cluster center was used that contained 93 UCAC2 standards (Zacharias et al. 2004). Of these, 72 were not saturated and appeared stellar and unblended. Fitting for a 6 parameter transformation, we obtained a solution giving residuals of $0\farcs056$ in R.A. and $0\farcs059$ in Decl.

The astrometry of the WFI image was then transferred to the two ACS/WFC chips (WFC1 and WFC2). We used DOLPHOT to generate positions and photometry for all stars on the ACS/WFC chips. These positions were corrected for the considerable geometric distortion using polynomials (Hack & Cox 2001)[3]. A selection of the stars on each chip (having $r_{625} < 18.0$) were matched against stars on the WFI image, where we used the distortion corrected positions of ACS/WFC for comparison with the calibrated position on the WFI. For WFC1, 174 stars were selected and outliers were removed through an iterative process. The astrometric solution converged using 147 stars, yielding residuals of $0\farcs016$ in R.A. and $0\farcs018$ in Decl. For WFC2, we started off with 206 stars, while the final solution has 155 stars with residuals of $0\farcs014$ in R.A. and $0\farcs016$ in Decl.

For the astrometric calibration of the archival *Hubble Space Telescope*/WFPC2 images, we first corrected all pixel positions of the stars for distortion and placed them on a common frame using the distortion corrections and relative chip positions and offsets by (Anderson & King 2003). The resulting positions were matched to those of stars on the WFI image, where the final astrometric solution used 207 stars giving residuals of $0\farcs022$ in RA and $0\farcs024$ in Decl.

For the *Chandra* image, we first used the Aspect Calculator[4] provided by the *Chandra* X-ray Center to correct the aspect offset. This will provide an absolute astrometry of $0\farcs6$ (90%). The shifts were small: $0\farcs07$ in right ascension and $0\farcs03$ in declination. Inspection of the 99%

[3] http://www.stsci.edu/hst/acs/documents/isrs/isr0108.pdf
[4] http://cxc.harvard.edu/ciao/threads/arcsec_correction/

Table 3.3: *Optical counterparts to Chandra X-ray sources. The last column gives a tentative classification; for the sources with two possible optical counterparts, this classification holds only for the actual counterpart. Ratio of X-ray to optical (r_{625}) flux, using* $\log(f_X/f_r) = \log f_X + 5.67 + 0.4 r_{625}$ *(Green et al. 2004); f_X is derived in the 0.3–7 keV band. The abbreviation CV stands for cataclysmic variable; AB for chromospherically active binary and AGN for active galactic nuclei.*

CX	$\Delta\alpha$	$\Delta\delta$	B_{435}	r_{625}	Hα_{658}	f_X/f_r	Classification
13a	+0.″09	−0.″31	24.96(4)	22.90(2)	22.58(5)	0.8	AB?
13b	+0.″42	−0.″08	26.04(9)	22.86(2)	22.34(4)	0.76	CV? AGN?
15	−0.″27	+0.″19	26.81(17)	25.78(19)	25.15(74)	11.6	AGN
18	−0.″10	−0.″26	22.73(1)	21.52(1)	21.16(2)	0.3	AB
19a	+0.″31	+0.″01	25.24(5)	25.33(11)	23.86(12)	13.7	AGN
19b	−0.″55	−0.″21	20.54(4)	19.73(4)	19.50(13)	0.08	AB
20a	−0.″10	+0.″09	27.51(29)	26.37(27)	24.78(42)	60.1	AGN
20b	+0.″16	−0.″03	25.42(6)	24.19(5)	23.74(12)	8.6	CV
24	−0.″17	+0.″01	24.88(4)	23.58(4)	23.47(10)	39.7	CV
25	+0.″30	−0.″05	26.92(19)	25.70(23)	24.05(19)	48.1	AGN

confidence error circles of the *Chandra* X-ray sources (using the positions from Table 3.1) on the WFI image yields several likely counterparts. X-ray sources CX 3, CX 12, CX 28, CX 30 appear to coincide with stellar objects, whereas CX 7, CX 8, CX 17, CX 22, CX 26, CX 32, CX 36 appear to coincide with extended objects, possibly background galaxies. Based on brightness, positional accuracy, and conformity of the image to the point spread function CX 28 and CX 30 are the most promising stellar counterparts. In addition, CX 28 and CX 30 are outside the half-mass radius, hence the stellar density from the cluster is relatively low implying a low probability of chance coincidences. Based on these two optical counterparts, the boresight correction that needs to be applied to the X-ray source positions is $0.''137 \pm 0.''104$ in R.A. and $-0.''055 \pm 0.''096$ in Decl.

3.4 Source identification and classification

To obtain optical identifications for the X-ray sources, we use the precise astrometry described in the previous sections. We searched for optical counterparts within the 95% *Chandra* error circle which is the quadratic sum of the positional uncertainty for the X-ray source, the uncertainty in the optical astrometry (UCAC2 to WFI astrometry and WFI to *Hubble Space Telescope*/ACS astrometry), and the uncertainty in the X-ray boresight correction. Within the ACS field-of-view, there are nine *Chandra* sources and we suggest optical counterparts based on positional coincidence alone to seven of them. In case of multiple sources inside the error circle, we included all the candidates within the 95% X-ray error circle. The results of each candidate optical counterpart are summarized in Table 3.3, and finding charts are shown in Fig. 3.4. Using the photometric data from the *Hubble Space Telescope* ACS, we constructed CMDs, shown in Fig. 3.3.

To help in assessing the nature of the optically identified sources, we show in Fig. 3.5 the X-ray luminosity as a function of the absolute magnitude, for low-luminosity X-ray sources in globular clusters. The large symbols in this figure indicate the X-ray sources with possible

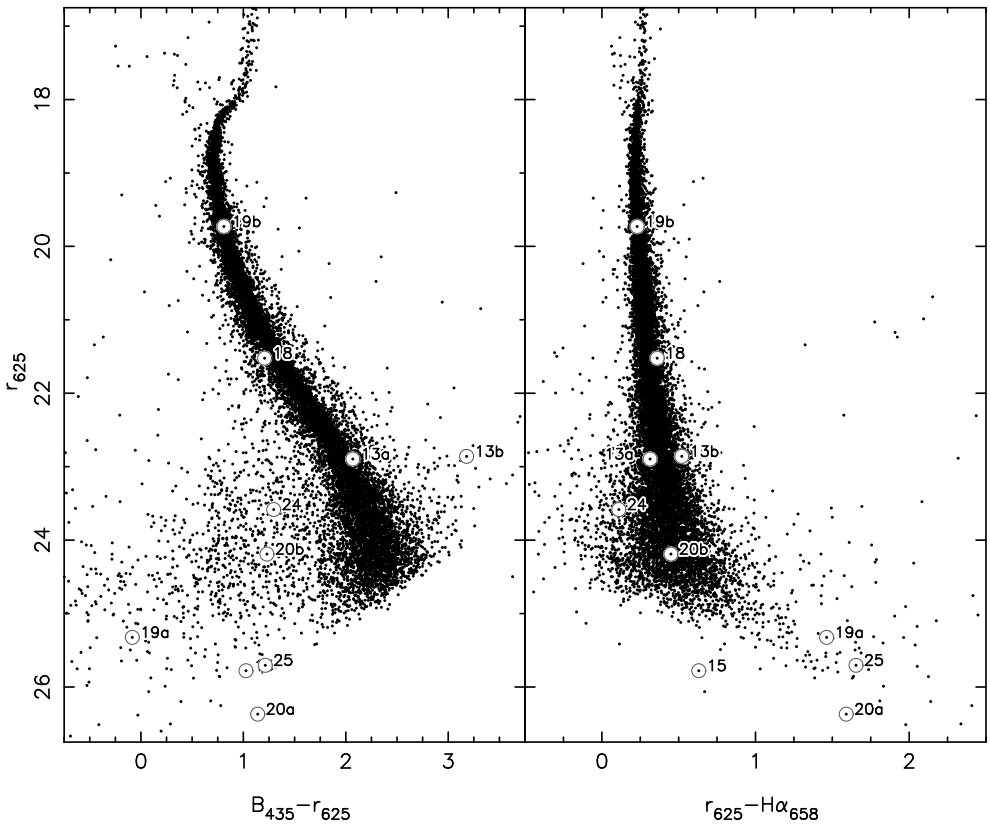

Figure 3.3: *Color-magnitude diagrams of the Hubble Space Telescope ACS observations of NGC 288. The numbers refer to the candidate optical counterparts to the X-ray sources.*

optical counterparts, in the field of view of our *Chandra* observation of NGC 288, the smaller symbols show objects found in other clusters, mostly 47 Tuc and M4 (see Bassa et al. 2004). We note that the absolute magnitudes and X-ray luminosities for the sources in our NGC 288 observations are computed under the assumption, which we will test below, that they are associated with NGC 288. As discussed earlier, we caution that the *Chandra* deep field data imply that for the 11 X-ray sources within the half-mass radius, there is a 30% probability that *all* of them are background sources.

We first consider the X-ray sources with only one suggested counterpart in the error circle. The ratio of the X-ray to optical flux locates CX 18 in the region of active binaries in Fig. 3.5, albeit close to the boundary with CVs. The star in the error circle of CX 18 is located on the main-sequence in the CMD of Fig. 3.3. Because it does not show noticeable Hα emission, is on the main sequence in $U_{336} - V_{555}$, and is not detected in the near ultraviolet, it is unlikely to be a CV, and we suggest that CX 18 is a chromosphically active binary.

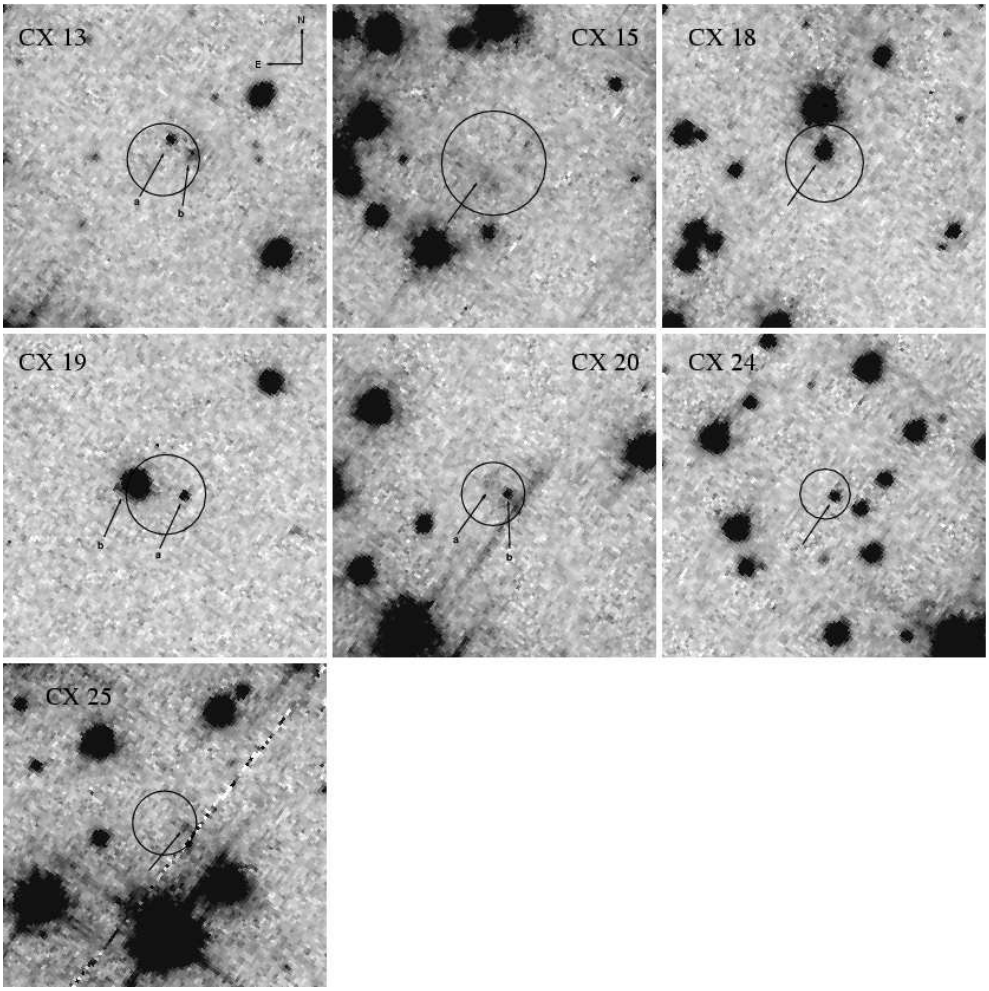

Figure 3.4: $5'' \times 5''$ *finding charts for the candidate optical counterparts, obtained from Hubble Space Telescope ACS observations. These images were taken in* B_{435}*. We have overlaid the 95% error circles for the Chandra source positions and the candidate stars themselves are indicated by arrows. All images have the same grey scale.*

The candidate cluster counterpart to CX 24 is blue with respect to the main sequence, and has no Hα emission, being located rather on the main sequence in the Hα diagram (Fig. 3.3). It has a high X-ray to optical flux ratio and a hard spectrum with 0.3–7 keV luminosity of $\sim 4 \times 10^{32}$ ergs s^{-1}. It is worth noting that CX 24 is the only X-ray source in the half-mass radius detected with *ROSAT* (Sarazin et al. 1999). Using the *Chandra* spectral fit, the X-ray luminosity during the *ROSAT* observations is about 10^{33} ergs s^{-1}, a factor of 2.5 higher than

our *Chandra* observation. We suggest that CX 24 is a CV, even though its Hα emission does not appear to be strong.

The sources CX 15 and CX 25 are optically extended, and thus almost certainly background galaxies. Indeed, if we compute their X-ray luminosity and optical magnitude under the wrong assumption that they are in NGC 288, we find that they are located in the $L_x - M_V$ diagram in an area where no genuine cluster sources have been found. A probable background quasar in the *Chandra* field of view of our M4 observation is in the same location of Fig. 3.5 (for the wrong assumption that it belongs to the cluster M4; Bassa et al. 2004, 2005; Bedin et al. 2003).

Turning now to the sources with more than one possible counterpart in the error circle, we first note that our suggested classifications depend on the optical object indeed being the counterpart. One star in the error circle of CX 13, CX 13a, is on the main sequence both in the CMD and in the Hα-r diagram. Like CX 18, it may be an active binary. The other star, CX 13b is redder than the main sequence. Its X-ray to optical flux ratio is somewhat high for an active binary. Possibly it is an (obscured?) active galaxy. Alternatively, its red color could be an artifact of variation of its blue magnitude, in which case it may be a CV. (Note that we have no evidence for such variation.) In the absence of more information, a secure classification of CX 13 thus is not possible.

Of the two objects in the error circle of CX 19, the brighter one (CX 19b) would a priori be the more probable counterpart, since the probability of a chance coincidence is higher for the more numerous faint objects. Its colors (Fig. 3.3) and X-ray to optical flux ratio (Fig. 3.4) then suggests that CX 19b is a chromospherically active binary. If the fainter object CX 19a is the counterpart, its X-ray to optical flux ratio (Fig. 3.4) suggests that it is a background galaxy/AGN.

The brighter object in the error circle of CX 20, CX 20b is blue, and has a relatively high X-ray to optical flux ratio (Fig. 3.5): it may be a CV. CX 20b was also imaged by WFPC2 with the V_{555} and I_{814} filters. It has $V_{555} = 24.34$ and is on the main-sequence in $V-I$ (similar to CVs in other clusters, e.g. NGC6397 and 47 Tuc; Cool et al. 1998; Edmonds et al. 2003a). On the other hand, CX 20a is extended, and therefore an galaxy, an active galaxy when it is the counterpart of CX 20. CX 20a is below the detection limit in the archival WFPC2 observations.

There are two unidentified X-ray sources (CX 16 and CX 21) in the ACS field-of-view. CX 16 is in between two bright stars and the spikes produced by these bright stars prevent us from searching for any faint optical sources inside the *Chandra* error circle. The region of CX 16 was also observed with the WFPC2, but neither do we find a counterpart inside the *Chandra* error circle in these data. CX 21 is near the edge of the field and part of the *Chandra* error circle is in the dithering pattern of the image. Therefore the sensitivity is greatly reduced. Two additional sources (CX 23 and CX 29) are inside the half-mass radius but were not observed with *Hubble Space Telescope*. In any case, if the identifications of CX 18 and CX 24 are correct, then these two remaining sources are very likely part of the extra-galactic background.

In summary, we find one good candidate CV (CX 24) and the source is already detected with ROSAT (Sarazin et al. 1999), and one good candidate active binary (CX 18). The X-ray

Table 3.4: *Scaling parameters of M4, NGC 6397, 47 Tuc and NGC 288. Values for central density (ρ_0), core-radius (r_c), distance (d) and absolute visual magnitude (M_V) originate from Harris (1996) (version of February 2003). For M4, the values of ρ_0 and M_V are computed for the distance and reddening of citetrfi+97. The collision number is computed from $\Gamma \propto \rho_0^{1.5}\, r_c^2$ and the half-mass from $M_h \propto 10^{-0.4 M_V}$. Values for Γ and M_h are normalized to the value of M4.*

Cluster	$\log \rho_0$ ($L_\odot\,pc^{-3}$)	r_c ($''$)	d (kpc)	M_V	Γ	M_h
M4	4.01	49.8	1.73	−6.9	1.0	1.0
NGC 6397	5.68	3.0	2.3	−6.6	2.1	0.76
47 Tuc	4.81	24.0	4.5	−9.4	24.9	10
NGC 288	1.80	85.0	8.4	−6.7	0.03	0.83

to optical luminosity ratio of CX 24 is in the upper range of the values observed for CVs in globular clusters so far, and the X-ray to optical luminosity ratio of CX 18 is amongst the highest observed so far for active binaries in globular clusters. In addition to these, we have possible cluster members and according classifications in the error circles of CX 13 (active binary or CV), CX 19 (active binary) and CX 20 (CV).

Lastly, we consider all the remaining *Chandra* sources outside the half-mass radius; we do not possess useful optical data for any of these. Statistically we do not expect any of the sources outside the half-mass radius to be associated with NGC 288 (see Sect. 3.2.2). From the *Chandra* deep field data, for the entire ACIS-S3 chip field of view, we expected that 0–10 sources are associated with NGC 288. If CX 18 and CX 24 (or indeed additionally CX 13, CX 19 and CX 20) are CVs or chromospherically active binaries (hence cluster members), then there are at most eight (five) additional X-ray sources associated with NGC 288. In the absence of information of the optical colors of the counterparts, it is not possible to pursue this question further for individual cases. Nevertheless, we here describe the X-ray properties, *assuming cluster membership*. The X-ray fluxes of all *Chandra* sources are listed in Table 3.1 and 3.2, and the luminosities (assuming 8.4 kpc) range from 7×10^{30} to 8×10^{32} ergs s^{-1}. CX 3 is one of the three brightest X-ray sources. It has a relatively soft spectrum (see Table 3.2) and is therefore inconsistent with a CV. It could be either a qLMXB or, of course, yet another background galaxy. In contrast, the brightest source, CX 27, has a hard spectrum, favoring a CV identification; it is also noteworthy as an X-ray variable; the *Chandra* spectrum indicates that it has a 0.3–7 keV flux of $8 - 9 \times 10^{-14}$ ergs cm^{-2} s^{-1}, but the source was not detected with *ROSAT* with a detection limit of 6×10^{-14} ergs cm^{-2} s^{-1}. Excluding the brightest three sources (CX 3, CX 24 and CX 27), the remainder have luminosities $< 10^{32}$ ergs s^{-1} with an average of 3×10^{31} ergs s^{-1}. This luminosity is at the lower end of quiescent neutron stars in the field. Moreover, the X-ray colors are harder than for neutron star systems. Hence, the remaining lower-luminosity X-ray sources outside the half-mass radius are very unlikely to be quiescent neutron stars. Of these, the X-ray luminosities of CX 6, and CX 17 are too high for any chromospherically active binary, and their relatively hard X-ray colors would indicate that they are probably CVs, or absorbed AGN.

3.5 Discussion

The luminosities of both good candidate members, CX24 and CX18, as well as those of the three less secure members CX13, CX19 and CX20, are above the lower limit of 4×10^{30} ergs s^{-1} in the 0.5–6.0 keV range used in the study by Pooley et al. (2003) into the relation between the stellar encounter rate and the incidence of X-ray sources in globular clusters. To see whether NGC 288 fits this relation we compare its collision number $\Gamma \equiv {\rho_0}^{1.5} {r_c}^2$ (Verbunt 2003) with those of some other clusters, using the parameters listed in Table 3.4. Here ρ_0 is the central density of the cluster, and r_c the core radius. The encounter number for NGC 288 is a about 650 times smaller than that of 47 Tuc, and 30 times smaller than that of M4. Pooley et al. (2003) reports 41 ± 2 sources above the lower luminosity limit in 47 Tuc (see also Grindlay et al. 2001a; the uncertainty is due to the estimated number of background sources), and thus, if the number of sources scales with the encounter rate, the presence of two to five sources in NGC 288 is a very significant overabundance, even if we take into account small number errors due to Poissonian fluctuations. The same conclusion is reached on the basis of comparison with M4. This indicates that the sources in NGC 288 are not formed via stellar encounters.

Indeed, for magnetically active binaries, an origin from a primordial binary is much more likely (Verbunt 2002). A scaling with the total mass of the cluster is expected in this case, provided that no large numbers of binaries have been destroyed by close encounters. In a low-density cluster like NGC 288, no such large scale destruction has taken place. Since our information on low-luminosity X-ray sources in most clusters is limited to the region within the half-mass radius, we compare also the masses within this radius. By definition, however, these masses are half of the total mass, and thus the scaling between clusters is the same as for the total mass. If the visual mass-to-light ratio is the same for all clusters listed in Table 3.4, the half masses scale with $10^{-0.4 M_V}$. Thus the half-mass radii of NGC 6397 and NGC 288 contain about 20% less mass than the half-mass radius of M4, which in turn contains a factor 10 less mass than the half-mass radius of 47 Tuc. Scaled by mass, the predicted number of active binaries $L_X > 4 \times 10^{30}$ erg s^{-1} 0.5–6 keV) in NGC 288 should be similar to those in NGC 6397 and M4, and about one tenth of those in 47 Tuc. This is indeed observed.

We consider this strong evidence that magnetically active binaries in globular clusters evolve from primordial binaries, much strengthening the conclusion based by Bassa et al. (2004) on the source numbers in M4.

As argued by Verbunt (2002), CVs take a position in between low-mass X-ray binaries with a neutron star or black hole, which are certainly formed from close encounters, and the magnetically active binaries, formed from primordial binaries. The scaling of source number with encounter number found for the sources with $L_X > 4 \times 10^{30}$ ergs s^{-1} (0.5–6 keV) by Pooley et al. (2003, see also Heinke et al. 2003) suggests that CVs are mostly made via stellar encounters as well. This is in agreement with the result by Davies (1997) that the formation of CVs via evolution from – relatively wide – primordial binaries is suppressed by the destruction of such binaries in dense cores of globular clusters. We do not expect even a single CV in NGC 288 if we scale with encounter numbers from any of the other clusters listed in Table 3.4. However, neither the observed scaling law nor the theoretical

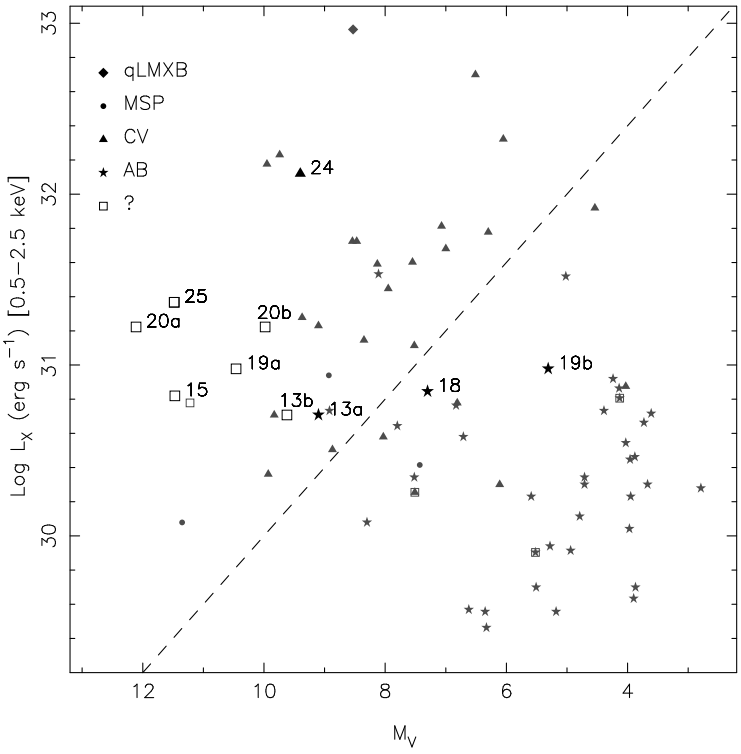

Figure 3.5: *X-ray luminosity as a function of the absolute magnitude, for low-luminosity X-ray sources in globular clusters. The large symbols in this figure indicate the optically identified X-ray sources in the field of view of our Chandra observation of NGC 288,* where we compute absolute magnitude and X-ray luminosity under the assumption that the sources are cluster members. *This assumption is probably correct for the candidate CV (large triangle) and the three candidate active binaries (large stars); the sources indicated with a large square are probably extragalactic sources. The smaller symbols in this figure indicate objects found in other clusters, mostly 47 Tuc and M4 (see fig. 2.6). Since we do not have observations of NGC 288 in the V-band, we estimate V from* $V = 0.5(B_{435} + r_{625})$. *The dashed line of constant X-ray to optical flux ratio roughly separates CVs from active binaries.*

computations extends to clusters with core densities or encounter rates as low as that of NGC 288. According to the computations by Davies (1997) a cluster core with a star density of 1000 pc^{-3} allows most of the CV progenitors to evolve into a CV. It is therefore probable that the CV, CX 24, in cluster with an even lower central number density, evolved from a primordial binary. As an even more extreme case than NGC 288, recent *Chandra* observation of the old open cluster M67 reveals a large number of BY Dra and RS CVn systems as well as interacting binary candidates (van den Berg et al. 2004). It is interesting to note that the total X-ray luminosity of M67 is dominated by binaries with giants, whereas no such binaries have been securely identified as optical counterpart to an X-ray source in any globular cluster

so far. Investigations of other globular clusters with low density cores must be done to verify these conclusions.

Chapter 4

Optical identification of the companion to PSR J1911−5958A, the pulsar binary in the outskirts of NGC 6752

C. G. Bassa, F. Verbunt, M. H. van Kerkwijk, L. Homer

Astronomy & Astrophysics 2003, 409, L31–L34

Abstract We report on the identification of the optical counterpart of the binary millisecond pulsar PSR J1911−5958A, located in the outskirts of the globular cluster NGC 6752. At the position of the pulsar we find an object with $V = 22.08$, $B - V = 0.38$, $U - B = -0.49$. The object is blue with respect to the cluster main sequence by 0.8 magnitudes in $B - V$. We argue that the object is the white dwarf companion of the pulsar. Comparison with white dwarf cooling models shows that this magnitude and colors are consistent with a low-mass white dwarf at the distance of NGC 6752. If associated with NGC 6752, the white dwarf is relatively young, $\lesssim 2$ Gyr, which sets constraints on the formation of the binary and its ejection from the core of the globular cluster.

4.1 Introduction

Recently, 5 millisecond pulsars have been discovered (D'Amico et al. 2002) towards the nearby galactic globular cluster NGC 6752. Three of them are located inside the 6.″7 core radius (Lugger et al. 1995) while the other two are outside the 1.′92 half-mass radius (Djorgovski 1993), at 2.′7 and 6.′4, respectively. The latter of these is a binary millisecond pulsar, PSR J1911−5958A (hereafter PSR A), and has a low-mass ($\gtrsim 0.19\,M_\odot$, assuming a $1.4\,M_\odot$ neutron star) companion in a 20 hour, highly circular ($e < 10^{-5}$) orbit (D'Amico et al. 2002). The pulsar period and period derivative suggest that it is a "canonical" recycled millisecond pulsar (see Phinney & Kulkarni 1994 for a review), and hence that the companion is likely a white dwarf.

The large separation of PSR A from the cluster center is puzzling. Colpi et al. (2002) have recently investigated possible scenarios, and found that both for the case of a primordial binary and for an exchange or scattering event with other cluster stars, it is very difficult to explain both the pulsar's current position and its close circular binary orbit. Instead, they suggest that the binary may have been scattered to its current position by a binary composed of two 3–100 $M_\odot$ black holes.

One might learn more about the system's origin (and verify cluster membership) if one can confirm that the companion is a white dwarf and measure its mass and age. Therefore, we searched for the optical counterpart in archival data. We report here on the results.

4.2 Observations and analysis

We searched the ESO and *Hubble Space Telescope* archives for images coincident with the pulsar position ($\alpha_{2000} = 19^{\rm h}11^{\rm m}42\overset{\rm s}{.}7562$, $\delta_{2000} = -59°58'26\overset{''}{.}900$; D'Amico et al. 2002). We found two images, taken with the Wide Field Imager (WFI) at the ESO 2.2 m telescope on La Silla. These observations, 4 minute B and V-band exposures, were taken during the night of May 13/14, 1999. The seeing was poor, $\sim 1\overset{''}{.}5$ in V. However, both images showed a faint object at the pulsar position (see below). This object was also present in two *HST* observations with the Wide Field Planetary Camera 2 (WFPC2; Holtzman et al. 1995b). Both observations, `U5FI07` and `U5FI03` (GO-8256), were imaged in the same filters and had similar exposure times, 42 s in F555W (hereafter V_{555}), 220 s in F439W (B_{439}), 660 s in F336W (U_{336}) and 1 800 s and 1 693.5 s in F255W (nUV_{255}) for the first and second field, respectively. The position of the pulsar coincides with the WF3 chip for the `U5FI07` dataset, while it is on the WF4 chip on the other dataset.

4.2.1 Astrometry

The WFI detector has an array of 8 CCDs (2 rows of 4), each CCD having a field of view of $8' \times 16'$, a total of $33' \times 34'$. The position of the pulsar was coincident with chip 6 of the V-band image. We found that there was some distortion over the whole chip. To minimize its effect we only used the upper half of this chip for the astrometric calibration. Stars on this $8' \times 8'$ sub-image were compared against entries in the USNO CCD Astrograph Catalog

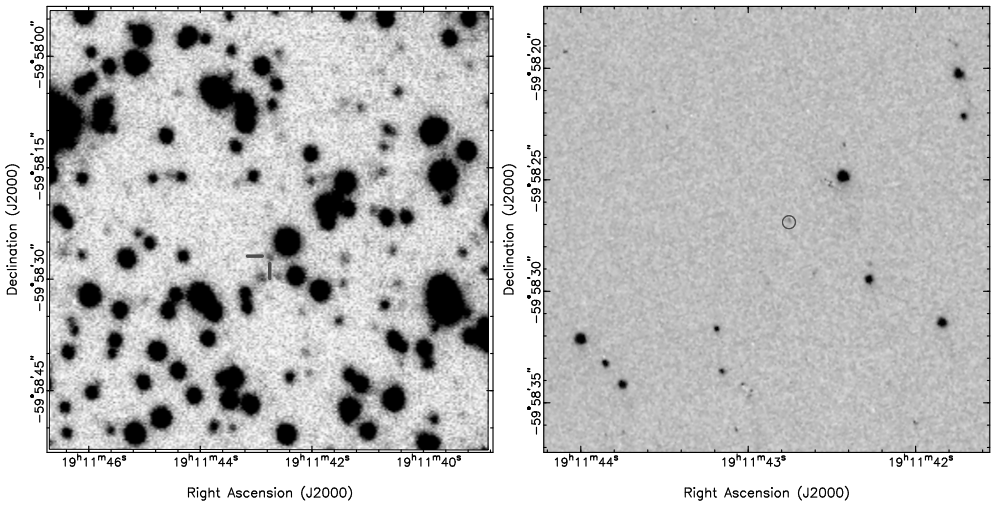

Figure 4.1: *Finding charts for PSR A. The upper image is a* $1' \times 1'$ *subsection of a V-band image obtained on May 14,1999 with the Wide Field Imager on the ESO 2.2 m telescope at La Silla. The* $2''$ *tick marks indicate the position of PSR A. The lower image is a* $20'' \times 20''$ *sub-image of the* HST/*WFPC2* V_{555} *(F555W) observation. The* $0.''235$ *(95% confidence) error circle is shown at the position of the pulsar.*

(UCAC; Zacharias et al. 2000). In total 68 UCAC stars coincided with this image and their centroids were measured. Of these 43 were not saturated and appeared stellar and unblended. One outlier, having a total residual of $0.''32$ was rejected. The remaining stars were used to calculate an astrometric solution, fitting for zero-point position, scale and position angle. This solution has root-mean-square (*rms*) residuals of $0.''06$ in both right ascension and declination. The statistical uncertainty in the astrometry is thus $0.''084$ in each coordinate.

We used the astrometrically calibrated WFI image to obtain astrometric solutions for the two *HST*/WFPC2 datasets. First, the WFPC2 pixel positions were corrected for geometric distortion and placed on a master-frame, using the prescription of Anderson & King (2003). We matched stars on the WFI image and fitted for zero-point position, scale and position angle against the WFPC2 master frame positions. Outliers having residuals larger than three times the *rms* residual of the fit are removed and a new solution is computed. This process is iterated until convergence. On average the converged astrometric solution used some 200–300 stars with *rms* residuals of the order of $0.''03$ in both right ascension and declination. The final uncertainty in the tie to the UCAC system is dominated by the step from the UCAC to the WFI sub-image, and is $\sim 0.''10$ in each coordinate.

4.2.2 Photometry

We started with the pipe-line calibrated *HST*/WFPC2 images, and used the HSTphot 1.1 (Dolphin 2000b) package for further reduction and photometry of the images. We followed

Table 4.1: *Positional and photometric data for the two archival* HST/*WFPC2 observations of PSR J1911−5958A.*

Dataset	Date (UT)		R.A. (J2000)	Decl. (J2000)
U5FI07	March 2, 2000 @ 10:29		$19^{\rm h}11^{\rm m}42\overset{\rm s}{.}756$	$-59°58'26\overset{''}{.}87$
U5FI03	March 3, 2000 @ 13:54		$19^{\rm h}11^{\rm m}42\overset{\rm s}{.}757$	$-59°58'26\overset{''}{.}83$
Dataset	$\rm nUV_{255}$	U_{336}	B_{439}	V_{555}
U5FI07	20.74 ± 0.23	21.49 ± 0.15	22.40 ± 0.21	22.10 ± 0.17
U5FI03	21.44 ± 0.24	21.78 ± 0.14	22.49 ± 0.17	22.09 ± 0.14

the recommended procedures to mask bad pixels, defects, cosmic ray hits and hot pixels. Next we used the main task *hstphot* to find stars, measure positions, and determine calibrated photometry. The latter uses the aperture corrections, charge-transfer efficiency corrections and zero-points of Dolphin (2000a).

4.2.3 The counterpart to PSR J1911−5958A

The UCAC catalog is on the ICRS at the 20 mas level (Assafin et al. 2003). Including this uncertainty in the uncertainty of the astrometric tie, we obtain 95% confidence radii for the WFI and *HST*/WFPC2 frames of $0\overset{''}{.}211$ and $0\overset{''}{.}235$, respectively. Within these radii there is a single object, see Fig. 4.1. The *HST*/WFPC2 positions and magnitudes are tabulated in Table 4.1.

The photometric measurements of the object in the two datasets are consistent for all filters except $\rm nUV_{255}$. The object is 0.7 magnitudes brighter in the first dataset than in the second. However, we compared the magnitudes of 240 stars that overlapped between the two datasets and found that, on average, stars in the first dataset were brighter by 0.34 magnitudes in $\rm nUV_{255}$, which removes the observed discrepancy. We have not, however, found an explanation for this large offset between the two datasets.

The magnitudes in the *HST* flight system filters (U_{336}, B_{439} and V_{555}) were transformed to the Johnson-Cousins *UBV* (Vega) system using the transformations by Holtzman et al. (1995a). The resulting average magnitudes for the object in this system are $U = 21.96 \pm 0.10$, $B = 22.46 \pm 0.14$ and $V = 22.08 \pm 0.11$. The object is blue by about 0.8 magnitudes with respect to the cluster main sequence in $B - V$ at the same B-band magnitude, Fig. 4.2. This is also confirmed by an instrumental color-magnitude diagram constructed from the WFI B and V-band images.

Given the density of objects on the *HST*/WFPC2 chips, there is a $\sim 1\%$ probability of a chance coincidence in the 95% confidence *HST* error circle. However, there are only a few stars that are blue with respect to the cluster main sequence, which greatly reduces the probability of a chance coincidence. The blue color, together with the positional coincidence, gives us confidence that we have detected the companion of PSR A.

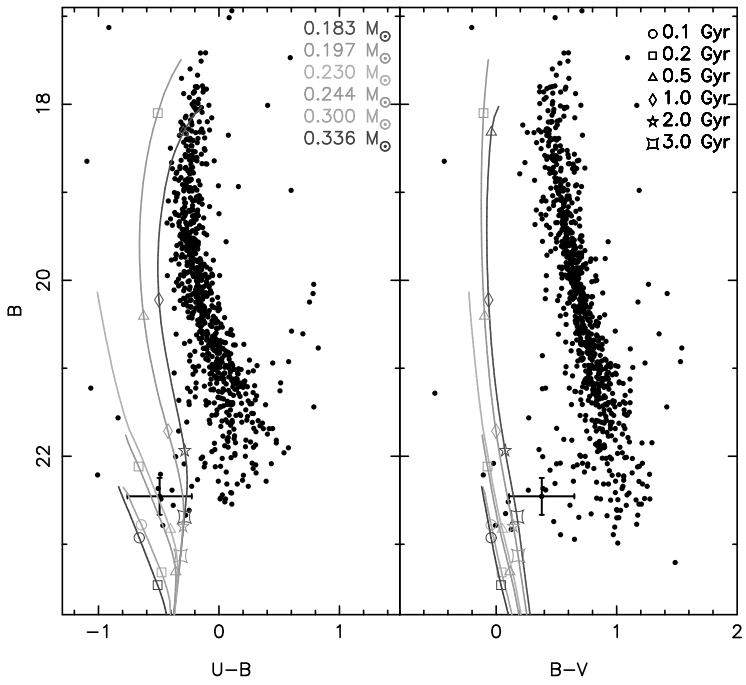

Figure 4.2: *Color-magnitude diagrams of the two* HST*/WFPC2 fields. The magnitudes are transformed from the* HST*/WFPC2 flight system to Johnson-Cousins UBV using the prescription by (Holtzman et al. 1995a). The average colors and magnitudes of the counterpart to PSR A are indicated with error bars. The errors include the uncertainty in the distance modulus and reddening. Also shown are Helium–core white dwarf cooling tracks (solid lines) by (Serenelli et al. 2002). The models have masses of 0.183, 0.197, 0.230, 0.244, 0.300 and 0.336 $M_\odot$, decreasing in mass to the red, for a metallicity of $Z = 0.001$. The age of the white dwarfs along the cooling track is indicated.*

4.3 Ramifications

The minimum mass for the companion is constrained by the pulsar mass function. For a pulsar mass of 1.35 $M_\odot$ (Thorsett & Chakrabarty 1999) this minimum mass is 0.185 $M_\odot$. The lower limit increases for heavier pulsars, roughly by 0.004 $M_\odot$ for every 0.05 $M_\odot$ step in the pulsar mass. Assuming a random probability distribution for the inclination of the binary, we find that there is 90% probability that the companion mass is less than 0.5 $M_\odot$. Given this range of masses and the fact that PSR A is a recycled millisecond pulsar, it is likely that the companion is a Helium-core white dwarf.

To verify whether our observations are compatible with a Helium-core white dwarf at the distance of the cluster, we compare our magnitudes with the predictions from the white dwarf cooling tracks of Serenelli et al. (2002). We use their tracks for $Z = 0.001$, as this metallicity provides the best match to the metallicity of NGC 6752 ([Fe/H] $= -1.43 \pm 0.04$; Gratton et al.

Table 4.2: *Fitting results for Helium–core white dwarf models with a metallicity of $Z = 0.001$. The observed absolute UBV magnitudes were fitted against the modelled values. The dereddened, observed values $U - B$, $B - V$ and M_V are given in the second row.*

M_{WD} ($M_\odot$)	T_{eff} (K)	τ_c (Gyr)	$(U-B)_0$	$(B-V)_0$	M_V	χ^2_ν
			−0.54	0.34	8.84	
0.183	10 600	2.30	−0.31	0.08	8.92	0.9
0.197	11 700	1.36	−0.37	0.03	8.98	1.1
0.230	14 700	0.37	−0.59	−0.06	9.14	3.4
0.244	15 600	0.27	−0.64	−0.08	9.18	4.2
0.300	19 100	0.07	−0.80	−0.13	9.29	8.1
0.336	20 300	0.05	−0.85	−0.14	9.33	9.5
0.380	21 600	0.05	−0.89	−0.16	9.34	10.6
0.390	22 100	0.04	−0.91	−0.16	9.34	11.1
0.422	23 800	0.03	−0.95	−0.18	9.39	12.9
0.449	24 700	0.06	−0.98	−0.19	9.40	13.7

2003). We also assume a V-band distance modulus $(m - M)_V = 13.24 \pm 0.08$ and reddening $E_{B-V} = 0.040$, as recently determined by Gratton et al. (2003), and use the relative extinction coefficients listed by Schlegel et al. (1998).

Figure 4.2 shows the cooling tracks for Helium-core white dwarfs with $Z = 0.001$ for masses in the range of 0.183 to 0.336 $M_\odot$. It appears that the magnitude and colors of the companion to PSR A are compatible with the two lowest-mass tracks, 0.183 and 0.197 $M_\odot$. Note that the 0.183 $M_\odot$ model is below the minimum mass inferred from the pulsar mass function.

We have fitted the observed absolute UBV magnitudes against the predictions from the $Z = 0.001$ Helium-core white dwarf models. A χ^2 statistic was computed for each entry in the model from the difference between the observed and modelled absolute magnitudes. Table 4.2 shows, for each model with a given mass, the properties of the white dwarf at the χ^2 minimum. Both Fig. 4.2 as Table 4.2 show that the lowest mass models, 0.197 to 0.244 $M_\odot$, are preferred. At these masses the white dwarf is rather hot, with $T_{eff} \approx 11\,000 - 16\,000$ K.

Given these high temperatures, the counterpart is relatively young, $\lesssim 2$ Gyr (see both Fig. 4.2 and Table 4.2). The precise value strongly depends on the mass, since white dwarfs with lower masses have relatively thick hydrogen envelopes, where residual hydrogen shell burning keeps the white dwarf hot. From the values listed in Table 4.2, one sees a jump in the cooling age between the 0.197 and 0.230 $M_\odot$ models. This reflects a dichotomy in the thickness of the hydrogen layer, where, above a certain critical mass, the thickness has been reduced by shell flashes early in the evolution (Althaus et al. 2001). As the shell burning is through the CNO cycle, the critical mass depends on the metallicity: $\sim 0.18\,M_\odot$ for solar metallicity, $\sim 0.22\,M_\odot$ for $Z = 0.001$ and $\sim 0.26\,M_\odot$ for $Z = 0.0002$ (Althaus et al. 2001; Serenelli et al. 2002).

We should note that the dichotomy in cooling age was not found by Driebe et al. (1998), who found the flashes hardly affected the thickness of the hydrogen layer. As a result, more massive white dwarfs cool slower and are older. However, for the mass range of interest here, their results are similar. Their 0.195 $M_\odot$ model has a cooling age of 1.2 Gyr, comparable to

the age of the Serenelli 0.197 $M_\odot$ model. For higher masses the cooling age decreases. The 0.300 $M_\odot$ model by Driebe et al. (1998) has a cooling age of 0.2 Gyr, down to 25 Myr for the heaviest model, with a mass of 0.414 $M_\odot$.

Finally, we note the similarity between the position in the color-magnitude diagram of the companion of PSR A and the companion of PSR J0024−7204W (Edmonds et al. 2002) in 47 Tucanae. On the basis of optical variability with the orbital period (3.2 h) and eclipses of the pulsar radio emission, the companion is argued to be a heated main sequence star. For PSR A, however, we can exclude this possibility: the spin-down luminosity is too low to lead to heating to the observed temperature.

4.4 Discussion and conclusions

We have detected the optical companion to the binary millisecond pulsar PSR J1911−5958A, which is located 6.″4 from the center of NGC 6752. The companion is blue with respect to the cluster main sequence by 0.8 magnitudes in $B-V$ and comparison of its colors and magnitude with white dwarf models shows that it is consistent with a Helium-core white dwarf at the distance of NGC 6752.

Irrespective of the cooling models we use, we find that the white dwarf is at most 2 Gyr old. This age is similar to the $\gtrsim 0.7$ Gyr the binary can be expected to stay in the outskirts if it is currently on a highly eccentric orbit in the cluster (Colpi et al. 2002), which suggests that the white dwarf formed during, or shortly after, an encounter that also ejected the binary from the core, in an exchange interaction involving a binary with another star or binary. In the scenarios in which the binary was formed in the periphery, or scattered by a binary black hole, the coincidence of the two time scales has to be due to chance.

One would expect the characteristic age of the pulsar to be similar to the cooling age of the white dwarf, as the pulsar starts to spin down after the cessation of mass transfer, while the white dwarf starts to cool. This seems not to be the case for PSR A, for the characteristic age of the pulsar is $P/(2\dot{P}) \sim 17$ Gyr (D'Amico et al. 2002). It may be instead that the assumption underlying the characteristic age is wrong, and that the period at which the pulsar started spinning is similar to the current one.

Compared to other white dwarf companions to milliseconds pulsars, the companion to PSR J1911−5958A is bright, $V \simeq 22$, which opens the possibility to determine detailed physical parameters (e.g., van Kerkwijk et al. 1996, Callanan et al. 1998). For instance, one could measure the white dwarf temperature and surface gravity through spectroscopy. By comparison with models, this would lead to a mass and radius of the white dwarf, as well as a much more precise cooling age. The radius would allow one to confirm the association of the binary with NGC 6752. If the association is confirmed, the more accurate distance to NGC 6752 provides additional constraints on the radius and thus the mass of the white dwarf. Combining the white dwarf mass with a radial-velocity orbit of the white dwarf (and thus a mass ratio), would give the mass of the pulsar.

Chapter 5

The masses of PSR J1911−5958A and its white dwarf companion

C. G. Bassa, M. H. van Kerkwijk, D. Koester, F. Verbunt

Astronomy & Astrophysics 2006, 456, 295–304

Abstract We present spectroscopic and photometric observations of the optical counterpart to PSR J1911−5958A, a millisecond pulsar located towards the globular cluster NGC 6752. We measure radial velocities from the spectra and determine the systemic radial velocity of the binary and the radial-velocity amplitude of the white-dwarf orbit. Combined with the pulsar orbit obtained from radio timing, we infer a mass ratio of $M_{\rm PSR}/M_{\rm WD} = 7.36 \pm 0.25$. The spectrum of the counterpart is that of a hydrogen atmosphere, showing Balmer absorption lines up to H12, and we identify the counterpart as a helium-core white dwarf of spectral type DA5. Comparison of the spectra with hydrogen atmosphere models yield a temperature $T_{\rm eff} = 10090 \pm 150\,{\rm K}$ and a surface gravity $\log g = 6.44 \pm 0.20\,{\rm cgs}$. Using mass-radius relations appropriate for low-mass helium-core white dwarfs, we infer the white-dwarf mass $M_{\rm WD} = 0.18 \pm 0.02\,{\rm M}_\odot$ and radius $R_{\rm WD} = 0.043 \pm 0.009\,{\rm R}_\odot$. Combined with the mass ratio, this constrains the pulsar mass to $M_{\rm PSR} = 1.40^{+0.16}_{-0.10}\,{\rm M}_\odot$. If we instead use the white-dwarf spectrum and the distance of NGC 6752 to determine the white-dwarf radius, we find $R_{\rm WD} = 0.058 \pm 0.004\,{\rm R}_\odot$. For the observed temperature, the mass-radius relations predict a white-dwarf mass of $M_{\rm WD} = 0.175 \pm 0.010\,{\rm M}_\odot$, constraining the pulsar mass to $M_{\rm PSR} = 1.34 \pm 0.08\,{\rm M}_\odot$. We find that the white-dwarf radius determined from the spectrum and the systemic radial velocity of the binary are only marginally consistent with the values that are expected if PSR J1911−5958A is associated with NGC 6752. We discuss possible causes to explain this inconsistency, but conclude that our observations do not conclusively confirm nor disprove the association of the pulsar binary with the globular cluster.

5.1 Introduction

The equation-of-state of matter at supra-nuclear densities together with general relativity imply a maximum mass for a rotating neutron star (e.g. Lattimer & Prakash 2004). Conversely, a measurement of a high neutron-star mass constrains the equation-of-state of this matter at these densities. Thorsett & Chakrabarty (1999) found that neutron stars in radio pulsars cover only a rather narrow range in mass; $1.35 \pm 0.04\,M_\odot$. However, their sample is statistically dominated by mildly recycled pulsars in relativistic double neutron-star binaries. Considerably higher masses (up to $\sim 2\,M_\odot$) are expected for millisecond pulsars with low-mass white-dwarf companions, since binary evolution predicts that several tenths of solar masses of material have been transferred from the progenitor of the white dwarf onto the pulsar, spinning it up to the currently observed (millisecond) periods (for reviews, see Verbunt 1993; Phinney & Kulkarni 1994; Stairs 2004).

About 40 of such systems are known (see review by van Kerkwijk et al. 2005), but neutron-star masses have been measured for only six of them. PSR J0751+1807 contains the heaviest neutron star known to date and with a mass of $2.1 \pm 0.2\,M_\odot$ (Nice et al. 2005b) this is the only system for which the mass is not consistent with a value near $1.4\,M_\odot$.

With the exception of PSR J1012+5307, these neutron-star masses are determined from radio timing of the millisecond pulsar; either due to the detection of general-relativistic effects or due to the detection of secular and annual variations because of the motion of the Earth. For PSR J1012+5307, the neutron-star mass was determined through optical spectroscopy of the white-dwarf companion to the pulsar. These measurements yield the radial-velocity amplitude of the white-dwarf orbit, which combined with the pulsar orbit, determines the mass ratio between the white dwarf and the pulsar. A model-atmosphere fit to the white-dwarf spectrum provides the effective temperature and surface gravity of the white dwarf. Combining these values with white-dwarf mass-radius relations yield the white-dwarf mass and radius and, through the mass ratio, the pulsar mass.

In this paper, we use this method to determine the mass of the binary millisecond pulsar PSR J1911−5958A. This pulsar is in a 20 h, highly circular ($e < 10^{-5}$) orbit around a low-mass companion and located at a projected offset of 6′.4 from the center of the globular cluster NGC 6752 (D'Amico et al. 2001a, 2002). D'Amico et al. (2002) argued that the pulsar binary is associated with the globular cluster NGC 6752 (cf. the discussion in Appendix 5.7). In order to explain the large distance of the pulsar from the cluster center (3.3 half-mass radii) and the circular orbit, Colpi et al. (2002) investigated several possible scenarios. They argued that if PSR J1911−5958A was ejected out of the core of NGC 6752 this may be the result of an encounter with a wide binary consisting of two black holes.

The optical counterpart to PSR J1911−5958A was discovered by Bassa et al. (2003b) and confirmed by Ferraro et al. (2003a). It was found that the colours and magnitudes of the counterpart are consistent with those of a 0.18–0.20 $M_\odot$ helium-core white dwarf at the distance of NGC 6752. The relative brightness of the counterpart ($V = 22.1$) and the fact that the field surrounding PSR J1911−5958A is not extremely crowded, motivated us to obtain phase-resolved spectroscopic observations of the companion of PSR J1911−5958A and determine the mass of the pulsar. In principle, these observations can also be used to verify

the membership of PSR J1911−5958A with NGC 6752 through the systemic radial velocity and the white-dwarf radius, which should be consistent with values expected for a system associated with the globular cluster. If the association is confirmed, the accurate distance to the globular cluster provides a separate constraint on the radius of the white dwarf and thus its mass.

This paper is structured as follows; in Sect. 5.2, we describe our spectroscopic observations and their reduction, as well as the analysis of archival photometric observations. The radial-velocity measurements are described in Sect. 5.3 and we determine the properties of the system in Sect. 5.4. We compare our results with the work by Cocozza et al. (2006) and present the overall discussion and conclusions in Sect. 5.5. In Appendix 5.6 we elaborate on the corrections we applied to the wavelength scale. Finally, we discuss the membership of PSR J1911−5958A with NGC 6752 in Appendix 5.7.

5.2 Observations and data reduction

5.2.1 Spectroscopy

Twenty-three long-slit spectra of the companion of PSR J1911−5958A were obtained with FORS1, the Focal Reducer and Low Dispersion Spectrograph of the ESO VLT at Cerro Paranal, on 8 different nights from May to August of 2004. A summary of the observations is given in Table 5.2. Between the first and second observing run, the instrument was moved from Unit Telescope 1 (UT1, Antu) to UT2 (Kueyen). The spectra were obtained with the 600 lines mm^{-1} "B" grism and a $1\farcs31$ slit, which gives a wavelength coverage from 3300–5690 Å. The standard-resolution collimator was used, resulting in a pixel size of $0\farcs2\,pix^{-1}$ in the spatial direction and $1.2\,Å\,pix^{-1}$ in the dispersion direction. All spectra had integration times of 2470 s and were sandwiched between two 30 s, *B*-band, through-the-slit images and preceded by one or more 30 s *B*-band acquisition images. The seeing, as determined from the width of the slit profiles, varied between $0\farcs5$ and $1\farcs0$, with only three spectra having a FWHM larger than $0\farcs8$. Generally, the conditions were good, with photometric skies. With this setup, the spectral resolution is set by the seeing, which is less than the slit width in all observations. For our average spectra, a resolution of 4.5 Å is inferred from the spectra of the reference star discussed below. Following the FORS1 calibration plan, bias, flat-field and wavelength calibration frames were obtained during twilight or daytime after each observing night, with the telescope pointed towards the zenith.

Given the proximity of a brighter star ($V = 17.3$) only $3\farcs1$ to the North-West of the pulsar companion, we chose to center the slit on both this star and the companion, see Fig. 5.1. We did this to use the star as a reference for the wavelength and flux calibration and to minimize the influence of this star on the spectrum of the white dwarf. Besides the pulsar companion and this bright star (which we henceforth call the reference star or star R), stars A, B and C (see Fig. 5.1) and D also fall on the slit. As a result of this setup, the position angle of the slit is fixed on the sky and differs from the parallactic angle, by an amount which depends on the hour angle of the observation. Any effects of differential atmospheric refraction, which become important when one does not observe with the slit parallel to the parallactic angle

(Filippenko 1982), are largely corrected for by the Atmospheric Dispersion Corrector (ADC) on the FORS1 instrument.

To account for slit losses and to allow for flux calibration, the exposure with the slit positioned closest to the parallactic angle (that from MJD 53229, see Table 5.2) was followed by exposures through a 2″ slit of both the pulsar companion (1600 s) and the spectro-photometric flux standard LTT 7987 (30 s; Hamuy et al. 1992, 1994). For these the conditions were photometric with 0.″7 seeing.

The images were reduced with the Munich Image Data Analysis System (MIDAS). All images were bias-corrected with the bias values from the overscan regions on the FORS1 chip and flat-fielded using lamp exposures. For the sky subtraction we used clean regions between the stars along the slit. The region extended to 26″ to each side of the pulsar companion, encompassing the pulsar companion, the reference star and star A, B and C. For star D a similar procedure was used. A polynomial was fitted to the spatial profile of these clean regions of the sky for each column in the dispersion direction. The order of the polynomial was predominantly zero; but first and second order fits were used when this significantly increased the goodness of the fit.

Spectra were extracted from the sky-subtracted images using an optimal extraction method similar to that of Horne (1986). Each of the extracted spectra was wavelength calibrated with the He Hg Cd wavelength calibration frames. Here we measured the positions of the lines in a row-averaged (in the spatial direction) multiplication of the wavelength calibration frame and the 2-dimensional (in the spatial and dispersion direction) slit profile of the star in question. A cubic polynomial fit was sufficient to describe the dispersion relation and gave root-mean-square (rms) residuals of less than 0.06Å. The wavelength calibrations were found to be stable between different observing nights; the rms scatter in the zero point was 0.041Å (corresponding to 2.7 km s^{-1} at 4500Å).

The last step was to calibrate the spectra for the instrumental response of the spectrograph, as derived from the observation of the flux standard. The spectrum of the standard was reduced in a similar manner as the pulsar companion and the other stars on the slit. Unfortunately, deriving the response was somewhat troublesome since the calibrated spectrum of the DA white dwarf LTT 7987 was tabulated at 50Å steps. With such a resolution the higher Balmer lines are poorly sampled which may result in systematic trends in the flux calibration at these wavelengths. We therefore analyzed two archival observations of Feige 110 (Oke 1990), tabulated at 1Å and 2Å steps, from June 28th and December 1st, 2004. The observations were taken with the same grism as the pulsar companion, though with 5″ MOS slits. The spectra were extracted and wavelength calibrated as before and corrected for atmospheric extinction using the average La Silla extinction curve (this relation is also suitable for Paranal). A comparison of the resulting response curves showed that these had a very similar shape, and that the ratio of the two curves could be well approximated with a linear polynomial, i.e. that the response was stable over time. We now used the response curve derived from the June 2004 observation of Feige 110 and fitted it against the extinction-corrected response of LTT 7987, fitting for a linear polynomial scaling factor. Using the *B*-band filter curve of Bessell (1990) and the zero point of Bessell et al. (1998) we obtain a synthetic *B*-band magnitude of 12.30 for LTT 7987, which compares well to $B = 12.28$ found by Hamuy

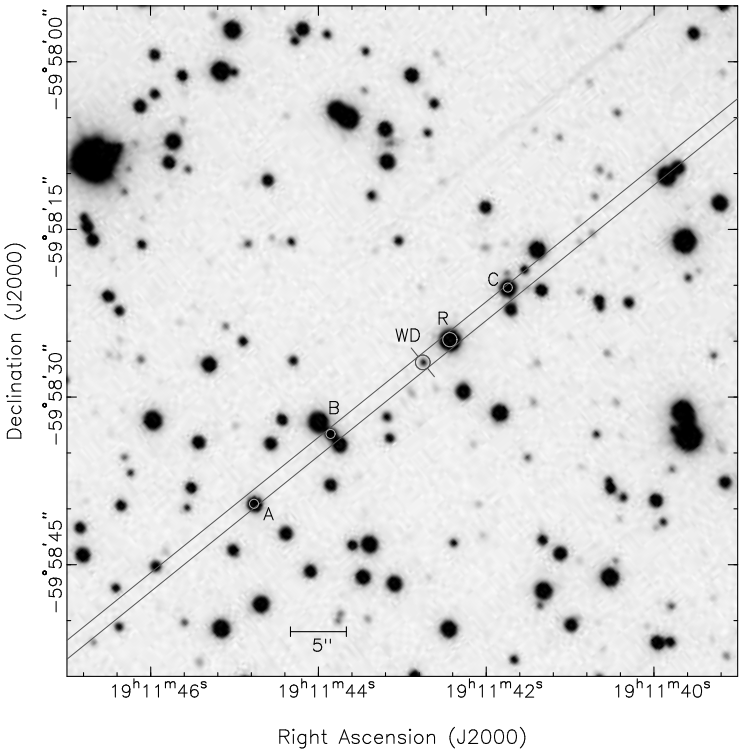

Figure 5.1: *The orientation of the slit on the sky. The* 1.″31 *slit is shown with the white-dwarf companion denoted as "WD". The nearby star used as a reference is denoted as "R", and names of some of the other stars on the slit are indicated. Star D is located outside the figure, to the North-West of PSR J1911−5958A. This* 60″ × 60″ *image is an average of two* 30 s *B-band acquisition images obtained during the first observing night.*

et al. (1992) and $B = 12.27$ by Landolt (1992).

We corrected all spectra for atmospheric extinction and calibrated them using this new response. Differences in continuum flux between the narrow and wide slit exposures were corrected for with a scaling factor that depends linearly on wavelength.

5.2.2 Photometry

We have analyzed all available FORS1 observations of the field containing PSR J1911−5958A. The data consists of i) three 1500 s U, five 360 s B and eight 220 s V-band images, taken with the high-resolution collimator (which has 0.″1 pix^{-1}) on 3 different nights in 2003 March, April and May under photometric conditions with good seeing (0.″5–0.″7); ii) three 32 s B-band and three 13 s V-band images that were obtained under photometric conditions with 0.″7 seeing on 2003 March 31 with the standard

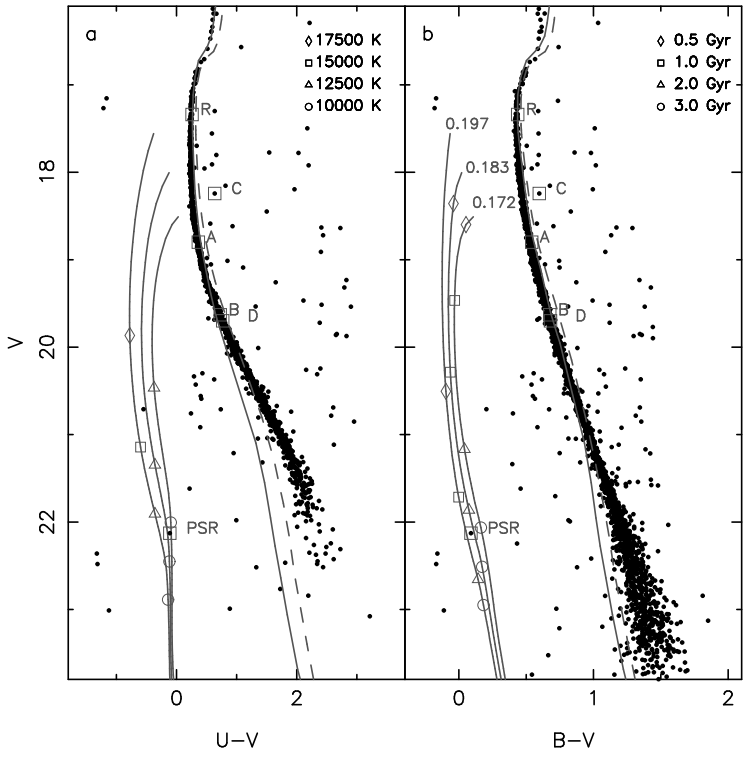

Figure 5.2: *Colour-magnitude diagrams of NGC 6752, constructed from archival FORS1 observations. The stars located on the slit are labeled. Shown as solid lines to the left of the cluster main-sequence are three $Z = 0.0010$ helium-core white dwarf cooling models of Serenelli et al. (2002). The masses of these models are as shown (in $M_\odot$), and temperatures are indicated along the track in panel* ***a****, while cooling ages are shown in panel* ***b****. Also shown are two isochrones from Girardi et al. (2000) for an age of 14.1 Gyr and a metallicity of $Z = 0.0004$ (solid line) and one for an age of 12.6 Gyr with $Z = 0.0010$ (dashed line). All models are placed at a distance of $(m - M)_V = 13.24$ with a reddening of $E_{B-V} = 0.040$, as determined by Gratton et al. (2003).*

collimator; iii) a series of thirty 30 s B-band acquisition images obtained prior to the spectral observations presented above, and iv) a series of twenty-three 600 s B-band images obtained on 2004 August 10–15 with the high resolution collimator during good to moderate seeing conditions (0.″5–1.″3).

All images were bias-subtracted and flat-fielded using twilight flats. The DAOPHOT II package (Stetson 1987), running inside MIDAS, was used for the photometry on the averaged images. We followed the recommendations of Stetson (1987), obtaining instrumental magnitudes through point-spread function (PSF) fitting. The B and V-band observations of March 31, 2003 include 20 photometric standards from Stetson (2000) of which 12 were unsaturated. The instrumental PSF magnitudes of these stars were directly compared against the

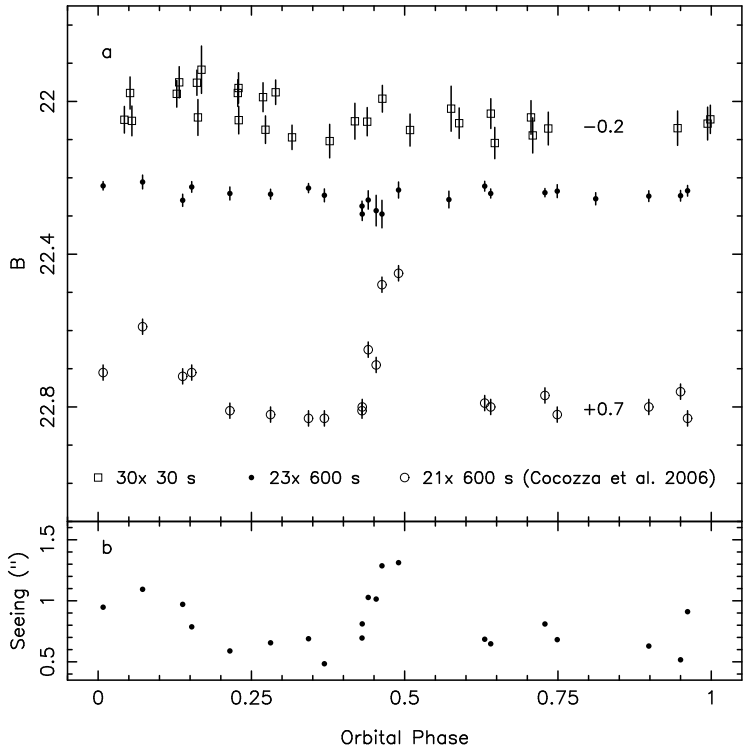

Figure 5.3: ***a*** *The B-band magnitude of the white-dwarf companion of PSR J1911−5958A as a function of orbital phase for the magnitudes determined from the thirty 30 s exposures (*open squares*, offset by −0.2 mag) and the twenty-three 600 s B-band exposures (*black dots*). Also shown are the B-band magnitudes determined by Cocozza et al. (2006) from the same 600 s exposures (*open circles*, read off from their Fig. 3, but offset by +0.7 mag).* ***b*** *The seeing of the 600 s B-band exposures, determined from the width of the point-spread-function. Note that the variations in the seeing and the magnitudes as measured by Cocozza et al. (2006) are highly correlated, indicating that their measurements are corrupted (see Sect. 5.5 for details).*

calibrated values to derive zero points and colour terms (no extinction coefficients are needed since the standards and target are at the same airmass), giving rms residuals of 0.01 mag in B and 0.03 mag in V. For the calibration of the U-band observations, we used 4 standard stars from the PG 1657+078 field (Landolt 1992). We fitted for zero point and colour term, using the standard ESO extinction coefficients of 0.46 and 0.25 mag per airmass for U and B-band respectively. These calibrations have rms residuals of 0.02 mag in U and B. The difference between the two B-band calibrations was less than 0.01 mag, hence we expect our zero-point uncertainties in B to be less than 0.02 mag, less than 0.03 mag in V, and allowing for the uncertainty in the U-band extinction coefficient, less than 0.05 mag in U. The resulting magnitudes of the stars on the slit are tabulated in Table 5.1.

Table 5.1: *VLT/FORS1 photometry of the white-dwarf companion of PSR J1911−5958A (denoted with WD) and stars on the slit. The nomenclature of the stars is according to Fig. 5.1, while star D is located outside the figure, on the North-West side of the slit. The uncertainties listed in parentheses are instrumental, i.e., they do not include the zero-point uncertainty in the photometric calibration (0.05 mag in U, 0.02 mag B and 0.03 mag in V). The celestial positions were obtained using the procedure outlined in Bassa et al. (2003b).*

ID	α_{2000} h m s	δ_{2000} ° ′ ″	U	B	V
WD	19 11 42.753	−59 58 26.89	22.02(5)	22.22(3)	22.13(2)
R	19 11 42.432	−59 58 24.90	17.60(5)	17.78(1)	17.34(1)
A	19 11 44.768	−59 58 39.58	19.16(5)	19.34(1)	18.80(1)
B	19 11 42.854	−59 58 33.34	20.36(5)	20.31(1)	19.63(1)
C	19 11 41.742	−59 58 20.25	18.88(5)	18.84(1)	18.24(1)
D	19 11 35.911	−59 57 45.35	20.47(5)	20.38(1)	19.70(1)

Colour-magnitude diagrams were constructed from the photometry and are shown in Fig. 5.2. We find that star R has the magnitude and colours of a cluster turn-off star while stars A, B and D are located further down the cluster main sequence. Star C, on the other hand, is not located on the main sequence, and is about a magnitude brighter than cluster stars with the same $U - V$ and $B - V$ colours. The pulsar companion is blue with respect to the cluster main-sequence by about 2 mag in $U - V$ and more than 1 mag in $B - V$.

We checked for variability of the pulsar companion using the twenty-three 600 s B-band images and the thirty 30 s B-band acquisition images. With a pixel scale of $0\farcs1\,\mathrm{pix}^{-1}$, the 600 s images are severely oversampled, and we rebinned the images to a pixel scale of $0\farcs2\,\mathrm{pix}^{-1}$ (averaging every 2×2 pixels). Next, instrumental magnitudes were determined through PSF fitting and calibrated to the photometry presented above. The resulting magnitudes are shown in Fig. 5.3. In both the 600 s and the 30 s images, the magnitudes of the pulsar companion do not significantly vary with orbital phase. For example, the rms scatter for the white dwarf around the average value in the 600 s and 30 s images is only 0.02 mag and 0.05 mag, respectively, and these values are comparable to that of stars of similar brightness.

5.3 Radial velocities

Radial velocities of the companion and the five stars on the slit were determined by comparing them with template spectra. In case of the white dwarf this was done iteratively, where we used the hydrogen atmosphere models from which we determined the surface gravity and effective temperature (see Sect. 5.4.2 and Fig. 5.5) as a template. A best-fit model was first determined for one of the single spectra. This model was then used as a velocity template to measure the velocities of the other spectra. These spectra were shifted to zero velocity and averaged. The final velocity template was found by fitting a new atmosphere model against the averaged spectrum. The actual velocities were measured by minimizing a χ^2 merit function, as defined in Bassa et al. (2003a), fitting for velocity and a 2nd order polynomial modelling continuum differences.

Table 5.2: *Radial-velocity measurements of the white-dwarf companion of PSR J1911−5958A and four stars on the slit. To put these velocities on an absolute scale, a velocity offset of* $-39 \pm 3\,km\,s^{-1}$ *should be added (see Appendix 5.6).*

MJD_{bar}[a]	ϕ_b[b]	v_{WD} ($km\,s^{-1}$)	v_R ($km\,s^{-1}$)	v_A ($km\,s^{-1}$)	v_C ($km\,s^{-1}$)	v_D ($km\,s^{-1}$)
53147.38143	0.1590	−29 ± 22	12.9 ± 8.1	18 ± 11	34 ± 16	21 ± 20
53198.11569	0.7664	3 ± 29	6.8 ± 7.8	−1 ± 11	18 ± 16	11 ± 22
53204.15036	0.9752	−233 ± 26	11.5 ± 8.2	23 ± 11	19 ± 16	−1 ± 20
53204.19242	0.0254	−219 ± 22	17.8 ± 8.1	13 ± 12	45 ± 16	13 ± 21
53204.22978	0.0701	−160 ± 25	8.8 ± 8.5	17 ± 11	58 ± 15	12 ± 21
53206.21868	0.4459	218 ± 23	16.8 ± 8.6	7 ± 11	33 ± 15	6 ± 22
53206.25549	0.4899	262 ± 20	10.8 ± 8.1	12 ± 11	38 ± 15	23 ± 21
53206.29500	0.5371	245 ± 23	10.3 ± 8.5	3 ± 11	31 ± 16	10 ± 20
53210.19705	0.1983	6 ± 25	15.4 ± 8.8	2 ± 11	35 ± 16	20 ± 20
53210.23098	0.2388	12 ± 22	−0.3 ± 8.0	−1 ± 12	30 ± 15	3 ± 20
53210.27816	0.2952	77 ± 24	−6.4 ± 7.6	12 ± 11	38 ± 16	2 ± 21
53210.31250	0.3362	148 ± 27	3.6 ± 7.8	−1 ± 11	33 ± 16	23 ± 26
53229.01322	0.6748	116 ± 23	6.2 ± 8.1	8 ± 11	27 ± 16	−1 ± 22
53231.02712	0.0805	−186 ± 25	0.3 ± 8.1	8 ± 11	12 ± 16	−12 ± 22
53231.06463	0.1253	−179 ± 27	3.8 ± 8.2	6 ± 11	19 ± 16	−8 ± 20
53231.11869	0.1899	−64 ± 26	16.3 ± 7.8	6 ± 11	33 ± 16	22 ± 21
53231.17422	0.2562	35 ± 25	−7.0 ± 7.9	4 ± 11	22 ± 16	−6 ± 20
53231.22574	0.3177	153 ± 29	7.7 ± 8.2	−6 ± 10	34 ± 16	−6 ± 21
53232.00988	0.2544	57 ± 22	1.2 ± 7.7	5 ± 11	9 ± 16	−8 ± 19
53232.04617	0.2978	42 ± 24	11.4 ± 8.1	13 ± 11	21 ± 15	9 ± 20
53232.08482	0.3439	142 ± 21	23.9 ± 8.2	15 ± 10	38 ± 15	16 ± 20
53232.13559	0.4046	200 ± 22	12.7 ± 8.4	0 ± 11	37 ± 17	−5 ± 20
53232.18610	0.4649	273 ± 32	−0.6 ± 9.2	3 ± 10	32 ± 17	−1 ± 21

[a] The time of the observation at mid-exposure, corrected to the solar system barycenter.
[b] Using the ephemeris of D'Amico et al. (2002): T_{asc} = MJD 51919.2064780(3), P_b = 0.837113476(1) days.

In the case of the reference star we used a somewhat different approach. Here, a template was constructed from fitting Lorentzian profiles to a single, normalized spectrum of the reference star. Eight lines (Hβ up to H11 and Ca K, but without the blend of Hϵ and Ca H) were simultaneously fitted, fitting for depth and width, but forcing the velocity to be the same for all lines. The resulting template was shifted to zero velocity and fitted against normalized spectra of the reference star by again minimizing a χ^2 merit function. To test for the stability of the radial velocities, we also used this template to determine radial velocities of the other four stars on the slit. These stars also display the hydrogen Balmer lines and Ca K, though the lines are not as strong as those of the reference star (see Fig. 5.9).

The radial velocity of the pulsar companion varied by as much as $470\,km\,s^{-1}$ between the different spectra, fully within the expectations for this system. From radio timing, it was found that the eccentricity of the orbit is $e < 10^{-5}$ (D'Amico et al. 2002). Hence, we fitted the barycentric radial velocities of the pulsar companion to a circular orbit, with the orbital period and time of the ascending passage node fixed to the values determined from the radio-timing solution by D'Amico et al. (2002). We find a radial-velocity amplitude $K_{WD} = 215 \pm 10\,km\,s^{-1}$ and a systemic velocity $\gamma = -30 \pm 7\,km\,s^{-1}$ for a reduced chi-squared

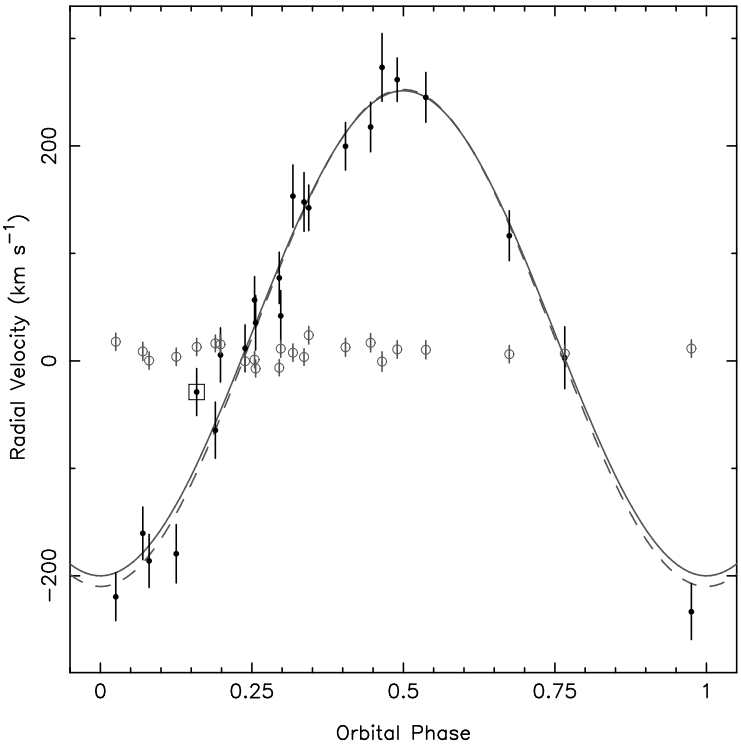

Figure 5.4: *The radial velocities of the white-dwarf companion of PSR J1911−5958A (*black dots*) and of the reference star R (*open circles*). The solid line represents the best-fit model for a circular orbit, using all data points, with the time of the ascending node passage and the orbital period fixed to the values determined from the radio-timing solution by D'Amico et al. (2002). The dashed line represents the best-fit model excluding the boxed data point. To put these velocities on an absolute scale, a velocity offset of* $-39 \pm 3\,km\,s^{-1}$ *should be added (see Appendix 5.6).*

$\chi^2_\nu = 1.67$ with 21 degrees-of-freedom. Here, the errors on $K_{\rm WD}$ and γ are scaled to give $\chi^2_\nu = 1$.

The velocity of the reference star, however, varied over a 120 km s^{-1} range, much larger than the 7 to 10 km s^{-1} error on the individual velocities. We feared that these velocity variations might also be a result of binarity, but the other stars on the slit displayed similar variations in velocity. In particular, the velocities of these stars displayed a trend when compared against the local hour angle of the observation, where the velocity decreased by about 16 km s^{-1} per hour prior or after culmination. Upon closer investigation this trend was found to be caused by two separate, systematic, effects. Because the effects are systematic, they can be corrected for.

For the first correction, we applied a shift to the wavelength calibration of each spectrum based on the difference between the measured wavelength of the O I λ5577 night sky emission

line in the spectrum and the laboratory value. This correction removes the global decrease of the velocities as a function of hour angle. The remaining scatter in the radial velocities is largely removed by correcting for the second effect, which is due to errors in the centering of the stars on the slit. For this correction, we determined the position of star R with respect to the center of the slit in the through-the-slit images obtained before and after each spectrum. We apply this offset as a shift in wavelength to the wavelength calibration of the corresponding spectrum. In Appendix 5.6 we describe these corrections in detail, while Table 5.2 lists the velocities that were determined from the corrected wavelength calibrations.

We now use the corrected radial velocities to determine the radial-velocity orbit of the white-dwarf companion of PSR J1911−5958A. Again fitting for a circular orbit, we find a radial-velocity amplitude $K_{\rm WD} = 226 \pm 9\,{\rm km\,s^{-1}}$ and a systemic velocity $\gamma = 26 \pm 6\,{\rm km\,s^{-1}}$ ($\chi^2_\nu = 1.45$ for 21 degrees-of-freedom). The errors on $K_{\rm WD}$ and γ are again scaled to give $\chi^2_\nu = 1$. This fit is represented in Fig. 5.4 with the solid line. If we exclude the single point (the boxed point in Fig. 5.4) that lies 3.2σ away from the best-fit, the fit improves to $\chi^2_\nu = 1.00$, giving $K_{\rm WD} = 231 \pm 8\,{\rm km\,s^{-1}}$ and $\gamma = 21 \pm 5\,{\rm km\,s^{-1}}$, depicted by the dashed curve in Fig. 5.4. Remarkably, this outlier corresponds to the spectrum taken during the first observing run, when, as mentioned in Sect. 5.2, FORS1 was still on UT1, unlike all other spectroscopic observations, when it was on UT2. We do not understand, however, how this could cause a difference, since differences in the flat-fields, wavelength calibration, and flux calibration should all be corrected for.

If we fit a circular orbit against the radial velocities of the pulsar companion relative to the radial velocities of the reference star R, we obtain $K_{\Delta v} = 225 \pm 10\,{\rm km\,s^{-1}}$, $\gamma_{\Delta v} = 17 \pm 6\,{\rm km\,s^{-1}}$, $\chi^2_\nu = 1.43$ for 21 degrees-of-freedom. Again excluding the outlier gives $K_{\Delta v} = 231 \pm 9\,{\rm km\,s^{-1}}$, $\gamma_{\Delta v} = 13 \pm 6\,{\rm km\,s^{-1}}$, with $\chi^2_\nu = 1.10$ for 20 degrees-of-freedom.

The differences in the radial velocity amplitudes $K_{\rm WD}$ are consistent within the errors. The same holds for the systemic velocities γ measured from the absolute and the relative velocities. For the remainder of this paper we will use the fit using absolute velocities, without the 3.2σ outlier; $K_{\rm WD} = 231 \pm 8\,{\rm km\,s^{-1}}$ and $\gamma = -18 \pm 6\,{\rm km\,s^{-1}}$ (here we corrected the systematic velocity for the $-39 \pm 3\,{\rm km\,s^{-1}}$ velocity offset which we determined in Appendix 5.6).

5.4 System properties

We use our measurements to determine the properties of the white dwarf and the pulsar. In our analysis, we distinguish between results that do and that do not depend on the assumption that the pulsar is a member of NGC 6752. We will see that our conclusions depend on that assumption; we will address this in detail in Appendix 5.7.

5.4.1 Minimum white dwarf mass

The radio timing observations by D'Amico et al. (2002) yielded a projected semi-major axis of the pulsar orbit of $a_{\rm PSR} \sin i/c = 1.206045 \pm 0.000002\,{\rm s}$, which, together with the orbital period $P_{\rm b}$ implies a radial-velocity amplitude of $K_{\rm PSR} = 31.40986 \pm 0.00005\,{\rm km\,s^{-1}}$. Combining this with the radial-velocity amplitude of the white dwarf determines the mass ratio

$q = M_{\rm PSR}/M_{\rm WD} = K_{\rm WD}/K_{\rm PSR} = 7.36 \pm 0.25$. Here, the error on q is dominated by the uncertainty in $K_{\rm WD}$.

We can use the mass ratio and the constraint that the inclination must be less than or equal to 90° to determine a lower limit to the white-dwarf mass. For this, we use the pulsar mass-function $f(M_{\rm PSR}) = M_{\rm WD}^3 \sin^3 i/(M_{\rm WD} + M_{\rm PSR})^2 = (2.687603 \pm 0.000013) \times 10^{-3}\,{\rm M}_\odot$, so that we can write $M_{\rm WD} \sin^3 i = (1 + q)^2 f(M_{\rm PSR})$. Setting the inclination at $i = 90°$ and using the mass ratio q as determined above we find a 1σ lower limit of $M_{\rm WD} > 0.177\,{\rm M}_\odot$. The 2σ lower limit is $M_{\rm WD} > 0.166\,{\rm M}_\odot$.

5.4.2 Effective temperature and surface gravity

The atmospheric parameters for the white dwarf were determined by fitting theoretical model atmospheres to the average of the velocity-corrected spectra (see Sect. 5.3). The theoretical models were taken from a grid of pure hydrogen models usually applied to normal DA white dwarfs, but extending down to surface gravities of $\log g = 5$. The methods and input physics are described in more detail in Finley et al. (1997) and Homeier et al. (1998). The best-fitting parameters are found with a Levenberg-Marquardt type χ^2 algorithm (Press et al. 1992). We also use a second, newly developed algorithm, which is less sophisticated but more transparent and robust than the Levenberg-Marquardt method. In essence it determines the χ^2 values for the models of the grid around the minimum and then fits the χ^2 surface with a paraboloid, from which the parameters and errors corresponding to the minimal χ^2 can be calculated. This avoids excessive interpolations between the models in the grid, which sometimes leads to artificial small-scale structure of the χ^2 surface. The results between the two methods did not differ significantly; the values given below are from the second method.

For the fit we used the spectral ranges from 3740–4440 and 4760–5030 Å, which contain the Balmer lines. The model was fitted to the observed spectrum and the χ^2 calculated from the fit to the continuum-normalized line profiles. The obtained parameters and their formal errors are $T_{\rm eff} = 10090 \pm 25\,{\rm K}$ and $\log g = 6.44 \pm 0.05\,{\rm cgs}$. The resulting best-fit model is shown in Fig. 5.5. With this temperature, the spectral type of the white dwarf is DA5 (Wesemael et al. 1993).

The model fits the observed Balmer lines extremely well up to H10. H11 and H12 are weaker and not as deep in the model as is observed. This may be an indication that the surface gravity is slightly lower than the formal fit. It may also indicate that the Hummer-Mihalas occupation probability theory (Hummer & Mihalas 1988; Mihalas et al. 1988, 1990) used in the models overestimates the quenching of the highest Balmer lines. The theoretical line profiles of H11 and H12 depend strongly on the Hummer-Mihalas formalism and as these lines are absent in the typical $\log g = 8$ white dwarf, the theory is difficult to calibrate. For a recent study on the influence of the Hummer-Mihalas formalism on the line profiles, see Koester et al. (2005).

The fit uncertainties include only the statistical errors, while systematic effects may be important (Reid 1996; Vauclair et al. 1997). We experimented with small changes in the continuum and fit regions, and other fitting parameters. The largest effect is from changes in the resolution: assuming that the resolution were 6.5Å instead of the 4.5Å inferred from the

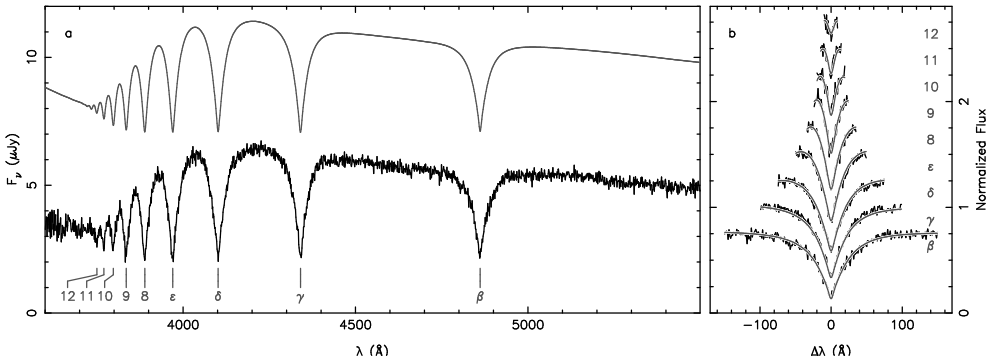

Figure 5.5: *Spectrum of the white-dwarf companion to PSR J1911−5958A. The lower curve in panel* ***a*** *shows the average of the 23 individual spectra, shifted to zero velocity. The hydrogen Balmer lines are seen from Hβ up to H12 as indicated. The top curve is the best-fit model spectrum, with* $T_{\rm eff} = 10090\,K$ *and* $\log g = 6.44\,cgs$*. It is shifted upwards by 5μJy. Panel* ***b*** *shows the flux-normalized line profiles superposed on the modelled profiles. The Hβ profile is shifted a quarter unit downwards from unity, while those of Hδ up to H12 are shifted upwards by multiples of the same amount.*

lines in the spectrum of the reference star, we find $T_{\rm eff} = 10135\,{\rm K}$ and $\log g = 6.20\,{\rm cgs}$. As we discuss in Appendix 5.7, rapid rotation may mimic a change in resolution. Since this is not secure, however, we decided to adopt conservative errors below, and use $T_{\rm eff} = 10090 \pm 150\,{\rm K}$ and $\log g = 6.44 \pm 0.20\,{\rm cgs}$

5.4.3 White dwarf mass and radius

The mass and radius of the white dwarf can be determined from the surface gravity using a mass-radius relation appropriate for a helium-core white dwarf at the observed temperature. Such mass-radius relations have been modelled by Panei et al. (2000) and we interpolate between their 8000 K and 12000 K tracks to obtain the relation at the observed temperature, as shown in Fig. 5.6, giving $M_{\rm WD} = 0.180 \pm 0.018\,{\rm M}_\odot$ and $R_{\rm WD} = 0.0423 \pm 0.0075\,{\rm R}_\odot$. Similar white-dwarf masses and radii are found from the evolutionary cooling tracks of Driebe et al. (1998) and Rohrmann et al. (2002). Here we obtain, for each model with a given mass, the radius and hence the surface gravity at the observed white-dwarf temperature and interpolate between the models to get the mass and radius at the observed $\log g$. The models by Rohrmann et al. (2002) give $M_{\rm WD} = 0.181 \pm 0.012\,{\rm M}_\odot$ with $R_{\rm WD} = 0.0424 \pm 0.0088\,{\rm R}_\odot$. The lowest mass model by Driebe et al. (1998) has $0.179\,{\rm M}_\odot$, so we extrapolate their models. This yields $M_{\rm WD} = 0.172 \pm 0.018\,{\rm M}_\odot$ and $R_{\rm WD} = 0.0414 \pm 0.0074\,{\rm R}_\odot$, though the uncertainties may be underestimated because of the extrapolation. The uncertainties of the Rohrmann et al. (2002) models are considerably smaller, as its mass-radius relation is steeper than those of the Panei et al. (2000) and Driebe et al. (1998). Finally, the mass-radius relations from the $Z = 0.0010$ and $Z = 0.0002$ models by Serenelli et al. (2002) are very similar and both predict a somewhat higher white-dwarf mass, of $M_{\rm WD} = 0.190 \pm 0.015\,{\rm M}_\odot$, and a radius of

$R_{\rm WD} = 0.0434 \pm 0.0084\,{\rm R}_\odot$.

We should note that the models by Driebe et al. (1998) and Rohrmann et al. (2002) are computed for white-dwarf progenitors with solar metallicity and are appropriate for field systems. As the metallicity of NGC 6752 is considerably smaller ([Fe/H]= -1.43 ± 0.04, Gratton et al. 2003), the Serenelli et al. (2002) models for white-dwarf progenitors with sub-solar metallicities (with $Z = 0.0010$ in particular) are more appropriate in the case that PSR J1911−5958A is associated with NGC 6752. The differences of about $0.01\,{\rm M}_\odot$ and $0.001\,{\rm R}_\odot$ in the predictions from different models, however, are similar in magnitude to the difference induced by different metallicities. For the remainder of the paper, we will use values that encompass all predictions from the effective temperature and surface gravity: $M_{\rm WD} = 0.18 \pm 0.02\,{\rm M}_\odot$ and $R_{\rm WD} = 0.043 \pm 0.009\,{\rm R}_\odot$.

5.4.4 Distance inferred from the white dwarf

The distance to the white dwarf can now be estimated using the observed and modelled flux and the radius of the white dwarf. We do this by writing the flux normalization $f = (R/d)^2\pi F$ between the observed flux f, the model flux πF, and the radius R over the distance d in terms of magnitudes; $M_\lambda = 43.234 - 5\log R/R_\odot - 2.5\log \pi F_\lambda + c_\lambda$, where M_λ is the absolute magnitude in a given filter, πF_λ the flux from the model in the same filter and c_λ the zero-point of the filter. By convolving the flux-calibrated best-fit model of the observed spectrum with the B and V-band filter curves from Bessell (1990), we obtain $\pi F_B = 9.45 \times 10^7\,{\rm erg\,cm^{-2}\,s^{-1}\,\AA^{-1}}$ and $\pi F_V = 6.26{\times}10^7\,{\rm erg\,cm^{-2}\,s^{-1}\,\AA^{-1}}$. The uncertainties on these fluxes are due to the uncertainties in $T_{\rm eff}$ and $\log g$ are about 5%. With the zero-points from Bessell et al. (1998), $c_B = -20.948$ and $c_V = -21.100$, we obtain $M_B = 9.63{\pm}0.46$, $M_V = 9.48{\pm}0.46$. The uncertainties are dominated by those on the white-dwarf radius.

Combined with the observed B and V-band magnitudes from Table 5.1, we obtain distance moduli of $(m - M)_B = 12.59 \pm 0.46$ and $(m - M)_V = 12.66 \pm 0.46$. Assuming a negligible reddening, the averaged distance modulus yields a distance of $d = 3.4 \pm 0.7$ kpc. Assuming a reddening of $E_{B-V} = 0.05$, the distance becomes $d = 3.1 \pm 0.7$ kpc.

5.4.5 Mass and radius from distance, flux and temperature

Now we determine the properties of the white dwarf based on the assumption that the distance of the binary is that of the globular cluster. From the values from Table 5.1, the distance modulus $(m - M)_V = 13.24 \pm 0.08$ and reddening $E_{B-V} = 0.046 \pm 0.005$ (Gratton et al. 2003, 2005), we obtain $M_B = 8.93 \pm 0.09$ and $M_V = 8.89 \pm 0.08$. The B and V-band fluxes and zero-points and the relation from Sect. 5.4.4 yield white-dwarf radii of $\log R/R_\odot = -1.226 \pm 0.021$ and $\log R/R_\odot = -1.249 \pm 0.018$ for the B and V-band values, respectively. As a conservative estimate, we will use $\log R/R_\odot = -1.238 \pm 0.030$, corresponding to $R = 0.058 \pm 0.004\,{\rm R}_\odot$, which encompasses both values.

The mass of the white dwarf can be determined from the radius using the mass-radius relations. The radius is shown with the horizontal lines in Fig. 5.6, together with the mass-radius relations. The models by Rohrmann et al. (2002) predict $M_{\rm WD} = 0.172 \pm 0.001\,{\rm M}_\odot$,

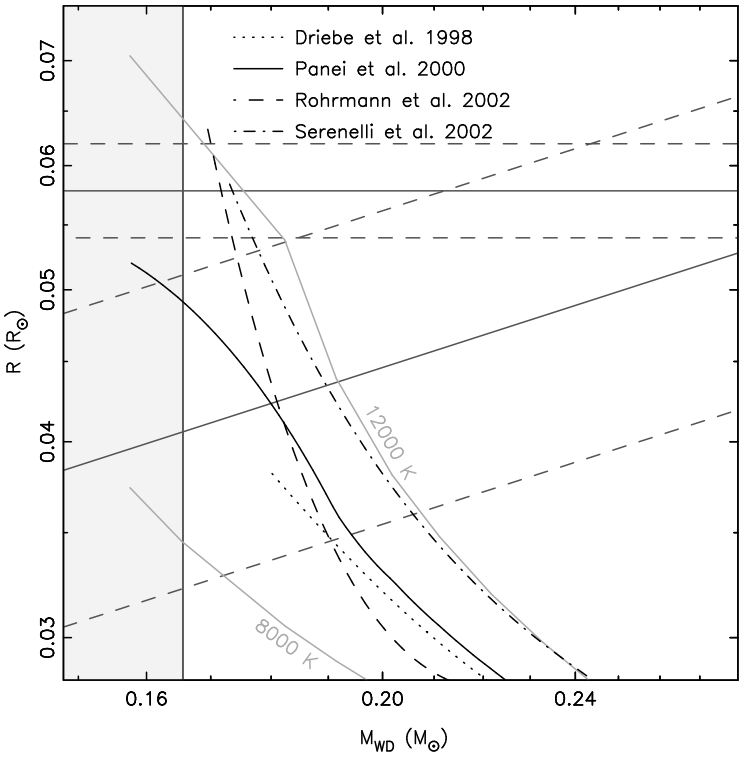

Figure 5.6: *White-dwarf mass-radius relations for a temperature of* $T_{\rm eff} = 10090 \pm 150\,K$. *Shown are the relations from Rohrmann et al. (2002)* (dashed line)*, Serenelli et al. (2002)* (dashed dotted)*, Driebe et al. (1998)* (dotted) *and Panei et al. (2000)* (solid lines)*. For the latter model, the 8 000 K and 12 000 K models used to obtain the mass-radius relation at the observed temperature are also shown. The diagonal solid and dashed lines depict the observed range* (1σ) *in surface gravity* ($\log g = 6.44 \pm 0.20$ *cgs, with* $g = GM/R^2$)*. The horizontal solid and dashed lines indicate the white-dwarf radius determined using the distance of NGC 6752. The filled light grey area depicts the region excluded by the* 2σ *lower limit on the white-dwarf mass* ($M_{\rm WD} > 0.166\,M_\odot$) *that was derived from the pulsar mass-function and the observed mass ratio.*

while the models of Serenelli et al. (2002) give $M_{\rm WD} = 0.175 \pm 0.002\,{\rm M}_\odot$. The mass-radius relation by Panei et al. (2000) and the evolutionary models by Driebe et al. (1998) do not reach these radii and provide no mass estimate. The surface gravity that corresponds with these masses and radii is about $\log g = 6.20$ cgs. Both the white-dwarf radius and the surface gravity are slightly outside the 1σ range of these values inferred from the spectrum (see Fig. 5.6). Because of the steepness of the mass-radius relations, the masses are in agreement. We do note that if the pulsar binary is at the distance of NGC 6752, the white-dwarf mass is slightly below our best estimate for the minimum mass, though they are consistent with the 2σ limit.

If the pulsar binary is associated with NGC 6752, the progenitor of the white dwarf must have evolved from a cluster star. Serenelli et al. (2002) computed white-dwarf cooling tracks for objects with sub-solar metallicities. Their $Z = 0.001$ models have a metallicity that is similar to that of NGC 6752 ([Fe/H]= -1.43 ± 0.04; Gratton et al. 2003), and for this reason, we use the corresponding mass estimate as the best value for the white-dwarf mass. To take into account the uncertainty in the white-dwarf mass-radius relation, we add $0.010\,\mathrm{M}_\odot$ in quadrature to the uncertainty in the mass. In summary, under the assumption that the binary system is a member of NGC 6752, we infer a radius of $R_{\mathrm{WD}} = 0.058 \pm 0.004\,\mathrm{R}_\odot$ and a mass of $M_{\mathrm{WD}} = 0.175 \pm 0.010\,\mathrm{M}_\odot$.

5.4.6 Pulsar mass

As for the white dwarf, we can determine a minimum mass for the pulsar from the mass ratio and the constraint that the inclination i is less than or equal to 90°. The white-dwarf mass-function is $f(M_{\mathrm{WD}}) = M_{\mathrm{PSR}}^3 \sin^3 i/(M_{\mathrm{WD}} + M_{\mathrm{PSR}})^2 = K_{\mathrm{WD}}^3 P_{\mathrm{b}}/(2\pi G) = 1.072 \pm 0.108\,\mathrm{M}_\odot$, which can be written to give $M_{\mathrm{PSR}} \sin^3 i = (1 + 1/q)^2 f(M_{\mathrm{WD}})$. With $\sin i \leq 1$, this yields a 1σ lower limit to the pulsar mass: $M_{\mathrm{PSR}} > 1.24\,\mathrm{M}_\odot$. The 2σ limit is $M_{\mathrm{PSR}} > 1.10\,\mathrm{M}_\odot$. These limits are model independent, as they only depend on three observables; the projected semi-major axis of the pulsar orbit $a_{\mathrm{PSR}} \sin i$ and the orbital P_{b}, as determined from pulsar timing, and the white-dwarf velocity amplitude K_{WD}, that we obtained from our spectroscopic observations.

In Fig. 5.7, we show the constraints set by the mass ratio and the two white-dwarf mass determinations. It is clear that a large part of the range allowed by these constraints is excluded by the pulsar mass function. As a result, the most probable value for the pulsar mass and the uncertainties on it are not normally distributed. Instead, we determined these values via a Monte Carlo error propagation method. For a million trial evaluations, values for P_{b}, $a_{\mathrm{PSR}} \sin i$, K_{WD} and M_{WD} were randomly drawn from Gaussian distributions with the appropriate means and widths to obtain the corresponding pulsar mass. Solutions that had $\sin i > 1$ were excluded. From the resulting distribution of solutions the most probable value for and the uncertainties on the pulsar mass were determined.

For a white-dwarf mass of $M_{\mathrm{WD}} = 0.18 \pm 0.02\,\mathrm{M}_\odot$, the mass of the pulsar is constrained to $M_{\mathrm{PSR}} = 1.40^{+0.16}_{-0.10}\,\mathrm{M}_\odot$ at 68% confidence. For the case that the white dwarf is associated with the globular cluster, the allowed range in pulsar mass is smaller, $1.34 \pm 0.08\,\mathrm{M}_\odot$ at 68% confidence. The uncertainties corresponding to 95% confidence are in both cases twice as large.

5.5 Discussion and conclusions

We have unambiguously identified the companion to PSR J1911−5958A as a Helium-core white dwarf and determined its mass. Together with the measurement of the mass-ratio of the binary, we obtain constraints on the pulsar mass. However, before we discuss our results, we compare our results to those presented by Cocozza et al. (2006).

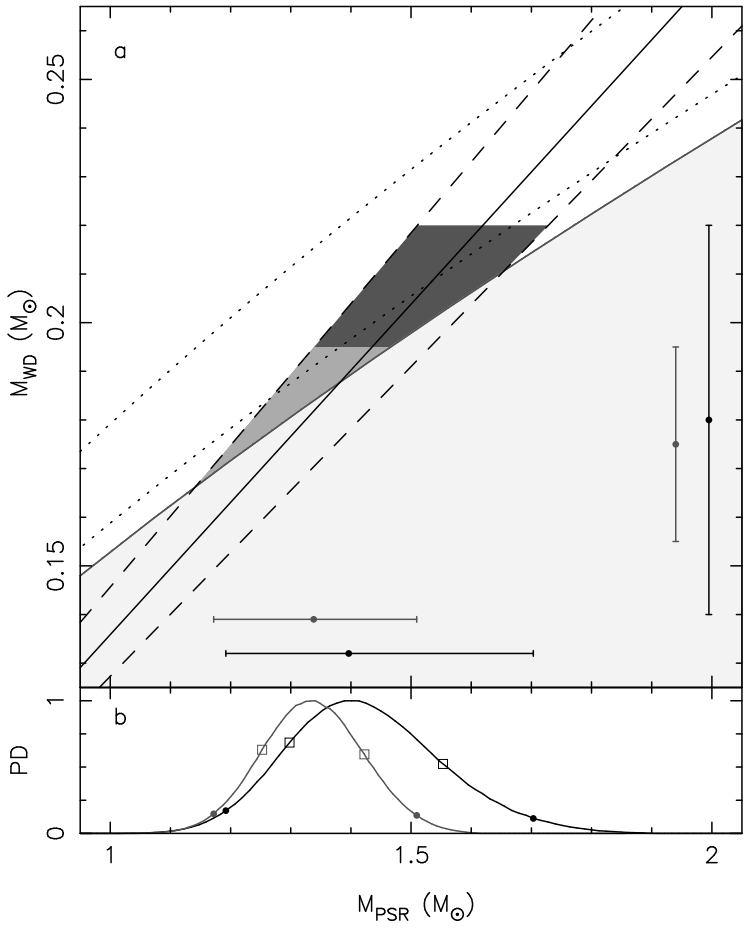

Figure 5.7: *The various constraints on the mass of PSR J1911−5958A. Panel **a** shows the constraint set by the mass ratio as the diagonal solid and dashed black lines. The large filled light grey area is excluded by the mass-function of the pulsar, as points in this area would require* $\sin i > 1$. *The line that borders this area is for the limit* $i = 90^\circ$ *in the pulsar mass-function. The two dotted lines depict inclinations of* $i = 75^\circ$ *(lower line) and* $i = 60^\circ$ *(upper line). Two pairs of vertical error bars on the right-hand side of the panel represent the two white-dwarf mass estimates and their uncertainties, where the larger error bar is for the mass determined from the surface gravity and effective temperature, whereas the smaller error bar is from the assumption that the binary is a member of NGC 6752. Allowed values for the pulsar mass exist in the light grey region for a white dwarf associated with NGC 6752, and the light and dark grey area for a white dwarf not associated with the globular cluster. The resulting pulsar masses, based on the Monte Carlo simulation, are indicated with the horizontal error bars. The uncertainties on the white-dwarf mass, pulsar mass, mass ratio and the mass-function are all 95% confidence (*2σ*). The probability densities as a function of pulsar mass are shown in panel **b**. The 68% and 95% confidence uncertainties based on these distributions are denoted by the open squares and the filled circles, respectively.*

Cocozza et al. found that the light-curve of the white dwarf companion to PSR J1911−5958A showed two phases of brightening by about 0.3 mag, located approximately at the quadratures of the orbit (phases $\phi = 0.0$ and $\phi = 0.5$). This result is at odds with our light-curve, which excludes variations larger than 0.02 mag. Fig. 5.3 shows a reproduction of the light-curve determined by Cocozza et al. (2006). This figure also shows the variation in the seeing under which these images were obtained; one sees that these closely follow the variations in the white-dwarf magnitude found by Cocozza et al. (2006). This suggests that seeing affects their photometry and that the variations they measure are due to variations in the seeing and not due to variations in the white-dwarf brightness. We found that we could reproduce their light-curve by defining the PSF over an area smaller than about $3\farcs1$ in radius. This distance corresponds to the distance between star R and the white dwarf, and if the PSF radius is chosen smaller than this value, flux in the wings of star R is not removed and added to the flux of the white dwarf. Hence, the effect increases for increasing seeing. We used a PSF radius that extends up to $4''$ from the center of each star and is still 2.5× larger than the width of the PSF in the images of the worst seeing. As such, our photometry is not affected by this error and excludes the 0.3 mag variations seen by Cocozza et al. (2006).

The radial-velocity curve of the white dwarf companion to PSR J1911−5958A is also presented in Cocozza et al. (2006). Their radial-velocity amplitude $K_{\rm WD}$ and systemic velocity γ are consistent with the values we found using the uncorrected velocities. We note that the uncertainty on our value for $K_{\rm WD}$ is about a factor two smaller. We believe this is caused by the fact that we used nine Balmer lines (Hβ up to H12) whereas Cocozza et al. (2006) only used four (Hβ up to Hϵ). Especially since the higher Balmer lines are narrower they will provide more accurate velocities. Cocozza et al. (2006) use their measurement of the systemic velocity of the pulsar binary ($\gamma = -28.1 \pm 4.9\,{\rm km\,s^{-1}}$) as an argument supporting the association of PSR J1911−5958A with NGC 6752. However, as Cocozza et al. (2006) did not correct for the systematic shifts in the wavelength scale that we identified and corrected for (see Appendix 5.7), their conclusion regarding the association between the binary and the cluster is meaningless.

We now turn to the conclusions that can be drawn from our results. In Appendix 5.7 we have used the available constraints set by our observations to test whether PSR J1911−5958A is associated with the globular cluster NGC 6752. Unfortunately, these tests are not conclusive and hence, we discuss both pulsar mass determinations below.

First, it is interesting to compare the mass of the white dwarf with the mass predicted by the theoretical relation between the white-dwarf mass and the orbital period (Joss et al. 1987). For short orbital periods, this relation is least secure, since mass transfer starts before the companion has a well-developed core (Ergma et al. 1998). Nevertheless, from earlier systems it seemed that the predictions by Tauris & Savonije (1999), which are strictly valid only for $P_{\rm b} > 2$ d, work well for binaries with orbital periods as short as 8 h (see Fig. 2 in van Kerkwijk et al. 2005). At the orbital period of PSR J1911−5958A, their relation predicts a white-dwarf mass between 0.18 and 0.20 $M_\odot$. This is again in very good agreement with our white-dwarf mass measurement (independent of whether the pulsar binary is associated with the globular cluster).

Binary evolution furthermore predicts that the progenitors of white dwarfs in low-mass

binary millisecond pulsars have lost $\gtrsim 0.6\,M_\odot$ of matter in order to form a $\sim 0.2\,M_\odot$ helium-core white dwarf. It is believed that at least a part of this matter is accreted onto the neutron star in order to spin it up to millisecond periods. As such, the neutron stars in low-mass binary pulsar systems are expected to be heavier than the canonical neutron star of $1.35 \pm 0.04\,M_\odot$ (Thorsett & Chakrabarty 1999).

For the case that PSR J1911−5958A is a field system, the mass of the pulsar ($M_{\rm PSR} = 1.40^{+0.16}_{-0.10}\,M_\odot$) is indeed heavier than the canonical value, though not by much. However, similarly small differences have been found for several of the other low-mass binary millisecond pulsars for which masses have been determined; PSR J1713+0747, $1.3 \pm 0.2\,M_\odot$ (Splaver et al. 2005), PSR J1909−3744, $1.438 \pm 0.024\,M_\odot$ (Jacoby et al. 2005), PSR J0437−4715 with $1.58 \pm 0.18\,M_\odot$ (van Straten et al. 2001), PSR B1855+09, $1.6 \pm 0.2\,M_\odot$ (Nice et al. 2005a) PSR J1012+5307, $1.6 \pm 0.2\,M_\odot$ (van Kerkwijk et al. 1996, 2005; Callanan et al. 1998). The only system for which the pulsar is significantly heavier than the $1.35\,M_\odot$ is PSR J0751+1807, with $2.1 \pm 0.2\,M_\odot$ (Nice et al. 2005b).

For the case that PSR J1911−5958A is associated with NGC 6752, the pulsar mass ($1.34 \pm 0.08\,M_\odot$) is consistent with the $1.35 \pm 0.04\,M_\odot$ found by Thorsett & Chakrabarty (1999) and is one of the least heavy neutron stars in low-mass binary millisecond pulsars. In this case, it is interesting to compare PSR J1911−5958A with PSR J0737−3039B, the 2.8 s non-recycled pulsar in the double pulsar system. If the mass of this pulsar ($1.250 \pm 0.005\,M_\odot$; Lyne et al. 2004) is indicative of the mass of a neutron star after is has been formed, it would only take less then $0.1\,M_\odot$ to recycle a normal neutron star to a millisecond pulsar spinning with a period of 3.26 ms.

Finally, our observations also constrain the inclination of the system. For the case that PSR J1911−5958A is not associated with NGC 6752, we have a 2σ limit of $\sin i > 0.923$ or $i > 67.^\circ4$. In the other case, $\sin i > 0.968$ and $i > 75.^\circ5$. Because of these high inclinations, the effects of Shapiro delay should be significant in the timing of the pulsar. Combined with our measurement of the white-dwarf mass, these limits on the inclination imply a Shapiro delay $\Delta_S > 5.7\,\mu$s. Unfortunately, for nearly circular orbits, the Shapiro delay is co-variant with the projected semi-major axis and the eccentricity, and a large part of the effect is absorbed in these two parameters. As a result, the effect that remains has a size of $\Delta_S{}' > 1.2\,\mu$s. Interestingly, if Shapiro delay is present, but neglected in the pulsar timing fit, it introduces an apparent eccentricity of $e > 1.3 \times 10^{-6}$ and places the longitude of periastron at $\omega = 90^\circ$. Though the small signal due to Shapiro delay may be difficult to detect, radio timing observations of PSR J1911−5958A may be used to obtain an upper limit on the inclination and the companion mass. For example, if $i = 85^\circ$, the timing signal due to Shapiro delay will be much larger, $\Delta_S = 11.2\,\mu$s and $\Delta_S{}' = 5.4\,\mu$s.

5.6 Appendix: Corrections to the wavelength calibration

First, according to the wavelength calibration of the different spectra, the wavelength of the O I λ5577 night sky emission line was offset from the laboratory value ($\lambda = 5577.34$ Å). The offsets varied over a range of 0.9Å or about $50\,{\rm km\,s^{-1}}$ and appeared to decrease with increasing hour angle, as shown in Fig. 5.8b. We believe this effect is the result of instrument flexure

due to differences in the pointing of the telescope, as the calibration frames are obtained with the telescope pointing towards the zenith, while the PSR J1911−5958A has $\sec z > 1.24$. We corrected for this effect by applying the measured offsets as a wavelength shift in the zero point of the wavelength calibrations of each individual spectrum.

However, as the O I λ5577 sky line lies redwards of the last arc line used for the wavelength calibration (Hg λ5460) we cannot verify that the polynomial used for the wavelength calibration is still valid at the wavelength of the skyline and that all systematic wavelength shifts are corrected for. We found, however, that the higher order terms of the polynomial are very similar between the calibration spectra extracted for the different stars; this is because the curvature of the calibration lines and the sky line at the positions of the stars is very small. As a result, we do not expect random effects to dominate the wavelength shift computed above, though the procedure may introduce a systematic wavelength shift affecting all spectra.

The second effect involved the centering of the stars on the 1.″31 slit. In general, when a star is not centered on the slit the offset of the star from the center of the slit will appear as a wavelength shift in the spectrum. This can clearly be seen by the velocities of star R and A in Fig. 5.8a, where the velocity of star A differs from that of star R by about 100 km s^{-1}; this is primarily due to the fact that compared to star R, star A is positioned closer to the right-hand (redwards) edge of the slit, see Fig. 5.1. Because of the magnitude of this effect, we determined the position of the reference star R with respect to the center of the slit from the through-the-slit images taken before and after the spectra. The positions on the 'before' images varied over a range of 0.68 pixels, whereas those on the 'after' images varied over 1.81 pixels. Interestingly, the 'after' positions with negative hour angles displayed positive shifts (redwards in wavelength) whereas those with positive hour angles displayed negative shifts. Fig. 5.8c shows these trends. We interpret the variations in centering of the reference star R on the 'before' images as simple scatter inherent to the centering of a star on the slit. The centering variations on the 'after' images clearly has a different cause, given its dependence on the hour angle. It may be that this is also related to flexure or differential atmospheric refraction. The averaged affect introduces the scatter in the velocities of the stars on the slit (Fig. 5.8a) and affects all stars in the same way.

To correct for this effect, we computed the position $\bar{x}_i$ of star i (in pixels) with respect to the center of the slit and applied it as a shift in wavelength in the zeropoint of the wavelength calibrations of each individual spectrum. The position is computed from $\bar{x}_i = \int_{-w/2}^{w/2} x\, \psi_{\rm PSF}(x - x_{\rm R} - \Delta x_i)\, {\rm d}x$, where $\psi_{\rm PSF}$ is the normalized point-spread function, as determined from fitting a Moffat function to the spatial stellar profile. Furthermore, $x_{\rm R}$ is the average of the 'before' and 'after' shifts in the position of the reference star R with respect to the center of the slit and w is the slit width (in pixels). Finally, Δx_i is the offset between the position of the reference star R and star i, measured in pixels in the dispersion direction. These offsets were computed from the five combined 360 s B-band exposures used for the photometry.

The resulting radial velocities of the pulsar companion and the other stars on the slit, corrected to the solar-system barycenter, are given in Table 5.2. The velocity of the reference star R now only varies over a range of 30 km s^{-1}, with an rms scatter of 11 km s^{-1}, comparable to the errors on the velocities tabulated in Table 5.2. For stars A, B, C, and D the rms scatter is

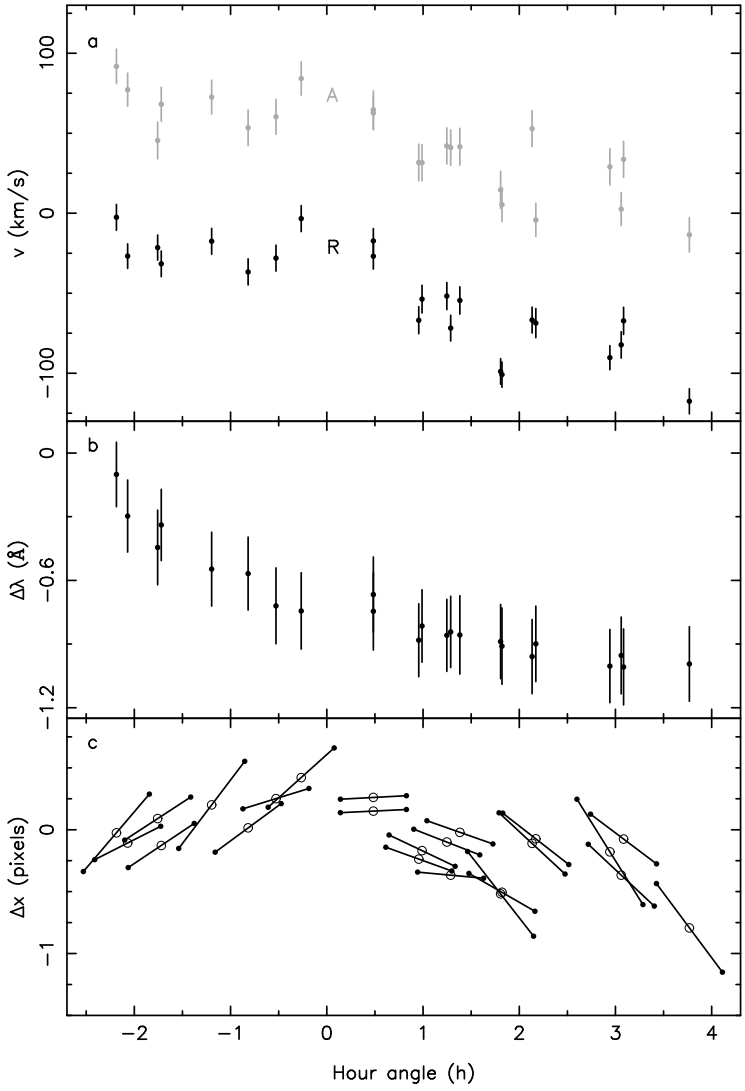

Figure 5.8: *The systematic effects that were present in the radial velocity study.* ***a*** *The uncorrected radial velocities of stars R and A as a function of hour angle. For both stars, the velocities decrease with increasing hour angle, while the scatter around the main trend is comparable for both stars.* ***b*** *The offset in the measured position of the* O I *λ*5577 *sky line compared to the laboratory value.* ***c*** *The centering of star R on the slit, as measured from the 'before' and 'after' through-the-slit images. Each line connecting the two black dots correspond to a single spectrum, where the left dot is the position determined in the 'before' image, and the right-hand dot the position in the 'after' image. The open circle is the average of the two positions in hour angle and pixel shift.*

comparable or somewhat larger, with 10, 50, 32 and 13 km s^{-1}, respectively. The large scatter in the radial velocities of star B is likely caused by secondary light from the two nearby stars (see Fig. 5.1), where variations in the seeing lead to shifts in the center of light in the dispersion direction, which in turn leads to velocity shifts. Therefore, we have not used star B in the further analysis.

The stars on the slit have systemic radial velocities of $\gamma_R = 8 \pm 2$ km s^{-1}, $\gamma_A = 7 \pm 2$ km s^{-1}, $\gamma_C = 30 \pm 2$ km s^{-1} and $\gamma_D = 6 \pm 2$ km s^{-1}. It is unexpected that all these stars have systemic velocities that are different from the radial velocity of the globular cluster NGC 6752 (-32.0 ± 1.6 km s^{-1}; Dubath et al. 1997), especially as all stars, except star C, have colours that place them on the narrow cluster main sequence in Fig. 5.2. Since star R, A and D have very similar systemic velocities, we conclude that these stars are cluster members, but that their velocities are off by -39 ± 3 km s^{-1}. We suspect that this systematic shift may have been introduced by the correction that we applied using the night-sky emission line. As this sky line was located redwards of the reddest wavelength calibration line, the polynomial could have introduced this systematic shift. However, as mentioned above, we do not expect that this influences relative velocities between different observations and different stars, since the shape of the polynomial did not vary between the different observations.

The one remaining issue is that of the systemic radial velocity of star C, which is different from that of the other stars. Star C may not be a cluster member, as it does not coincide with the cluster main sequence. Furthermore, its spectral features, as displayed in Fig. 5.9, are distinct from those of the other stars. In this figure, the normalized spectra of the stars are sorted in order of increasing V-band magnitude, so that when the stars are cluster members their spectra should be ordered on spectral type and their spectral features should change accordingly. Approximate spectral types for these stars were determined by comparing the spectra to those in the atlas of Le Borgne et al. (2003). We see that both the spectral features and the spectral type of star C show more resemblance with that of star D than they do to star R or A. From this we conclude that star C is not a cluster member and therefore its radial velocity may differ from that of the cluster.

5.7 Appendix: Is the binary associated with NGC 6752?

We use our observations and the properties of the white dwarf and the pulsar that we derived from them, to test if these support the assumption that PSR J1911−5958A is a member of the globular cluster NGC 6752.

If the pulsar binary is a member of the globular cluster, the systemic radial velocity of the binary should be compatible with the radial velocity of the cluster, -32.0 ± 1.6 km s^{-1} (Dubath et al. 1997).

The absolute systemic velocity of the pulsar binary is $\gamma = -18 \pm 6$ km s^{-1}. This differs from the radial velocity of the cluster by 14 ± 6 km s^{-1} and is consistent with the systemic velocity of the binary $\gamma_{\Delta\nu} = 13 \pm 6$ km s^{-1} which we determined from the fit of the white dwarf velocities relative to those of star R.

The velocity difference needs to be corrected for the gravitational redshift of the white dwarf and the reference star R. Using the mass and radius of the white dwarf determined in

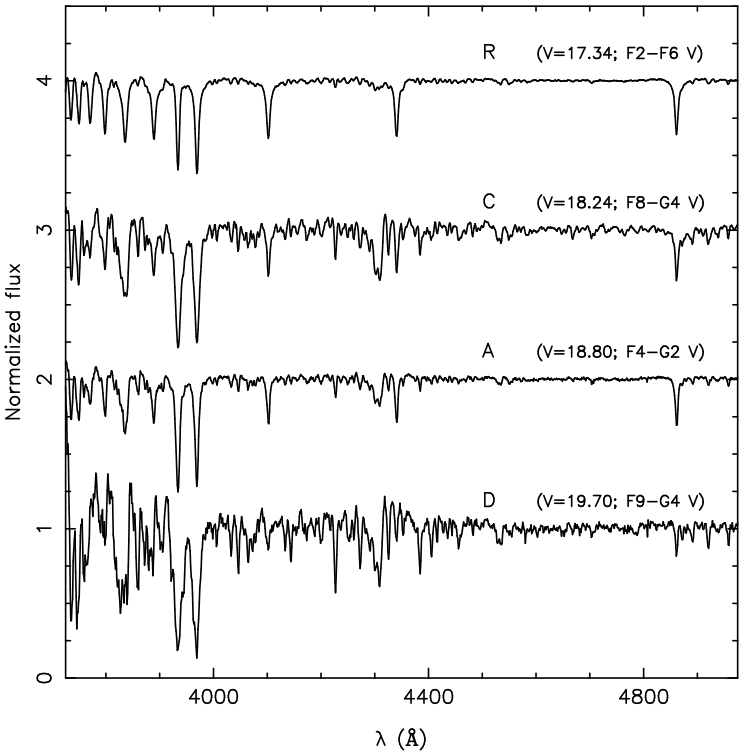

Figure 5.9: *Normalized spectra of the stars on the slit. The spectra are ordered from the star with the lowest V-band magnitude, star D, to the brightest, star R. Each consecutive spectrum is shifted by one unit.*

Sect. 5.4.3, and the mass and radius of star R determined from the its absolute magnitude and the models by Girardi et al. (2000) plotted in Fig. 5.2; we obtain 2.7 km s^{-1} and 0.5 km s^{-1} for the white dwarf and star R, respectively. This reduces the velocity difference to 11 ± 6 km s^{-1}, amounting to about a 2σ difference between the velocity of the binary and the velocity of the cluster. A part of this velocity difference may be due to the dispersion in the velocity between the pulsar binary and the reference star R. From the scatter in the velocities of stars R, A and D, we estimate that the velocity dispersion is of the order of ~ 2 km s^{-1}.

Also important is the local escape velocity at the pulsar position relative to the cluster center. To estimate the escape velocity $v_{\rm esc} = 2GM/r$ at the projected distance $r_\perp$ of PSR J1911−5958A, we compute the mass $M(r_\perp)$ inside a sphere of radius $r_\perp$ using relation A3 from the simplified cluster model presented in the Appendix of Freire et al. (2005). Here, we used a core-radius of $r_{\rm c} = 6\farcs7$ (Lugger et al. 1995), a distance of $d = 4.14$ kpc (Gratton et al. 2003), a central velocity dispersion of $\sigma_z(0) = 4.5$ km s^{-1} (Dubath et al. 1997) and $r_\perp = 6\farcm37$ to obtain $M(r_\perp) = 27 \times 10^3\,{\rm M}_\odot$ and $v_{\rm esc} = 5.7$ km s^{-1}. This velocity should be regarded as an upper limit since only the projected distance to the cluster center is known

and not the actual distance $r^2 = r_\perp^2 + r_\parallel^2$, with $r_\parallel$ the distance along the line-of-sight towards NGC 6752.

We conclude that, taking into account the velocity range expected due to the velocity dispersion and the escape velocity, the systemic velocity of PSR J1911−5958A is only marginally consistent (at the 2σ level) with the radial velocity of NGC 6752.

From Sect. 5.4, we found that the white-dwarf radius determined from the effective temperature and surface gravity is outside the 1σ uncertainty on the radius derived if the white dwarf is assumed to be at the distance of NGC 6752. This suggests that the pulsar binary is not a member of the globular cluster. There may be additional uncertainties in some of the parameters that were used. Here we discuss some of the sources of uncertainty that may explain the discrepancy in the white-dwarf properties.

As a result of the discrepancy in the white-dwarf radius, there is a discrepancy in the distance to the white dwarf. The distance modulus $(m - M)_V = 12.66 \pm 0.46$ derived from the combination of the atmospheric properties of the white dwarf and the mass-radius relation (Sect. 5.4.4) is only marginally consistent with the distance modulus $(m-M)_V = 13.24 \pm 0.08$ (Gratton et al. 2003) determined for NGC 6752. Though there is a considerable spread in the distance modulus measurements, ranging from $(m - M)_V = 13.17 \pm 0.13$ ($d = 4.0 \pm 0.3$ kpc) from white-dwarf cooling sequence fitting (Renzini et al. 1996), to $(m - M)_V = 13.32 \pm 0.04$ ($d = 4.31 \pm 0.08$ kpc) from main-sequence fitting (Carretta et al. 2000), no distance determination places NGC 6752 so close. Similarly, the spread in reddening measurements, $E_{B-V} = 0.035$ to 0.046 (Gratton et al. 2003, 2005), does not help to explain the radius discrepancy.

It also seems unlikely that our photometry is in error by as much as the 0.6 mag or more needed to match the distance and hence the white-dwarf radius. Our *UBV* magnitudes are consistent with those given by Ferraro et al. (2003a), but have significantly smaller uncertainties. The presence of photometric *B* and *V* standards on the science images removed any uncertainties on the airmass dependence. Also, the *B*-band calibrations taken on two different nights were consistent with each other, having only a 0.01 mag difference. Finally in Sect. 5.2.2, we found that the white-dwarf companion is not variable (down to 0.02 mag) and this eliminates the possibility that the *UBV* photometry was taken at an extremum in white-dwarf brightness.

As was found in Sect. 5.4.2, a lower surface gravity, which would imply a lower mass and a larger radius, was found when the spectral resolution was decreased to 6.5 Å. Though this is considerably larger than the 4.5 Å determined from the width of the lines in the spectrum of star R, the Balmer lines in the spectrum of the white dwarf may be broadened. In order to broaden the lines from 4.5 Å to 6.5 Å a velocity smearing of ~ 300 km s^{-1} is required.

One source of broadening is due to the fact that in a single observation, the 2470 s exposure time covers about $\Delta\phi = 3.5\%$ of the 20 h orbit. This introduces a maximum change in velocity (at $\phi = 0.25$ and $\phi = 0.75$) of about $2\pi\Delta\phi K_{\rm WD} \simeq 50$ km s^{-1}, which is much less than required[1].

Another source of broadening could be due to rotation. To estimate the rotational veloc-

[1] It also causes a reduction in inferred radial-velocity amplitude by a factor $\sin(\pi\Delta\phi)/\pi\Delta\phi = 0.998$. This is sufficiently small that we have chosen to ignore it.

ity of the white dwarf, we follow the reasoning used in van Kerkwijk & Kulkarni (1995) to explain the variations seen in the spectrum of the white-dwarf companion to PSR B0655+64. During the period of mass transfer, the progenitor of the white dwarf, a giant, filled its Roche lobe and tides ensured the system was synchronized and circularized. When mass transfer ceased and the pulsar companion started to contract to a white dwarf, the tides became inefficient and the rotational evolution of the companion was determined by conservation of angular momentum. Thus, the rotational periods scale inversely with the moments of inertia.

The moment of inertia of the progenitor can be separated in that of the core and the envelope; $I_{\rm prog} = I_{\rm core} + I_{\rm env}$ with $I_{\rm core} = k^2_{\rm core} M_{\rm core} R^2_{\rm core}$ and $I_{\rm env} = k^2_{\rm env} M_{\rm env} R^2_{\rm env}$, where k is the gyration radius. As the progenitor fills its Roche-lobe of radius $R_{\rm L}$, we have $R_{\rm env} = R_{\rm L}$. After mass transfer, when the envelope has contracted to form the white dwarf, the white dwarf has $I_{\rm WD} = k^2_{\rm WD} M_{\rm WD} R^2_{\rm WD}$. Assuming that $I_{\rm core} \approx I_{\rm WD}$ and ignoring differences in the gyration radii, conservation of angular momentum gives $\Omega_{\rm rot}/\Omega_{\rm orb} \simeq 1 + M_{\rm env} R^2_{\rm L} / M_{\rm WD} R^2_{\rm WD}$. Here, two assumptions lead to an overestimate of the spin up; the envelope will be more centrally concentrated than the white dwarf, such that $k_{\rm env} < k_{\rm WD}$, while tidal dissipation will be important in the initial stages of contraction. On the other hand, the hot core of the progenitor will be larger than the white dwarf, so $I_{\rm core} > I_{\rm WD}$ (though generally this effect should be small, since in most cases $I_{\rm core} \ll I_{\rm env}$).

For a white dwarf with a mass of 0.17–0.18 $M_\odot$ and a radius of 0.042–0.058 $R_\odot$, and for the observed mass ratio of $q = 7.36$ and orbital period of 20 h, the Roche-lobe radius of the progenitor is about $R_L = 0.96\,{\rm R}_\odot$. After cessation of mass transfer, the remaining envelope has a mass of about $0.01\,{\rm M}_\odot$. With these values we estimate that the rotational period of the white dwarf is about 20–30 times faster than the orbital period, so $P_{\rm rot} \approx 1$ to 0.6 h. In that case, the rotational velocity $v_{\rm rot} \sin i$ would be of the order of 50–100 km s^{-1}. This is smaller than the 300 km s^{-1} estimated above, and since our assumptions likely led us to overestimate the rotational velocity, it seems unlikely that rotational broadening alone could explain the discrepancy between the surface gravity inferred from the spectrum and that inferred from the radius assuming that PSR J1911−5958A is a member of NGC 6752.

D'Amico et al. (2002) give two arguments for the association of PSR J1911−5958A with NGC 6752. The first one is that it was discovered in an observation of a globular cluster: the dedicated globular cluster observations with Parkes together cover a relatively small area compared to the whole sky, and the detection of a rare millisecond pulsar in this area suggests membership of the cluster. The problem is that the dedicated cluster observations are much deeper than most other pulsar observations, and that the number of millisecond pulsars at the flux level of PSR J1911−5958A, 0.22 mJy at 1400 MHz, and their distribution on the sky, are not known. Estimates based on extrapolation are uncertain. The accuracy of the estimate by D'Amico et al. of a 10^{-5} probability for a chance coincidence is therefore not clear. D'Amico et al. (2002) used the center beam of the Parkes multibeam receiver in their discovery observation. The diameter of that beam is about 14′ (Manchester et al. 2001), and thus *any* pulsar detected in the globular cluster survey must lie within 7′ from the cluster center. We conclude that the argument from the probability of chance coincidence is less solid than the number 10^{-5} might suggest.

The second argument of D'Amico et al. (2002) is that PSR J1911−5958A has a dispersion

measure DM = 33.7 pc cm^{-3}, almost the same as the dispersion measure DM = 33.3 pc cm^{-3} of the three pulsars in the cluster core, two of which certainly belong to the cluster as proven by a negative period derivative. According to the Taylor & Cordes (1993) model, the maximum dispersion measure in the direction of NGC 6752 and PSR J1911−5958A is $\mathrm{DM_{max}} \approx 42\,\mathrm{pc\,cm^{-3}}$. Since the DM values of the pulsars in the core of NGC 6752 (and of PSR J1911−5958A) are less than this, the pulsar would be almost at the distance of the cluster. However, the maximum to the dispersion measure arises because the electron layer in our Galaxy has a finite scale height of 0.5 to 1 kpc, and this implies that all pulsars above the electron layer have the same dispersion measure in the same direction (Bhattacharya & Verbunt 1991). Since NGC 6752 is at a distance of $d = 4.14$ kpc and a Galactic latitude of $b = -25\overset{\circ}{.}6$, it is well above the electron layer, and its observed DM must be equated with the actual $\mathrm{DM_{max}}$ in that direction. (This is compatible with the uncertainty of about $\sqrt{4\mathrm{DM_{max}}}$ in the model value of $\mathrm{DM_{max}}$, which gives 13 pc cm^{-3} for $\mathrm{DM_{max}} \approx 42\,\mathrm{pc\,cm^{-3}}$; Nelemans et al. 1997). We conclude that the dispersion measure of PSR J1911−5958A does not prove that it is a member of the cluster, but merely that it is above the galactic electron layer, i.e., at a distance $d \gtrsim 2.4$ kpc.

Finally, we cannot discard the possibility that the white-dwarf models themselves are uncertain. This can already be seen from the mass-radius relations shown in Fig. 5.6. These relations are for the observed temperature of $T_{\mathrm{eff}} = 10090$ K, but, for a given mass of say, 0.20 $\mathrm{M_\odot}$, the predicted radii show a spread of about 0.01 $\mathrm{R_\odot}$.

A part of this problem is the lack of low-mass, helium-core white dwarfs for which accurate parameters have been determined and which could be used to calibrate the evolution, cooling and atmospheric properties of these systems.

Summarizing the results of this section, we see that, at face value, the systematic radial velocity and radius estimate indicates that PSR J1911−5958A is not a member of NGC 6752. Furthermore, we have argued that the similarity in dispersion measure for all all five pulsars located towards NGC 6752 does not necessarily imply that they are all at the same distance.

However, our observations do not conclusively rule out the membership of the pulsar and the globular cluster either. All constraints are consistent at the 2σ level, and the inconsistencies of the constraints may be removed when we take into account that there is an allowed range in radial velocity due to the velocity dispersion, that there may be broadening of the Balmer lines in the spectrum of the white dwarf and that there are possible uncertainties in the white-dwarf models themselves. As such, it is for future observations to decide between either possibility.

Chapter 6

Celestial position of the companion of PSR J1740−5340

C. G. Bassa, B. W. Stappers

Astronomy & Astrophysics 2004, 425, 1143–1145

Abstract We present optical astrometry of archival ground and space based imaging of the companion to PSR J1740−5340. The optical position of the companion is significantly offset from the timing position of the pulsar. We briefly investigate the effects of this inconsistency on other timing parameters and compare our position with an improved position of PSR J1740−5340 from recent, preliminary, timing results.

6.1 Introduction

In many ways, the binary millisecond pulsar PSR J1740−5340 (D'Amico et al. 2001b), located in the nearby (2.3 kpc) galactic globular cluster NGC 6397, is an exceptional system; it shows irregular eclipses over a wide range of orbital phases and it has the largest orbital period and the heaviest binary companion among all currently known eclipsing pulsars, including those in globular clusters[1]. An optical variable, discovered by Taylor et al. (2001), was identified as the pulsar companion by Ferraro et al. (2001) on the basis of positional coincidence with the timing position of the pulsar. These and later photometric and spectroscopic observations (Orosz & van Kerkwijk 2003; Kaluzny et al. 2003; Ferraro et al. 2003b) have revealed that both the brightness and the radial velocity of the companion vary with the orbital period and phase of the pulsar, unambiguously linking this star as the companion to PSR J1740−5340.

The observed pulsar period P and period derivative $\dot{P}$ give rise to a large spin-down luminosity, $L_{\rm SD} \propto \dot{P}/P^3 \approx 1.4 \times 10^{35}$ erg s^{-1} (D'Amico et al. 2001b), which is among the highest found for millisecond pulsars. Though part of the period derivative may not be intrinsic, due to accelerations in the potential of the globular cluster, the effects of irradiation of the companion by the pulsar would give rise to heating. No evidence of heating of the pulsar companion, at the level expected from the spin-down luminosity, are found (Orosz & van Kerkwijk 2003).

From accurate absolute optical astrometry of *HST*/WFPC2 observations of NGC 6397 we have found that the optical position of the companion of PSR J1740−5340 is inconsistent with the position of the pulsar D'Amico et al. (2001b). A preliminary timing solution (A. Possenti, priv. comm.) provides a celestial position that is in much better agreement with our optical position, but moreover, predicts a significantly different spin-down luminosity, now in agreement with the observed lack of heating of the pulsar companion.

6.2 Observations and data reduction

The method that was employed to determine the optical position of the companion of PSR J1740−5340 is similar to that described in Bassa et al. (2003b); we will focus on the differences. We used an archival 4 minute V-band exposure, obtained with the Wide Field Imager (WFI) at the ESO 2.2 m telescope at La Silla**,** during the night of May 14, 1999. A total of 248 stars from the UCAC2, the 2nd version of the USNO CCD Astrograph Catalog[2] (Zacharias et al. 2004), coincident with an $8' \times 8'$ subsection of the chip containing the cluster center, were selected for the astrometry and their positions were measured. Of these, 88 stars were not saturated and appeared stellar and unblended. An astrometric solution, fitting for zero-point position, scale and position angle, was computed and 6 outliers, having residuals in excess of $0\farcs25$, were iteratively removed. The final solution of 82 stars had rms residuals of $0\farcs068$ in both coordinates.

[1] For an up-to-date list, see http://www.naic.edu/~pfreire/GCpsr.html
[2] UCAC, http://ad.usno.navy.mil/ucac/

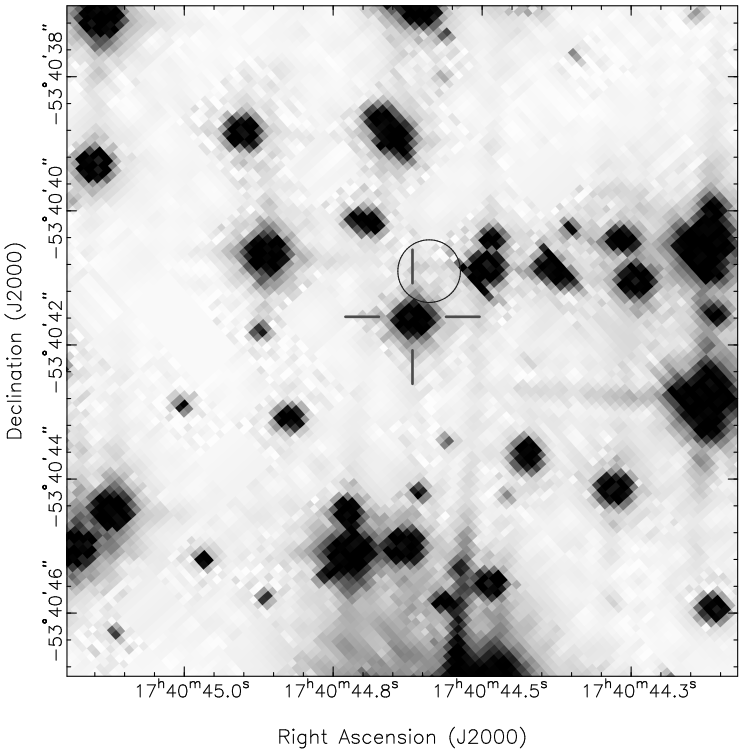

Figure 6.1: *A* $10'' \times 10''$ *subsection of a 249 s* V_{555} *image from the* HST/*WFPC2 GO5929 dataset. The 99% confidence level on the position of PSR J1740−5340 by (D'Amico et al. 2001b) is indicated with a circle. The radius of the circle is* $0\farcs47$ *and incorporates the uncertainties in the pulsar position, in the astrometric tie between the WFI and the UCAC2 and in the tie between the WFI and the* HST/*WFPC2 image. The position of the pulsar companion, as identified by Ferraro et al. (2001) is indicated with tickmarks (*$0\farcs5$ *in length).*

This solution was transferred to F555W (hereafter V_{555}) images of *HST*/WFPC2 datasets GO5929 and GO7335. As the pulsar companion is bright ($V_{555} = 16.9$), we only used 4 V_{555} images, with a total exposure time of 89 s, from both datasets. Positions of stars on these images were obtained with the HSTphot 1.1.5b package (Dolphin 2000b). We matched stars that were common to the *HST*/WFPC2 datasets and the WFI image and fitted for zero-point position, scale and position angle between the WFI pixel positions and the distortion corrected *HST*/WFPC2 master frame positions (Anderson & King 2003). Outliers were iteratively removed until the astrometric solution converged. The final astrometric solution contained 154 (190) stars, resulting in rms residuals of $0\farcs045$ ($0\farcs056$) in right ascension and $0\farcs050$ ($0\farcs061$) in declination for the GO5929 (GO7335) dataset.

The position of the optical companion to PSR J1740−5340 in the WFI image and the two *HST*/WFPC2 datasets is given in Table 6.1 while Fig. 6.1 shows a finding chart. The

Table 6.1: *Celestial position of the companion to PSR J1740−5340.*

Dataset	Date (UT)	α_{J2000}	δ_{J2000}
WFI	May 14, 1999	$17^h40^m44\overset{s}{.}611(10)$	$-53°40'41\overset{''}{.}57(9)$
GO5929	March 6–7, 1996	$17^h40^m44\overset{s}{.}617(9)$	$-53°40'41\overset{''}{.}58(8)$
GO7335	April 3, 1999	$17^h40^m44\overset{s}{.}617(10)$	$-53°40'41\overset{''}{.}62(9)$
Mean:		$17^h40^m44\overset{s}{.}615(8)$	$-53°40'41\overset{''}{.}59(7)$

uncertainty in the position of the companion in the WFI image is the quadratic sum of the uncertainty in the tie between the UCAC2 and the WFI and the positional uncertainty of the companion, about $0\overset{''}{.}06$. In the *HST*/WFPC2 datasets the positional uncertainty of the companion is much smaller, and hence the uncertainty is dominated by that of the tie between the UCAC2 and the WFI and that of the tie between the WFI and the *HST*/WFPC2 images.

The astrometry provided in the UCAC2 is on the Hipparcos system, i.e. the International Celestial Reference System (ICRS), on which the pulsar timing observations are based. Random positional uncertainties of the UCAC2 stars range from $0\overset{''}{.}020$ for 10 to 14th magnitude stars upto $0\overset{''}{.}070$ for 16th magnitude stars (Zacharias et al. 2004). These uncertainties are incorporated in the uncertainty in the tie between the UCAC2 and the WFI. A comparison of UCAC positions with the International Celestial Reference Frame (ICRF), the primary representation of the ICRS (Feissel & Mignard 1998), is presented in Assafin et al. (2003).

6.3 Discussion and conclusions

The timing position of PSR J1740−5340 as published by D'Amico et al. (2001b) is inconsistent with the optical position of the pulsar companion. The timing position, $\alpha_{J2000} = 17^h40^m44\overset{s}{.}589(4)$, $\delta_{J2000} = -53°40'40\overset{''}{.}9(1)$ (D'Amico et al. 2001b) is offset from the optical position by $-0\overset{''}{.}23(8)$ and $0\overset{''}{.}69(12)$ in right ascension and in declination, respectively. We attempted to use this position to fit simulated TOAs generated using the ephemeris of D'Amico et al. but found that even with quite large changes in the period derivative it was not possible to get a good fit of the TOAs. This indicated that there was perhaps something wrong with the existing timing solution.

Recent timing results, using a longer data span, also revealed the inconsistent position (A. Possenti, private communication). It was found that, as the radio signal of PSR J1740−5340 is eclipsed at phases far from inferior conjunction, the reliability of TOAs is hard to assess, and, as a result, the errors appeared more uncertain than those quoted in the D'Amico et al. (2001b) ephemeris. Improved astrometry (Possenti et al., in preparation) is in much better agreement with our optical position; a preliminary position by Possenti et al. (2005) is offset from the position of the companion by $0\overset{''}{.}13(7)$ in right ascension and $-0\overset{''}{.}16(9)$ in declination. Though still outside the 1σ errors the accurate optical position of the companion might aid future timing of PSR J1740−5340.

As a result of the change in position, the preliminary ephemeris (Possenti et al. 2005) has an updated pulse period derivative that is significantly different from that of D'Amico et al. (2001b). Hence, the spin-down luminosity of PSR J1740−5340 is decreased by over a factor

5; $L_{SD} \approx 3.3 \times 10^{34}$ erg s^{-1}. This value is in much better agreement with the lack of heating of the companion by the pulsar as expected by Orosz & van Kerkwijk (2003).

Chapter 7

The ultra-cool white dwarf companion of PSR J0751+1807

C. G. Bassa, M. H. van Kerkwijk, S. R. Kulkarni

Astronomy & Astrophysics 2006, 450, 295–303

Abstract We present optical and near-infrared observations with Keck of the binary millisecond pulsar PSR J0751+1807. We detect a faint, red object – with $R = 25.08 \pm 0.07$, $B - R = 2.5 \pm 0.3$, and $R - I = 0.90 \pm 0.10$ – at the celestial position of the pulsar and argue that it is the white dwarf companion of the pulsar. The colours are the reddest among all known white dwarfs, and indicate a very low temperature, $T_{\rm eff} \approx 4000$ K. This implies that the white dwarf cannot have the relatively thick hydrogen envelope that is expected on evolutionary grounds. Our observations pose two puzzles. First, while the atmosphere was expected to be pure hydrogen, the colours are inconsistent with this composition. Second, given the low temperature, irradiation by the pulsar should be important, but we see no evidence for it. We discuss possible solutions to these puzzles.

7.1 Introduction

Among the pulsars in binaries, the largest group, the low-mass binary pulsars, has low-mass white-dwarf companions. Before the companions became white dwarfs, their progenitors filled their Roche lobe and mass was transferred to the neutron stars, thereby spinning them up and decreasing their magnetic fields. Considerations of the end of this stage, where the white dwarf progenitor's envelope becomes too tenuous to be supported further, allow one to make predictions for relations between the orbital period and white dwarf mass, and orbital period and eccentricity (for a review, e.g., Phinney & Kulkarni 1994; Stairs 2004). Furthermore, after the cessation of mass transfer, two clocks will start ticking at the same time: the neutron star, now visible as a millisecond pulsar, will spin down, while the secondary will contract to a white dwarf and start to cool. Consequently, the spin-down age of the pulsar should equal the cooling age of the white dwarf.

From optical observations of white-dwarf companions to millisecond pulsars one can estimate the white-dwarf cooling age and compare it with the pulsar spin-down age. Initial attempts to do this (Hansen & Phinney 1998a,b; Schönberner et al. 2000) revealed a dichotomy in the cooling properties of white dwarfs in the sense that some white dwarf companions to older pulsars have cooled less than those of younger pulsars. In particular, the companions of PSR J0437−4715 (Danziger et al. 1993; van Straten et al. 2001) and PSR B1855+09 (van Kerkwijk et al. 2000; Ryba & Taylor 1991) have temperatures of about 4000–5000 K, with characteristic pulsar ages of 5 Gyr. This is in contrast to the companion of PSR J1012+5307 (Lorimer et al. 1995; van Kerkwijk et al. 1996; Callanan et al. 1998), which has a higher temperature (8600 K), while it orbits an older pulsar (8.9 Gyr).

A likely cause for this dichotomy is the difference in the thickness of the envelope of hydrogen surrounding the helium core of the white dwarf (Alberts et al. 1996). After the cessation of mass transfer, the white dwarfs have relatively thick ($\sim 10^{-2}\,M_\odot$) hydrogen envelopes which are able to sustain residual hydrogen shell-burning, keeping the white dwarf hot and thereby slowing the cooling (Driebe et al. 1998). The shell burning, however, can become unstable and lead to thermal flashes which can reduce the mass of the envelope. White dwarfs with such reduced, relatively thin ($\lesssim 10^{-3}\,M_\odot$) hydrogen envelopes cannot burn hydrogen and, as a result, cool faster. The transition between thick and thin hydrogen envelopes was predicted to lie near 0.18–0.20 $M_\odot$ (where heavier white dwarfs have thin envelopes; Alberts et al. 1996; Sarna et al. 2000; Althaus et al. 2001).

Until recently, PSR J1012+5307, with an orbital period $P_b = 0.60$ d, was the only system for which a thick hydrogen envelope was required to match the two timescales. Given the relation between the white dwarf mass and the orbital period (Joss et al. 1987; Rappaport et al. 1995; Tauris & Savonije 1999), companions in similar or closer orbits should have similar or lower mass, and thus have thick hydrogen envelopes as well. This was confirmed by the recent discovery of two new, nearby, binary millisecond pulsars with orbital periods similar to that of PSR J1012+5307; PSR J1909−3744 (1.53 d, Jacoby et al. 2005) and PSR J1738+0333 (0.354 d, Jacoby et al., in prep.; see van Kerkwijk et al. 2005 for preliminary results). For both, the temperatures and characteristic ages are similar to those of PSR J1012+5307, and thus one is led to the same need for a thick hydrogen envelope. These discoveries, combined

with the thin envelopes inferred for PSR J0034−0534 (1.59 d) and binaries with longer periods, suggest that the transition occurs at a mass that corresponds to an orbital period just over 1.5 d (van Kerkwijk et al. 2005). All systems with shorter orbital periods should have thick hydrogen envelopes.

The two known millisecond pulsars with white dwarf companions that have shorter orbital periods than PSR J1012+5307 but do not have optical counterparts, are PSR J0613−0200, with a 1.20 d period, and PSR J0751+1807, which has the shortest orbital period of all binary millisecond pulsars with $M_c > 0.1\,M_\odot$ companions, 0.26 d (Lundgren et al. 1995). The latter system is of particular interest because the companion mass has been determined from pulse timing ($M_{WD} = 0.19 \pm 0.03\,M_\odot$ at 95% confidence; Nice et al. 2005b), so that one does not have to rely on the theoretical period-mass relationship. Intriguingly, for PSR J0751+1807, optical observations from Lundgren et al. (1996) set a limit to the temperature of 9000 K, which is only marginally consistent with it having a thick hydrogen envelope. Based on this, Ergma et al. (2001), suggested the hydrogen envelope may have been partially lost due to irradiation by the pulsar.

The faintness of the companion to PSR J0751+1807 aroused our curiosity and motivated us to obtain deep observations to test the theoretical ideas discussed above. We describe our observations in Sect. 7.2, and use these to determine the temperature, radius and cooling history in Sect. 7.3. In Sect. 7.4, we investigate irradiation by the pulsar, finding a surprising lack of evidence for any heating. We discuss our results in Sect. 7.5.

7.2 Observations and data reduction

The PSR J0751+1807 field was observed with the 10 meter Keck I and II telescopes on Hawaii on five occasions. On December 11, 1996 the Low Resolution Imaging Spectrometer (LRIS, Oke et al. 1995) was used to obtain *B* and *R*-band images, while the Echellette Spectrograph and Imager (ESI, Sheinis et al. 2002) was used on December 21, 2003 to obtain deeper *B* and *R*-band, as well as *I*-band images. The *R*-band filter used that night was the non-standard "Ellis *R*" filter. The observing conditions during the 1996 night were mediocre, with 0.″8–1.″1 seeing and some cirrus appearing at the end of the night. The conditions were photometric during the 2003 night, and the seeing was good, 0.″6–0.″8. The third and fourth visit were with LRIS again, now at Keck I, on January 7 and 8, 2005. The red arm of the detector was used to obtain *R*-band images. The seeing on the first night in 2005 was rather bad, about 1.″5 and improved to about 1.″0 on the second night. The conditions on these nights were not photometric. Finally, a series of 36 dithered exposures, each consisting of 5 co-added 10 s integrations, were taken through the K_s filter with the Near Infrared Camera (NIRC; Matthews & Soifer 1994) on January 26, 2005. The conditions were photometric with 0.″6 seeing. Standard stars (Landolt 1992; Stetson 2000) were observed in 1996 and 2003, while a 2MASS star (Cutri et al. 2003) in the vicinity of PSR J0751+1807 was observed to calibrate the NIRC data. A log of the observations is given in Table 7.1.

The images were reduced using the Munich Image Data Analysis System (MIDAS). The *BRI* images were bias-subtracted and flat-fielded using dome flats. The longer exposures in each filter were aligned using integer pixel offsets, and co-added to create average images.

Table 7.1: *Observation log.*

Field	Time (UT)	Filter	$t_{\rm int}$ (s)	sec z
December 11, 1996, LRIS				
SA 95	08:23–08:25	R	2 + 10	1.07
	08:27–08:29	B	2 + 10	1.07
SA 95	09:28–09:31	B	2 + 10	1.07
	09:33–09:35	R	2 + 10	1.08
PSR J0751+1807	09:45	R	10	1.39
	09:47–09:59	R	2 × 300	1.36
	10:01	R	600	1.31
	10:13	B	600	1.26
December 21, 2003, ESI				
PSR J0751+1807	10:06–10:27	R	3 × 360	1.14
	10:29–10:57	I	6 × 240	1.08
	11:00–11:33	B	3 × 600	1.04
NGC 2419	11:40	B	10 + 30	1.06
	11:44	R	10 + 30	1.06
	11:47	I	10 + 30	1.06
January 7, 2005, LRIS				
PSR J0751+1807	11:54–12:53	R	5 × 600	1.05
January 8, 2005, LRIS				
PSR J0751+1807	11:42–12:51	R	6 × 600	1.05
January 26, 2005, NIRC				
PSR J0751+1807	08:06–08:56	$K_{\rm s}$	36 × 50	1.07
2MASS star[1]	08:59	$K_{\rm s}$	0.4	1.02

The near-infrared images were corrected for dark current using dark frames with identical exposure times and number of co-adds as those used for the science frames. Next, a flatfield frame was created by median combining the science frames. After division by this flatfield, the science frames were registered using integer pixel offsets and averaged.

7.2.1 Astrometry

For the astrometric calibration, we selected 14 stars from the second version of the USNO CCD Astrograph catalogue (UCAC2; Zacharias et al. 2004) that overlapped with the 10 s R-band LRIS image of December 1996. Of these, 11 were not saturated and appeared stellar and unblended. The centroids of these objects were measured and corrected for geometric distortion using the bi-cubic function determined by J. Cohen (1997, priv. comm.)[2]. We fitted for zero-point position, plate scale and position angle. The inferred uncertainty in the single-star measurement of these 11 stars is 0.″057 and 0.″083 in right ascension and declination, respectively, and is consistent with expectations for the UCAC measurements of approximately 0.″020 for stars of 14th magnitude and 0.″070 for stars 2 magnitudes fainter.

This solution was transferred to the 10 min R-band LRIS image using 91 stars that were present on both images and were stellar, unsaturated and not blended. Again the zero-point

[2] http://alamoana.keck.hawaii.edu/inst/lris/coordinates.html

position, plate scale and position angle were left free in the fit and the final residuals were 0.″016 and 0.″019 in right ascension and declination. The UCAC is on the International Celestial Reference System (ICRS) to $\lesssim 0.''01$, and hence the final systematic uncertainty with which our coordinates are on the ICRS is dominated by our first step, and is $\sim 0.''03$ in each coordinate.

Our images, with the position of PSR J0751+1807 (Nice et al. 2005b) indicated, are shown in Figure 7.1. On the 10 min LRIS *R*-band images from 1996 and 2005, we find a faint object, hereafter star X, at the position of the pulsar. It is also, though marginally, present in the two 5 min *R*-band images from 1996, but not detected in the 10 min *B*-band LRIS image of that observing run. Star X is clearly present in the 2003 ESI *R* and *I*-band images, and marginally in the *B*-band image. It is not detected in the near-infrared observations (Fig. 7.1).

Positions for star X and other objects inferred using the astrometry of the 10 min LRIS *R*-band image are listed in Table 7.2. The pulsar position at the time of the 1996 LRIS observation, using the Nice et al. (2005b) position and proper motion, is $\alpha_{\rm J2000} = 07^{\rm h}51^{\rm m}09^{\rm s}.1574(1)$, $\delta_{\rm J2000} = +18°07'38.''624(10)$. We find that star X is offset from the pulsar position by $-0.''01 \pm 0.''06$ in right ascension and $0.''04 \pm 0.''06$ in declination, well within the 1σ uncertainties (including those on the pulsar position). Given the low density of about 47 stars per square arcminute and the excellent astrometry, the probability of a chance coincidence in the 95% confidence error circle, which has a radius of 0.″24, is only 0.1–0.2%. Since, as we will see, it is hard to envisage how the companion could be fainter than the object detected, we are confident that star X is the companion of PSR J0751+1807.

7.2.2 Photometry

The DAOPHOT II package (Stetson 1987), running inside MIDAS, was used for the photometry on the averaged images. We followed the recommendations of Stetson (1987): instrumental magnitudes were obtained through point spread function (PSF) fitting and aperture photometry on brighter stars was used to determine aperture corrections.

For the calibration of the optical images, instrumental magnitudes of the standard stars, determined using aperture photometry, were compared against the values of Stetson (2000). We used the standard Keck extinction coefficients of 0.17, 0.11 and 0.07 mag per airmass for *B*, *R* and *I*, respectively. Colour terms were not required for the LRIS *B* and *R* bands, but were significant for the ESI bands: $0.107(B-R)$ for *B*, $0.083(B-R)$ for *R*, and $-0.004(R-I)$ for *I*, i.e., the ESI *B*, *R* are redder than the standard bands, while ESI *I* is slightly bluer. The root-mean-square residuals of the ESI calibrations are about 0.05 mag in *B*, and 0.03 mag in *R* and *I*, while those of the LRIS calibration are 0.08 mag in *B* and 0.05 mag in *R*; we adopt these as the uncertainty in the zero-points. The near-infrared observations were calibrated through aperture photometry with 1.″5 (10 pix) apertures using the 2MASS star, fitting for a zero-point only, as the difference in airmass between the science and calibration images is small. We adopt an uncertainty in the $K_{\rm s}$ zero-point of 0.1 mag.

Calibrated ESI magnitudes for star X and selected other stars in the field are listed in Table 7.2. Star X is barely above the detection limit of the ESI *B*-band observations, hence the large error. It is not detected in the LRIS *B*-band and the NIRC $K_{\rm s}$-band observations,

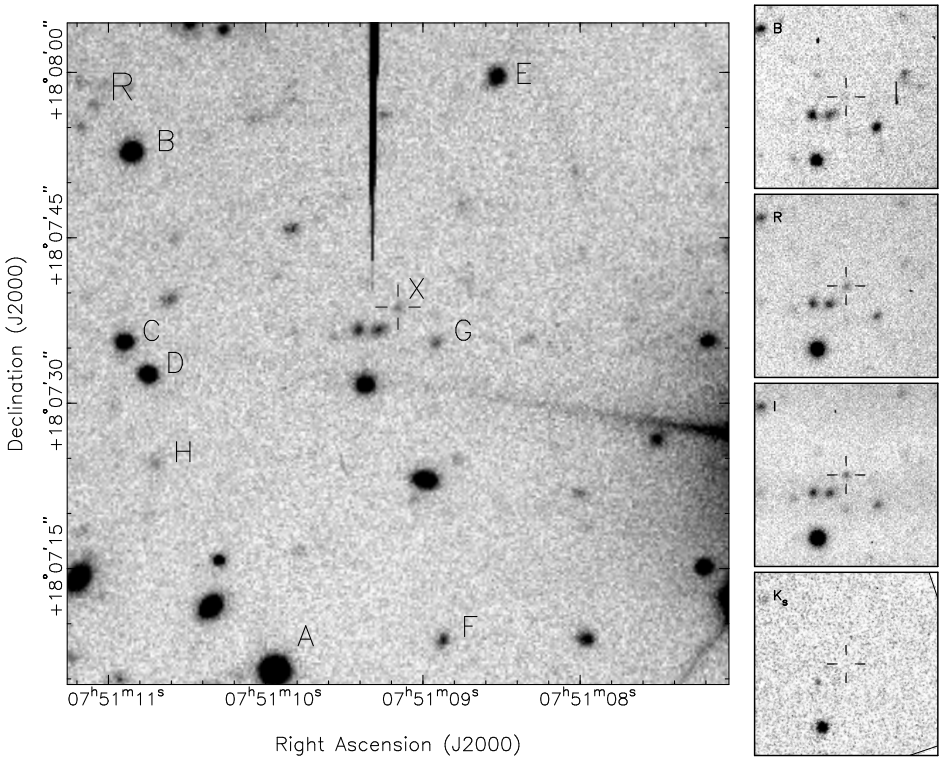

Figure 7.1: *Images of the field of PSR J0751+1807. The left-hand figure shows a* $1' \times 1'$ *subsection of the averaged* $6 \times 10\,m$ *R-band image obtained with LRIS on January 8, 2005. The right-hand four figures show* $20'' \times 20''$ *subsections of the B, R and I-band averages observed with ESI in 2003 and the* K_s*-band image observed with NIRC in 2005. The tick marks all have a length of* $1''$ *and are centered on the pulsar timing position.*

and, scaling from the magnitude of a star with a signal-to-noise ratio of about 10 and 6, we estimate the 3σ detection limits at $B = 26.8$ and $K_s = 21.3$, respectively. The former is consistent with the ESI detection. None of the stars in Table 7.2 are covered by the small $38'' \times 38''$ field-of-view of NIRC, hence we do not have near-infrared magnitudes for these.

The 1996 LRIS R-band magnitude is 25.13 ± 0.11, which is consistent with the ESI measurement. Since the conditions during the 1996 LRIS observations may not have been photometric, however, this may be a coincidence. To check for variability, we tied the instrumental LRIS R band magnitudes directly to the ESI R and I ones, using 38 stars that both images had in common and that had magnitude uncertainties below 0.1 mag. As expected given the non-standard "Ellis R" filter on ESI, we required a large colour term, $-0.302(R_{\rm inst} - I_{\rm inst})$, but with this the fit was adequate, with root-mean-square residuals of 0.14 mag. Compared to the fit, the ESI minus LRIS difference in R-band magnitude is insignificant, -0.03 ± 0.13 mag. Similarly, comparing instrumental R-band magnitudes from 2005 January 7 with those taken 2005

Table 7.2: *LRIS Astrometry and ESI photometry of the companion of PSR J0751+1807 and stars in the field. The nomenclature of the stars is according to Fig. 7.1. The uncertainties listed in parentheses are instrumental, i.e., they do not include the zero-point uncertainty in the astrometric tie (about 0.″03 in each coordinate) or of photometric calibration (0.05 mag in B and 0.03 mag in both R and I).*

ID	α_{2000}	δ_{2000}	B	R	I
X	$07^h51^m09^s.158(4)$	$+18°07'38''.66(6)$	27.56(25)	25.08(7)	24.18(7)
A	$07^h51^m09^s.933(1)$	$+18°07'05''.97(1)$	21.73(1)	19.30(1)	18.31(1)
B	$07^h51^m10^s.844(1)$	$+18°07'52''.91(1)$	22.80(1)	21.03(1)	20.32(1)
C	$07^h51^m10^s.891(1)$	$+18°07'35''.69(1)$	24.30(2)	21.81(1)	20.63(1)
D	$07^h51^m10^s.739(1)$	$+18°07'32''.79(1)$	24.28(6)	22.50(5)	21.99(6)
E	$07^h51^m08^s.519(1)$	$+18°07'59''.89(2)$	24.56(7)	22.87(5)	22.38(8)
F	$07^h51^m08^s.859(2)$	$+18°07'08''.83(3)$	24.94(4)	24.00(5)	23.29(4)
G	$07^h51^m08^s.908(4)$	$+18°07'35''.71(5)$	25.65(8)	24.51(5)	23.85(6)
H	$07^h51^m10^s.691(3)$	$+18°07'24''.69(6)$	25.69(7)	24.94(9)	24.34(8)

January 8 and 1996 December 11, fitting for an offset only, results in magnitude differences of 0.03 ± 0.07 and -0.16 ± 0.12 mag, respectively. Thus, no large variations in brightness are seen; we will see in Sect. 7.4 that this is somewhat surprising.

7.3 Temperature, radius, and cooling history

We use our observations of star X, the companion of PSR J0751+1807, to constrain its temperature, radius, and atmospheric constituents, and discuss our result that the white dwarf does not have the expected thick hydrogen envelope.

7.3.1 Colours, temperature, and atmospheric composition

We first use the colours of star X to constrain its temperature. The red colours are largely intrinsic, as the maximum reddening towards PSR J0751+1807 ($l = 202.73$, $b = 21.09$) is small, $E_{B-V} = 0.05 \pm 0.01$ (Schlegel et al. 1998). This value is consistent with the low value found for the interstellar absorption $N_H \sim 4 \times 10^{20}\,\mathrm{cm}^{-2}$, as estimated from *ROSAT* X-ray observations of PSR J0751+1807 by Becker et al. (1996). For comparison, the relation by Predehl & Schmitt (1995) predicts an $N_H \approx 3 \times 10^{20}\,\mathrm{cm}^{-2}$ for the above reddening. Given the distance of ~ 0.6 kpc (Nice et al. 2005b), we expect most of the reddening to be in the foreground to the pulsar. Hence, the dereddened colours are $(B-R)_0 = 2.40 \pm 0.27$ and $(R-I)_0 = 0.86 \pm 0.10$.

In Fig. 7.2a, we compare the intrinsic colours of star X with those of other white-dwarf companions of millisecond pulsars, other white dwarfs, and models. We find that the colours of star X are the reddest for any known millisecond pulsar companion or white dwarf. The pulsar companion that comes closest is that of PSR J0437−4715 ($B - R = 2.12 \pm 0.06$, $R - I = 0.56 \pm 0.02$ [Danziger et al. 1993] and negligible extinction[3]); the most similar white

[3] As inferred from the dust maps of Schlegel et al. (1998); Danziger et al. (1993) estimate $E_{B-V} = 0.07$ from the work of Knude (1979).

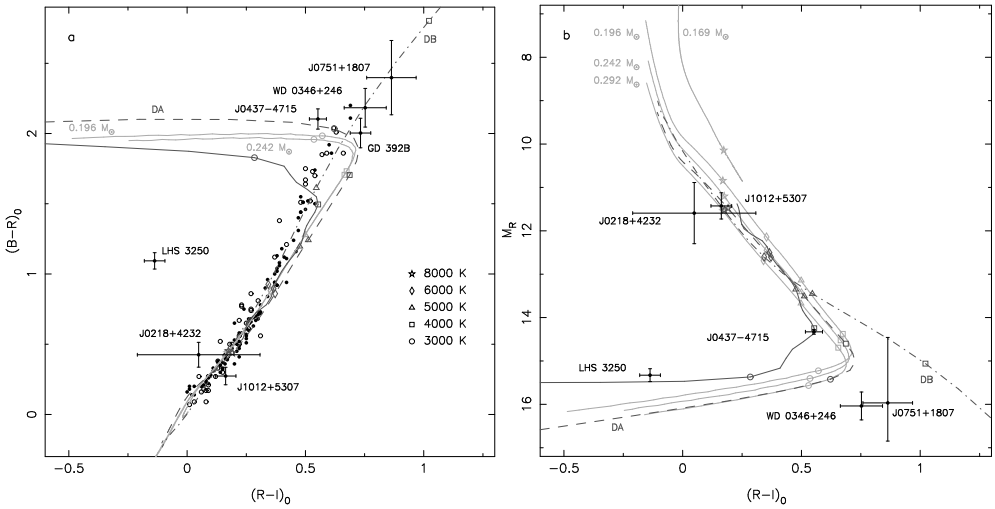

Figure 7.2: a *Colour-colour and* **b** *colour-magnitude diagram for the companion of PSR J0751+1807, other millisecond pulsar companions, field white dwarfs, and model predictions. Shown with error bars are PSR J0437−4715 (Danziger et al. 1993), PSR J1012+5307 (Lorimer et al. 1995), PSR J0218+4232 (Bassa et al. 2003a) and PSR J0751+1807 (this work), as well as the ultra-cool field white dwarfs LHS 3250 (Harris et al. 1999), WD 0346+246 (Oppenheimer et al. 2001), and GD 392B (Farihi 2004). In the colour-colour diagram, also the full sample of field white dwarfs of Bergeron et al. (2001) is shown, with filled and open circles indicating white dwarfs with and without Hα in their spectrum, respectively. For the colour-magnitude diagram, we used parallax distances where available and distances inferred from the pulsar dispersion measure otherwise; we omitted the Bergeron et al. sample because of the large scatter (even though it likely is largely intrinsic). In both panels, the continuous light grey lines depict helium-core white dwarf cooling models by Serenelli et al. (2001), with masses as indicated. The continuous dark-grey track is for a 0.2 $M_\odot$ model by B. Hansen (priv. comm.; see description in Hansen & Phinney 1998a). The dark-grey dashed and dashed-dotted lines are updates of the white dwarf models by Bergeron et al. (1995), for DA (hydrogen rich) and DB (helium rich) composition, respectively, both with* $\log g = 7$. *Temperatures for all models are indicated by different symbols along the track.*

dwarf is WD 0346+246 ($B - R = 2.2 \pm 0.1$, $R - I = 0.76 \pm 0.08$, Oppenheimer et al. 2001). Thus, star X is likely as cool or even cooler than the $T_{\rm eff} \simeq 3700$ K inferred for those two sources (PSR J0437−4715: Danziger et al. 1993; Hansen 2002, priv. comm.; WD 0346+246: Oppenheimer et al. 2001; Bergeron 2001).

Also shown in Fig. 7.2a are colours expected from model atmospheres of Serenelli et al. (2001) and of Hansen (2004, priv. comm.), which are specifically tailored to the low-mass, helium-core companions of millisecond pulsars, as well as those for updated low-gravity ($\log g = 7$), pure hydrogen atmosphere models of Bergeron et al. (1995). One sees that the colours of the companion of PSR J0437−4715, as well as those of the hotter companions of PSR J1012+5307 and J0218+4232, are consistent with these models. For star X, however,

the colours are not consistent, as the models never venture red-wards of $R - I \approx 0.7$ and $B - R \approx 2.0$.

The change in direction of the tracks is seen in all models for hydrogen-rich, metal-free atmospheres; it reflects a change in the dominant source of opacity, from bound-free absorption of H^- at higher temperatures to collision-induced absorption of H_2 at lower ones (Lenzuni et al. 1991; Saumon et al. 1994; Hansen 1998). The latter process is highly non-grey, and leads to absorption predominantly long-ward of the R-band. As a result, the $R - I$ colour becomes bluer with decreasing temperatures, while $B - R$ remains roughly constant.

Could star X have a different composition? Due to the high gravity of white dwarfs, metals settle out of the atmosphere. However, some white dwarfs have atmospheres dominated not by hydrogen, but by helium. For the latter, the opacity sources are all fairly grey, and hence the colours continue to redden with decreasing temperatures. Indeed, the colours of star X are consistent with the predictions of the updated $\log g = 7$ pure helium models after Bergeron et al. (1995) at $T_{\rm eff} \simeq 4200$ K (Fig. 7.2a).

From an evolutionary perspective, however, a pure helium atmosphere is not expected. Low-mass white dwarfs such as the companions to millisecond pulsars are all formed from low-mass stars whose evolution was truncated by mass transfer well before helium ignition (for recent models, see Tauris & Savonije 1999; Nelson et al. 2004). As a result, they should have helium cores surrounded by relatively thick, 0.01 to 1% of the mass, hydrogen envelopes (Driebe et al. 1998; Althaus et al. 2001). Indeed, among the low-mass white-dwarf companions to pulsars (van Kerkwijk et al. 2005) as well as among low-mass white dwarfs in general (Bergeron et al. 2001), only hydrogen-dominated atmospheres have been observed.

In principle, at low temperatures, the hydrogen envelope might become mixed in with the helium core. Even if fully mixed, however, the remaining amounts of hydrogen would strongly influence the spectrum. Indeed, the effects of collision-induced absorption *increase* with increasing helium abundance up to $N(\mathrm{He})/N(\mathrm{H}) \simeq 10^5$ (Bergeron & Leggett 2002).

From Fig. 7.2a, it is clear that the predictions for hydrogen-dominated atmospheres are also a somewhat poor match to the colours of the cooler normal white dwarfs with hydrogen in their atmospheres (as inferred from absorption at Hα, Bergeron et al. 2001; filled circles in the figure). For most, this appears to be due to missing blue opacity in the models (see Bergeron et al. 2001 for a detailed study); the visual through infrared fluxes are reproduced well by the models, and show unambiguously that collision-induced absorption by H_2 is important. Indeed, the absorption is evident in the optical colours of some objects, in particular LHS 3250 (shown in Fig. 7.2) and SDSS J133739.40+000142.8 (Bergeron & Leggett 2002 and references therein).

For our purposes, however, the case of the ultra-cool white dwarf WD 0346+246 is most relevant. For this source, the colours cannot be reproduced with either pure hydrogen or helium, but require a mixed atmosphere, dominated by helium (with fractional hydrogen abundances ranging from 10^{-9} to 10^{-1}, depending on assumptions about the contribution of other opacity sources; Oppenheimer et al. 2001; Bergeron 2001, though recent work puts these abundances in to doubt, P. Bergeron 2005, priv. comm.). For all cases, the temperature is around 3700 K. The similarity in the colours of WD 0346+246 and star X would suggest that star X has a similar, maybe slightly lower, temperature.

From the above, we find that we cannot determine the temperature of the companion of PSR J0751+1807 with certainty, since we do not know its composition. Most likely, however, it is somewhere between the temperature inferred for WD 0346+246 and that indicated by the (pure helium) models, i.e. in the range of, say 3500–4300 K.

A more stringent test could be provided by the near-infrared observations, as the $R-K$ colour (which is similar to $R-K_s$) differs for different predictions. At a temperature of 4000 K the $\log g = 7$ Bergeron et al. (1995) models predict $R-K$ colours of 2.7 and 1.6 for pure helium and pure hydrogen atmospheres, respectively. For the same temperature, $R-K = 1.6$ is predicted by the $0.196\,M_\odot$ model by Serenelli et al. (2001). Finally, for WD 0346+246, with presumably a mixed hydrogen/helium atmosphere, Oppenheimer et al. (2001) observed $R-K = -0.7$. Unfortunately, our near-infrared observations only limit the colour to $R-K < 3.8$, which does not constrain any of these predictions.

7.3.2 Brightness, distance and radius

So far, we have only discussed the colours and temperature. We now turn to the absolute magnitude and radius. In Fig. 7.2b, we show M_R as a function of $R-I$. For star X, we computed the absolute R-band magnitude M_R using the parallax of $\pi = 1.6 \pm 0.8$ mas as measured through radio timing (Nice et al. 2005b). The resulting distance of $0.6^{+0.6}_{-0.2}$ kpc is consistent with that estimated from the dispersion measure which predicts 1.1 ± 0.2 kpc, using a dispersion measure of 30.2489 ± 0.003 pc cm^{-3} (Nice et al. 2005b) and the recent model of the Galactic electron distribution of Cordes & Lazio (2002). Correcting for the reddening, this implies $M_R = 15.97^{+0.88}_{-1.51}$.

Given the similarities in the above absolute magnitude of star X and that of WD 0346+246 ($M_R = 16.1 \pm 0.3$; Hambly et al. 1999; Oppenheimer et al. 2001), and assuming similar temperature, one finds that the radius of star X should be comparable to the $R = 0.010\,R_\odot$ for WD 0346+246 (Bergeron 2001). However, the large uncertainty in the parallax of PSR J0751+1807 allows radii between 0.007–0.021 $R_\odot$. For the white-dwarf mass of $\sim 0.19\,M_\odot$ inferred from pulse timing (Nice et al. 2005b), this is consistent the $\sim 0.022\,R_\odot$ expected from the $0.196\,M_\odot$ model by (Serenelli et al. 2001).

As can be seen in Fig. 7.2, the absolute magnitude is also consistent with the predicted values from the $\log g = 7$ pure helium model by Bergeron et al. (1995). At a temperature of $T_{\rm eff} = 4250$ K, this model has a radius of $0.020\,R_\odot$ and a mass of $0.15\,M_\odot$, somewhat smaller than the observed $0.19\,M_\odot$. To correct for the small difference in mass, we computed white dwarf radii for the observed temperature and mass of the companion and used these to scale the absolute magnitudes of the pure helium track in Fig. 7.2. At $0.19\,M_\odot$ and $T_{\rm eff} = 4000$ K, the Panei et al. (2000) helium core white dwarf mass-radius relation predicts $0.021\,R_\odot$. This is very similar to the radius predicted by the Bergeron et al. (1995) $\log g = 7$ pure helium models, and as such, the absolute magnitudes are comparable. We conclude that, with in the large uncertainties on the parallax distance, the absolute magnitude and radius that we derive for the companion of PSR J0751+1807 are consistent with the predictions for a pure helium atmosphere.

We note that of the models presented in Fig. 7.2, those of Bergeron et al. (1995) have been

extensively tested to explain the population of nearby white dwarfs (Bergeron et al. 2001; Bergeron 2001; Bergeron & Leggett 2002) and use a very detailed description of the white dwarf atmosphere combined with the latest opacities (P. Bergeron 2005, priv. comm.). This is not the case for the models of Serenelli et al. and Hansen, and thus we should be careful in using their models quantitatively. Indeed, as can be seen from Fig. 7.2, their models do not reproduce the observations of cool white dwarfs well. For instance, for the companion of PSR J0437−4715, which has a well-determined mass of $0.236 \pm 0.017\,M_\odot$ and distance of 139 ± 3 pc (van Straten et al. 2001), the models of Serenelli et al. (2001), while consistent with the observed $B - R$ and $R - I$ well, do not reproduce $R - I$ and M_R simultaneously. In contrast, the $0.2\,M_\odot$ model of Hansen (2004, priv. comm.) does pass through the $R - I$, M_R point, but cannot reproduce both colours. It may be that both problems reflect uncertainties in the model atmospheres used by Hansen and Serenelli et al. (2001). It would be worthwhile to couple the evolutionary models of these authors with the updated, very detailed atmospheric model of Bergeron et al. (1995).

7.3.3 Cooling history and nature of the envelope

Despite the uncertainty in the models and in the composition of the atmosphere, our observations show that the companion of PSR J0751+1807 has cooled much more than expected if the amount of hydrogen was thick enough for significant residual nuclear burning (Sect. 7.1). Indeed, the temperature is as expected if no residual hydrogen burning occurred. For instance, at the characteristic age of the pulsar, $\tau = 7.1$ Gyr (Nice et al. 2005b), the $0.196\,M_\odot$ of Serenelli et al. (2001), which has a thin envelope, predicts a temperature of about 3200 K, which is roughly consistent with what is observed. With a pure helium atmosphere, a slightly colder temperature, of ~ 2500 K, is expected, though this is a less secure estimate due to uncertainties in the opacities (Hansen & Phinney 1998a)

The presence of a thin (or no) hydrogen envelope is not expected, however, since thick envelopes are inferred for other optically identified companions in short-period systems (see Sect. 7.1). What could be wrong with this expectation? It was based on two theoretical ideas: (i) that below a certain critical mass, no shell flashes occur and hydrogen layers will be thick; and (ii) that the companion mass monotonously increases with increasing orbital period. These assumptions appeared to be confirmed by the available data: for PSR J0751+1807, with a period of 0.26 d, the companion mass of 0.16–0.21 $M_\odot$ (95% conf.; Nice et al. 2005b) is similar to what is found for two other short-period systems with companions for which thick hydrogen envelopes are inferred, and less than the masses for longer period systems with thin-envelope companions. Specifically, PSR J1012+5307 (0.60 d, 0.12–0.20 $M_\odot$) and PSR J1909−3744 (1.53 d, 0.19–0.22 $M_\odot$) have thick envelopes while PSR J0437−4715 (5.74 d, 0.20–0.27 $M_\odot$) and PSR B1855+09 (12.33 d, 0.24–0.29 $M_\odot$) have thin envelopes (see Fig. 7.3 and van Kerkwijk et al. 2005 and reference therein). Thus, while the uncertainties do not exclude that the companion of PSR J0751+1807 is so massive that it its envelope was diminished by shell flashes, the existing data make it unlikely.

Two explanations for a thin envelope remain. First, there may be differences in metallicity among the progenitors of pulsar companions. Serenelli et al. (2002) studied the evolution of

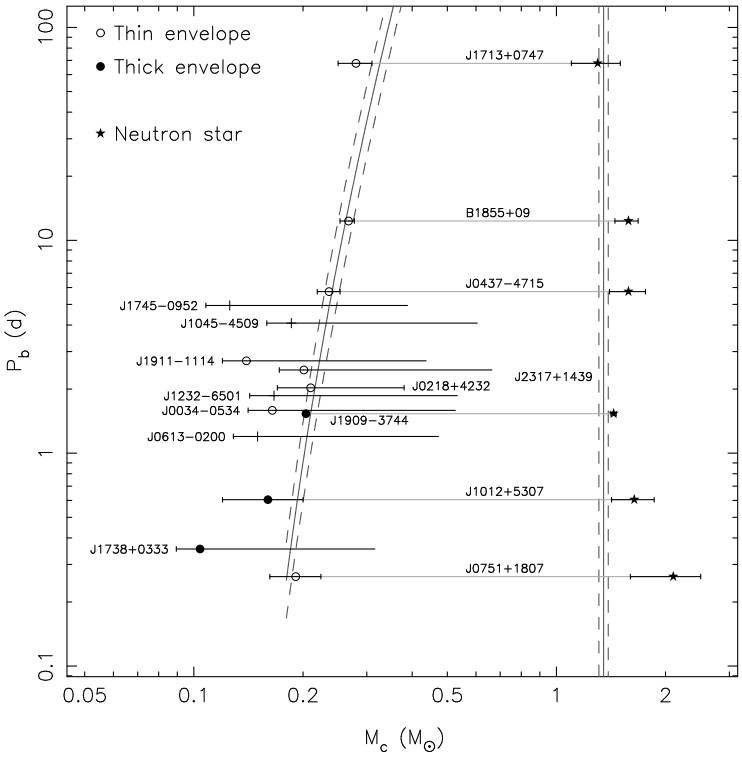

Figure 7.3: *The orbital period as a function of companion mass for a selection of low-mass binary pulsars outside globular clusters (either with $P_b < 5\,d$ and $M_{WD,min} > 0.1\,M_\odot$, or with $P_b < 100\,d$ and a secure companion mass determination). The data is compiled from the ATNF Pulsar Catalogue (Manchester et al. 2005), Stairs (2004) and van Kerkwijk et al. (2005) and references therein. Companion masses are either determined (double error bars, 95% confidence) or based on the assumption of a 1.35 $M_\odot$ neutron star and an inclination of $i = 90°$ (left error bar, minimum mass), 60° (central symbol, median mass) or 18° (right side, 5% probability that i is lower than this value and that the companion is heavier). Different central symbols indicate companions for which a thick or thin hydrogen envelope is inferred from optical measurements. The systems for which the neutron star mass is measured are indicated and connected by a gray line with their companions. The vertical grey lines indicate the $1.35 \pm 0.04\,M_\odot$ neutron star mass range determined by Thorsett & Chakrabarty (1999), while the curved grey lines represent the theoretical relation by Tauris & Savonije (1999) between the white dwarf mass and the orbital period.*

low-mass pulsar companions with sub-solar metallicity and found that, since the thermonuclear flashes are induced by the reactions of the CNO-cycle, the threshold mass between thin and thick hydrogen envelopes increases with decreasing metallicity of the white dwarf progenitor. Thus, it may be that the companion of PSR J0751+1807 had a sufficiently higher metallicity that it was above the threshold for shell flashes, while companions in other short-

period systems had lower metallicity and hence were below the threshold, despite having higher masses.

The next possibility is that the white dwarf was indeed formed with a thick envelope, which was subsequently removed by an action other than shell flashes. Based on the upper limit on the temperature of Lundgren et al. (1996), Ergma et al. (2001) already argued that the pulsar companion could not have the thick hydrogen envelope, and they proposed a scenario where part of the envelope was removed by pulsar irradiation. Ergma et al. found that irradiation driven mass-loss could remove as much as $0.01\,M_\odot$ from the thick hydrogen envelope (mostly while the companion is contracting following the cessation of mass transfer).

A possible problem with the above suggestions, is that none predict the removal of the entire hydrogen envelope, while the observed colours seem most consistent with a pure helium or at least helium-dominated atmosphere.

7.4 Irradiation by the pulsar?

Above, we have treated the companion as if it were an isolated object rather than member of a binary system. Might the presence of a relatively energetic pulsar influence our observations?

The observed pulsar period and period derivative imply a spin-down luminosity $L_{\rm SD} = (2\pi)^2 I\dot{P}/P^3 = 7.5 \times 10^{33}\, I_{45}\,{\rm ergs\,s^{-1}}$ (Lundgren et al. 1995; Nice et al. 2005b), where $I = 10^{45}\, I_{45}\,{\rm g\,cm^2}$ is the pulsar moment of inertia. For a $2.1\,M_\odot$ pulsar and a $0.19\,M_\odot$ companion, the orbital separation is $a = 2.3\,R_\odot$, and, consequently, the irradiative flux of the pulsar wind incident on the companion is $f_{\rm irr} = 2.1 \times 10^{10}\, I_{45}\,{\rm erg\,s^{-1}\,cm^{-2}}$. This is about twice the flux of the companion itself, $f_{\rm th} = \sigma T_{\rm eff}^4 = 1.06 \times 10^{10}\,{\rm erg\,s^{-1}\,cm^{-2}}$ for $T_{\rm eff} = 3700\,{\rm K}$. Therefore, the presence of the pulsar and its irradiation may be important.

Given the irradiation, one would expect the side of the companion facing the pulsar to be brighter than the side facing away from it. Thus, from Earth, the companion should appear faintest at phase 0.25 and brightest at phase 0.75 (using the convention that at phase 0, the pulsar is at the ascending node). This is indeed seen in other pulsar binaries, with the black widow pulsar PSR B1957+20 perhaps the most spectacular example (van Paradijs et al. 1988; Fruchter et al. 1988).

For star X, assuming a fraction η of the incident flux is absorbed and reradiated as optical flux, the flux from the bright side of the companion should be a factor $1 + \frac{2}{3}\eta f_{\rm irr}/f_{\rm th}$ brighter (here, the factor $\frac{2}{3}$ reflects projection effects). Observationally, the inferred values of η range from 0.1 to 0.6 (Orosz & van Kerkwijk 2003, and references therein), and thus one expects a maximum change in bolometric flux by a factor 1.13 to 1.8. For the R-band flux, the range is 1.2 to 2.2 (assuming it scales like a black-body spectrum, $\propto T^6$ around 3700 K). We confirmed this using a detailed light-curve synthesis model (described briefly in Stappers et al. 1999).

For star X, no effect is seen. Using the PSR J0751+1807 ephemeris from Nice et al. (2005b), we find that during the ESI R-band observations the orbital phase ranged from 0.22 to 0.25, while the 1996 LRIS R-band images were taken at phases 0.86–0.90, and the 2005 LRIS images at phases 0.01–0.14 on January 7, and 0.77–0.93 on January 8. Thus, these observations span the orbital phases necessary to test for any modulation in brightness. Indeed, using the inclination inferred from timing, $i = 66^{+4}_{-7}\,{\rm deg}$ (Nice et al. 2005b), we find that

during the ESI observations only 4 to 5% of the irradiated part of the companion surface was in view, while during the 1996 LRIS observations is was 78% to 85%. As a consequence, we expect to see nearly the maximum change in brightness. Nevertheless, in Sect. 7.2.2, we found no significant variation, $R_{\rm LRIS} - R_{\rm ESI} = 0.03 \pm 0.13$; thus, to $\sim 99\%$ confidence, the variation is smaller than 0.3 mag, which implies $\eta < 0.15$.

The lack of observed modulation could be taken to indicate that the irradiation is not very effective, e.g., because the albedo is large (i.e., η is small), the pulsar emission is non-isotropic, or the spin-down luminosity is overestimated. We believe these options are not very likely (for a discussion in a slightly different context, see Orosz & van Kerkwijk 2003), which leads us to consider the only alternative, that one of the assumptions underlying the above estimates is wrong.

In particular, we assumed implicitly that irradiated flux is reprocessed and re-emitted instantaneously, i.e., transfer of flux inside and around the companion are assumed to have negligible effect. For the companions of black-widow pulsars, this is reasonable, since for these relatively large objects, tides will have ensured synchronous rotation. Any flux transfer would thus have to be due to winds and/or convection, which plausibly happens on a timescale long compared to the thermal time of the layer in which the pulsar flux is reprocessed.

The companion of PSR J0751+1807, however, is well within its Roche-lobe, and tidal dissipation should be negligible. We can estimate its current rotation period from its prior evolution, following the reasoning used by van Kerkwijk & Kulkarni (1995) for the companion of PSR B0655+64. Briefly, during mass transfer, the companion filled its Roche-lobe and tides ensured the system was synchronized and circularized. Once mass transfer ceased and the companion started to contract to a white dwarf, however, the tides became inefficient, and the rotational evolution of the companion was determined by conservation of angular momentum.

For our estimates, we split the total moment of inertia of the progenitor into two parts, one from the core, $I_{\rm core} = k^2_{\rm core} M_{\rm core} R^2_{\rm core}$ and one from the envelope, $I_{\rm env} = k^2_{\rm env} M_{\rm env} R^2_{\rm L}$; here k is the radius of gyration and $R_{\rm L}$ is the radius of the Roche lobe. After contraction of the envelope, one is left with a white dwarf with $I_{\rm WD} = k^2_{\rm WD} M_{\rm WD} R^2_{\rm WD}$. If we now assume that $I_{\rm core} \simeq I_{\rm WD}$ and ignore differences in radius of gyration, conservation of angular momentum yields $\Omega_{\rm rot}/\Omega_{\rm orb} \simeq 1 + M_{\rm env} R^2_{\rm L} / M_{\rm WD} R^2_{\rm WD}$. In reality, likely the envelope will be more centrally concentrated than the white dwarf, i.e., $k_{\rm env} < k_{\rm WD}$, and tidal dissipation will be important in the initial stages of the contraction. This will reduce the spin-up. On the other hand, the hot core of the progenitor will be larger than the white dwarf, i.e., $I_{\rm core} > I_{\rm WD}$. In any case, it follows that unless the envelope mass is very small, the white dwarf should be significantly spun up.

Model predictions for the envelope mass of helium-core white dwarfs differ. The $0.196\,{\rm M}_\odot$ model by Serenelli et al. (2001), has an envelope mass of $6.7 \times 10^{-3}\,{\rm M}_\odot$ (as given in Althaus et al. 2001), whereas a model of similar mass ($M_{\rm WD} = 0.195\,{\rm M}_\odot$) by Driebe et al. (1998) has one of $3.1 \times 10^{-2}\,{\rm M}_\odot$. Using these values, taking $M_{\rm WD} = 0.19\,{\rm M}_\odot$, $R_{\rm WD} = 0.021\,{\rm R}_\odot$ and $R_{\rm L} = 0.48\,{\rm R}_\odot$, and ignoring differences in k, we find current rotation periods a factor 18–85 faster than the orbital period, or 20 to 5 minutes. Given that thick envelopes seem inconsistent with the low observed temperature (Sect. 7.3), the slower end of

the range seems more likely.

To estimate the timescale on which the pulsar flux is reprocessed, we assume that the incident particles are predominantly highly energetic, and that they penetrate to, roughly, one Thompson optical depth. This corresponds to a column depth of $N = 1.5 \times 10^{24}\,\mathrm{cm}^{-2}$, for which the thermal timescale $t \simeq NkT/\sigma T_{\mathrm{eff}}^4 \simeq 1\,\mathrm{min}$, where the numerical estimate is for $T = T_{\mathrm{eff}} = 3700\,\mathrm{K}$. This is shorter than the rotation periods estimated above, suggesting that rotation may not be too important. On the other hand, our estimate is very rough. For instance, at one Thompson depth, the opacity at optical wavelengths is much smaller than unity for the cool temperatures under consideration (Saumon et al. 1994). Thus, the material likely radiates less efficiently than a black body, which would make the thermal timescale longer. Furthermore, the irradiation will change the temperature and ionization structure of the atmosphere, further complicating matters. (Indeed, could this be the underlying cause for the fact that the colours deviate so strongly from those expected for a pure hydrogen atmosphere?) Finally, it might induce strong winds which equalize the temperature on both hemispheres (as is the case for Jupiter).

7.5 Conclusions

We have optically identified the white dwarf companion of the binary millisecond pulsar PSR J0751+1807. We find that the companion has the reddest colours of all known millisecond pulsar companions and white dwarfs. These colours indicate that the companion has a very low (ultra-cool) temperature of $T_{\mathrm{eff}} \sim 3500 - 4300\,\mathrm{K}$. Furthermore, the colours suggest that the white dwarf has a pure helium atmosphere, or a helium atmosphere with some hydrogen mixed in, as invoked for the field white dwarf WD 0346+246 which has similar colours (Oppenheimer et al. 2001; Bergeron 2001).

Our observations are inconsistent with evolutionary models, from which one would expect a pure hydrogen atmosphere. Indeed, as for other short-period systems, the hydrogen envelope is expected to be thick enough to sustain significant residual hydrogen burning, leading to temperatures far in excess of those observed. It may be that the mass of the envelope was reduced due to shell flashes or irradiation by the pulsar, as was proposed by Ergma et al. (2001).

However, we see no evidence for irradiation, despite the fact that the pulsar spin-down flux impinging on the white dwarf is roughly double the observed thermal flux. Clues to what happens might be found from more detailed studies of the spectral energy distribution, or more accurate phase-resolved photometry.

Finally, a deeper observation at infrared wavelengths would allow one to distinguish between the different atmosphere compositions for the companion: for a pure helium atmosphere, black-body like colours are expected, while if any hydrogen is present, the infrared flux would be strongly depressed (as is seen for WD 0346+246). With adaptive optics instruments, such observations should be feasible.

Chapter 8

Two new candidate ultra-compact X-ray binaries

C. G. Bassa, P. G. Jonker, J. J. M. in 't Zand, F. Verbunt

Astronomy & Astrophysics 2006, 446, L17–L20

Abstract We present the identification of the optical counterparts to the low-mass X-ray binaries 1A 1246−588 and 4U 1812−12. We determine the X-ray position of 1A 1246−588 from *ROSAT*/PSPC observations and find within the error circle a blue star with $V = 19.45$, $B-V = 0.22$ and $R-I = 0.22$ which we identify as the counterpart. Within the *Chandra* error circle of 4U 1812−12, a single star is present which appears blue with respect to the stars in the vicinity. It has $R = 22.15$, $R-I = 1.53$. Distance estimates for both systems indicate that the optical counterparts are intrinsically faint, suggesting that they are ultra-compact X-ray binaries. These identifications would increase the number of candidate ultra-compact X-ray binaries from 2 to 4, whereas orbital periods are measured for only 7 systems in the Galactic disk.

8.1 Introduction

The canonical low-mass X-ray binary consists of a neutron star or black hole and a low-mass main-sequence or (sub)giant donor star, and has an orbital period longer than one hour, up to several hundred days.

Recently, it has been found that the class of ultra-compact low-mass X-ray binaries makes up about half (5 out of 12) of the low-mass X-ray binaries in globular clusters (e.g., review by Verbunt & Lewin 2006), whereas a growing number of such systems is also discovered in the Galactic disk (7 with measured periods, and 2 candidates, see e.g., Juett & Chakrabarty 2003; Nelemans et al. 2004; Wang & Chakrabarty 2004). In addition, observations with the Wide Field Cameras (WFCs) of *BeppoSAX* have found a new class of low-mass X-ray binaries, bursters with (very) low persistent X-ray emission (Cocchi et al. 2001). The distribution of the sources in this class is more concentrated towards the Galactic center than that of the canonical low-mass X-ray binaries (Cornelisse et al. 2002).

To elucidate the evolutionary status and history of these systems, observations at longer wavelengths, in particular optical/infrared, are crucial. Such observations may reveal the orbital period, directly or indirectly (e.g., van Paradijs & McClintock 1994), or provide information about the donor and its chemical composition (e.g. Nelemans et al. 2004). The first step to such studies is the optical identification of the X-ray binary. In this letter we report two new optical identifications, which may be ultra-compact X-ray binaries.

8.2 X-ray observations

4U 1812−12 ($l = 18\overset{\circ}{.}03$, $b = 2\overset{\circ}{.}40$) has been observed by various X-ray satellites, but the observations with *BeppoSAX*/WFC and *Chandra* are most relevant for this paper. Type I X-ray bursts with photospheric radius expansion have been observed with the former, providing an unabsorbed bolometric peak flux of $(1.5 \pm 0.3) \times 10^{-7}$ erg cm^{-2} s^{-1} (Cocchi et al. 2000). A 1 ks observation with the back-illuminated S3 CCD aboard *Chandra* was analyzed by Wilson et al. (2003), yielding an accurate position of 4U 1812−12; $\alpha_{J2000} = 18^{h}15^{m}06\overset{s}{.}18$, $\delta_{J2000} = -12°05'47\overset{''}{.}1$, with an uncertainty limited by the *Chandra* bore-sight ($0\overset{''}{.}6$, 90% confidence; Aldcroft et al. 2000). A flux of 4.4×10^{-10} erg cm^{-2} s^{-1} (1–10 keV) and absorption of $N_{\rm H} = (1.1 \pm 0.2) \times 10^{22}$ cm^{-2} were determined from spectral fits.

1A 1246−588 ($l = 302\overset{\circ}{.}70$, $b = 3\overset{\circ}{.}78$) has received much less attention, though it has been observed serendipitously by several X-ray observatories. A type I X-ray burst was observed with *BeppoSAX*/WFC (Piro et al. 1997) and a short (0.85 ks) follow-up observation with *ROSAT*/PSPC linked it to 1A 1246−588 (Boller et al. 1997). In this observation $N_{\rm H}$ was measured to be $(2.9\pm0.9)\times10^{21}$ cm^{-2} and the 0.1–2.4 keV flux was 1.7×10^{-10} erg cm^{-2} s^{-1} (Boller et al. 1997). We have reanalyzed the *ROSAT*/PSPC observations of the field of 1A 1246−588 using standard routines from the EXSAS distribution (Zimmermann et al. 1996). In the 0.85 ks exposure obtained in February 1997, the X-ray binary is only 7′ off-axis, compared to 39′ in the much longer PSPC observation from 1993, and the shorter observation provides the best source position. In this observation the X-ray binary has $\alpha_{J2000} = 12^{h}49^{m}39\overset{s}{.}61$, $\delta_{J2000} = -59°05'13\overset{''}{.}3$, with an internal uncertainty of $0\overset{''}{.}3$ on each coordinate. The exter-

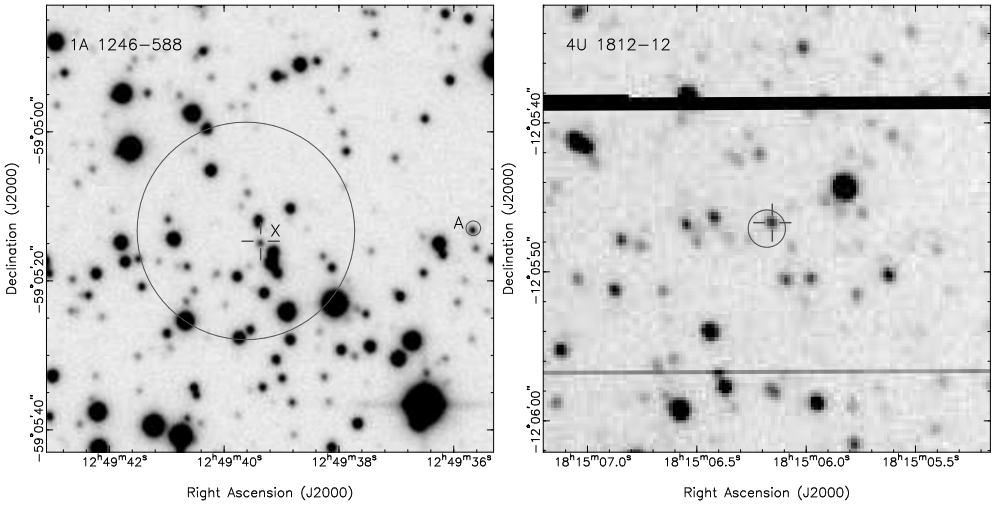

Figure 8.1: *(*left*) A* $1' \times 1'$ *subsection of the combined 2 min R-band WFI image of 1A 1246−588. The 95% confidence error circle on the* ROSAT *position has a radius of* $14\farcs6$ *and is depicted with the large circle. The proposed optical counterpart, star X, is indicated with the tick marks, while another blue star, star A, which is located outside the error circle, is encircled. (*right*) A* $30'' \times 30''$ *subsection of the 5 min R-band IMACS image of 4U 1812−12. The horizontal black bar in the top part of the image is a read out streak of a bright star, whereas the grey streak in the bottom part is a dead column of the CCD. The* Chandra *error circle (95% confidence,* $1\farcs25$ *in radius) is depicted with the circle. The proposed optical counterpart is indicated with the tick marks.*

nal uncertainty on this position, the uncertainty in the bore-sight of the satellite, is about $6''$ (Ayres 2004). Due to the short exposure only a few X-ray sources are present in the PSPC observation, and none of them are coincident with bright stars. Thus, no bore-sight correction is possible and the uncertainty on the position is dominated by the pointing uncertainty of *ROSAT*.

1A 1246−588 and 4U 1812−12 have been persistently detected in X-rays by the All Sky Monitor (ASM) onboard the Rossi X-ray Timing Explorer (RXTE). Both during, a few days before and a few days after the time of the optical observations described below both sources were detected at daily averaged count rates of at least 1 ASM count per second.

8.3 Optical observations

We retrieved archival observations of 1A 1246−588 obtained with the Wide Field Imager (WFI) at the ESO 2.2 metre telescope on La Silla on March 26/27, 2000. A series of dithered 4 *B*, 6 *V*, 5 *R* and 5 *I*-band images were taken, all with exposure times of 2 min under clear conditions with $0\farcs8$–$1\farcs0$ seeing. The field of 4U 1812−12 was imaged with the 6.5 metre Inamori Magellan Areal Camera and Spectrograph (IMACS) at the Magellan Baade telescope

on Las Campanas on July 6/7, 2005. A single 5 min image was obtained in both *R* and *I* under 0.″6 seeing. Both IMACS and WFI are mosaics of eight 4k×2k detectors and we analyzed the images from the detector containing the X-ray binaries (chip 8 for 4U 1812−12 and chip 2 for 1A 1246−588). The WFI images have a pixel scale of 0.″24 pix^{-1}, while IMACS observations were taken with 2×2 binning, yielding a pixel scale of 0.″22 pix^{-1}. The science images were corrected for bias and flatfielded with domeflats using standard routines running within MIDAS.

Large-scale variations in the background of the *I*-band images, known as fringing, were present in the WFI observations. We corrected for this with a fringe frame. This fringe frame was constructed by median combining a set of 20 *I*-band images obtained earlier that night, such that it contained only the contributions of the sky and the fringe variations. The level of the sky was estimated and subtracted from this image, leaving only the fringe variations. This result was scaled to the fringe variations in the *I*-band images of the X-ray binary and subsequently subtracted from these images.

For the WFI observations, the images taken through the same filter were aligned using integer pixel offsets and median combined to remove image artifacts and increase the overall signal-to-noise ratio. Finally, a $4' \times 4'$ subsection of the averaged images, centered on the nominal position of the X-ray binary, was extracted and used for the astrometry and photometry. For 4U 1812−12, a $3.'8 \times 3.'8$ subsection of the IMACS *R* and *I*-band images was extracted.

For the astrometry of the WFI observations of 1A 1246−588 we measured the centroids of all 31 astrometric standards from the second version of the USNO CCD Astrograph Catalog (UCAC2; Zacharias et al. 2004) that overlapped with the $4' \times 4'$ subsection of the combined *R*-band image and that were not saturated and appeared stellar and unblended. We removed one outlier that had a total residual of 0.″74, and the remaining stars were used to compute an astrometric solution, fitting for zero-point position, scale and position angle. The astrometric solution has root-mean-square (rms) residuals of 0.″054 in right ascension and 0.″047 in declination. We used a similar approach for the IMACS observations of 4U 1812−12, but had to use the USNO-B1 catalog (Monet et al. 2003) as very few UCAC2 standards overlapped with the IMACS images. About 70 USNO-B1 standards were used to calibrate a $3.'8 \times 3.'8$ subsection of the *R*-band image, giving a solution with rms residuals of 0.″19 in right ascension and 0.″21 in declination.

The DAOPHOT II package (Stetson 1987), running inside MIDAS, was used to determine instrumental magnitudes through point spread function (PSF) fitting. Aperture photometry of several bright stars was used to determine aperture corrections. For the calibration of the WFI observations we determined instrumental magnitudes of some 100 photometric standards in the standard field SA 98 and calibrated these against the calibrated values by Stetson (2000), fitting for zero-point and colour coefficients. We assumed extinction coefficients of 0.22, 0.19, 0.14 and 0.11 mag per airmass for *B*, *V*, *R* and *I*-band, respectively, taken from the WFI webpage[1]. The rms residuals of the calibration were 0.04 mag in *B* and *R*, 0.03 in *V* and 0.05 mag in *I*. The IMACS observations were calibrated using 11 standards in the T Phe field, again using values from Stetson (2000) and fitting for zero-point and colour coefficients.

[1] http://www.ls.eso.org/lasilla/sciops/2p2/E2p2M/WFI/zeropoints/

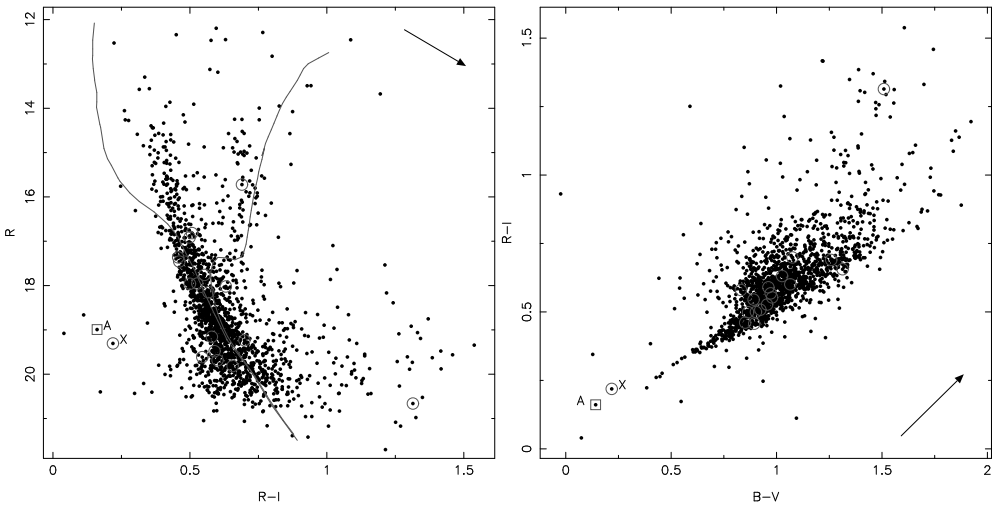

Figure 8.2: *(*left*) A colour-magnitude and colour-colour diagram (*right*) of the BVRI photometry of the 1A 1246−588 region. Stars inside the* ROSAT *error circle (Fig. 8.1) are encircled. Also shown in the CMD are two solar metallicity isochrones from Girardi et al. (2000), placed at a distance of 4.0 kpc and an absorption of $A_V = 1.0$. The left is for an age of 0.1 Gyr, while the right has an age of 10 Gyr. These isochrones are merely to guide the eye, as there will be a spread in distance, age, metallicity and absorption. The arrows indicate the effects of absorption, where the length of the arrow is for an extra absorption of $\Delta A_V = 1.0$. Of the stars present in the error circle, star X is exceptionally blue and the likely optical counterpart to 1A 1246−588. Star A has similar colours and magnitudes as star X, but is located outside the 95% confidence error circle.*

The standard field was imaged at similar airmass as the 4U 1812−12 field and no extinction coefficients were used. The rms residuals of the calibration were 0.05 mag in R and 0.07 mag in I.

In Fig. 8.1 we present finding charts for the regions of 1A 1246−588 and 4U 1812−12. We searched for optical counterparts to the X-ray sources in 95% confidence error circles on the *ROSAT* and *Chandra* position. For 4U 1812−12, a single star is located in the 1.″25 error circle, while several stars lie inside the 14.″6 error circle on the position of 1A 1246−588. We note that as both X-ray binaries are expected to have an accretion disk, the optical colours should display an excess of emission at blue wavelengths and thus appear blue, typically having $(B-V)_0 \approx 0.0$ (van Paradijs & McClintock 1995).

In Figure 8.2 we show the colour-magnitude diagram (CMD) and a colour-colour diagram of the *BVRI* photometry of all stars on the $4' \times 4'$ image of 1A 1246−588. To illustrate the structure seen in the CMD, we have overplotted isochrones from Girardi et al. (2000). There are 3 stars that are exceptionally blue (having $B-V < 0.25$ and $R-I < 0.25$) and two of them, stars A and X, are near the error circle (Fig. 8.1). Star X has $V = 19.45 \pm 0.02$, $B-V = 0.22 \pm 0.03$, $V-R = 0.14 \pm 0.03$ and $R-I = 0.22 \pm 0.06$, while star A has $V = 18.99 \pm 0.01$, $B-V = 0.15 \pm 0.02$, $V-R = -0.01 \pm 0.02$ and $R-I = 0.16 \pm 0.04$. The mean

colour and standard deviation of all stars in the 1A 1246−588 region is $B - V = 1.03 \pm 0.22$ and $R - I = 0.73 \pm 0.28$, and both star X and A are significantly bluer than this. Furthermore, at the observed R-band magnitude and $R - I$ colour, both stars are about half a magnitude bluer than the bulk of the stars at the same R-band magnitude. The optical position of star X is $\alpha_{J2000} = 12^h49^m39\overset{s}{.}364 \pm 0\overset{''}{.}06$, $\delta_{J2000} = -59°05'14\overset{''}{.}68 \pm 0\overset{''}{.}05$, which is only $2\overset{''}{.}4$ from the *ROSAT* position and well within the 1σ uncertainty of $6''$. Star A on the other hand has $\alpha_{J2000} = 12^h49^m35\overset{s}{.}660 \pm 0\overset{''}{.}06$, $\delta_{J2000} = -59°05'12\overset{''}{.}94 \pm 0\overset{''}{.}05$, which is $30''$ (about 5σ) from the *ROSAT* position. We estimate that the probability of finding a star as blue as star X within the 95% confidence error circle of 1A 1246−588 is about 2%. Hence, we identify star X as the optical counterpart to 1A 1246−588.

A single star is present within the *Chandra* error circle of 4U 1812−12 at $\alpha_{J2000} = 18^h15^m06\overset{s}{.}155 \pm 0\overset{''}{.}19$, $\delta_{J2000} = -12°05'46\overset{''}{.}70 \pm 0\overset{''}{.}21$. This position is only $0\overset{''}{.}5$ from the X-ray position of 4U 1812−12 (Wilson et al. 2003). From the photometry we obtain $R = 22.15 \pm 0.02$ and $R - I = 1.53 \pm 0.03$. This star is not as blue as the counterpart of 1A 1246−588, however, in light of the larger absorbing column for 4U 1812−12, this is not surprising. Still, the counterpart is bluer than the bulk of the stars in the 4U 1812−12 region, which have $R - I = 1.88 \pm 0.23$. Furthermore, there are 9 stars within a radius of $5''$ from the *Chandra* position of 4U 1812−12, and all, except the candidate counterpart, are redder than $R - I = 1.73$. Finally, we note that the probability of a chance coincidence of a star within the 95% confidence error circle is about 0.15%. We conclude that the star inside the error circle is the optical counterpart to 4U 1812−12.

8.4 Discussion

We have identified the optical companions to the low-mass X-ray binaries 1A 1246−588 and 4U 1812−12 based on their positional coincidence with the X-ray position and their colours. The counterpart to the first has $V = 19.45$, $B - V = 0.22$, while that of 4U 1812−12 is somewhat fainter at $R = 22.15$, $R - I = 1.53$.

Due to its position somewhat out of the Galactic plane, the hydrogen absorption column N_H towards 1A 1246−588 is moderate and suggests $A_V = 1.7$ (Predehl & Schmitt 1995). This is smaller than the maximum absorption in this line-of-sight, which is predicted to reach $A_V = 1.9$ around $d = 7$ kpc by the model of Drimmel et al. (2003). This limit constrains the absolute magnitude of the companion of 1A 1246−588 to $M_V \gtrsim 3.5$. Though this reasoning assumes that both the model by Predehl & Schmitt (1995) and Drimmel et al. (2003) are correct, this distance is in agreement with estimates from *BeppoSAX*/WFC and RXTE/ASM observations of photospheric radius expansion bursts of 1A 1246−588, which suggest a distance of 5 kpc (in't Zand et al. in prep.).

For 4U 1812−12, the photospheric radius expansion bursts that have been observed by Cocchi et al. (2000) provide an estimate on the distance to this LMXB. Assuming an Eddington peak luminosity of $L_X = 3.8 \times 10^{38}$ erg s^{-1} for the accretion of helium-rich material (Kuulkers et al. 2003), the distance is estimated at 4.6 kpc. If hydrogen-rich material is accreted instead, the Eddington luminosity of $\sim 2 \times 10^{38}$ erg s^{-1} reduces the distance to 3.4 kpc (see also Jonker & Nelemans 2004). Furthermore, the value of N_H derived from the X-ray

absorption suggests $A_V = 6.4$ (Predehl & Schmitt 1995) and, using the relative extinction coefficients of Schlegel et al. (1998), $A_R = 5.2$. As such, the optical companion of 4U 1812−12 has an absolute R-band magnitude in the range of 3.6–4.2. If we assume that the counterpart has the same intrinsic colours as the counterpart of 1A 1246−588, which has $(V-R)_0 = -0.2$, this would translate to $M_V = 3.4$–4.0.

These absolute magnitudes place both systems amongst the intrinsically fainter of the LMXBs known. According to van Paradijs & McClintock (1994), this suggests that these systems are ultra-compact X-ray binaries (UCXBs; having an orbital period below an hour). Here, the faintness of the counterpart is due to the reprocessing of X-rays in a physically small accretion disk. However, these systems remain candidate UCXBs until the orbital period is determined, i.e. either through optical/IR or X-ray observations.

If these systems indeed turn out to have ultra-compact orbits, it is interesting to note that for the observed X-ray luminosities of $L_X \approx 0.9{\times}10^{36}$ erg s^{-1} (1–10 keV) for 4U 1812−12 and $L_X \lesssim 10^{36}$ erg s^{-1} (0.1–2.4 keV) for 1A 1246−588, these systems satisfy the notion presented by in't Zand et al. (2005); that LMXBs with persistent luminosities with $L_X \lesssim 10^{36}$ erg s^{-1} may be ultra-compact X-ray binaries.

Chapter 9

The neutron star soft X-ray transient 1H 1905+000 in quiescence

P. G. Jonker, C. G. Bassa, G. Nelemans, A. M. Juett, E. F. Brown, D. Chakrabarty

Monthly Notices of the Royal Astronomical Society 2006, 368, 1803–1810

Abstract In this Paper we report on our analysis of a $\sim$ 25 ks *Chandra* X-ray observation of the neutron star soft X-ray transient (SXT) 1H 1905+000 in quiescence. Furthermore, we discuss our findings of the analysis of optical photometric observations which we obtained using the Magellan telescope and photometric and spectroscopic observations which we obtained using the Very Large Telescope at Paranal. The X–ray counterpart of 1H 1905+000 was not detected in our *Chandra* data, with a 95% confidence limit to the source count rate of 1.2×10^{-4} counts s^{-1}. For different spectral models this yields an upper limit on the luminosity of 1.8×10^{31} erg s^{-1} (for an upper limit on the distance of 10 kpc). This luminosity limit makes 1H 1905+000 the faintest neutron star SXT in quiescence observed to date. The neutron star luminosity is so low that it is similar to the lowest luminosities derived for black hole SXTs in quiescence. This low luminosity for a neutron star SXT challenges the hypothesis presented in the literature that black hole SXTs in quiescence have lower luminosities than neutron star SXTs as a result of the presence of a black hole event horizon. Furthermore, the limit on the neutron star luminosity obtained less than 20 years after the outburst has ceased, constrains the thermal conductivity of the neutron star crust. Finally, the neutron star core must be so cold that unless the time averaged mass accretion rate is lower than 2×10^{-12} M$_\odot$ yr^{-1}, core cooling has to proceed via enhanced neutrino emission processes. The time averaged mass accretion rate can be derived from binary evolution models if the orbital period of the system is known. Our optical observations show that the optical counterpart discovered when the source was in outburst has faded. Near the outburst optical position we find two stars with a separation of 0.7″and $I = 19.3 \pm 0.1$ and 21.3 ± 0.1. VLT optical spectroscopy revealed that

the spectrum of the brighter of the two sources is a G5-7V star. However, the outburst astrometric position of the optical counterpart does not coincide with the position of the G5-7V star nor with that of the fainter star. We derive a limit on the absolute I-band magnitude of the quiescent counterpart of $M_I > 7.8$ assuming the source is at 10 kpc. This is in line with 1H 1905+000 being an ultra-compact X-ray binary, as has been proposed based on the low outburst V-band absolute magnitude.

9.1 Introduction

Low–mass X–ray binaries are binary systems in which a $\lesssim 1\,M_\odot$ star transfers matter to a neutron star or a black hole. A large fraction of the low–mass X–ray binaries are transient systems – the so called soft X–ray transients (SXTs; e.g. see Chen et al. 1997). Before the launch of the XMM–Newton and *Chandra* satellites only a few (mostly) nearby SXTs could be studied in quiescence (e.g. the black hole candidates A 0620−00 and V404 Cyg and the neutron star systems Cen X–4 and Aql X–1; Wagner et al. 1994; McClintock et al. 1995; van Paradijs et al. 1987). Using the XMM–Newton and *Chandra* satellites many more systems were studied in quiescence in the initial years of operation (see e.g. Garcia et al. 2001; Kong et al. 2002; Rutledge et al. 2002b; Wijnands et al. 2001; Campana et al. 2002; Hameury et al. 2003; Jonker et al. 2004). Contemporaneous theoretical progress provided the framework for the interpretation of these observations (Narayan & Yi 1994; Narayan et al. 1997; Brown et al. 1998; Colpi et al. 2001; Zavlin et al. 1996; Gänsicke et al. 2002) which turned out to have a profound impact on two important areas of high energy astrophysics.

First, comparing the quiescent luminosity of neutron star SXTs with that of black hole SXTs it was found that black hole (BH) SXTs are systematically fainter in quiescence than neutron stars (Narayan et al. 1997; Menou et al. 1999; Garcia et al. 2001; Kong et al. 2002). This has been interpreted as evidence for advection of energy across a BH event horizon. If true this would constitute the first confirmation of a prediction of Einstein's Theory of General Relativity in the strong field regime. Despite many objections to this interpretation (Campana & Stella 2000; Abramowicz et al. 2002), alternative explanations for the difference in quiescent luminosity (Fender et al. 2003), and neutron stars which turned out to be fainter than initially found to be the rule (e.g. SAX J1808.4–3658, Campana et al. 2002; EXO 1747–214; Tomsick et al. 2005), none of the neutron star SXTs have quiescent luminosities as low as the faintest BH SXTs, which have 0.5–10 keV luminosities $< 10^{31}\,\mathrm{erg\,s^{-1}}$; (e.g. Kong et al. 2002; Hameury et al. 2003). Hence, irrespective of the interpretation, the difference in quiescent luminosity between BH and neutron star SXTs seems to be one of the very few distinct characteristics between BHs and neutron stars.

Secondly, the quiescent spectra of neutron star SXTs are well–fit by a neutron star atmosphere model (NSA) sometimes supplemented with a power–law component. Especially in sources with a quiescent luminosity near $10^{33}\,\mathrm{erg\,s^{-1}}$ the spectrum is dominated by a strong thermal component (Jonker et al. 2004). The thermal component is thought to be due to the hot neutron star core moderated by the neutron star atmosphere. The neutron star core temperature can be calculated by combining well established theories about the time–averaged mass accretion rates in neutron star SXTs (Kraft et al. 1962; Verbunt & van den Heuvel 1995),

the pycnonuclear reactions taking place in the neutron star crust (Salpeter & van Horn 1969; Haensel & Zdunik 1990; Kitamura 2000) and theoretical neutron star cooling predictions (see Yakovlev & Pethick 2004 for a review). Therefore, in theory, an NSA–fit provides means to measure the mass and radius of the neutron star and hence constrain the equation of state (EoS) of matter at supranuclear densities. The description of the relations between pressure and density of matter (the EoS) under the extreme conditions encountered in neutron stars is one of the ultimate goals of the study of neutron stars.

In practice, numbers typical for a canonical neutron star were found (e.g. Heinke et al. 2003), rendering support for this interpretation. However, there is an ongoing debate whether the temperature of the thermal (NSA) component is varying on short timescales (cf. Rutledge et al. 2002a; Campana et al. 2004, and Jonker et al. 2005). Small temperature changes could be explained by changes in the neutron star atmosphere due to ongoing low–level accretion (Brown et al. 2002). Large changes on short timescales would render it unlikely that the soft/thermal component is due to cooling of the neutron star, limiting the applicability of the NSA model fit. Finally, there are currently two sources known which returned to quiescence after a several year–long accretion epoch (i.e. KS 1731–260 and MXB 1659–298). As a result of these long accretion episodes the neutron star *crust* is heated to temperatures larger than that of the core. The observed thermal spectral component has been identified as cooling of the neutron star crust (Wijnands et al. 2002; Rutledge et al. 2002b). As the crust cools the X–ray spectral properties also change slightly (Wijnands et al. 2004).

Recent *Chandra* observations of accretion powered millisecond X–ray pulsars in quiescence found that the quiescent luminosity of many of those observed so far, not just SAX J1808.4–3658, is low (Wijnands et al. 2005; Campana et al. 2005). A possible exception could be the accretion–powered millisecond X–ray pulsar IGR J00291+5934 (Jonker et al. 2005). Furthermore, the X–ray spectrum is in most cases dominated by a power–law component similar to that of quiescent BH (Wijnands et al. 2005). Hence, the dichotomy between the BH and neutron star quiescent luminosity may not be as large as previously derived (see also Jonker & Nelemans 2004). We note however, that reliable distance estimates could be made for only 2 accretion powered millisecond systems, SAX J1808.4−3658 and XTE J1814−338 (in't Zand et al. 2001; Strohmayer et al. 2003). For the other systems the distance estimates are rather uncertain, making the quiescent luminosity uncertain as well. The low–luminosity and the small contribution of a thermal spectral component to the luminosity of SAX J1808.4–3658 (<10%; Campana et al. 2002, although see the comment about this upper limit in Yakovlev et al. 2005) hint at a massive neutron star ($M > 1.7\,\mathrm{M}_{\odot}$; Yakovlev et al. 2003; Yakovlev & Pethick 2004). The upper limit on the thermal spectral component implies that the neutron star core of SAX J1808.4−3658 must release the energy produced in the crust due to pycnonuclear reactions rapidly via enhanced neutrino emission. This enhanced neutrino emission can only occur when the neutron star mass is larger than the canonical 1.4 $\mathrm{M}_{\odot}$.

1H 1905+000 was first detected on MJD 42368 (UTC) by Ariel 5 (Seward et al. 1976). Six type I X–ray bursts were discovered on different occasions by SAS–3 firmly establishing the nature of the compact object as a neutron star (Lewin et al. 1976). The last reported detection of the source was that by EXOSAT on MJD 46316 (UTC). A radius expansion burst

was detected on this occasion (Chevalier & Ilovaisky 1990). During the period of activity the source has also been detected with HEAO–1 and Einstein (Reid et al. 1980 and Christian & Swank 1997, respectively). However, the source was not detected in the ROSAT All Sky Survey (Juett & Chakrabarty 2005). The source likely went to quiescence at the end of the 1980s/early 1990s. Next, 1H 1905+000 was observed for 5 ks with the back–illuminated S3 CCD–chip of the Advanced CCD Imaging Spectrometer (ACIS) detector on board the *Chandra* satellite with the High–Energy Transmission Grating inserted (Juett & Chakrabarty 2005). Again no source was detected at the position of the optical counterpart discovered when the source was in outburst (Chevalier et al. 1985). The derived upper limit on the unabsorbed 0.5–10 keV flux for 1H 1905+000 was 1×10^{-14} erg cm^{-2} s^{-1} for an assumed black body spectrum with a temperature of 0.3 keV. The distance for 1H 1905+000 derived from the observed radius expansion burst peak flux is 7.3 or 10 kpc (Jonker & Nelemans 2004; the values assume hydrogen and helium bursts, respectively). From Einstein observations Christian & Swank (1997) determined that the interstellar extinction, $N_{\rm H}$, to 1H 1905+000 is $(1.9 \pm 0.2) \times 10^{21}$ cm^{-2}. This yields an upper limit to the intrinsic (i.e. corrected for the interstellar extinction) 0.5–10 keV source luminosity of 1.0–1.7$\times 10^{32}$ erg s^{-1} for 1H 1905+000. In summary, it is likely that the source had been accreting steadily at $L_{\rm X} \sim 4 \times 10^{36}$ erg s^{-1} for more than 10 years before returning to quiescence. In this Paper we present our analysis of a $\sim$ 25 ks *Chandra* observation of this neutron star SXT in quiescence. Furthermore, our analysis of Very Large Telescope and Magellan optical observations of the region of the source in quiescence is also presented.

9.2 Observations, analysis and results

9.2.1 Optical Magellan, VLT, archival WHT and CFHT observations

In order to determine the best (optical) position of 1H 1905+000 and to search for the optical counterpart in quiescence, we have obtained *I*-band images with exposure times of 10 s and 2×300 s using the Inamori–Magellan Areal Camera and Spectrograph (IMACS) instrument mounted on the 6.5 m Magellan–Baade telescope on July 7, 2005, 03:03 UTC (MJD 53558.14594 UTC). The seeing was 0.″69. Using the second USNO CCD Astrograph Catalog (UCAC2) catalogue (Zacharias et al. 2004) we determined the position of 71 bright, unsaturated, stars in the 10 s IMACS image to obtain an astrometric solution (the rms of the fit was 0.″060 both in right ascension [α] and in declination [δ]). Subsequently, the astrometric solution of the 10 s frame was transferred to the 300 s images using 1397 stars. In this the uncertainty was 0.″017 in α and 0.″015 in δ. Hence, the absolute uncertainty in the optical astrometry of the 300 s images is 0.″062 in α and 0.″061 in δ. Next, standard image processing was done in MIDAS, the Munich Image Data Analysis System (i.e. bias subtraction and flatfield correction.) The two 300 s observations were averaged (see Fig. 9.1). We have observed standard stars on the same CCD close in time and airmass to the IMACS observations of 1H 1905+000. Using point spread function (PSF) fitting techniques we found that the star present near the optical position of the counterpart discovered in outburst consists of two stars close together (within 0.″7) with *I*-band magnitudes 19.3 ± 0.1 (star A) and

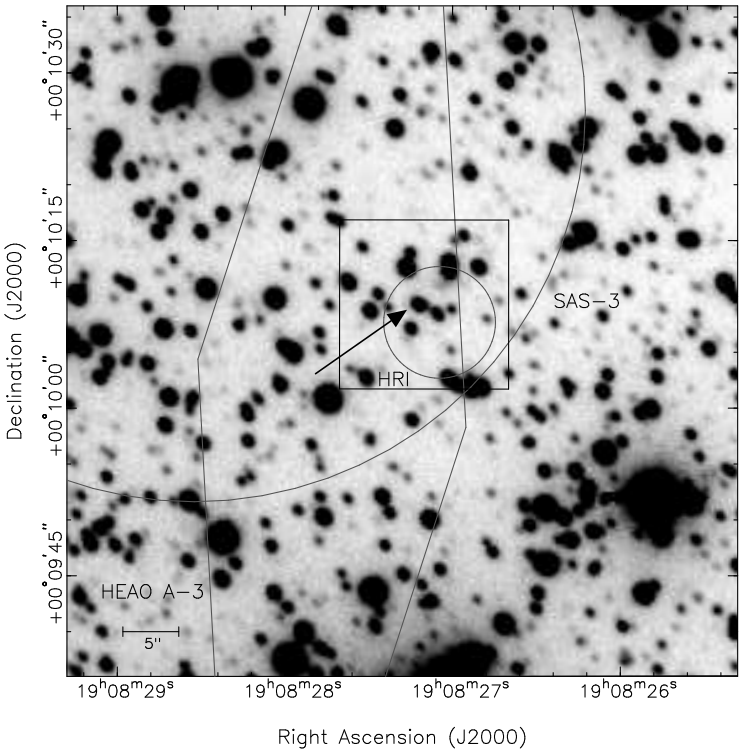

Figure 9.1: *A 1′ × 1′ I-band finder chart of the field of 1H 1905+000 obtained by combining the two 300 s images obtained with Magellan/IMACS. Overplotted are the HEAO A–3 (diamond shape), the Einstein HRI (small circle) and the SAS–3 (large circle) error regions. The box shows the region plotted in Figure 2. The arrow indicates the approximate position of the blue counterpart discovered when 1H 1905+000 was in outburst (Chevalier et al. 1985). PSF-fitting showed that this star consists of two stars separated by 0.″7 (see Fig. 9.2).*

21.3 ± 0.1 (star D; see Fig. 9.2). Star A has a position $\alpha_{J2000.0} = 19^{\rm h}08^{\rm m}27\overset{\rm s}{.}217 \pm 0\overset{\prime\prime}{.}063$, $\delta_{J2000.0} = +00^\circ10'09\overset{\prime\prime}{.}42 \pm 0\overset{\prime\prime}{.}062$. Star D has a position $\alpha_{J2000.0} = 19^{\rm h}08^{\rm m}27\overset{\rm s}{.}171 \pm 0\overset{\prime\prime}{.}063$, $\delta_{J2000.0} = +00^\circ10'09\overset{\prime\prime}{.}29 \pm 0\overset{\prime\prime}{.}062$ (68 per cent confidence uncertainty; the uncertainty in this position is the square root of the quadratically added internal uncertainty [0.″01 in both α and δ] and the uncertainty in the absolute calibration of the astrometric solution mentioned earlier). As a (conservative) limit on the detection limit of the 2 × 300 s I-band image we determined the magnitude of the faintest star detected at 5σ; it has $I = 23.5$.

We have also obtained 14 white light images with the FOcal Reducer and low dispersion Spectrograph 2 (FORS2) mounted on the 8.2 m Very Large Telescope (VLT) Yepun (images were obtained on MJD 53135.3668, 53135.3714, 53143.3471, 53143.3504, 53144.1639, 53146.3858, 53146.3901, 53148.2501, 53148.2555, 53148.2656, 53148.2665, 53148.302, 53148.3606, 53148.3624 UTC). Each of these images has an exposure time of 10 s. We cor-

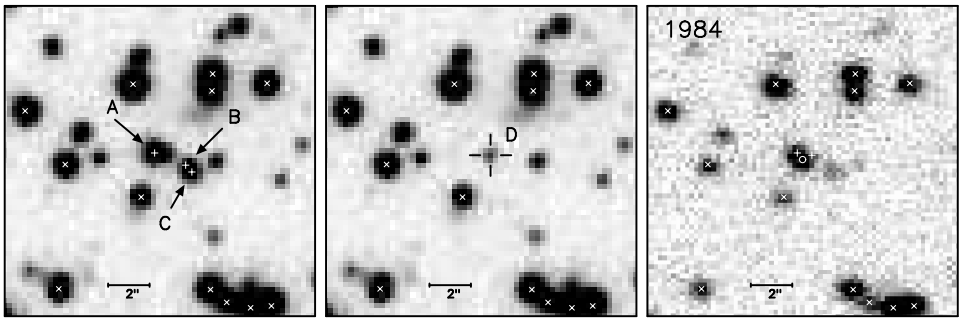

Figure 9.2: *Left: A median combined image of six 10 s VLT FORS2 white light observations of 1H 1905+000 obtained under excellent seeing conditions (< 0.″6). Middle: The three stars (A, B, C) indicated with a small, white plus sign in the left image have been subtracted using PSF-fitting. A star very close to the position of the optical counterpart in outburst remains (we call this star D). Right: The 1984 CFHT V-band observation presented in Chevalier et al. (1985) with crosses overplotted on the reference stars and "+" signs on the G-star and star D. The outburst optical position depicted by a small circle is offset from both the centroid position of the G-star and that of star D.*

rected for bias using the overscan region of the CCD, however, no white light flatfield images are available since these images were acquisition images for spectroscopic observations (see below). Therefore, we could not correct for pixel–to–pixel variations in sensitivity. We used PSF-fitting in order to determine the relative brightness of the two stars present close to the position of the optical counterpart in outburst (see Fig. 9.2). We were able to use 12 out of the 14 acquisition observations for which the seeing conditions were 0.″45–0.″82 to search for white light variability. The rms scatter in the magnitude of star D is 0.11 mag. However, this variability could have been introduced by the PSF-fitting technique since the rms variability in the fainter of the two stars in another star-pair of similar brightness ratio and separation was 0.09 mag. We conclude that star D did not vary significantly over the course of our observations. We median combined six of the 10 s images with the best seeing (seeing < 0.″6). Next, we again used the UCAC2 catalogue (Zacharias et al. 2004) to determine the position of 23 bright, unsaturated, stars in the resultant image to obtain an astrometric solution (the rms of the fit was 0.″063 in α and 0.″082 in δ. The position of star A and D are consistent with being the same as during the IMACS observations.

As mentioned above the white light images are acquisition images for spectroscopic observations. We have obtained VLT/FORS2 spectra of star A (cf. Fig. 9.1 & 9.2) using the 600B and 600RI gratings with an exposure time of ∼2750 s on MJD 53146.4006, 53148.3059, 53148.3659 and MJD 53135.3744, 53143.3541, 53143.3883, 53148.2690, respectively. Hence, the total exposure in the 600B grating spectrum was ∼2.3 h and in the 600RI grating spectrum it was ∼3.05 h. A slit width of 1″was used on each occasion. The dispersion was 1.5 Å pixel^{-1} at 4429 Å with the 600B grating and 1.65 Å pixel^{-1} at 6552 Å with the 600RI grating. With a slit width of 1″, the spectral resolution varies from approximately 400 km s^{-1} at 4430 Å to 300 km s^{-1} at 6550 Å. The spectra were extracted and reduced

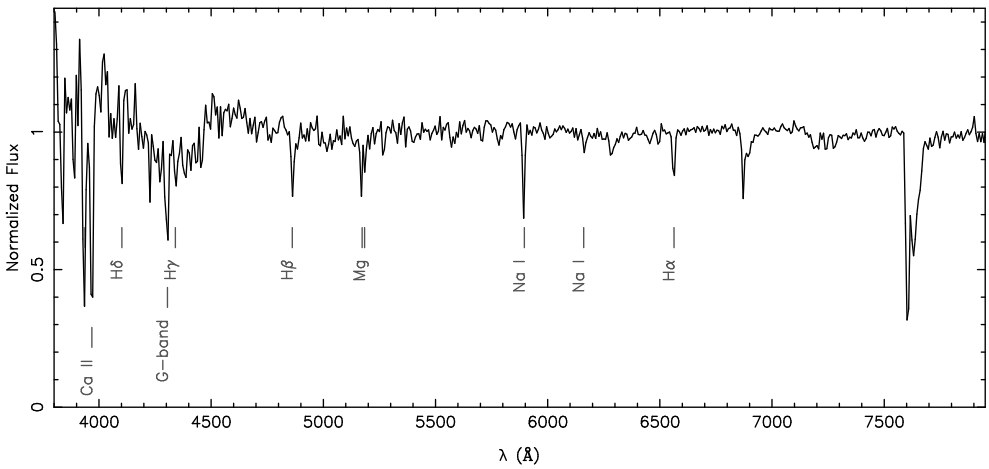

Figure 9.3: *The combined, normalised VLT FORS2 600B (2.3 h total exposure) and 600RI (3.05 h total exposure) grating spectrum of the star at the position of the outburst optical counterpart of 1H 1905+000. The spectrum resembles that of a G5–7V–star.*

using IRAF[1]. Once the spectra were reduced the spectral analysis was done using Molly. The spectrum of this star is consistent with a G5–7V star (see Fig. 9.3).

We have median combined 14 archival V-band observations of the field of 1H 1905+000 obtained with the AUX port camera mounted on the 4.2 m William Herschel Telescope located at the Roque de Los Muchachos Observatory, La Palma, Spain on July 30, 1994 (MJD 49563 UTC). These images have been retrieved from the ING Archive. In total 100 images had been obtained but we only selected the 14 with best seeing conditions (seeing $< 0\farcs8$). The G-star is detected at a magnitude $V = 20.61 \pm 0.01$ (statistical error only) and star D is barely detected at $V = 23.3 \pm 0.1$. We note however that only one standard star was observed and only one filter was obtained. Hence, colour corrections could be important (these systematic uncertainties are not included). The positions of both sources is consistent with that derived from the IMACS images.

Finally, we have obtained a subsection ($37'' \times 37''$) of the 1984 V-band outburst Canada-France-Hawaii Telescope (CFHT) image published by Chevalier et al. (1985; Ilovaisky 2005, priv. comm.). We have astrometrically tied this image to the 10 s IMACS I-band image. The uncertainty in the tie is $0\farcs050$ in α and $0\farcs055$ in δ. Although the resolution of the image is worse than that of the FORS2 and IMACS images, it is clear that there is excess emission compared to that contributable to stars at the position of star A and D (Fig. 5). Using a Gaussian for the PSF of the outburst image, we have fitted the stars on the image with the aim to determine the position of the source in outburst taking into account the flux from star A and D. The positions of the stars in the IMACS I-band observations were transformed to the CFHT image and kept fixed during the fitting process. As such, we only fitted for the overall

[1]IRAF is distributed by the National Optical Astronomy Observatories

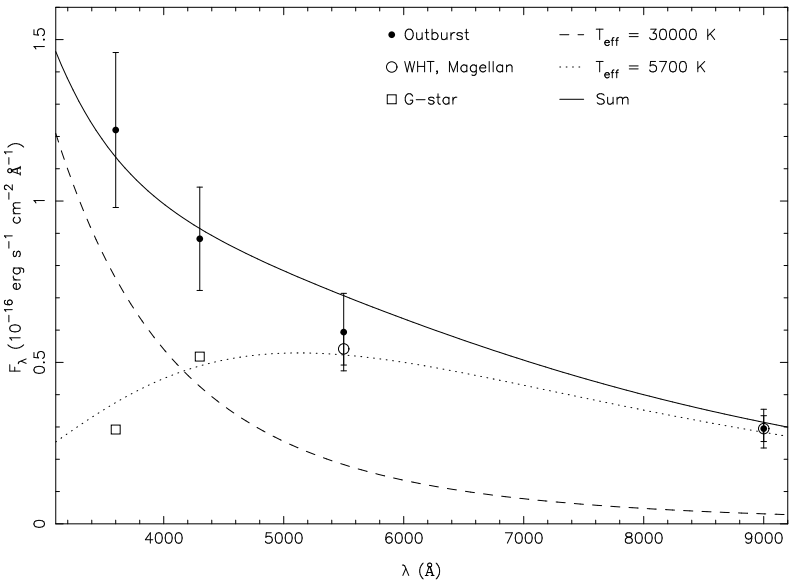

Figure 9.4: *The optical spectral energy distribution of the outburst source and the G5-7 star. As can be seen the outburst SED can be explained as the superposition (solid line) of a hot, small black body component ($T = 30000\,K$, $R = 0.08\,R_\odot$; dotted line) and the G-star ($T = 5700\,K$, $R = 1\,R_\odot$; dashed line). Note that the lines (dotted, dashed and drawn) do not represent formal fits to the data points. The circles with error bars represent the dereddened optical outburst measurements (CFHT measurements; Chevalier et al. 1985). The squares are the dereddened observed magnitudes corresponding to the G-star when the low-mass X-ray binary was in quiescence (WHT and Magellan measurements; this work). The diamonds are the dereddened magnitudes derived using the observed spectral type and the source distance necessary to explain the G-star I-band magnitude.*

background, the fluxes of the IMACS stars and the flux and position of the source in outburst. For the latter we obtain $\alpha = 19^{\rm h}08^{\rm m}27\overset{\rm s}{.}200$, $\delta = +00^\circ10'09\overset{''}{.}10$. Here, the intrinsic uncertainty on the source position is $0\overset{''}{.}03$ in both α and δ. For the absolute uncertainty this should be quadratically added to the uncertainties of the ties between the CFHT V-band and IMACS I-band image (see above) and the IMACS I-band image and the UCAC2 catalog ($0\overset{''}{.}060$ in both α and δ). However, for comparison of the outburst position with that of star A and D, we can directly compare the outburst position with the positions on the 300 s IMACS I-band image. For this, we can neglect the IMACS-UCAC2 uncertainty, but must include the uncertainty in the tie between the 10 s and 5 m IMACS images ($0\overset{''}{.}017$ in α and $0\overset{''}{.}015$ in δ). As such, star A is offset from the outburst position by $-0\overset{''}{.}255 \pm 0\overset{''}{.}062$ in α and $-0\overset{''}{.}320 \pm 0\overset{''}{.}065$ in δ, while star D is offset by $0\overset{''}{.}435 \pm 0\overset{''}{.}062$ and $-0\overset{''}{.}190 \pm 0\overset{''}{.}065$. These offsets correspond to 4.5σ for star A and 5.3σ for star D. In the righthand panel of Fig. 9.2 we have overplotted with small crosses the position of several reference stars detected in the other panels of Fig. 9.2 and with a small circle the position of the outburst optical counterpart. As can be seen it is unlikely

that the outburst counterpart can be associated with star D unless that star has a high proper motion of 24 mas yr^{-1}. At a distance of 10 kpc this would convert into a rather large velocity of $\sim$ 1100 km s^{-1}. Finally, we have investigated whether the differential Galactic rotation at $l^{ii} = 35°$ can be used to explain the observed offset of star D from the outburst optical position, under the assumption that star D arises due to the companion star and/or accretion disc of 1H 1905+000 at 10 kpc or at 7.5 kpc. The change in position with respect to other field stars is less than 0.″1 over the 20 yrs that separate the CFHT V-band outburst observations and the Magellan I-band observations. This is insufficient to explain the observed offset. We conclude that star D is not the quiescent optical counterpart to 1H 1905+000.

As mentioned above, the G-star contributes significantly to the outburst V-band magnitude measured by Chevalier et al. (1985). We used the properties of the G5–7V star and the V and I-band magnitudes observed when the low-mass X-ray binary was in quiescence to determine the G-star distance. In this we follow Chevalier et al. (1985) who noted that the interstellar extinction does not increase significantly in the direction of 1H 1905+000 for sources with a distance larger than 4 kpc. Hence, we used the same $N_{\rm H}$ for the G-star as was found for 1H 1905+000 in outburst. We used Rieke & Lebofsky (1985) to convert $N_{\rm H}$ to an A_V and the tables of Schlegel et al. (1998) to convert A_V to A_U, A_B and A_I. We corrected the observed magnitudes for the interstellar extinction and plotted the optical SED for the outburst source as well as for the G-star (see Figure 9.4). To indicate the contribution of the outburst accretion disc, we included in the plot the SED contribution of a small, spherical, hot component. For the G-star we find a distance of 8.5 kpc (fixing the radius to 1,R$_\odot$), for the accretion disc we took 10 kpc for its distance and we get a radius of $\approx$0.08 R$_\odot$ for a temperature of 3×10^4 K. Such a temperature is in the range of temperatures found for accretion discs around low-mass X-ray binaries (see for instance van Paradijs & McClintock 1995 and references therein). The fact that only such a small disc can be accommodated adds to the evidence that 1H 1905+000 is an ultra-compact X-ray binary.

9.2.2 *Chandra* X–ray observations

We observed 1H 1905+000 with the back-illuminated S3 CCD-chip of the Advanced CCD Imaging Spectrometer (ACIS) detector on board the *Chandra* satellite. The observations started on MJD 53425.852665 (UTC; Feb. 24, 2005). The net, on-source exposure time was $\sim$ 24.8 ks. The data telemetry mode was set to *very faint* to allow for a better background subtraction. After the data were processed by the *Chandra* X-ray Center (ASCDS version 7.5.0), we analyzed them using the *CIAO 3.2.1* software developed by the Chandra X-ray Center. We reprocessed the data to clean the background and take full advantage of the *very faint* data mode. We searched the data for background flares but none were found, hence we used all data in our analysis. We detect three sources in the field of view of the ACIS-S3 CCD.

Since one of the detected X–ray sources (source 1 below) has an optical counterpart detectable in our FORS2 white light images, we use the accurate optical position of this source to apply a boresight correction to the *Chandra* observation and hence improve the astrometric accuracy of the *Chandra* observation. The boresight shift that we find is:

Table 9.1: *Upper limits to the unabsorbed 0.5–10 keV source flux (f_X) and 0.5–10 keV luminosity (L_X) for various values of the interstellar extinction, different spectral energy distributions of the source, and using 7.5 and 10 kpc for the distance of 1H 1905+000. α denotes the photon index of a power law (PL) spectrum and T the temperature of a black body (BB) spectrum.*

N_H (cm^{-2})	Model	f_X ($erg\,cm^{-2}\,s^{-1}$)	L_X ($erg\,s^{-1}$)	
			$d = 7.5$ kpc	$d = 10$ kpc
2.1×10^{21}	PL $\alpha = 2.0$	1.2×10^{-15}	1.4×10^{31}	8.1×10^{30}
2.1×10^{21}	PL $\alpha = 1.5$	1.5×10^{-15}	1.8×10^{31}	1.0×10^{31}
2.1×10^{21}	BB $kT = 0.2$ keV	8.3×10^{-16}	9.9×10^{30}	5.6×10^{30}
2.1×10^{21}	BB $kT = 0.3$ keV	7.3×10^{-16}	8.7×10^{30}	4.9×10^{30}
1.9×10^{21}	PL $\alpha = 2.0$	1.2×10^{-15}	1.4×10^{31}	7.8×10^{30}
1.9×10^{21}	PL $\alpha = 1.5$	1.5×10^{-15}	1.8×10^{31}	1.0×10^{31}
1.9×10^{21}	BB $kT = 0.2$ keV	7.8×10^{-16}	9.4×10^{30}	5.3×10^{30}
1.9×10^{21}	BB $kT = 0.3$ keV	7.0×10^{-16}	8.4×10^{30}	4.7×10^{30}
1.7×10^{21}	PL $\alpha = 2.0$	1.1×10^{-15}	1.3×10^{31}	7.5×10^{30}
1.7×10^{21}	PL $\alpha = 1.5$	1.5×10^{-15}	1.7×10^{31}	9.8×10^{30}
1.7×10^{21}	BB $kT = 0.2$ keV	7.4×10^{-16}	8.8×10^{30}	5.0×10^{30}
1.7×10^{21}	BB $kT = 0.3$ keV	6.7×10^{-16}	8.0×10^{30}	4.5×10^{30}

$\Delta\alpha = -0\farcs210 \pm 0\farcs071$, $\Delta\delta = +0\farcs080 \pm 0\farcs088$. The J2000.0 α and δ of the three detected X–ray sources are: (1) $\alpha_{J2000.0} = 19^h08^m34\fs094$, $\delta_{J2000.0} = +00°11'39\farcs09$ (with an error of $0\farcs078$ in α and $0\farcs094$ in δ) (2) $\alpha_{J2000.0} = 19^h08^m22\fs183$, $\delta_{J2000.0} = +00°07'33\farcs65$ (with an error of $0\farcs11$ in α and $0\farcs12$ in δ) (3) $\alpha_{J2000.0} = 19^h08^m19\fs878$, $\delta_{J2000.0} = +00°06'18\farcs20$ (with an error of $0\farcs13$ in α and $0\farcs15$ in δ). We assign the following names to these sources CXOU J190834.1+001139, CXOU J190822.2+000734, CXOU J190819.9+000618, respectively. The X-ray source closest to the position of the optical counterpart found in outburst (Chevalier et al. 1985) is more than 2′ away. We do not detect a source at the position of the optical outburst source as measured in the CFHT V-band image in our ∼25 ks long *Chandra* observation. Furthermore, we detect no X–ray photons within a 1″ circle centered on the optical outburst position. Following Gehrels (1986), we take an upper limit of 3 source photons to determine the ∼95% upper limit on the source count rate of 1.2×10^{-4} counts s^{-1}. We used PIMMS version 3.6a[2] to estimate upper limits on the source flux for a given interstellar extinction and an (assumed) spectral energy distribution for the source. In Table 9.1 we give these upper limits to the unabsorbed 0.5–10 keV source flux and 0.5–10 keV source luminosity.

9.3 Discussion

We have observed the field of the neutron star SXT 1H 1905+000 in X-rays with the *Chandra* satellite for ∼ 25 ks, but did not detect the source in quiescence. Depending on the assumed spectral energy distribution, the interstellar extinction, and the distance we derive an upper limit to the 0.5–10 keV luminosity for 1H 1905+000 of $L_X < 1.8 \times 10^{31}$ erg s^{-1} for a distance

[2] available at http://cxc.harvard.edu/toolkit/pimms.jsp

of 10 kpc, whereas $L_X < 1.0 \times 10^{31}$ erg s^{-1} for a distance of 7.5 kpc. If we assume a neutron star of radius 10 km and a neutron star atmosphere model as given by Zavlin et al. (1996) then the upper limit on the 0.5–10 keV luminosity can be converted to an upper limit on the effective temperature of $T_{\rm eff} < 7.5 \times 10^5$ K. These upper limits imply that the quiescent X-ray luminosity of 1H 1905+000 is the lowest of any neutron star SXT observed so far for which there is a reliable distance estimate. It was found earlier that the outburst absolute V-band magnitude of the system was $M_V = 4$ (assuming a distance of 10 kpc; Chevalier et al. 1985). Compared with other SXTs in outburst this is rather low, which is typical for systems with orbital periods less than $\sim$ 80 m (also known as ultra-compact systems; see van Paradijs & McClintock 1994). Furthermore, from our optical Magellan/IMACS I-band observations of the system in quiescence and the precise astrometry we conclude that we do not detect the optical counterpart of 1H 1905+000 in quiescence, which for a distance of 10 kpc gives a limit on the absolute I-band magnitude of 1H 1905+000 in quiescence of $M_I > 7.8$. In this we took $N_{\rm H} = 1.9 \times 10^{21}$ cm^{-2} as found during outburst, used Rieke & Lebofsky (1985) to convert $N_{\rm H}$ to an A_V and the tables of Schlegel et al. (1998) to convert A_V to A_I. Our conservative upper limit on the quiescent optical absolute magnitude is completely consistent with the proposed ultra-compact nature of 1H 1905+000. In order to fit observations the companion star has to be fainter than an M2V star (Cox 2000). Hence, a (hot) brown dwarf companion star such as that of SAX J1808.4−3658 (Bildsten & Chakrabarty 2001) would also be consistent with the current constraints.

The low quiescent X-ray luminosity of this source shows that the difference in the quiescent luminosity of black hole and neutron star SXTs found initially (e.g. Garcia et al. 2001) may have been a selection effect (see also Tomsick et al. 2005). The observations reported here show that at least some of the neutron star SXTs can be as faint as the faintest black hole SXTs in quiescence. The claim that the comparison between the black hole and neutron star luminosity in SXTs in quiescence provides evidence for a black hole event horizon is hence difficult to maintain. When comparing Eddington scaled neutron star and black hole luminosities, as has been done often in the literature, black hole SXTs are still less luminous than their neutron star counterparts. The reasoning behind such a scaling stems from the notion that at orbital periods of the order of hours the gravitational wave radiation driven mass transfer rate for neutron stars and black holes is roughly similar when scaled to the Eddington rate *if the companion stars are main sequence stars* (Menou et al. 1999). However, for ultra-compact systems (as 1H 1905+000 likely is) the companion star cannot be a main sequence star making the Eddington scaling arbitrary. Furthermore, it is unclear whether the mass transfer rate set by the orbital period and the instantaneous mass accretion rate have a one-to-one correspondence in quiescent systems.

The low luminosity in quiescence can potentially be used together with the neutron star cooling theory to put constraints on the presence of condensates in the neutron star core Yakovlev & Pethick (2004). Besides the core cooling mechanism we can constrain the thermal relaxation time and hence thermal conductivity of the neutron star crust. Since we do not detect the neutron star less than 20 yr after the 11 yr long outburst the neutron star crust must have a thermal relaxation time less than 20 yr. However, presently the data does not allow us to distinguish between crustal conductivity set by electron-phonon conductivity (Baiko &

Yakovlev 1995) or by electron-ion scattering (Yakovlev & Urpin 1980), since the inclusion of Cooper-pair neutrino emission in the crust alters the description considerably with respect to the status presented in Ushomirsky & Rutledge (2001) (e.g. see Yakovlev et al. 1999). Currently, less than 20 yr after the outburst, the quiescent luminosity is determined by the core cooling processes again. However, to estimate the core temperature the average mass accretion rate over the last 10^4-10^5 yrs has to be known (Colpi et al. 2001). This we can estimate from binary evolution theory. A primer for the evolutionary state of the low-mass X-ray binary (outside globular clusters) is the orbital period. In case of 1H 1905+000 the orbital period is unknown. However, as explained above, it is likely that 1H 1905+000 is an ultra-compact X-ray binary. The mass accretion rate for an ultra-compact system depends on the exact orbital period and the nature and age of the companion star but it can be as low as $\sim 10^{-13}\,\mathrm{M_\odot\,yr^{-1}}$ if the system is ~ 10 Gyr old and if the orbital period is 60–90 minutes (e.g. Verbunt & van den Heuvel 1995, Deloye & Bildsten 2003, see also King & Wijnands 2006). If indeed the time averaged mass accretion rate is this low, the current limit on the luminosity does not provide a constraint on the core cooling. However, at such low mass transfer rates it might be difficult to feed an outburst that lasts longer than 11 yr where the X-ray luminosity is $\sim 4 \times 10^{36}$ erg,s^{-1} as in the case of 1H 1905+000[3]. In order to sustain such an accretion rate for 11 yr the neutron star should have accreted $\approx 4 \times 10^{-9}\,\mathrm{M_\odot}$. If the mass transfer rate is $10^{-13}/10^{-12}\,\mathrm{M_\odot\,yr^{-1}}$ then it would take at least $3.5 \times 10^4/3.5 \times 10^3$ yr to build-up the accretion disc. In both cases this is a significant fraction of the core heating timescale. Brown et al. (1998) showed that in such a case the fraction of the heat released deep in the crust that is used to heat the core is smaller than 1. Assuming that the fraction is not less than 0.1 in 1H 1905+000 then, following Brown et al. (1998) we derive that for a time averaged mass accretion rate larger than $2 \times 10^{-12}\,\mathrm{M_\odot\,yr^{-1}}$, enhanced neutrino emission processes must be operating in the core.

Next, we discuss the possibility that systematic effects make 1H 1905+000 appear faint in quiescence whereas the true luminosity in quiescence is significantly higher. We shall show, however, that this is unlikely. If the distance is systematically underestimated the source luminosity may be higher. However, the distance for 1H 1905+000 is derived from the observed radius expansion burst peak flux. Kuulkers et al. (2003) have calibrated this distance estimation method comparing the distances derived from the burst peak fluxes of sources in globular clusters to the accurately known distances of those globular clusters. From their work it can be seen that if the composition of the burning material is known (hydrogen or helium rich burning material) the peak burst flux gives a reliable estimate of the distance (to within approximately 15%). In ultra-compact systems hydrogen is likely depleted (Nelson et al. 1986; see Podsiadlowski et al. 2002 for a possible binary evolutionary scenario leading to ultra-compact systems with some hydrogen still present). Therefore, it is save to assume that the radius expansion burst peak flux corresponds to the helium Eddington limit luminosity. In case of 1H 1905+000 this helium radius expansion burst limit on the distance is 10 kpc (see Jonker & Nelemans 2004). If however, hydrogen was present in the burning material the distance becomes smaller, making the upper limit on the quiescent luminosity more stringent still. The interstellar extinction, N_H, towards 1H 1905+000 is low compared to that

[3] 1H 1905+000 is only the third transient known to date that returned to quiescence after a long–duration outburst.

found for most other low-mass X-ray binaries. From Einstein observations obtained when the source was in outburst Christian & Swank (1997) determined that the $N_{\rm H}$ to 1H 1905+000 is $(1.9 \pm 0.2) \times 10^{21}$ cm^{-2}. Typically, for many SXTs it is found that the interstellar extinction probed by N_H is somewhat higher in outburst than in quiescence (Jonker & Nelemans 2004). For that reason it is unlikely that the neutron star quiescent luminosity is much higher but that the source is hidden from our view due to an interstellar extinction that is much larger than measured in outburst.

Previous observations of several accretion-powered millisecond X-ray pulsars in quiescence have also shown that many of those sources have a low quiescent luminosity (e.g. SAX J1808.4−3658, Campana et al. 2002, XTE J0929−314 and XTE J1751−305, Wijnands et al. 2005, XTE J1807−294, Campana et al. 2005). However, except for SAX J1808.4−3658, the distance estimates for these systems are uncertain which makes the quiescent luminosity uncertain as well. Although, in order for these systems to have a luminosity $\sim 10^{33}$ erg s^{-1}, i.e. similar to that observed for Aql X-1 and XTE J1709−267 (Rutledge et al. 2002a; Jonker et al. 2003), the distance has to be unrealistically large, e.g. ~ 40 kpc for XTE J0929−314. The planned deep (300 ks) *Chandra* X-ray observation of 1H 1905+000 will provide new constraints on or a measurement of the quiescent neutron star luminosity in this system.

Hoofdstuk 10

Nederlandse samenvatting

Dit proefschrift gaat over dubbelsterren: twee sterren die als gevolg van de zwaartekracht om elkaar heen draaien. Deze systemen zijn van groot belang voor de sterrenkunde, omdat ze de mogelijkheid bieden om unieke eigenschappen van deze sterren te bepalen. De systemen die in dit proefschrift onderzocht worden zijn compacte dubbelsterren, met baanperiodes korter dan enkele dagen tot minder dan een uur, die of tot een bolvormige sterrenhoop behoren of waarvan een van de twee sterren een neutronenster is. Door middel van voornamelijk optische, maar ook röntgen-waarnemingen, worden sommige van de eigenschappen van deze compacte dubbelsterren bepaald.

10.1 De evolutie van enkele sterren...

Sterren onstaan uit in elkaar stortende wolken van interstellair gas en stof. In het centrum van zo'n wolk zullen de dichtheid en temperatuur stijgen totdat de gasdeeltjes zo krachtig met elkaar botsen dat ze beginnen te fuseren. Bij dit proces, wat kernfusie wordt genoemd, wordt waterstof omgezet tot helium en komt energie vrij, wat het instorten van de wolk zal stoppen. De wolk zal in een toestand komen waarbij de energie-productie in het centrum in evenwicht is met het energie-verlies aan het oppervlak (het uitstralen van licht). Voor het grootste gedeelte van hun leven zullen sterren in hun kern waterstof fuseren tot helium.

Sterren in deze fase van hun leven worden hoofdreeks-sterren genoemd. De Zon is zo'n hoofdreeks-ster[1], en voor haar zal deze fase zal zo'n 10 miljard jaar duren (met een leeftijd van ongeveer 4.5 miljard jaar is de Zon ruwweg halverwege deze fase). Voor sterren zwaarder dan de Zon is het kernfusie-proces veel sneller en wordt er meer energie geproduceerd. Om toch in evenwicht te blijven zijn deze sterren groter, heter aan het oppervlak en stralen ze meer licht uit dan een ster als de Zon. Tevens leven deze sterren veel korter dan de Zon. Een

[1] De Zon heeft een massa van 2×10^{30} kg ($1\,M_\odot$; een 2 met 30 nullen), een straal van 700 000 km ($1\,R_\odot$) en een lichtkracht van 4×10^{26} Watt ($1\,L_\odot$).

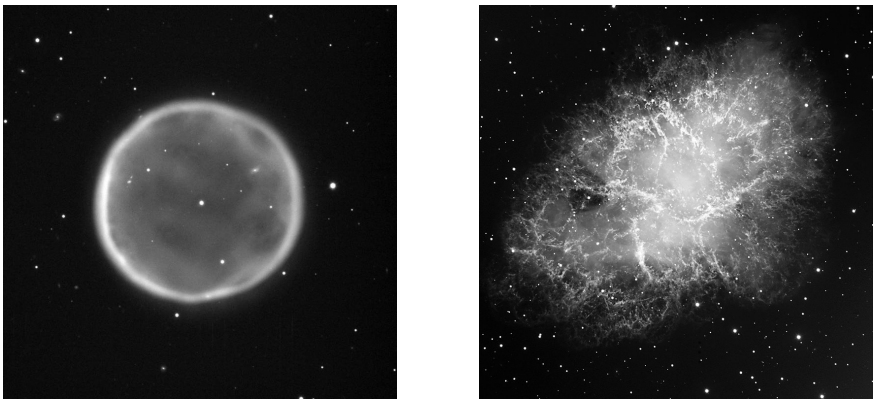

Figuur 10.1: Links: *De planetaire nevel Abell 39 is het overblijfsel van een lichte ster. De weggeblazen mantel van de ster is te zien als een schil om de witte dwerg in het centrum. (Oorsprong: WIYN/NOAO/NSF.)* Rechts: *In 1054 zag men in China een nieuwe ster aan de hemel verschijnen. Tegenwoordig zien we op deze plek aan de hemel de restant van een zware ster die toen een supernova explosie onderging: de Krabnevel. In het centrum van deze supernova restant staat een radio pulsar (een snel roterende neutronenster). (Oorsprong: ESO.)*

ster die 5 keer zwaarder is dan de zon leeft maar 120 miljoen jaar. Voor lichtere sterren geldt het omgekeerde: ze zijn kleiner, koeler, stralen minder licht uit en leven langer.

Wanneer de waterstofvoorraad in de kern van een ster opraakt zal ze waterstof gaan fuseren in een schil rond een kern van helium. In deze kern zal kan daarna weer helium worden gefuseerd tot koolstof en zuurstof. Bij deze fusie-processen komt zoveel energie vrij dat de ster maar moeilijk het evenwicht tussen energie-productie en energie-verlies kan bewaren. Als gevolg hiervan zal ze enorm opzwellen en in helderheid toenemen (de Zon zal 200 keer groter en 10 000 keer helderder worden dan ze nu is) en wordt de ster een rode reus. Ook zal de ster delen van haar buitenlaag wegblazen (zie Fig. 10.1). Wat overblijft hangt af van de beginmassa van de ster. Voor sterren die lichter zijn dan ongeveer $8\,M_\odot$ zal alleen de kern van de ster overblijven en een witte dwerg vormen. Witte dwergen zijn ongeveer zo groot als de Aarde (ongeveer 10 000 km) en hebben een massa van $0.6\,M_\odot$ en dus een enorme dichtheid. Er vind geen kernfusie meer plaats in een witte dwerg, en ze zullen dus heel erg langzaam de nog aanwezige energie in de kern uitstralen, waardoor ze afkoelen en krimpen. Het leven van sterren zwaarder dan $8\,M_\odot$ zal eindigen met het instorten van de kern. In plaats van een witte dwerg te vormen zal de kern van zo'n ster verder instorten en wordt de materie van de kern omgezet tot neutronen. Bij dit proces komt zoveel energie vrij dat de buitenlagen van de ster explosief het heelal worden ingeslingerd. We zien dit als een supernova explosie. Het overblijfsel van de ineengestorte kern van de oorspronkelijke ster heeft een massa van ongeveer $1.4\,M_\odot$, een straal van 10 km en bestaat volledig uit neutronen: een neutronenster.

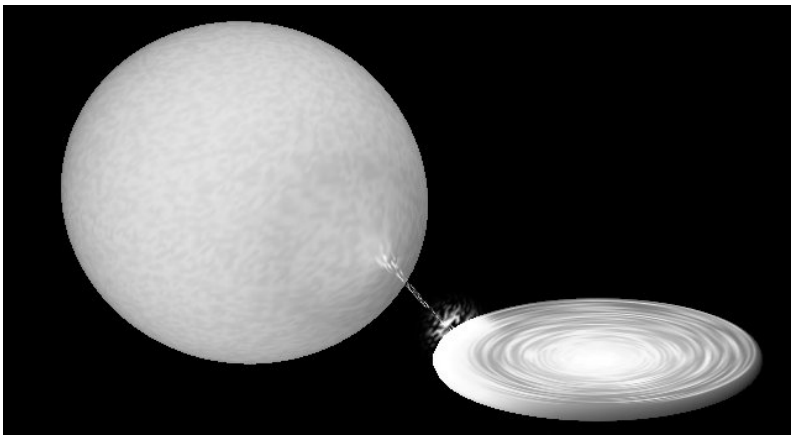

Figuur 10.2: *Een artistieke impressie van een röntgendubbelster (naar Rob Hynes). Materie van een normale ster (links) stroomt via een accretieschijf naar een compact object (rechts).*

10.2 . . . en van dubbelsterren

In het algemeen zullen sterren in dubbelsterren anders evolueren ten opzichte van een enkele ster met dezelfde eigenschappen. De oorzaak hiervan ligt bij het feit dat sterren in de eindfasen van hun leven enorm opzwellen. Omdat de materie van de uitdijende ster ook door de andere wordt aangetrokken bestaat er een punt waarop de aantrekkingskracht van beide sterren even sterk is. Als de uitdijende ster dit punt bereikt zal materie van die ster naar de dubbelsterbegeleider stromen, met dramatische gevolgen voor beide sterren. De massa-verliezende ster zal lichter worden en daardoor als een lichtere ster verder evolueren. De ster kan zelfs haar hele mantel verliezen waardoor ze op een veel vroeger stadium in een witte dwerg evolueert. De ster die de massa ontvangt zal zwaarder worden en zal dus als een zwaardere ster evolueren. Op deze manier kan een ster die oorspronkelijk tot een witte dwerg zou evolueren een neutronenster achterlaten. Door middel van de overdracht van materie tussen sterren wordt de evolutie van beide sterren dus dramatisch beïnvloed. Verder zal de baan van de dubbelster krimpen of uitzetten, afhankelijk of de materie van een zware naar een lichte ster stroomt of andersom.

Bij de overdracht van materie tussen een normale ster en een compacte ster (een witte dwerg of neutronenster) zal de materie eerst een schijf om de compacte ster vormen voordat het op de massa-ontvangende ster valt (Fig. 10.2). De materie stroomt van de buitenkant van de schijf, die een accretie-schijf wordt genoemd, langzaam naar de binnenkant, waarbij het steeds sneller om de compacte ster heen gaat draaien en steeds heter wordt. Hierdoor gaat de accretie-schijf ultraviolet licht uitstralen. Wanneer de materie uiteindelijk op het compacte object valt komt de bewegingsenergie vrij als röntgenstraling. De systemen waar een witte dwerg de materie ontvangt noemen we cataclysmische variabelen, terwijl systemen met een neutronen ster als massa-ontvanger (lage massa) röntgendubbelsterren worden genoemd.

De massa-verliezende sterren in röntgendubbelsterren zullen uiteindelijk zoveel materie

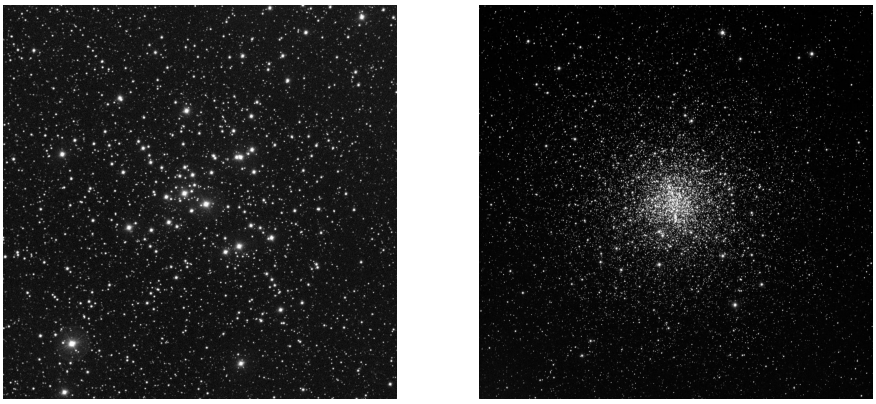

Figuur 10.3: *De open sterrenhoop M41 en de bolvormige sterrenhoop M4 (zie hoofdstuk 2). (Oorsprong: WIYN/NOAO/NSF.)*

verliezen dat er lage-massa witte dwergen overblijven, waarbij de overdracht van materie stopt. Op deze manier onstaan dus dubbelsterren met korte baanperiodes die bestaan uit twee witte dwergen of uit een witte dwerg en een neutronenster. De witte dwergen zullen afkoelen en snel zwakker worden zodat we ze niet of nauwelijks meer kunnen zien, maar in het geval van röntgendubbelsterren met neutronensterren kan iets speciaals gebeuren als de witte dwerg gevormd wordt. Door de materie-overdracht is de neutronenster zo snel rond gaan draaien (enkele honderden keren per seconde) dat ze radiostraling uitzendt: de neutronenster is een milliseconde-pulsar geworden. Terwijl de witte dwerg steeds zwakker wordt kan de neutronenster nog steeds waarneembaar blijven met radiotelescopen.

10.3 Dubbelsterren in bolvormige sterrenhopen en de Melkweg

Sterren worden meestal niet alleen gevormd. Waar kleine gaswolken enkele sterren of dubbelsterren zullen vormen, onstaan uit grote gaswolken groepen van sterren, ook wel sterrenhopen genaamd. In onze Melkweg zijn deze sterrenhopen in twee groepen te verdelen. Aan de ene kant zijn er de open sterrenhopen, zoals de Pleiaden en Hyaden die met het blote oog te zien zijn, en aan de andere kant zijn er de bolvormige sterrenhopen (zie Fig. 10.3). Waar open sterrenhopen enkele duizenden sterren bevatten en een jonge tot middelmatige leeftijd hebben, bevatten bolvormige sterrenhopen enkele honderd-duizenden tot meer dan een miljoen sterren en behoren ze tot de oudste objecten in de Melkweg (10 tot 13 miljard jaar oud).

De combinatie van de leeftijd en het aantal sterren in een bolvormige sterrenhoop klinkt op het eerste gezicht als een *contradictio in terminis*: alle sterren trekken elkaar aan en de sterrenhoop zou in moeten storten, zodat ze nooit zo oud kan worden. Het blijkt nu dat dubbelsterren een hoofdrol spelen in de evolutie van bolvormige sterrenhopen. Wanneer de sterrenhoop probeert in te storten neemt de sterdichtheid in de kern van de bolhoop zo toe dat losse sterren met dubbelsterren interacties ondergaan en onderling energie uit wisselen. Via

deze manier werken dubbelsterren als een reservoir van energie wat de ineenstorting van (de kern van) bolvormige sterrenhopen tegen kan gaan.

De grote dichtheid aan sterren in bolvormige sterrenhopen zal tot verschillende exotische processen leiden. In bolvormige sterrenhopen zullen dus naast normale dubbelsterren ook systemen ontstaan uit ontmoetingen van enkele sterren. Bijna altijd zijn dit systemen waarvan één van de sterren een neutronenster is. Verder zal de energie die uitgewisseld wordt in ontmoetingen tussen dubbelsterren en enkele sterren meestal leiden tot het compacter worden van de dubbelster, terwijl de enkele ster een grotere snelheid krijgt. Het kan zelfs gebeuren dat in zo'n ontmoeting een ster in een dubbelster van plaats wisselt met de enkele ster. In zo'n geval is het meestal de lichtste ster in de dubbelster die als enkele ster verder gaat. Als gevolg van de zwaartekracht zullen de zwaardere sterren (en dus ook de dubbelsterren) naar de kern van de bolhoop zakken, terwijl de lichtere sterren naar de buitengebieden zullen bewegen. Al deze processen zullen bijdragen aan de dynamische vorming van dubbelsterren in bolvormige sterrenhopen.

In de Melkweg (het sterrenstelsel waartoe ons planetenstelsel behoort) is de sterdichtheid over het algemeen veel lager (tot wel een miljoen keer lager). Zodoende zullen de dubbelsterren met neutronensterren in de Melkweg niet door dynamische processen gevormd zijn, maar van oorspronkelijke dubbelsterren evolueren. Toch bevat de Melkweg redelijk veel dubbelsterren, simpelweg omdat ze zo'n 100 miljard sterren bevat. Er zijn zo'n 150 röntgendubbelsterren en ongeveer 70 dubbelsterren met milliseconde pulsars bekend.

10.4 Dit proefschrift

In dit proefschrift onderzoek ik compacte dubbelsterren in bolvormige sterrenhopen en vergelijkbare systemen in de Melkweg. Door op verschillende golflengten naar deze systemen te kijken probeer ik eigenschappen van de dubbelsterren te bepalen om zo vraagstukken over de systemen te beantwoorden.

Hoofdstuk 2 en 3

In deze hoofdstukken onderzoeken we of de dubbelsterren in de bolvormige sterrenhopen M4 (zie Fig. 10.3) en NGC 288 door dynamische processen zijn gevormd of van oorspronkelijke systemen zijn ge-evolueerd. In tegenstelling tot de meeste eerder onderzochte bolvormige sterrenhopen hebben deze twee een redelijk lage centrale sterdichtheid, en verwachten we dat dynamische vormingsprocessen een minder belangrijke rol spelen dan in de dichtere bolhopen.

Voor het onderzoek gebruiken we röntgenwaarnemingen met de *Chandra* röntgensatelliet (zie Fig. 10.4) om röntgenbronnen in deze sterrenhopen te vinden. Door de posities van de röntgenbronnen te vergelijken met posities van optische sterren in waarnemingen van de *Hubble* ruimtetelescoop kunnen we de optische tegenhangers identificeren en de röntgenbronnen classificeren. In beide bolhopen vinden we enkele dubbelsterren met witte dwergen, en in M4 zien we een bekende milliseconde-pulsar (met een witte dwerg begeleider) als röntgenbron. Het overgrote deel van de röntgenbronnen zijn magnetisch actieve

Figuur 10.4: Links: *Het* Chandra X-ray Observatory*, de röntgensatelliet waarmee de röntgenwaarnemingen van hoofdstukken 2, 3 en 9 zijn verkregen. (Oorsprong: NASA)* Midden: *Eén van de vier optische telescopen van de* Very Large Telescope *van de Europese Zuidelijke Sterrenwacht (ESO). Zie hoofdstuk 5 en 9. (Oorsprong: ESO)* Rechts: *Sommige van de optische waarnemingen in hoofdstukken 2, 3, 4 en 6 zijn verkregen met de* Hubble Space Telescope*. (Oorsprong: NASA)*

dubbelsterren, bestaande uit twee hoofdreeks-sterren. In deze systemen draait één (of beide) van de sterren snel om zijn as waardoor de magnetische activiteit van de ster veel hoger is dan wanneer de ster niet in een dubbelster zou zitten. Dit komt omdat de door de zwaartekracht opgewekte getijden de spinperiode van de ster synchronizeert met de oploopperiode van de dubbelster[2]. Een ster als de Zon, die eens per maand om haar as draait, doet dat nu drie keer per dag.

Door de aantallen van de geclassificeerde bronnen te vergelijken met die in andere bolhopen kunnen we achterhalen of deze dubbelsterren een dynamische oorsprong hebben. Voor de magnetisch actieve dubbelsterren zien we dat dit duidelijk niet het geval is. We vinden tevens dat het aantal actieve dubbelsterren lijkt te schalen met de massa van de kern van de bolhoop.

Hoofdstuk 4 en 5

In 2002 werd er een milliseconde pulsar in een dubbelster gevonden die in de buurt van een bolvormige sterrenhoop stond. Dit wekte de vraag of het systeem daadwerkelijk bij de sterrenhoop hoort en als dat het geval was, hoe het dan zover van de kern van de bolhoop kon komen te staan. De dubbelster zou een van de zwaarste systemen in de sterrenhoop zijn en dus snel naar de kern moeten zakken. Er werd geopperd dat het systeem door een interactie met andere sterren (of zelfs zwarte gaten) uit de kern van de bolhoop was geslingerd.

Om deze vragen verder te bestuderen hebben we archief-waarnemingen met de *Hubble Space Telescope* onderzocht, en hier vonden we een ster die precies op de positie van de pulsar stond (Fig. 4.1). Verder had de ster de helderheid en de kleur die je zou verwachten voor een witte dwerg op de afstand van de bolhoop, zodat we konden concluderen dat deze ster de dubbelsterbegeleider van de pulsar was, en dat het systeem zeer waarschijnlijk bij de

[2]Dit doet de Maan met de Aarde: we zien altijd hetzelfde halfrond van de Maan omdat de spinperiode van de Maan gesynchronizeert is met de oploopperiode van de Maan rond de Aarde.

bolhoop hoort.

Om het systeem verder te onderzoeken hebben we nieuwe waarnemingen van de witte dwerg aangevraagd met de *Very Large Telescope* in Chili. Met deze waarnemingen konden we de massa's van de witte dwerg en de neutronenster bepalen, en kregen we extra informatie over het lidmaatschap van de dubbelster en de bolvormige sterrenhoop. Uit de straal en de temperatuur van de witte dwerg konden we onafhankelijk de afstand van de witte dwerg bepalen, en tevens konden we de snelheid van de witte dwerg langs de gezichtslijn vergelijken met de snelheid van de bolhoop. Als de dubbelster bij de sterrenhoop zou horen dan zouden deze metingen overeen moeten komen met de getallen van de bolvormige sterrenhoop. Helaas vonden we dat, binnen de onzekerheid van onze metingen, de eigenschappen *net niet* compatibel waren. Zodoende konden we niet met zekerheid zeggen of het systeem nu wel of niet bij de sterrenhoop hoort, zodat de controverse rond dit systeem nog steeds niet is opgelost.

Hoofdstuk 6

PSR J1740−5340 in de bolvormige sterrenhoop NGC 6397 is een heel uniek systeem omdat de milliseconde pulsar een hoofdreeks-ster als dubbelster-begeleider heeft. Uit de rotatie eigenschappen van de pulsar (spin periode en de snelheid waarmee deze afneemt) blijkt dat de energie die de pulsar verliest door het langzamer te gaan draaien, de begeleider zou moeten verhitten, wat er toe zou moeten leiden dat de begeleider op een bepaalde manier in helderheid zou moeten varieren. Vreemd genoeg wordt dit door de waarnemingen geheel uitgesloten. Verschillende scenaria zijn bedacht om dit te verklaren, maar geen enkele gaf een geloofwaardige oplossing.

Toevallig vonden we dat de positie van de hoofdreeks-ster aan de hemel niet consistent was met die van de pulsar, wat wel het geval zou moeten zijn. Omdat de positie sterk gecorreleerd is met de rotatie eigenschappen van de pulsar, wees dit erop dat deze eigenschappen van de pulsar wellicht fout zouden zijn. Nader onderzoek van de groep die de pulsar had ondekt bevestigde onze vermoedens: de nieuwe positie van de pulsar kwam beter overeen met onze optische positie. Als gevolg van de nieuwere positie veranderden de eigenschappen van de pulsar, wat het probleem rond de helderheidsvariaties oploste.

Hoofdstuk 7

In dit hoofdstuk hebben we PSR J0751+1807 onderzocht, een dubbelster bestaande uit een milliseconde pulsar met een witte-dwerg begeleider, behorende tot het Melkweg-vlak. Uit waarnemingen is gebleken dat vergelijkbare systemen met baanperiodes korter dan 2 dagen de witte dwerg nog een relatief dikke waterstof laag (5% van de witte-dwerg massa) om de kern van helium moet hebben. Zodoende koelen deze witte dwergen langzamer en zijn ze langer waar te nemen dan systemen met langere baanperiodes, die dunne waterstof-lagen hebben. Met een baanperiode van iets meer dan 6 uur, heeft dit systeem de korste baanperiode van alle milliseconde pulsars/witte dwerg dubbelsterren in de Melkweg.

Waar we een warme witte dwerg met een dikke waterstof laag verwachtten te zien, toonden onze waarnemingen aan dat de witte dwerg juist koel was. Uit de waarnemingen bleek dat de laag aan het oppervlak van de witte dwerg of uit helium of een mengsel van

helium en waterstof bestaat. Het is geopperd dat de waterstof-laag door de wind van de pulsar is weggeblazen, maar hiervoor vinden we geen bewijs.

Hoofdstuk 8

Het is over het algemeen moeilijk om de baanperiode van een (lage massa) röntgendubbelster te bepalen. Voor sommige systemen schuift de normale ster periodiek voor de neutronenster en de accretieschijf langs, zodat uit variaties van de röntgenhelderheid de baanperiode kan worden bepaald, terwijl bij andere systemen helderheidsvariaties in de optische helderheid het mogelijk maken om de baanperiode af te leiden. Er zijn ook indirecte methodes, en een zo'n methode gaat ervan uit dat de optische helderheid wordt veroorzaakt door röntgenstraling die in de accretieschijf wordt omgezet in zichtbaar licht. Zodoende verwacht men een relatie tussen de optische helderheid van een röntgendubbelster, de röntgenhelderheid en de grootte van de accretieschijf. Dit laatste hangt af van de baanperiode, en zo kan men uit alleen de optische en de röntgenhelderheid van een röntgendubbelster een idee krijgen van de baanperiode van het systeem.

In dit hoofdstuk passen we deze methode toe op twee lage-massa röntgendubbelsterren waarvan het vermoeden bestaat dat ze een baanperiode van 1 uur of korter hebben. Onze waarnemingen laten zien dat volgens deze methode, de systemen inderdaad zulke korte baanperiodes moeten hebben. In deze ultra-compacte röntgendubbelsterren past geen normale ster (hoofdreeks of rode reus) meer in een baan rond een neutronenster, en de begeleider moet zodoende een witte dwerg zijn. In deze systemen ontvangt de neutronenster dus materie van een witte dwergen, en in tegenstelling tot materie van normale sterren, kan de materie dus uit helium, koolstof/zuurstof of zelfs zwaardere elementen bestaan. Ultra-compacte röntgendubbelsterren zijn dus unieke systemen om de samenstelling van witte dwergen (en dus van de kernen van sterren) te onderzoeken.

Hoofdstuk 9

In het laatste hoofdstuk onderzoeken we een andere lage massa röntgendubbelster met een mogelijk ultra-compacte baan. Deze röntgenbron is vanaf 1975 door verschillende röntgensatellieten waargenomen, maar vanaf 1985 tot 1990 is de bron niet meer gezien.

In een röntgenwaarneming met de *Chandra* satelliet zien we de bron nog steeds niet, wat erop duidt dat de hoeveelheid materie die naar de neutronenster stroomt erg is afgenomen. We gebruiken dit om de snelheid waarmee een neutronenster afkoelt te begrenzen. Verder analyseren we optische waarnemingen van de positie aan de hemel waar de röntgenbron stond toen deze nog helder was. We zien ook de optische begeleider niet, wat erop duidt dat deze intrinsiek zwak is. Dit klopt met de suggestie dat dit systeem een ultra-compacte röntgendubbelster is.

References

Abramowicz, M. A., Kluźniak, W., & Lasota, J.-P. 2002, A&A, 396, L31

Alberts, F., Savonije, G. J., van den Heuvel, E. P. J., & Pols, O. R. 1996, Nature, 380, 676

Albrow, M. D., Gilliland, R. L., Brown, T. M., et al. 2001, ApJ, 559, 1060

Aldcroft, T. L., Karovska, M., Cresitello-Dittmar, M. L., Cameron, R. A., & Markevitch, M. L. 2000, in Proc. SPIE Vol. 4012, p. 650-657, X-Ray Optics, Instruments, and Missions III, Joachim E. Truemper; Bernd Aschenbach; Eds., ed. J. E. Truemper & B. Aschenbach, 650–657

Alpar, M. A., Cheng, A. F., Ruderman, M. A., & Shaham, J. 1982, Nature, 300, 728

Althaus, L. G., Serenelli, A. M., & Benvenuto, O. G. 2001, MNRAS, 324, 617

Anderson, J. & King, I. R. 2003, PASP, 115, 113

Arnaud, K. A. 1996, in ASP Conf. Ser. 101: Astronomical Data Analysis Software and Systems V, ed. G. H. Jacoby & J. Barnes, 17

Assafin, M., Zacharias, N., Rafferty, T. J., et al. 2003, AJ, 125, 2728

Ayres, T. R. 2004, ApJ, 608, 957

Baiko, D. A. & Yakovlev, D. G. 1995, Astronomy Letters, 21, 702

Bassa, C., Pooley, D., Homer, L., et al. 2004, ApJ, 609, 755

Bassa, C., Pooley, D., Homer, L., et al. 2005, ApJ, 619, 1189

Bassa, C. G., van Kerkwijk, M. H., & Kulkarni, S. R. 2003a, A&A, 403, 1067

Bassa, C. G., Verbunt, F., van Kerkwijk, M. H., & Homer, L. 2003b, A&A, 409, L31

Becker, W., Trumper, J., Lundgren, S. C., Cordes, J. M., & Zepka, A. F. 1996, MNRAS, 282, L33

Bedin, L. R., Anderson, J., King, I. R., & Piotto, G. 2001, ApJ, 560, L75

Bedin, L. R., Piotto, G., King, I. R., & Anderson, J. 2003, AJ, 126, 247

Bellazzini, M., Fusi Pecci, F., Montegriffo, P., et al. 2002, AJ, 123, 2541

Belloni, T., Verbunt, F., & Mathieu, R. 1998, A&A, 339, 431

Bergeron, P. 2001, ApJ, 558, 369

Bergeron, P. & Leggett, S. K. 2002, ApJ, 580, 1070

Bergeron, P., Leggett, S. K., & Ruiz, M. T. 2001, ApJS, 133, 413

Bergeron, P., Wesemael, F., & Beauchamp, A. 1995, PASP, 107, 1047

Bessell, M. S. 1990, PASP, 102, 1181
Bessell, M. S., Castelli, F., & Plez, B. 1998, A&A, 333, 231
Bhattacharya, D. & Verbunt, F. 1991, A&A, 242, 128
Bildsten, L. & Chakrabarty, D. 2001, ApJ, 557, 292
Biretta, J. A., e. a. 2000, WFPC2 Instrument Handbook Version 5.0 (Baltimore, STScI)
Boller, T., Haberl, F., Voges, W., Piro, L., & Heise, J. 1997, IAU Circ., 6546
Bolte, M. 1992, ApJS, 82, 145
Brandt, W. N., Alexander, D. M., Hornschemeier, A. E., et al. 2001, AJ, 122, 2810
Broos, P. S., Townsley, L. K., Getman, K., & Bauer, F. E. 2002, ACIS Extract, An ACIS Point Source Extraction Package (University Park, Pennsylvania State Univ.)
Brown, E. F., Bildsten, L., & Chang, P. 2002, ApJ, 574, 920
Brown, E. F., Bildsten, L., & Rutledge, R. E. 1998, ApJ, 504, L95
Callanan, P. J., Garnavich, P. M., & Koester, D. 1998, MNRAS, 298, 207
Camilo, F. & Rasio, F. A. 2005, in ASP Conf. Ser. 328: Binary Radio Pulsars, ed. F. A. Rasio & I. H. Stairs, 147
Campana, S., Ferrari, N., Stella, L., & Israel, G. L. 2005, A&A, 434, L9
Campana, S., Israel, G. L., Stella, L., Gastaldello, F., & Mereghetti, S. 2004, ApJ, 601, 474
Campana, S. & Stella, L. 2000, ApJ, 541, 849
Campana, S., Stella, L., Gastaldello, F., et al. 2002, ApJ, 575, L15
Carretta, E., Gratton, R. G., Clementini, G., & Fusi Pecci, F. 2000, ApJ, 533, 215
Chen, W., Shrader, C. R., & Livio, M. 1997, ApJ, 491, 312
Chevalier, C. & Ilovaisky, S. A. 1990, A&A, 228, 115
Chevalier, C., Ilovaisky, S. A., & Charles, P. A. 1985, A&A, 147, L3
Christian, D. J. & Swank, J. H. 1997, ApJS, 109, 177
Clark, G. 1975, ApJ, 199, L143
Clark, G., Markert, T., & Li, F. 1975, ApJ, 199, L93
Cocchi, M., Bazzano, A., Natalucci, L., et al. 2001, A&A, 378, L37
Cocchi, M., Bazzano, A., Natalucci, L., et al. 2000, A&A, 357, 527
Cocozza, G., Ferraro, F. R., Possenti, A., & D'Amico, N. 2006, ApJ, 641, L129
Colpi, M., Geppert, U., Page, D., & Possenti, A. 2001, ApJ, 548, L175
Colpi, M., Mapelli, M., & Possenti, A. 2003, ApJ, 599, 1260
Colpi, M., Possenti, A., & Gualandris, A. 2002, ApJ, 570, L85
Cook, G. B., Shapiro, S. L., & Teukolsky, S. A. 1994, ApJ, 424, 823
Cool, A., Grindlay, J., Cohn, H., Lugger, P., & Bailyn, C. 1998, ApJ, 508, L75
Cordes, J. M. & Lazio, T. J. W. 2002, astro-ph/0207156
Cornelisse, R., Verbunt, F., in't Zand, J. J. M., Kuulkers, E., & Heise, J. 2002, A&A, 392, 931
Cox, A. N. 2000, Allen's astrophysical quantities (Allen's astrophysical quantities, 4th ed. Publisher: New York: AIP Press; Springer, 2000. Edited by Arthur N. Cox.)
Cudworth, K. M. & Rees, R. 1990, AJ, 99, 1491
Curtis, H. D. 1906, ApJ, 23, 351
Cutri, R. M., Skrutskie, M. F., van Dyk, S., et al. 2003, VizieR Online Data Catalog, 2246
D'Amico, N., Lyne, A. G., Manchester, R. N., Possenti, A., & Camilo, F. 2001a, ApJ, 548,

L171
D'Amico, N., Possenti, A., Fici, L., et al. 2002, ApJ, 570, L89
D'Amico, N., Possenti, A., Manchester, R. N., et al. 2001b, ApJ, 561, L89
Danziger, I. J., Baade, D., & della Valle, M. 1993, A&A, 276, 382
Davies, M. 1997, MNRAS, 288, 117
Deloye, C. J. & Bildsten, L. 2003, ApJ, 598, 1217
Dempsey, R., Linsky, J., Fleming, T., & Schmitt, J. 1993, ApJS, 86, 599
Dieball, A., Knigge, C., Zurek, D. R., et al. 2005, ApJ, 634, L105
Djorgovski, S. 1993, in ASP Conference Series, Vol. 50, Structure and Dynamics of Globular Clusters, ed. S. Djorgovski & G. Meylan (ASP), 373–382
Dolphin, A. E. 2000a, PASP, 112, 1397
Dolphin, A. E. 2000b, PASP, 112, 1383
Driebe, T., Blöcker, T., Schönberner, D., & Herwig, F. 1999, A&A, 350, 89
Driebe, T., Schönberner, D., Blöcker, T., & Herwig, F. 1998, A&A, 339, 123
Drimmel, R., Cabrera-Lavers, A., & López-Corredoira, M. 2003, A&A, 409, 205
Dubath, P., Meylan, G., & Mayor, M. 1997, A&A, 324, 505
Edmonds, P. D., Gilliland, R. L., Camilo, F., Heinke, C. O., & Grindlay, J. E. 2002, ApJ, 579, 741
Edmonds, P. D., Gilliland, R. L., Heinke, C. O., & Grindlay, J. E. 2003a, ApJ, 596, 1177
Edmonds, P. D., Gilliland, R. L., Heinke, C. O., & Grindlay, J. E. 2003b, ApJ, 596, 1197
Edmonds, P. D., Gilliland, R. L., Heinke, C. O., Grindlay, J. E., & Camilo, F. 2001, ApJ, 557, L57
Ergma, E., Sarna, M. J., & Antipova, J. 1998, MNRAS, 300, 352
Ergma, E., Sarna, M. J., & Gerškevitš-Antipova, J. 2001, MNRAS, 321, 71
Fabian, A. C., Pringle, J. E., & Rees, M. J. 1975, MNRAS, 172, 15P
Farihi, J. 2004, ApJ, 610, 1013
Feissel, M. & Mignard, F. 1998, A&A, 331, L33
Fender, R. P., Gallo, E., & Jonker, P. G. 2003, MNRAS, 343, L99
Ferraro, F. R., Possenti, A., D'Amico, N., & Sabbi, E. 2001, ApJ, 561, L93
Ferraro, F. R., Possenti, A., Sabbi, E., & D'Amico, N. 2003a, ApJ, 596, L211
Ferraro, F. R., Sabbi, E., Gratton, R., et al. 2003b, ApJ, 584, L13
Filippenko, A. V. 1982, PASP, 94, 715
Finley, D. S., Koester, D., & Basri, G. 1997, ApJ, 488, 375
Freeman, P. E., Kashyap, V., Rosner, R., & Lamb, D. Q. 2002, ApJS, 138, 185
Freire, P. C. C., Hessels, J. W. T., Nice, D. J., et al. 2005, ApJ, 621, 959
Fruchter, A. S., Gunn, J. E., Lauer, T. R., & Dressler, A. 1988, Nature, 334, 686
Gänsicke, B. T., Braje, T. M., & Romani, R. W. 2002, A&A, 386, 1001
Garcia, M. R., McClintock, J. E., Narayan, R., et al. 2001, ApJ, 553, L47
Gehrels, N. 1986, ApJ, 303, 336
Gendre, B., Barret, D., & Webb, N. 2003, A&A, 403, L11
Giacconi, R., Murray, S., Gursky, H., et al. 1974, ApJS, 27, 37
Giacconi, R., Rosati, P., Tozzi, P., et al. 2001, ApJ, 551, 624
Girardi, L., Bressan, A., Bertelli, G., & Chiosi, C. 2000, A&AS, 141, 371

Goodman, J. 1987, ApJ, 313, 576
Gratton, R. G., Bragaglia, A., Carretta, E., et al. 2003, A&A, 408, 529
Gratton, R. G., Bragaglia, A., Carretta, E., et al. 2005, A&A, 440, 901
Green, P. J., Silverman, J. D., Cameron, R. A., et al. 2004, ApJS, 150, 43
Grindlay, J., Heinke, C., Edmonds, P., , & Murray, S. 2001a, Science, 292, 2290
Grindlay, J., Heinke, C., Edmonds, P., et al. 2001b, ApJ, 563, L53
Hack, W. & Cox, C. 2001, Revised IDCTAB Definition: Application to HST Data (Instrum. Sci. Rep. ACS 2001-008; Baltimore: STScI)
Haensel, P. & Zdunik, J. L. 1990, A&A, 227, 431
Hambly, N. C., Smartt, S. J., Hodgkin, S. T., et al. 1999, MNRAS, 309, L33
Hameury, J.-M., Barret, D., Lasota, J.-P., et al. 2003, A&A, 399, 631
Hamuy, M., Suntzeff, N. B., Heathcote, S. R., et al. 1994, PASP, 106, 566
Hamuy, M., Walker, A. R., Suntzeff, N. B., et al. 1992, PASP, 104, 533
Hansen, B. M. S. 1998, Nature, 394, 860
Hansen, B. M. S. & Phinney, E. S. 1998a, MNRAS, 294, 557
Hansen, B. M. S. & Phinney, E. S. 1998b, MNRAS, 294, 569
Harris, H. C., Dahn, C. C., Vrba, F. J., et al. 1999, ApJ, 524, 1000
Harris, W. 1996, AJ, 112, 1487
Heinke, C., Edmonds, P., Grindlay, J., et al. 2003, ApJ, 590, 809
Heinke, C. O., Grindlay, J. E., Edmonds, P. D., et al. 2005, ApJ, 625, 796
Heinke, C. O., Grindlay, J. E., Lugger, P. M., et al. 2003, ApJ, 598, 501
Heintz, W. D. 1988, PASP, 100, 834
Herschel, W. 1803, Philosophical Transactions Series I, 93, 339
Hertz, P. & Grindlay, J. 1983, ApJ, 275, 105
Hills, J. G. 1976, MNRAS, 175, 1P
Holtzman, J. A., Burrows, C. J., Casertano, S., et al. 1995a, PASP, 107, 1065
Holtzman, J. A., Hester, J. J., Casertano, S., et al. 1995b, PASP, 107, 156
Homeier, D., Koester, D., Hagen, H.-J., et al. 1998, A&A, 338, 563
Homer, L., Charles, P., Naylor, T., et al. 1996, MNRAS, 282, L37
Horne, K. 1986, PASP, 98, 609
Hummer, D. G. & Mihalas, D. 1988, ApJ, 331, 794
Hut, P., McMillan, S., Goodman, J., et al. 1992, PASP, 104, 981
Hut, P. & Verbunt, F. 1983, Nature, 301, 587
in't Zand, J. J. M., Cornelisse, R., Kuulkers, E., et al. 2001, A&A, 372, 916
in't Zand, J. J. M., Cornelisse, R., & Méndez, M. 2005, A&A, 440, 287
Jacoby, B. A., Hotan, A., Bailes, M., Ord, S., & Kulkarni, S. R. 2005, ApJ, 629, L113
Johnston, H. & Verbunt, F. 1996, A&A, 312, 80
Jonker, P. G., Campana, S., Steeghs, D., et al. 2005, MNRAS, 361, 511
Jonker, P. G., Galloway, D. K., McClintock, J. E., et al. 2004, MNRAS, 354, 666
Jonker, P. G., Méndez, M., Nelemans, G., Wijnands, R., & van der Klis, M. 2003, MNRAS, 341, 823
Jonker, P. G. & Nelemans, G. 2004, MNRAS, 354, 355
Joss, P. C., Rappaport, S., & Lewis, W. 1987, ApJ, 319, 180

Joy, A. H. & Sanford, R. F. 1926, ApJ, 64, 250
Juett, A. M. & Chakrabarty, D. 2003, ApJ, 599, 498
Juett, A. M. & Chakrabarty, D. 2005, ApJ, 627, 926
Kaluzny, J., Rucinski, S. M., & Thompson, I. B. 2003, AJ, 125, 1546
Kaluzny, J., Thompson, I. B., & Krzeminski, W. 1997, AJ, 113, 2219
Katz, J. I. 1975, Nature, 253, 698
King, A. R. & Wijnands, R. 2006, MNRAS, 366, L31
Kitamura, H. 2000, ApJ, 539, 888
Knude, J. 1979, A&A, 71, 344
Koester, D., Napiwotzki, R., Voss, B., Homeier, D., & Reimers, D. 2005, A&A, 439, 317
Kong, A. K. H., McClintock, J. E., Garcia, M. R., Murray, S. S., & Barret, D. 2002, ApJ, 570, 277
Kraft, R. P., Mathews, J., & Greenstein, J. L. 1962, ApJ, 136, 312
Kuulkers, E., den Hartog, P. R., in't Zand, J. J. M., et al. 2003, A&A, 399, 663
Landolt, A. U. 1992, AJ, 104, 340
Lange, C., Camilo, F., Wex, N., et al. 2001, MNRAS, 326, 274
Lattimer, J. M. & Prakash, M. 2004, Science, 304, 536
Le Borgne, J.-F., Bruzual, G., Pelló, R., et al. 2003, A&A, 402, 433
Lenzuni, P., Chernoff, D. F., & Salpeter, E. E. 1991, ApJS, 76, 759
Lewin, W. H. G., Li, F. K., Hoffman, J. A., et al. 1976, MNRAS, 177, 93P
Liu, Q. Z., van Paradijs, J., & van den Heuvel, E. P. J. 2001, A&A, 368, 1021
Lorimer, D. R., Lyne, A. G., Festin, L., & Nicastro, L. 1995, Nature, 376, 393
Lugger, P. M., Cohn, H. N., & Grindlay, J. E. 1995, ApJ, 439, 191
Lundgren, S. C., Cordes, J. M., Foster, R. S., Wolszczan, A., & Camilo, F. 1996, ApJ, 458, L33
Lundgren, S. C., Zepka, A. F., & Cordes, J. M. 1995, ApJ, 453, 419
Lynden-Bell, D. & Wood, R. 1968, MNRAS, 138, 495
Lyne, A., Bigss, J., Brinklow, A., Ashworth, & McKenna, J. 1988, Nature, 332, 45
Lyne, A. G., Burgay, M., Kramer, M., et al. 2004, Science, 303, 1153
Manchester, R. N., Hobbs, G. B., Teoh, A., & Hobbs, M. 2005, AJ, 129, 1993
Manchester, R. N., Lyne, A. G., Camilo, F., et al. 2001, MNRAS, 328, 17
Mathieu, R. D., van den Berg, M., Torres, G., et al. 2003, AJ, 125, 246
Matthews, K. & Soifer, B. T. 1994, in ASSL Vol. 190: Astronomy with Arrays, The Next Generation, 239
McClintock, J. E., Horne, K., & Remillard, R. A. 1995, ApJ, 442, 358
Menou, K., Esin, A. A., Narayan, R., et al. 1999, ApJ, 520, 276
Michell, J. 1767, Philosophical Transactions Series I, 57, 234
Mihalas, D., Dappen, W., & Hummer, D. G. 1988, ApJ, 331, 815
Mihalas, D., Hummer, D. G., Mihalas, B. W., & Daeppen, W. 1990, ApJ, 350, 300
Mochejska, B. J., Kaluzny, J., Thompson, I., & Pych, W. 2002, AJ, 124, 1486
Monet, D. G., Levine, S. E., Canzian, B., et al. 2003, AJ, 125, 984
Narayan, R., Garcia, M. R., & McClintock, J. E. 1997, ApJ, 478, L79
Narayan, R. & Yi, I. 1994, ApJ, 428, L13

Nelemans, G., Hartman, J. W., Verbunt, F., Bhattacharya, D., & Wijers, R. A. M. J. 1997, A&A, 322, 489
Nelemans, G. & Jonker, P. G. 2006, astro-ph/0605722
Nelemans, G., Jonker, P. G., Marsh, T. R., & van der Klis, M. 2004, MNRAS, 348, L7
Nelson, L. A., Dubeau, E., & MacCannell, K. A. 2004, ApJ, 616, 1124
Nelson, L. A., Rappaport, S. A., & Joss, P. C. 1986, ApJ, 304, 231
Nice, D. J., Splaver, E. M., & Stairs, I. H. 2005a, in ASP Conference Series, Vol. 328, Binary Radio Pulsars, ed. F. A. Rasio & I. H. Stairs, 371
Nice, D. J., Splaver, E. M., Stairs, I. H., et al. 2005b, ApJ, 634, 1242
Oke, J. B. 1990, AJ, 99, 1621
Oke, J. B., Cohen, J. G., Carr, M., et al. 1995, PASP, 107, 375
Oppenheimer, B. R., Saumon, D., Hodgkin, S. T., et al. 2001, ApJ, 550, 448
Orosz, J. A. & van Kerkwijk, M. H. 2003, A&A, 397, 237
Panei, J. A., Althaus, L. G., & Benvenuto, O. G. 2000, A&A, 353, 970
Peterson, C. J. 1993, in ASP Conf. Ser. 50: Structure and Dynamics of Globular Clusters, ed. S. G. Djorgovski & G. Meylan, 337
Phinney, E. S. & Kulkarni, S. R. 1994, ARA&A, 32, 591
Piro, L., Heise, J., Jager, R., et al. 1997, IAU Circ., 6538
Podsiadlowski, P., Rappaport, S., & Pfahl, E. D. 2002, ApJ, 565, 1107
Pooley, D., Lewin, W., Homer, L., et al. 2002a, ApJ, 569, 405
Pooley, D., Lewin, W., Verbunt, F., et al. 2002b, ApJ, 573, 184
Pooley, D., Lewin, W. H. G., Anderson, S. F., et al. 2003, ApJ, 591, L131
Possenti, A., D'Amico, N., Corongiu, A., et al. 2005, in ASP Conf. Ser. 328: Binary Radio Pulsars, ed. F. A. Rasio & I. H. Stairs, 189
Poutanen, J. 2005, astro-ph/0510038
Predehl, P. & Schmitt, J. 1995, A&A, 293, 889
Press, W. H., Teukolsky, S. A., Vetterling, W. T., & Flannery, B. P. 1992, Numerical recipes: The art of scientific computing (Cambridge: University Press, 2nd ed.)
Rappaport, S., Podsiadlowski, P., Joss, P. C., Di Stefano, R., & Han, Z. 1995, MNRAS, 273, 731
Reid, C. A., Johnston, M. D., Bradt, H. V., et al. 1980, AJ, 85, 1062
Reid, I. N. 1996, AJ, 111, 2000
Renzini, A., Bragaglia, A., Ferraro, F. R., et al. 1996, ApJ, 465, L23
Richer, H., Fahlman, G., Ibata, R., & et. al. 1995, ApJ, 451, L17
Richer, H. B., Fahlman, G. G., Ibata, R. A., et al. 1997, ApJ, 484, 741
Richer, H. B., Ibata, R., Fahlman, G. G., & Huber, M. 2003, ApJ, 597, L45
Rieke, G. H. & Lebofsky, M. J. 1985, ApJ, 288, 618
Ritter, H. & Kolb, U. 2003, A&A, 404, 301
Rohrmann, R. D., Serenelli, A. M., Althaus, L. G., & Benvenuto, O. G. 2002, MNRAS, 335, 499
Rutledge, R., Bildsten, L., Brown, E., Pavlov, G., & Zavlin, V. 2002, ApJ, 578, 405
Rutledge, R. E., Bildsten, L., Brown, E. F., Pavlov, G. G., & Zavlin, V. E. 1999, ApJ, 514, 945

Rutledge, R. E., Bildsten, L., Brown, E. F., Pavlov, G. G., & Zavlin, V. E. 2002a, ApJ, 577, 346
Rutledge, R. E., Bildsten, L., Brown, E. F., et al. 2002b, ApJ, 580, 413
Ryba, M. F. & Taylor, J. H. 1991, ApJ, 371, 739
Salpeter, E. E. & van Horn, H. M. 1969, ApJ, 155, 183
Sarazin, C., Irwin, J., Rood, R., & et al. 1999, ApJ, 524, 220
Sarna, M. J., Ergma, E., & Gerškevitš-Antipova, J. 2000, MNRAS, 316, 84
Saumon, D., Bergeron, P., Lunine, J. I., Hubbard, W. B., & Burrows, A. 1994, ApJ, 424, 333
Savonije, G. J., de Kool, M., & van den Heuvel, E. P. J. 1986, A&A, 155, 51
Schönberner, D., Driebe, T., & Blöcker, T. 2000, A&A, 356, 929
Schlegel, D. J., Finkbeiner, D. P., & Davis, M. 1998, ApJ, 500, 525
Serenelli, A. M., Althaus, L. G., Rohrmann, R. D., & Benvenuto, O. G. 2001, MNRAS, 325, 607
Serenelli, A. M., Althaus, L. G., Rohrmann, R. D., & Benvenuto, O. G. 2002, MNRAS, 337, 1091
Seward, F. D., Page, C. G., Turner, M. J. L., & Pounds, K. A. 1976, MNRAS, 175, 39P
Sheinis, A. I., Bolte, M., Epps, H. W., et al. 2002, PASP, 114, 851
Sigurdsson, S., Richer, H. B., Hansen, B. M. S., Stairs, I. H., & Thorsett, S. E. 2003, Science, 301, 193
Splaver, E. M., Nice, D. J., Stairs, I. H., Lommen, A. N., & Backer, D. C. 2005, ApJ, 620, 405
Stairs, I. H. 2004, Science, 304, 547
Stappers, B. W., van Kerkwijk, M. H., Lane, B., & Kulkarni, S. R. 1999, ApJ, 510, L45
Stępień, K., Schmitt, J. H. M. M., & Voges, W. 2001, A&A, 370, 157
Stebbins, J. 1914, ApJ, 39, 459
Stella, L., Priedhorsky, W., & White, N. 1987, ApJ, 312, L17
Stetson, P. B. 1987, PASP, 99, 191
Stetson, P. B. 2000, PASP, 112, 925
Strohmayer, T. E., Markwardt, C. B., Swank, J. H., & in't Zand, J. 2003, ApJ, 596, L67
Tauris, T. M. & Savonije, G. J. 1999, A&A, 350, 928
Taylor, J. H. & Cordes, J. M. 1993, ApJ, 411, 674
Taylor, J. M., Grindlay, J. E., Edmonds, P. D., & Cool, A. M. 2001, ApJ, 553, L169
Thorsett, S., Arzoumanian, Z., Camilo, F., & Lyne, A. 1999, ApJ, 523, 763
Thorsett, S. E. & Chakrabarty, D. 1999, ApJ, 512, 288
Tomsick, J. A., Gelino, D. M., & Kaaret, P. 2005, ApJ, 635, 1233
Trager, S., Djorgovski, S., & King, I. 1993, in ASP Conference Series, Vol. 50, Structure and Dynamics of Globular Clusters, ed. S. Djorgovski & G. Meylan (ASP), 347–355
Tutukov, A. V., Fedorova, A. V., Ergma, E. V., & Yungel'Son, L. R. 1985, Pis ma Astronomicheskii Zhurnal, 11, 123
Ushomirsky, G. & Rutledge, R. E. 2001, MNRAS, 325, 1157
van den Berg, M., Tagliaferri, G., Belloni, T., & Verbunt, F. 2004, A&A, 418, 509
van der Sluys, M. V., Verbunt, F., & Pols, O. R. 2005a, A&A, 431, 647
van der Sluys, M. V., Verbunt, F., & Pols, O. R. 2005b, A&A, 440, 973

van Kerkwijk, M. H., Bassa, C. G., Jacoby, B. A., & Jonker, P. G. 2005, in ASP Conference Series, Vol. 328, Binary Radio Pulsars, ed. F. A. Rasio & I. H. Stairs (ASP), 357
van Kerkwijk, M. H., Bell, J. F., Kaspi, V. M., & Kulkarni, S. R. 2000, ApJ, 530, L37
van Kerkwijk, M. H., Bergeron, P., & Kulkarni, S. R. 1996, ApJ, 467, L89
van Kerkwijk, M. H. & Kulkarni, S. R. 1995, ApJ, 454, L141
van Paradijs, J., Allington-Smith, J., Callanan, P., Hassall, B. J. M., & Charles, P. A. 1988, Nature, 334, 684
van Paradijs, J. & McClintock, J. E. 1994, A&A, 290, 133
van Paradijs, J. & McClintock, J. E. 1995, in X-ray Binaries, ed. W. H. G. Lewin, J. van Paradijs, & E. P. J. van den Heuvel (Cambridge Astrophysics Series, Cambridge, MA: Cambridge University Press), 58
van Paradijs, J., Verbunt, F., Shafer, R., & Arnaud, K. 1987, A&A, 182, 47
van Straten, W., Bailes, M., Britton, M., et al. 2001, Nature, 412, 158
Vauclair, G., Schmidt, H., Koester, D., & Allard, N. 1997, A&A, 325, 1055
Verbunt, F. 1987, ApJ, 312, L23
Verbunt, F. 1993, ARA&A, 31, 93
Verbunt, F. 2001, A&A, 368, 137
Verbunt, F. 2002, in ASP Conf. Ser. 265: Omega Centauri, A Unique Window into Astrophysics, ed. F. van Leeuwen, J. D. Hughes, & G. Piotto, 289
Verbunt, F. 2003, in New horizons in globular cluster astronomy, ed. S. D. G. Piotto, G. Meylan & M. Riello (ASP Conf. Ser. Vol. 296), 245–254
Verbunt, F., Belloni, T., Johnston, H., van der Klis, M., & Lewin, W. 1994, A&A, 285, 903
Verbunt, F. & Hut, P. 1987, in The Origin and Evolution of Neutron Stars, IAU Symposium No. 125, ed. D. Helfand & J.-H. Huang (Dordrecht: Reidel), 187–197
Verbunt, F. & Johnston, H. 2000, A&A, 358, 910
Verbunt, F. & Lewin, W. H. G. 2006, Globular cluster X-ray sources (Compact stellar X-ray sources. Edited by Walter Lewin & Michiel van der Klis. Cambridge Astrophysics Series, No. 39. Cambridge, UK: Cambridge University Press), 341–379
Verbunt, F. & van den Heuvel, E. 1995, Formation andevolution of neutron stars and black holes in binaries, eds Lewin, van Paradijs, van den Heuvel (Cambridge University Press, 1995.)
Wagner, R. M., Starrfield, S. G., Hjellming, R. M., Howell, S. B., & Kreidl, T. J. 1994, ApJ, 429, L25
Wang, Z. & Chakrabarty, D. 2004, ApJ, 616, L139
Webbink, R. F. 1975, MNRAS, 171, 555
Webbink, R. F. 1985, in IAU Symp. 113: Dynamics of Star Clusters, ed. J. Goodman & P. Hut, 541–577
Wesemael, F., Greenstein, J. L., Liebert, J., et al. 1993, PASP, 105, 761
Wijnands, R. 2005, `astro-ph/0501264`
Wijnands, R., Guainazzi, M., van der Klis, M., & Méndez, M. 2002, ApJ, 573, L45
Wijnands, R., Homan, J., Heinke, C. O., Miller, J. M., & Lewin, W. H. G. 2005, ApJ, 619, 492
Wijnands, R., Homan, J., Miller, J. M., & Lewin, W. H. G. 2004, ApJ, 606, L61

Wijnands, R., Miller, J. M., Markwardt, C., Lewin, W. H. G., & van der Klis, M. 2001, ApJ, 560, L159
Wilson, C. A., Patel, S. K., Kouveliotou, C., et al. 2003, ApJ, 596, 1220
Yakovlev, D. G., Kaminker, A. D., & Levenfish, K. P. 1999, A&A, 343, 650
Yakovlev, D. G., Levenfish, K. P., & Gnedin, O. Y. 2005, The European Physical Journal A, Volume 25, Supplement, Issue 1, pp.669-672, 25, 669
Yakovlev, D. G., Levenfish, K. P., & Haensel, P. 2003, A&A, 407, 265
Yakovlev, D. G. & Pethick, C. J. 2004, ARA&A, 42, 169
Yakovlev, D. G. & Urpin, V. A. 1980, Soviet Astronomy, 24, 303
Yungelson, L. R., Nelemans, G., & van den Heuvel, E. P. J. 2002, A&A, 388, 546
Zacharias, N., Urban, S. E., Zacharias, M. I., et al. 2000, AJ, 120, 2131
Zacharias, N., Urban, S. E., Zacharias, M. I., et al. 2004, AJ, 127, 3043
Zavlin, V. E., Pavlov, G. G., & Shibanov, Y. A. 1996, A&A, 315, 141
Zimmermann, H., Becker, W., Belloni, T., et al. 1996, EXSAS User's Guide: Extended scientific analysis system to evaluate data from the astronomical X-ray satellite ROSAT, Edition 5, Tech. rep., MPE

List of publications

Refereed

Bassa, C.G., van Kerkwijk, M.H., Kulkarni, S.R., 2003, *"Temperature and cooling age of the white dwarf companion of PSR J0218+4232"*, A&A 403, 1067–1075

Bassa, C.G., Verbunt, F., van Kerkwijk, M.H., Homer, L., 2003, *"Optical identification of the companion to PSR J1911−5958A, the pulsar binary in the outskirts of NGC 6752"*, A&A 409, L31–L34 (Chapter 4)

Ransom, S.M., Stairs, I.H., Backer, D.C., Greenhill, L.J., Bassa, C.G., Hessels, J.W.T., Kaspi, V.M., 2004, *"Green Bank Telescope discovery of two binary millisecond pulsars in the globular cluster M30"*, ApJ 604, 328–338

Bassa, C., Pooley, D., Homer, L., Verbunt, F., Gaensler, B. M., Lewin, W. H. G., Anderson, S. F., Margon, B., Kaspi, V. M., van der Klis, M., 2004, *"X-ray sources and their optical counterparts in the globular cluster M4"*, ApJ 609, 755–765 (Chapter 2)

Bassa, C. G., Stappers, B. W., 2004, *"Celestial position of the companion of PSR J1740−5340"*, A&A 425, 1143–1145 (Chapter 6)

Bassa, C., Pooley, D., Homer, L., Verbunt, F., Gaensler, B. M., Lewin, W. H. G., Anderson, S. F., Margon, B., Kaspi, V. M., van der Klis, M., 2005, Addendum: *"X-ray sources and their optical counterparts in the globular cluster M4"*, ApJ 619, 1189 (Chapter 2)

Bassa, C.G., Jonker, P.G., in 't Zand, J.J.M., Verbunt, F., 2006, *"Two new candidate ultra-compact X-ray binaries"*, A&A 446, L17–L20 (Chapter 8)

Bassa, C.G., van Kerkwijk, M.H., Kulkarni, S.R., 2006, *"The ultra-cool white dwarf*

companion of PSR J0751+1807", A&A 450, 295–303 (Chapter 7)

Jonker, P.G., Bassa, C.G., Nelemans, G., Juett, A.M., Brown, E.F., Chakrabarty, D., 2006, *"The neutron star soft X-ray transient 1H 1905+000 in quiescence"*, MNRAS 368, 1803–1810 (Chapter 9)

Kong, A.K.H., Bassa, C.G., Pooley, D., Lewin, W.H.G., Homer, L., Verbunt, F., Anderson, S.F., Margon, B. 2006, *"Chandra and Hubble Space Telescope Study of the Globular Cluster NGC 288"*, ApJ 647 1065–1074 (Chapter 3)

Bassa, C.G., van Kerkwijk, M.H., Koester, D., Verbunt, F., 2006, *"The masses of PSR J1911−5958A and its white dwarf companion"*, A&A 456, 295–304 (Chapter 5)

Conference proceedings

Verbunt, F., Bassa, C. 2003, *"X-ray sources in globular clusters"*, Chin. J. Astron. Astrophys. Vol. 3, Suppl., 225–234

van Kerkwijk, M. H., Bassa, C. G., Jacoby, B. A., Jonker, P. G., 2005, *"Optical studies of companions to millisecond pulsars"*, in "Binary Radio Pulsars", ASP Conference Series, Vol. 328, 357–369, eds. F. A. Rasio and I. H. Stairs.

In press

Jonker, P.G., Nelemans, G., Bassa, C.G., 2006, *"Detection of the radial velocity curve of the B5-A0 supergiant companion of Cir X-1?"*, MNRAS, accepted.

Submitted

Jonker, P.G. Bassa, C.G., Wachter, S., 2006, *"The neutron star soft X-ray transient 1M 1716−315 in quiescence"*, MNRAS, in press.

Curriculum vitae

Op 16 oktober 1978 ben ik in het ziekenhuis te Tiel geboren. Ik volgde de lagere school op de basisschool *de Lingelaar* te Beesd, waarna ik in 1991 aan de MAVO op het *Prins Willem Alexander College* te Leerdam begon. Na twee brugklassen te hebben doorlopen behaalde ik in 1997 mijn VWO diploma.

In september van dat jaar begon ik aan de studie Natuur en Sterrenkunde aan de Universiteit Utrecht. Mijn propedeutisch examen behaalde ik in januari 2000. Onder begeleiding van prof. dr. M. H. van Kerkwijk startte ik in oktober 2001 met mijn afstudeeronderzoek aan waarnemingen van de witte dwerg begeleider van PSR J0218+4232, wat resulteerde in een artikel in het tijdschrift Astronomy & Astrophysics. Het doctoraal examen in de Natuur- en Sterrenkunde behaalde ik op 28 oktober 2002.

Onder begeleiding van prof. dr. F. W. M. Verbunt startte ik per 1 januari 2003 als assistent in opleiding in het Sterrenkundig Instituut van de Universiteit Utrecht. Tijdens het promotieonderzoek ben ik voor samenwerkingen in Seattle, Toronto, Pasadena en Boston geweest. Daarnaast heb ik deelgenomen aan conferenties en workshops in Santa Barbara, Aspen, Céfalu, en Lund. Ik heb waargenomen met optische telescopen vanaf Mauna Kea, Hawaii en Cerro Tololo, Chili.

Dankwoord/Acknowledgements

Een proefschrift maak je niet alleen, en mijn dank gaat uit naar diegenen die er direct en indirect aan hebben bijgedragen.

Allereerst wil ik mijn promotoren bedanken. Frank, ik kan me niet meer herinneren hoevaak ik mezelf heb verbaasd om je kennis van zaken binnen en buiten de sterrenkunde, en ik heb hier veel van geleerd. Deze gesprekken kleurden menige wandeling van en naar de warme chocolademelk op het SRON. Ik heb de afgelopen jaren als heel prettig ervaren en ik heb veel plezier beleefd aan onze gesprekken over het fitten van data, positionele en historische sterrenkunde en wat al niet meer zij.

Marten, als afstudeerbegeleider heb je me de beginselen van de reductie van data bijgebracht. Deze kennis staat aan de basis van alle hoofdstukken van dit proefschrift. Ik heb je nooit echt kunnen bedanken voor het begeleiden van mijn afstudeeronderzoek, dus ik was erg blij dat je, naast co-auteur op bijna de helft van de voorgaande hoofdstukken, ook als promotor bij dit proefschrift betrokken wilde zijn. Bedankt voor je bijdrage en de altijd snelle antwoorden op mijn vragen per e-mail. Ik hoop dat we in Canada verder en nader kunnen blijven samenwerken.

Graag bedank ik ook de leden van de beoordelingscomissie, Christoph Keller, Johan Bleeker, John Heise, Michiel van der Klis en Gijs Nelemans, voor hun commentaar op dit proefschrift.

Furthermore, I would like to thank Lee Homer and Dave Pooley for their cooperation. It is a pity the globular cluster project never got rolling the way we planned. Also, thanks to Shri Kulkarni for inviting me to Caltech and for an observing run at Keck. Ben Stappers, thanks for inviting me to the Dutch pulsar meetings, answering my questions regarding timing and for writing a letter of recommendation.

Peter, sinds we voor het eerst bij de SRON koffie over optische waarnemingen begonnen te praten heb je me bij allerlei projecten betrokken, waaronder de tien nachten CTIO tijd in Chili. Ik vond het erg leuk om met je samen te werken, en daar zal ook nog wel even geen eind aan komen (1 down, 200 GB more to go).

Beste Arend Jan, al ruim 5 jaar bezetten we kamer 702a, maar ik heb het gevoel dat het veel langer is. Ik wil je bedanken voor het delen van elkanders ervaringen en problemen

omtrent onderzoek, promotie(begeleider) en het leven binnen en buiten de universiteit.

Voor het oplossen van allerhande problemen met computers en netwerk wil ik Ed en Sake graag bedanken. Nu ik zie hoe het er op andere instituten aan toe gaat ben ik dankbaar dat er in Utrecht wel support op dezelfde gang zit (en dat verstandig gebruik van het root-wachtwoord wordt gedoogd). Ook wil ik Marion bedanken voor haar hulp bij alle problemen waar je als afstudeerstudent en promovendus tegen aan loopt. Verder bedank ik alle collega's op het SIU, waar onder ook oudgedienden (Alfred, Ferdi, Joeri, Marc en Mark).

Voor de leuke tijd tijdens de studie en daarna ben ik Channah, Peter (van G.), Ronald, Peter (den H.), en Joke erg dankbaar. Zonder jullie zou ik nooit zover zijn gekomen. Verder wil ik Rob bedanken voor de gesprekken in de trein en op de fiets, en samen met Rietje voor de geslaagde eclips-expedities.

Wilma, Jos, Coen en Linda bedank ik voor de gezelligheid in Oss. Als laatste wil ik mijn zusjes, Elise, Janneke en Marry en mijn ouders, Gert en Marian bedanken voor hun steun en interesse. De boerderij is altijd een plaats geweest waar andere dingen belangrijk waren en waar zorgen en problemen in perspectief gezet werden. Er zal voor ons allemaal veel veranderen.

Gemma, ik prijs me gelukkig mijn leven te kunnen delen met je. Wat de toekomst ook mag brengen, ik hoop dat we het samen beleven.